INSIGHTS INTO THE EVOLUTION OF THE GALÁPAGOS ARCHIPELAGO AND ITS MANTLE SOURCE FROM MONOGENETIC NEAR-ISLAND SEAMOUNTS

by

Darin M. Schwartz

A dissertation

submitted in partial fulfillment

of the requirements for the degree of

Doctor of Philosophy in Geosciences

Boise State University

August 2019

BOISE STATE UNIVERSITY GRADUATE COLLEGE

DEFENSE COMMITTEE AND FINAL READING APPROVALS

of the thesis submitted by

Darin M. Schwartz

Thesis Title: Insights into the Evolution of the Galápagos Archipelago and Its Mantle Source from Monogenetic Near-Island Seamounts

Date of Final Oral Examination: 31 July 2019

The following individuals read and discussed the thesis submitted by student Darin M. Schwartz, and they evaluated his presentation and response to questions during the final oral examination. They found that the student passed the final oral examination.

V. Dorsey Wanless, Ph.D.	Chair, Supervisory Committee
Mark Schmitz, Ph.D.	Member, Supervisory Committee
Brittany Brand, Ph.D.	Member, Supervisory Committee
Corey Wall, Ph.D.	Member, Supervisory Committee

The final reading approval of the thesis was granted by V. Dorsey Wanless, Ph.D., Chair of the Supervisory Committee. The thesis was approved by the Graduate College.

DEDICATION

This is dedicated to my friends and family who support me in the things I do.

ACKNOWLEDGEMENTS

I would first like to acknowledge my advisor, Dorsey Wanless for her mentorship throughout my dissertation, providing immense amounts of critical feedback and time discussing all aspects of the scientific processes with me, as well as facilitating all of the research that I have been a part of while at Boise State University (BSU). I would also like to thank Mark Schmitz for his mentorship, especially that related to the analytical details of this dissertation as well as offering many thought-provoking discussions and his general open mindedness. I am grateful to my other committee members including Brittany Brand for tireless field training and guidance in writing and Corey Wall for many enthusiastic discussions related to the more perplexing subject matter in this dissertation. Together, I thank the above for serving on my dissertation committee. I thank other mentors of mine including Adam Soule, Dan Fornari, Karen Harpp, Keegan Schmidt and Reed Lewis who are gratefully acknowledged for taking me on as a lifetime pupil of theirs.

I am grateful to all of the facilities, lab operators and technicians who have allowed me to work in their space and who have shared their knowledge with me throughout my time at BSU. This includes Marion Lytle, Jim Crowley, Matt Kohn and the administrative staff at Boise State; Scott Boroughs at Washington State University; Mark Kurz and Joshua Curtice at Woods Hole Oceanographic Institute.

I thank all who have aided in data collection and sample processing for all of the projects comprising my dissertation. This includes shipboard personnel and scientists

aboard the M/V *Alucia* and R/V *Nautilus*. We gratefully acknowledge colleagues at the Charles Darwin Foundation and the Galápagos National Park and Ecuadorian Navy for facilitating research in the Galápagos. I thank all who have helped me prepare samples for analysis, specifically including Emma McCully, Jessie Bell and Cecelia Wheeler for exceptionally large portions of help as well as innumerable other students and friends for assistance along the way.

I have many academic colleagues to thank for many long discussions regarding the work presented herein, whose inspiring conversations, thoughts and ideas go back to before my time at BSU. In relatively chronological order I thank Erika Rader, Madison Meyers, James Muirhead, Matt Pendleton, Thomas Morrow, Alex Moody, Emily Wilson, Jeff Larimer, Meghan Jones, Amanda Drewicz, Andrew Gase, Nick Pollock, Erin Murray, John Shuler, Alex Witsil, Robin Trayler, Molly Anderson, Mike Mohr, Emma McCully, Carson MacPherson-Krutsky, Gavin Kenny. I thank all of my unnamed friends and family for their presence in my life, both in and outside of academia.

This work has been conducted with financial support from Boise State University the National Science Foundation, Dalio Foundation and Ocean Exploration Trust and a Scholarship from the Society for Mining, Metallurgy and Exploration. Following each chapter is an acknowledgement section, which credits these funding sources individually where they are due.

ABSTRACT

Lavas erupted at ocean island volcanoes are classically used as probes of the deep Earth, with ultimate goals of discerning the compositional heterogeneity, structure and dynamics of the Earth's mantle. However, sampling restricted to volcanic islands and large, submarine volcanic constructs alone likely results in limited spatial resolution of the mantle's composition and structure, owing to homogenization in sub-island magma reservoirs. Further, islands provide poor temporal resolution given that their multigenetic construction can overprint any time progressive chemical variations and they subside with age making detailed sampling difficult. For my dissertation I investigate whether seamounts surrounding islands in the Galápagos Archipelago preserve a more spatially distributed record of punctuated, point-source magmatism, providing a different perspective on these deeper processes. The first chapter investigates the physical characteristics of the near-island seamounts resulting in the derivation of a 0.2-0.4 m/ka subsidence rate for the archipelago. Chapters two and three evaluate the magmatic relationship of the seamounts to the islands that they surround. From this, it appears seamounts are closely related to the islands but do indeed preserve a higher resolution picture related to evolution and mantle zonation. An important component of my dissertation has been to mix and calibrate a Pb double spike for internal mass-dependent fractionation correction of Pb isotope measurements at Boise State University in an effort to collect highly accurate and precise isotopic data of the seamount lavas to complement the high-resolution sampling of the seamounts themselves (Chapter 4). Finally, the fifth

chapter uses high precision Pb isotopes to show that all of the isotopic end members in the Galápagos can be produced from the recycling of a single oceanic package.

TABLE OF CONTENTS

LIST OF TABLES

LIST OF FIGURES

INTRODUCTION

Ocean islands are volcanic constructions, which can occur off of major plate boundaries (Weinstein and Olson, 1989). For this reason, their formation is broadly associated with the term ‘hotspot’ that implies a rather anomalous origin, relative to the theory of plate tectonics (Wilson, 1963). Although not all hotspots are created equal (Courtillot et al., 2003), there is broad consensus that magmas sourcing the construction of all ocean islands must be derived from various portions of the deep Earth (i.e., mantle; Hofmann, 1997). Thus, the composition of lavas erupted at ocean islands, similar to ridges, is a function of their mantle source, modified by magmatic processes (melting; e.g., Kamenetsky and Maas, 2002; and crystallization; e.g., Zielinski, 1975) and subsequent alteration after eruption (Hart et al., 1974). Interestingly, from a compositional perspective, it is clear that the mantle source of some hotspots varies from that which sources mid-ocean ridges (Gale et al., 2013). This observation is significant because, what is obviously different from the geochemical lens is not obviously observed in the mantle itself, owing to its general inaccessibility for direct observation and sampling. In turn, the compositional signals within ridges and hotspots are together used as probes of the deep Earth (Hofmann, 1997; Dixon et al., 2017). These signals are translated to depict the structure of the Earth’s mantle as well as its relationship to both the core, and its outermost layers like the crust, biosphere and atmosphere.

The mantle picture resulting from a combined view of geochemical signatures of global hotspot volcanism and that of mid-ocean ridges has significantly evolved since the

conception of plate tectonics and hotspot theory nearly a half-centrury ago (Wilson, 1963). Early interpretations of chemical diversity of lavas at ocean islands versus ridges resulted in a stratified mantle with distinct reservoirs representing the depleted upper mantle, which was the primary source of mid-ocean ridge basalt and deeper, isolated primitive mantle (e.g., Schilling, 1973). This interpretation has been replaced by models that include whole mantle convection (Hart et al., 1992), limiting the reservoir for storing a significant portion of primitive mantle, or a hybrid of the two (Olson et al., 1990). Other geochemical flavors sampled primarily by hotspots, termed enriched mantle reservoirs, are resultant from subduction zone recycling of oceanic crust (Hofmann and White, 1982), continental crust and pelagic sediments (Zindler and Hart; 1986). While the exact interpretation of the array of geochemical flavors is not fixed, there is general consensus that all of these reservoirs exist in the mantle and are sampled by various hotspots around the world, at least to some degree (Hart et al., 1992; Hofmann, 1997).

Another observation from hotspots is that integrated over the archipelago to global scale there are geographically coherent signatures spanning >50 Ma (e.g., Hawaii; Weis et al., 2011; Galápagos; Hoernle et al., 2000 Samoa; Jackson et al., 2014; Society; Payne et al., 2013). These coherencies have been linked to anomalies, which are presently observed in tomographic models of the core mantle boundary (Castillo, 1988). The link between chemical reservoirs and what can be interpreted from seismic images is an exciting prospect, which combines the point-scale observations of ocean islands to global roadmap of the mantle afforded by geophysical observations. However, despite this correlation, the notion of a chemically stratified mantle is at odds with what is predicted by geodynamic simulations of the Earth that indicate material, which enters the

mantle at subduction zones, may be stretched and folded into the ambient mantle and homogenized on relatively short timescales (van Keken et al., 2002). Perhaps this disparity comes from biases arising from the sampling of ocean islands themselves.

Over long timescales, ocean island chains are formed from the dynamic interaction of Earth's mobile lid and hotspot melting anomalies. Relative motions between the two ultimately lead to the cyclic death of one volcanic island and the emergence of another, in the direction of plate motion (Morgan, 1971). At the leading edge of the hotspot, ocean islands are the most active, and their morphology dominated by constructional processes (Ramalho et al., 2013). High magma flux leads to their rapid construction, which ultimately repaves the volcano's surface, obscuring chemical variations arising through time. As islands are transported away from their hotspot source, magma supply wanes and their morphology become dominated by destructive processes subject to erosion and thermal subsidence as the Earth's lithosphere returns to its natural state, out of the influence of the hotspot (Ramalho et al., 2013). The combined effect of these processes leads to the ultimate demise of the ocean island, where it is eventually consumed beneath the sea, to become a seamount. Although this does not preclude their access for observation, it has in the past severely limited the detail by which observations are made, which is a potential limitation surrounding ocean island research. Due to accessibility, a majority of the sampling of OIB is from the subarial portion of these systems or through submarine dredging, which by nature can effectively target only prominent seamounts (Fornari, 2010). The timescales and efficiency of the repaving and subsidence process varies globally based lithospheric properties as well as the rates of cooling and erosion (Detrick and Crough, 1978).

Ocean islands form by partial melting of the mantle (Hofmann, 1997). Thus, the composition of any ocean island lava serves only as a proxy of the composition of the mantle, which care can be translated to directly represent the mantle based on empirical or theoretical relationships (e.g., Zou, 1998). This proxy issue serves as a second major limitation of ocean island's utility in studying the mantle. Degree of melting strongly modulates the absolute and relative abundances of trace elements in a magma (Kamenetsky and Maas, 2002). Once formed, these melts must be transported to the shallow crust where they can erupt on the Earth's surface. Through this magmatic process primary melts of the mantle are compositionally altered through mixing, crystallization and assimilation (e.g., Spiegelman and Kelemen, 2003). Thus, mantle composition including magnitude and spatial scale of a particular reservoir is blurred to an unknown degree. Further, the depth and location of melting is, at least partially, a function of the relative fusibility of compositional zones in the mantle, where easily melted things are the first to be consumed, in a process referred to as dynamic melting (Davies, 2011). In the case of a dynamic mantle, this could lead to spatial variations in lava chemistry that are not related to spatial variation of heterogeneities in the mantle (Jones et al., 2016). In short, dynamic melting is difficult to untangle from source heterogeneity especially related to the interpretation of spatial variations in magma chemistry.

Despite the complexities described above, one geochemical signature is immune to mechanical fractionation, and has become the primary means for interpreting mantle source variations: heavy radiogenic isotopes. In general, mass variations of heavy elements (atomic # > ~75) resulting from less or more neutrons resulting in isotopic variations, are insignificant in affecting their behavior at terrestrial pressures and

temperatures. This is because the mass difference between two heavy isotopes of the same heavy element is relatively small. Thus, the only isotopic variations for heavy elements on Earth occur as a result of loss or addition from radioactive decay. The parent isotope is the radioactive atom, which decays and is lost, and the daughter is the radiogenic atom, generally a different element is what is added. Thus, isotopic composition of a radioactive, non-radiogenic parent element (e.g., Rb, Sm), is a function only of time. By comparison, a non-radioactive element which has a stable daughter isotope (Sr and Nd, relative to the parent isotopes mentioned above) will be a function of time and the relative abundance of the parent and daughter element in whatever geochemical reservoir is of interest. Combined, multiple isotope ratios (classically of Sr, Nd and Pb; e.g., Zindler and Hart., 1986), which are resultant from parent daughter fractionation, whose magnitudes vary by process within a single sample, become a powerful tool by which to understand the origins of heterogeneities observed in ocean islands (e.g., Hofmann, 1997).

The ability to discern endmembers and relationships between various reservoirs using heavy radiogenic isotopes is a function of both analytical precision and availability of samples. For the former, improvements in instrumentation have largely reduced these uncertainties to negligible values for Sr and Nd isotopes (e.g., Yang et al., 2009). However, amidst instrumental and analytical technique driven improvements, high uncertainties under the same circumstances persist for the Pb system in particular, owing to the inability to independently correct for mass dependent fractionation occurring upon analyses (Thirlwall, 2002). Unfortunately, Pb is particularly useful for discerning time and process as there are multiple parent isotopes of different elements that decay to

multiple Pb isotopes (e.g., Stacey and Krammers, 1975). For the latter, care must be taken to design experiments with either accentuates or minimizes the troublesome web of processes laid out in the previous paragraphs.

In this dissertation, I attempt to address the shortcomings and potential biases associated with studying the mantle through ocean island basalts through careful sampling and analysis of lavas from small near-island seamounts. For this work, I focus specifically on the Galápagos hotspot, which has at least three geochemical endmembers that persist with apparent geographic coherence for more than 90 Ma (Gazel et al., 2018). The seamounts targeted in this investigation surround islands, which represent the three dominant geochemical domains pervasive in the geologic record of the hotspot. The seamounts are utilized three-fold, (1) to understand the mechanisms and timescales for island subsidence as the Nazca plate moves over the Galápagos hotspot (Chapter One), (2) use the chemistry of the seamounts to investigate how well do volcanoes serve as mirrors of the mantle from which they overlie (Chapters Two and Three) and (3) what does high precision isotopic analyses (described initially in Chapter Four) and sampling resolution improve the mantle picture with respect to the origins of ocean island geochemical heterogeneities (Chapter Five).

References

Castillo, P., 1988. The Dupal anomaly as a trace of the upwelling lower mantle. Nature 336, 667.

Courtillot, V., Davaille, A., Besse, J., Stock, J., 2003. Three distinct types of hotspots in the Earth's mantle. Earth Planet. Sci. Lett. 205, 295–308.

Davies, G.F., 2011. Dynamical geochemistry of the mantle. Solid Earth 2, 159–189.

Detrick, R.S., Crough, S.T., 1978. Island subsidence, hot spots, and lithospheric thinning. J. Geophys. Res. Solid Earth 83, 1236–1244.

Dixon, J.E., Bindeman, I.N., Kingsley, R.H., Simons, K.K., Le Roux, P.J., Hajewski, T.R., Swart, P., Langmuir, C.H., Ryan, J.G., Walowski, K.J., 2017. Light stable isotopic compositions of enriched mantle sources: Resolving the dehydration paradox. Geochemistry, Geophys. Geosystems 18, 3801–3839.

Fornari, Dan, 2010. Seafloor Rock Dredging – A Primer. Appendix VIII in Cruise Report MV1007 R/V Melville, 1-11. 10.7284/903799

Gale, A., Dalton, C.A., Langmuir, C.H., Su, Y., Schilling, J.-G., 2013. The mean composition of ocean ridge basalts. Geochemistry, Geophys. Geosystems 14, 489–518.

Gazel, E., Trela, J., Bizimis, M., Sobolev, A., Batanova, V., Class, C., Jicha, B., 2018. Long-Lived Source Heterogeneities in the Galápagos Mantle Plume. Geochemistry, Geophys. Geosystems 19, 2764–2779.

Hart, S.R., Erlank, A.J., Kable, E.J.D., 1974. Sea floor basalt alteration: some chemical and Sr isotopic effects. Contrib. to Mineral. Petrol. 44, 219–230.

Hart, S.R., Hauri, E.H., Oschmann, L.A., Whitehead, J.A., 1992. Mantle Plumes and Entrainment : Isotopic Evidence. Science (80-.). 256, 517–520.

Hoernle, K., Werner, R., Morgan, J.P., Garbe-Schönberg, D., Bryce, J., Mrazek, J., 2000. Existence of complex spatial zonation in the Galápagos plume. Geology 28, 435–438.

Hofmann, A.W., 1997. Mantle geochemistry: the message from oceanic volcanism. Nature 385, 219.

Hofmann, A.W., White, W.M., 1982. Mantle plumes from ancient oceanic crust. Earth Planet. Sci. Lett. 57, 421–436.

Jackson, M.G., Hart, S.R., Konter, J.G., Kurz, M.D., Blusztajn, J., Farley, K.A., 2014. Helium and lead isotopes reveal the geochemical geometry of the Samoan plume. Nature 514, 355.

Jones, T.D., Davies, D.R., Campbell, I.H., Wilson, C.R., Kramer, S.C., 2016. Do mantle plumes preserve the heterogeneous structure of their deep-mantle source? Earth Planet. Sci. Lett. 434, 10–17.

Kamenetsky, V.S., Maas, R., 2002. Mantle-melt evolution (dynamic source) in the origin of a single MORB suite: a perspective from magnesian glasses of Macquarie Island. J. Petrol. 43, 1909–1922.

Morgan, W.J., 1971. Convection plumes in the lower mantle. Nature 230, 42.

Olson, P., Silver, P.G., Carlson, R.W., 1990. The large-scale structure of convection in the Earth's mantle. Nature 344, 209.

Payne, J.A., Jackson, M.G., Hall, P.S., 2013. Parallel volcano trends and geochemical asymmetry of the Society Islands hotspot track. Geology 41, 19–22.

Ramalho, R.S., Quartau, R., Trenhaile, A.S., Mitchell, N.C., Woodroffe, C.D., Avila, S.P., 2013. Coastal evolution on volcanic oceanic islands: A complex interplay between volcanism, erosion, sedimentation, sea-level change and biogenic production. Earth-Science Rev. 127, 140–170.

Schilling, J.-G., 1973. Iceland mantle plume: geochemical study of Reykjanes Ridge. Nature 242, 565.

Spiegelman, M., Kelemen, P.B., 2003. Extreme chemical variability as a consequence of channelized melt transport. Geochemistry, Geophys. Geosystems 4.

Stacey, J.S. t, Kramers, 1JD, 1975. Approximation of terrestrial lead isotope evolution by a two-stage model. Earth Planet. Sci. Lett. 26, 207–221.

Thirlwall, M.F., 2002. Multicollector ICP-MS analysis of Pb isotopes using a 207Pb-204Pb double spike demonstrates up to 400 ppm/amu systematic errors in Tl-normalization. Chem. Geol. 184, 255–279.

van Keken, P.E., Hauri, E.H., Ballentine, C.J., 2002. Mantle mixing: the generation, preservation, and destruction of chemical heterogeneity. Annu. Rev. Earth Planet. Sci. 30, 493–525.

Weinstein, S.A., Olson, P.L., 1989. The proximity of hotspots to convergent and divergent plate boundaries. Geophys. Res. Lett. 16, 433–436.

Weis, D., Garcia, M.O., Rhodes, J.M., Jellinek, M., Scoates, J.S., 2011. Role of the deep mantle in generating the compositional asymmetry of the Hawaiian mantle plume. Nat. Geosci. 4, 831–838.

Wilson, J.T., 1963. A possible origin of the Hawaiian Islands. Can. J. Phys. 41, 863–870.

Yang, L., 2009. Accurate and precise determination of isotopic ratios by MC-ICP-MS: A review. Mass Spectrom. Rev. 28, 990–1011.

Zielinski, R.A., 1975. Trace element evaluation of a suite of rocks from Reunion Island, Indian Ocean. Geochim. Cosmochim. Acta 39, 713–734.

Zindler, A., Hart, S., 1986. Chemical geodynamics. Annu. Rev. Earth Planet. Sci. 14, 493–571.

Zou, H., 1998. Trace element fractionation during modal and nonmodal dynamic melting and open-system melting: a mathematical treatment. Geochim. Cosmochim. Acta 62, 1937–1945.

CHAPTER ONE: IDENTIFICATION OF EROSIONAL TERRACES ON SEAMOUNTS: IMPLICATIONS FOR INTERISLAND CONNECTIVITY AND SUBSIDENCE IN THE GALÁPAGOS ARCHIPELAGO

This chapter was published by Frontiers in the journal *Frontiers in Earth Science* and should be referenced appropriately as below.

Schwartz, D. M., Soule, S. A., Wanless, V. D., & Jones, M. R. (2018). Identification of erosional terraces on seamounts: implications for interisland connectivity and subsidence in the Galápagos Archipelago. Frontiers in Earth Science, 6, 88.

Abstract

Shallow seamounts at ocean island hotspots and in other settings may record emergence histories in the form of submarine erosional terraces. Exposure histories are valuable for constraining paleo-elevations and sea levels in the absence of more traditional markers, such as drowned coral reefs. However, similar features can also be produced through primary volcanic processes, which complicate the use of terraced seamounts as an indicator of paleo-shorelines. In the western Galápagos Archipelago, we utilize newly collected bathymetry along with seafloor observations from human-occupied submersibles to document the location and depth of erosional terraces on seamounts near the islands of Santiago, Santa Cruz, Floreana, Isabela, and Fernandina. We directly observed erosional features on 22 seamounts with terraces. We use these observations and bathymetric analysis to develop a framework to identify terrace-like morphologic features and classify them as either erosional or volcanic in origin. From this framework we identify 79 erosional terraces on 30 seamounts that are presently found at depths of 30 to 300 m. Although intermittent subaerial connectivity between the islands has been hypothesized, the depths of these erosional terraces in the Santiago region are the first direct evidence of paleo-connectivity in the modern archipelago. Collectively, the terraces have non-randomly distributed depths. We suggest that peaks in the distribution of terrace depths likely represent long durations of exposure (i.e., sea-level still or lowstands). By comparing these peaks to those of subsidence adjusted sea-level curves, we identify the average subsidence rate that best reproduces the observed terrace distributions. These rates are 0.2–0.4 m/ka for this portion of the central Galápagos, since the formation of the seamounts, consistent with previous independent

estimates. Using these subsidence rates and evidence for erosional terraces at depths up to 300 m, we conclude that all islands in the central archipelago have been intermittently connected starting between 435 and 900 ka. Individual island pairs have likely been repeatedly subaerially connected for short intervals since that time.

Introduction

Volcanic seamounts generated at oceanic hotspots grow over short durations, compared to the subaerial islands that they typically surround (Clague et al., 2000). These volcanic landforms help to resolve the spatial and temporal variability of magmatism, which is largely obscured by superimposed lava flows exposed on polygenetic islands (e.g., Moore et al., 1982). Furthermore, the morphology and lithology of the seamounts record information about the conditions during and after their formation (e.g., Ramalho et al., 2013; Huppert et al., 2015; Casalbore, 2018). In other words, if individual seamounts are active for only short durations, but seamounts are generated throughout the volcanic life of the hotspot, they provide a semi-continuous record of magmatic and environmental conditions above a mantle plume. The scarcity of detailed bathymetric mapping and difficulty in making direct observations at these submarine features has previously limited their utility for this purpose. In this study, we utilize new multi-beam bathymetric data and observations of seamounts in the western Galápagos Archipelago to constrain models for ocean island evolution and theories related to natural selection, which are both a function of paleogeography. Although there is strong evidence for past subaerial connectivity between the islands via genetics (e.g., Ali and Aitchison, 2014), landforms that can explain these connections mostly sit at depths greater than would be exposed

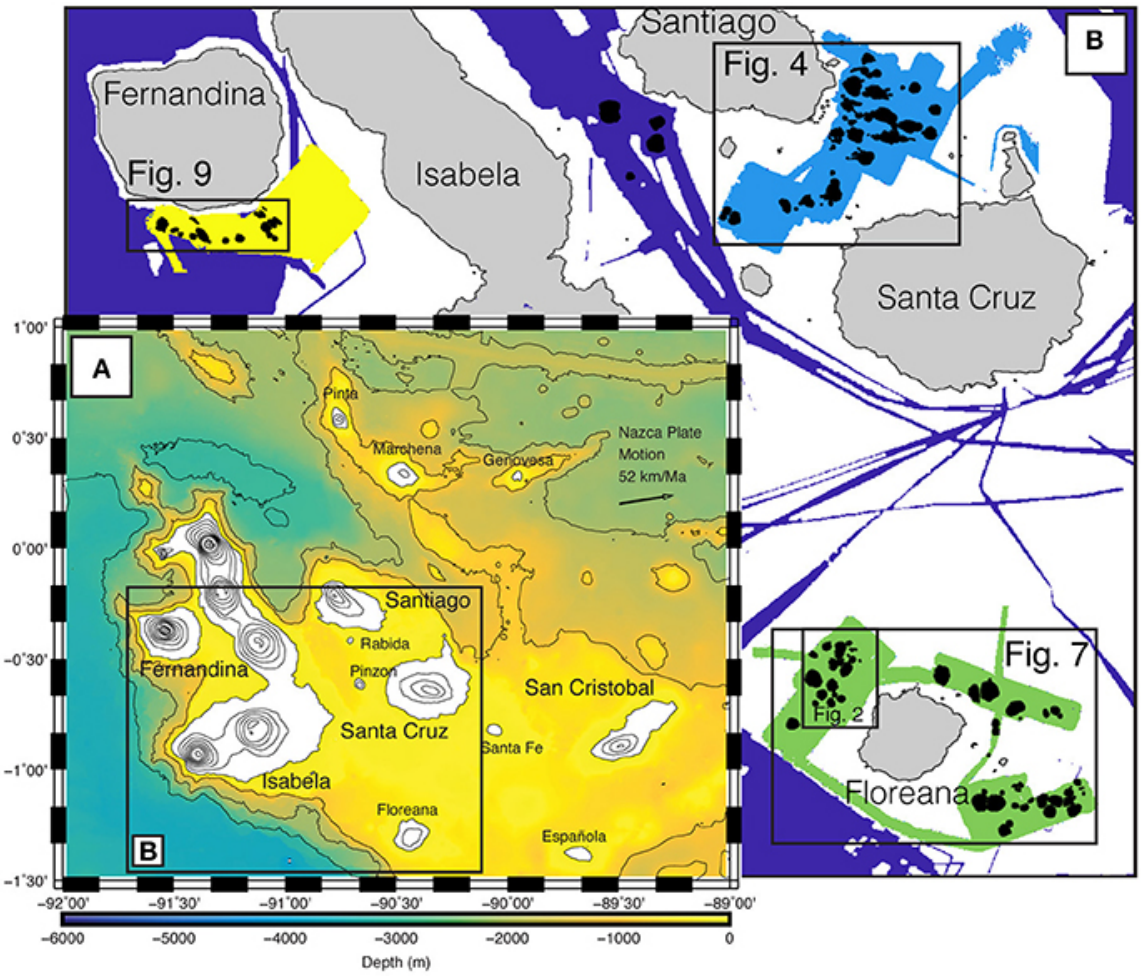

Figure 1.1. (A) Map of the Galápagos Archipelago. Subaerial contours show elevations at 200 m intervals (Weatherall et al., 2015). Submarine contours show bathymetry at 500 m intervals. Solid black box indicates location of (B) in this figure. (B) Mapped regions and seamounts. Gray polygons show island locations. Dark violet polygon shows previously collected bathymetry, other colored polygons (light blue, yellow, green) show mapping locations from this study and are shown in more detail in Figures 1.4, 1.7, 1.9. Solid black polygons show footprints of newly located seamounts.

during glacial maxima over the past 1 Ma. Our investigation of the seamounts is used to corroborate claims that combined sea level changes and subsidence have resulted in subaerial connectivity between the islands in the archipelago's past.

We report on new bathymetric mapping in the Galápagos that has revealed > 100 seamounts with summit depths from near sea level to 1,000 m, many of which were not

previously known (Figure 1.1). The new mapping reveals complex morphological characteristics of the seamounts that were previously unresolvable, including terraced summits and flanks (Figures 1.2, 1.3A). Preserved terraces and beach cobble deposits in ocean island systems and on continental margins are commonly interpreted to be the result of wave abrasion at the coastline during sea level still-stands (Trenhaile, 2000; Ramalho et al., 2013 and references therein; Zecchin et al., 2015; Casalbore et al., 2017). Wave action at the coastlines of volcanic islands creates shore platforms by quarrying and dislodgement of joint blocks and abrasion (Ramalho et al., 2013; Quartau et al.,

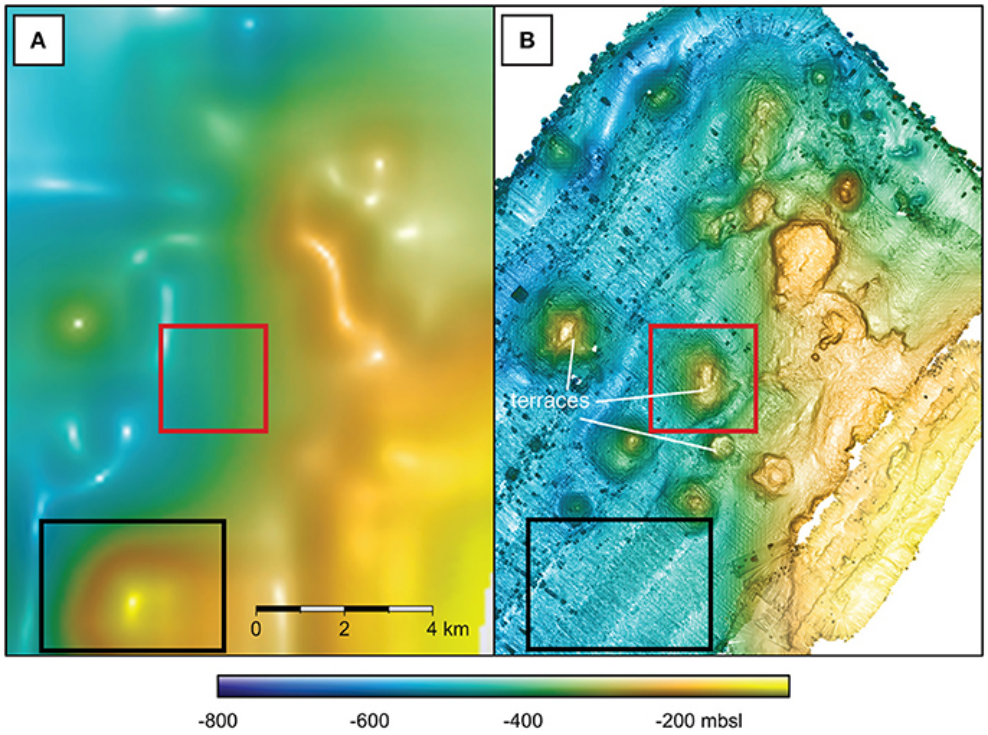

Figure 1.2. Comparison of global bathymetry to M/V Alucia multibeam NW of Floreana, location of figure is indicated in Figure 1.1. (A) Bathymetry derived from sparse sounding data and gravity anomalies calculated from satellite altimetry, gridded at ~900 m (Smith and Sandwell, 1997; Weatherall et al., 2015). (B) Mulitbeam bathymetry encompassing the identical area as in (A), data are gridded at 10 m. Note large anomaly in (A) (apparent seamount indicated by the black box) does not appear in (B). Numerous smaller features not visible in the altimetry-based data appear in the multibeam data, including seamounts (indicated by the red box). and terraces are identified in the multibeam data.

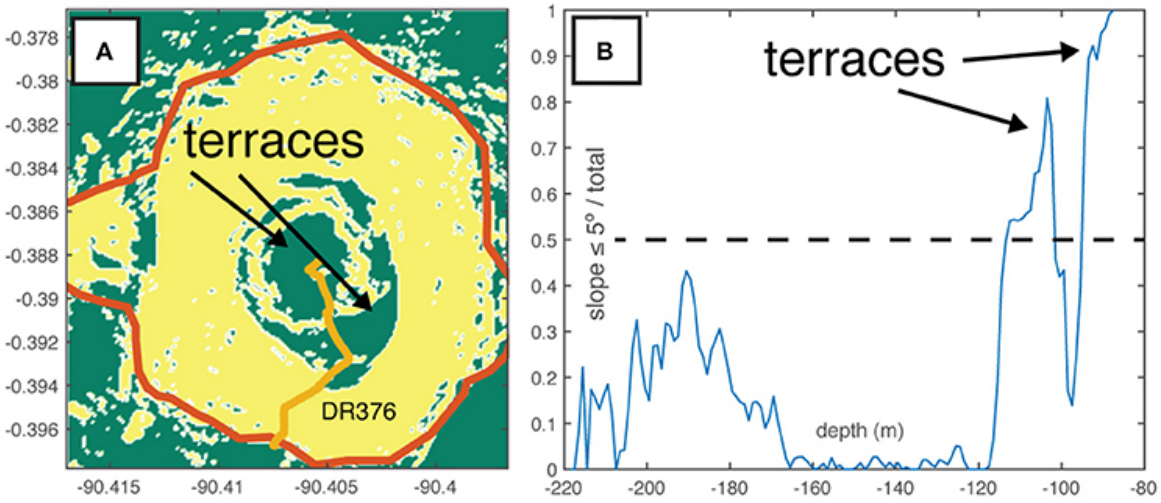

Figure 1.3. Example of terrace identification. (A) Slope map of a seamount where two terraces have been identified. Areas where slopes are ≤ 5°(terraces) are shown in green and slopes > 5° are shown in yellow. Seamount footprint is shown as a thick red line and was manually digitized as the break in slope ≥ 5°. Gold line shows the dive track for seamount DR376. (B) ratio of pixels with slope ≤ 5° to all pixels at that depth within the seamount footprint. Peaks in the distribution where ratio is > 50% are identified as terraces.

2014, 2016). The effectiveness of these processes is thought to decrease rapidly at water depths of a few meters for bedrock and up to 50 m for clastic deposits (e.g., Menard and Ladd, 1963; Kokelaar and Durant, 1983; Romagnoli and Jakobsson, 2015). Seamounts large enough to reach the sea surface should, in theory, record the same coastal erosion processes, and provide useful constraints on ocean island paleogeographies and vertical motions in the absence of more traditional markers, such as drowned coral reefs (Campbell, 1984; Moore and Fornari, 1984; Rubin et al., 2000; Huppert et al., 2015). However, volcanic processes that are independent of depth can result in features that mimic erosional terraces, including submarine lava ponding (e.g., Clague et al., 2000), lava flows with primarily concave-out morphologies (Geist et al., 2006, 2008) and laminar spreading and deposition of near-surface pyroclastic deposits, which should be relatively smooth features with gentle upper flank slopes (Mitchell et al., 2012; Casalbore

et al., 2015). Despite work toward characterizing morphologies associated with these processes (e.g., Chaytor et al., 2007), there is no systematic way to delineate seamount terraces as primary (volcanic) or secondary (erosional) features. From our observations, we develop a binary framework for determining the origins of terraces based on their morphology, which may be applicable to other seamount systems.

Background and Methods

Direct observations of paleo-elevations at some ocean islands are made possible through the dating of drowned coral reefs (e.g., Hawaii; Moore and Fornari, 1984; Ludwig et al., 1991) as well as transitions from subaerial to submarine lavas in boreholes (e.g., Ascension; Minshull et al., 2010). These measurements, along with sea level reconstructions, are used to constrain island vertical motions through time (e.g., Huppert et al., 2015). These vertical motions are primarily the combined result of topographic loading and flexure (e.g., Moore, 1970; Watts and Ten Brink, 1989), cooling and deepening of the lithosphere as it ages (e.g., Marty and Cazenave, 1989) and/or transport over and away from the hotspot swell (e.g., Detrick and Crough, 1978). However, a large number of ocean islands are devoid of large carbonate platforms despite supporting reefs, likely due to low average annual water temperatures (Kleypas et al., 1999; Couce et al., 2012), and lack borehole data, thus vertical motions cannot be constrained using these approaches.

The Galápagos Archipelago is a hotspot sourced volcanic island chain located in the equatorial Pacific ~1,000 km west of South America. The Galápagos consists of 13 major volcanic islands, numerous smaller islands, and volcanic seamounts (Figure 1.1; McBirney and Williams, 1969; Christie et al., 1992; Sinton et al., 2014; Chapter 1). The

central and eastern islands rise from a shallow volcanic platform that stands ~3,000 m above the surrounding seafloor (Geist et al., 2008) and comprises the majority of the archipelago's erupted volume. The hotspot center lies southwest of Fernandina volcano (Kurz and Geist, 1999; Villagómez et al., 2014), which is the westernmost and most active volcanic island in the Galápagos (Allan and Simkin, 2000). There is a general age progression and corresponding decrease in eruption rate from west to east across the archipelago (White et al., 1993). The youngest island in the archipelago is Fernandina, which emerged at ~70 ka (Kurz et al., 2014). Volcanoes get progressively older to the east, where the emergence of Santiago is ~1 Ma, Santa Cruz and Floreana ~2.3 Ma and San Cristobal ~6 Ma (Geist et al., 2014). There are numerous “drowned” islands, which lie to the southeast (Christie et al., 1992) and east (Sinton et al., 2014) of the present archipelago extending the age of emergence for the archipelago to at least 9 Ma.

Vertical motions in the Galápagos have been estimated based upon measurements of the maximum height of islands and large seamounts, as well as platform depth, as a function of distance from the plume center (Geist, 1984; Geist et al., 2014). Trends in subsidence rate derived from these measurements follow an exponential decrease, that peaks at 2 m/ka at Fernandina and rates asymptotically approach 0.4–0.5 m/ka at the distance of Santiago, Floreana, and Santa Cruz (Equation 8.6; Geist et al., 2014). These rates are comparable to those of the Hawaiian Islands for islands of similar ages (0–4 m/ka for islands younger than 1 Ma; Huppert et al., 2015). The estimate of Galápagos rates relies upon the assumption that the Galápagos plume flux has contributed uniformly to archipelago formation for the past several million years. This is uncertain due to clear evidence for variable plume-ridge interaction in the archipelago's past (e.g., Harpp and

Geist, 2002; Harpp et al., 2003; Sinton et al., 2014). Moreover, the relative contribution of the plume to volcanism on the Nazca and Cocos plates has fluctuated through time due to variations in the relative position of the mantle plume to the ridge and position beneath respective plates (e.g., Werner et al., 2003) and continued ridge jumps (Mittelstaedt et al., 2012).

In 2015 we conducted a research cruise in the western Galápagos Archipelago aboard the M/V *Alucia*. During the cruise we conducted seafloor mapping with a ship-mounted Reson multibeam sonar (yellow, light-blue and green areas in Figure 1.1). In addition, we collected seafloor observations and samples with two 1,000-m rated human occupied vehicles (HOVs), Deep Rover 2 and Nadir (gold lines in Figures 1.4–1.9). Through a combination of morphology from seafloor mapping and direct seafloor observations we develop a framework to distinguish between morphological features resulting from coastal (i.e., erosional) processes and those resulting from primary volcanic (i.e., constructional) processes within the mapped region. With this framework we are able to identify erosional terraces across the study area to (1) provide the first direct observations of interisland connections via erosional features in the modern archipelago, and (2) document how the combination of sea-level change and island subsidence contribute to the paleogeography of the archipelago through the use of comparative statistics.

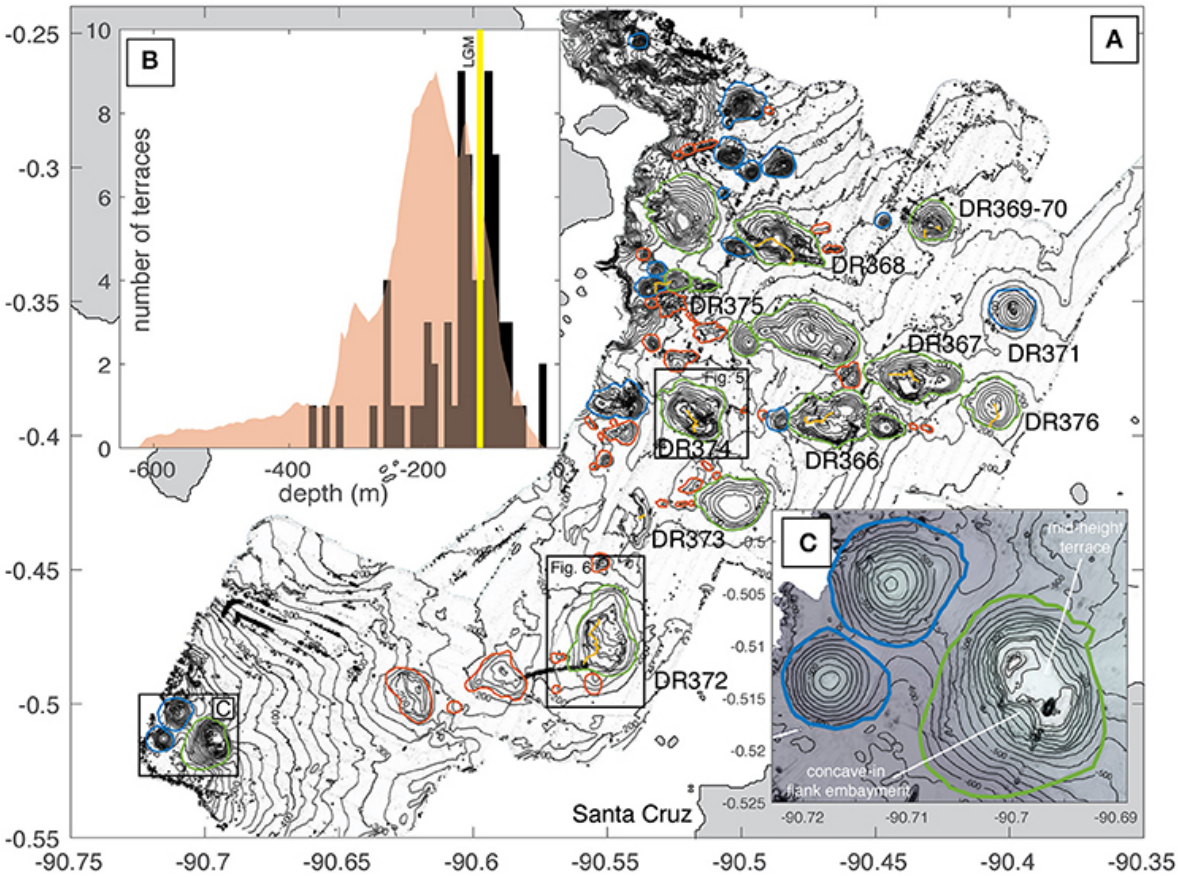

Figure 1.4. (A) Bathymetric map of the Santiago seamounts. Gray polygons locate islands. Bathymetric contour interval is 20 m. Green lines locate seamounts > 100 m of relief that have identified terraces. Blue lines locate other mapped seamounts > 100 m. Red lines locate mapped seamounts, which are < 100 m in relief. Gold lines indicate dive tracks. Locations of inset (C) and Figures 1.4, 1.5 are indicated by black boxes. (B) Black/gray bars are histogram of depths of all identified terraces. Semi-transparent red polygon shows the probability distribution of all depths within the mapped seamount footprints. Yellow bar indicates the depth of the last glacial maximum sea-level lowstand (Bintanja et al., 2005) (C) Seamount with summit depth ~300 m with identified terrace and summit embayment and irregular shaped summit features.

Mapping the Galápagos Platform and Seamounts

Bathymetric mapping focused on three regions on the Galápagos platform, east and south of Santiago Island, surrounding Floreana Island and south of Fernandina Island (between 20 and 2,000 m water depth; Figure 1.1). Surveys were conducted on M/V *Alucia* using a Reson 7160 44 kHz multibeam sonar with Reson SeaBat acquisition software and PDS2000 for real time viewing and adjustment of sonar settings to optimize data quality, including frequency, depth range, beam steering, and gain. Swath widths were typically 5x water depth, but decreased at depths greater than 1,500 m.

Data processing was conducted with Caris™ HIPS and SIPS. Navigation and attitude data were verified and a tide correction was applied based on observed tides from the Instituto Oceanográfico de la Armada (INOCAR) station at Baltra Island. Sound velocity corrections were applied based on XBT data, which were collected at least once every 12 h of multibeam operations. Sonar data was automatically filtered at beam angles > 65°, manually edited to remove outliers, and gridded at 10 m for analysis. Remarkably little of the Galápagos volcanic platform has been mapped prior to this study, thus the best available bathymetric data was from global data sets derived from sparse echo-soundings and global gravity anomalies derived from satellite altimetry (e.g., Smith and Sandwell, 1997). The new mulibeam bathymetry is 90x higher resolution than the existing global data (Figure 1.2; Geist et al., 2006; Weatherall et al., 2015) for the study area. As a result, the new bathymetry allows identification of seamounts with relief greater than 10 m, most of which were previously undetectable (Figure 1.2). Although correspondence of larger seamounts between satellite-derived bathymetry and the new multibeam data is good, we find numerous examples of both undetected and spurious

seamounts in satellite-derived bathymetry when compared to the new multibeam data (Figure 1.2).

Using criteria of Bohnenstiehl et al. (2012), seamount extents were defined by the break in slope from the seafloor > 5° and their footprints were manually digitized using QGIS software. For seamounts with >100 m of relief, spatial statistics including summit and base depth, relief, and diameter were collected using MATLAB software and are summarized in Table 1 for seamounts visited by HOV. Seamount slopes were binned into two categories of ≤ 5°(terraces) and >5°(seamount flanks) and integrated as a function of depth. The ratio of pixels ≤ 5° and > 5° was then calculated for these depth distributions (e.g., Passaro et al., 2011). Terraces were identified as peaks in those final distributions where ≥ 50% of pixels at a given depth have slopes of ≤ 5° (Figure 1.3). Once identified, seamounts with terraces were manually evaluated for concave-in flank embayments, which have been interpreted as erosion-induced collapse in other volcanic seamounts (e.g., Chaytor et al., 2007) (Table 1). These and constructional features, such as summit craters (Clague et al., 2000; Chaytor et al., 2007), convex out lobes formed at lava flow boundaries (Geist et al., 2006) are corroborated with seafloor observations (e.g., Figures 1.5, 1.6, 1.8, 1.9). Although terraces were also identified on seamounts < 100 m in relief and seamounts in the older coarser resolution bathymetry, including one seamount visited by HOV (DR375; Figure 1.4A), we do not include these seamounts because sonar sounding density is insufficient to confidently discriminate between erosional and primary volcanic features. From our observations, we suggest that features should have relief of at least 10x the spatial resolution of the bathymetric data in order to confidently identify terraces.

Table 1.1 Table of seamounts visited by HOV relating direct seafloor observations to bathymetric features.

ID	lat	long	dive	summit depth (m)	relief (m)	terrace	mid-terrace	concentric	irreg./flank embayment	rounded clasts/ abrasional textures
	Santiago									
114	-0.3948	-90.4700	DR366	24.486	189	yes	yes	yes	yes	yes
119	-0.3776	-90.4360	DR367	27.848	191	yes	yes	yes	yes	yes
127	-0.3265	-90.4890	DR368	98.436	219	yes	no	-	no	no
117	-0.3209	-90.4300	DR369-70	91.221	179	yes	yes	yes	no	yes
116	-0.3530	-90.3990	DR371	45.556	165	no	-	-	no	yes
104	-0.4773	-90.5550	DR372	22.929	145	yes	yes	yes	yes	yes
111	-0.3917	-90.5180	DR374	18.994	230	yes	yes	yes	yes	yes
24	-0.3462	-90.5350	DR375	54.123	153	no	-	-	no	yes
25	-0.3429	-90.5260	DR375	162.51	121	yes	yes	yes	no	yes
3	-0.3884	-90.4060	DR376	86.999	107	yes	yes	yes	no	yes
	Floreana									
130	-1.2040	-90.5790	DR377	253.17	292	yes	yes	yes	yes	yes
40	-1.1598	-90.5410	DR379	299.59	140	no	-	-	yes	yes
49	-1.1795	-90.5410	DR379	252.29	90	yes	no	-	yes	yes
35	-1.2283	-90.5490	DR380	302.85	82	yes	no	-	no	no
36	-1.2141	-90.5510	DR380	257.92	159	yes	no	-	yes	yes
131	-1.1994	-90.3870	DR381	23.317	242	yes	yes	yes	yes	yes
46	-1.1773	-90.5240	DR382	183.98	175	no	-	-	yes	yes
	Fernand.									
12	-0.5222	-91.5580	DR383	577.69	487	no	-	-	no	no
29	-0.5349	-91.5020	DR384-5	607.22	301	yes	yes	no	no	no
100	-0.5165	-91.3870	DR386	623.39	147	no	-	-	no	no
129	-0.5447	-91.4420	DR387	692.7	320	no	-	-	no	no

Seafloor Observations and Sample Collection

HOV dives were conducted on 25 seamounts in the three study regions (Table 1). Each dive consisted of tandem launches of the Nadir and Deep Rover 2 submersibles. Typically, dives started at or near the base of a target seamount and proceeded up to the seamount summit. Continuous high definition video was collected throughout the dive and samples were collected where obvious changes in lithology were observed (Table 1;

Supplementary Data 1.1). Following the cruise, the video data was classified based on the observed morphology and inferred lithology using the collected samples. Two additional seamounts were visited on a previous cruise and are included in our evaluation (Carey et al., 2016).

Results

Observational Results

From the 150 seamounts that were digitized from the new and existing multibeam bathymetry, 76 are > 100 m in relief, and 34 of these seamounts have terraces. Most terraces occur between the seamount base and summit (mid-height terraces; N = 24), the rest are found at or near (within 10 m) the summit (summit terraces; N = 10). Terraces are identified in all three mapping regions and range in depth from 15 to 1,100 m (Figures 1.4–1.9).

We recovered 147 rock samples from 22 dives on 25 seamounts. Of the samples collected, 127 are basaltic lavas and the remaining 20 are of lithified volcaniclastic deposits. The samples are correlated with seafloor morphology using continuous dive video (Table 1). We categorized seafloor morphology into primary volcanic features/textures formed during emplacement or secondary features/textures formed during exposure. Primary volcanic features include pillow lavas (e.g., Figure 1.9C) and rough aa-like lava flow textures (Supplementary Data 1.1; Image DR372-1655). Secondary features include rounded beach cobble deposits (Figures 1.5B,C, 1.6B,C, 1.8B,D), smoothed abrasional rocky surfaces (Figures 1.5B,C), erosional cliffs (Figure 1.5D),

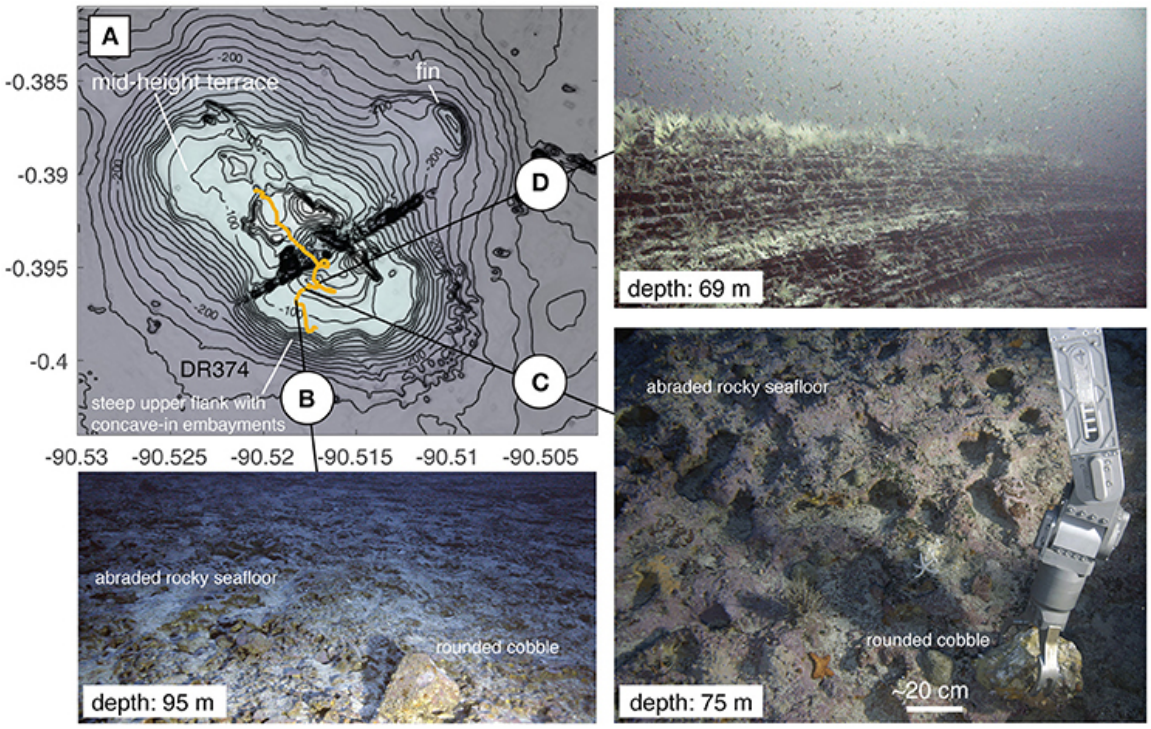

Figure 1.5. Map and images of DR374 seamount. (A) Bathymetric contour interval is 10 m. Gold line shows dive track for seamount DR374. The seamount has steep upper flanks and a broad mid-height terrace that is concentric about the seamount's summit (i.e., encircles the entire seamount). The contour of the terrace edge is irregular and includes flank embayments giving it a scalloped shape. There are multiple irregular spines and fins protruding from the seamount's flank and summit. NE-SW striking linear feature near the summit of the seamount is a data artifact. (B) Rounded boulder on smoothed bedrock material constituting the seamount's terrace. (C) Collection of rounded cobbles and detailed view of smoothed bedrock constituting the seamount's terrace. (D) Truncated outcrop of thinly bedded volcaniclastic material near the seamount's summit. Depths in photos indicate the depth of the seafloor at the point of image capture.

terraces (Figures 1.5B,C), and spires (Supplementary Data 1.1, Image 375–1558; e.g., Trenhaile, 1987). We use the presence of rounded cobbles on terraces to definitively identify exposure to abrasional processes at or near the sea surface (e.g., Ramalho et al., 2013; Table 1). Further, we equate variations in observed morphologic features from smooth to more bulbous rocky surfaces to be the result of abrasion by water-borne particles on various volcanic lithologies ranging from basalts to hyaloclastities and/or pyroclastic deposits (e.g., Ramalho et al., 2013). Bedded pyroclastic deposits were

commonly observed (Figures 1.5D, 1.8C) and although we do not necessarily ascribe them to primary or secondary volcanic features, they are evidence of shallow eruption processes (e.g., Cas, 1992) or reworking of material at or near the sea surface (Ramalho et al., 2013).

Santiago Seamounts

In the Santiago region, terraces are present at water depths from 20 to 375 m and have principle modes at depths of 110 and 130 m (Figure 1.4B), with minor modes at greater depths. Typically, terraces in this region occur as mid-height features whose outer edges are concentric with contours on the seamount slope and about the seamount's midpoint (Figures 1.4A, 1.5A). Seamounts with terraces are irregular in plan view (Figures 1.5A, 1.6A) and are adorned by steep cliffs (Figure 1.5A) and vertical fins or spires, which are visible in the maps (e.g., Figure 1.5) and on smaller scales in photos collected from the submersibles (e.g., Supplementary Data 1.1; Image DR375-1558). On nine of the 10 seamounts visited in this region we observed rounded cobbles and smoothed and bulbous surfaces, indicative of exposure to waves at or near sea surface (Figures 1.5, 1.6). Of these nine seamounts, all but two have mid-height terraces and/or summit terraces. Only one seamount had a morphologically identified terrace (at its summit) but no obvious evidence for erosional features from direct seafloor observations (DR368). Intact pillow lavas were observed from the submersibles on this seamount's flanks, the only observation of pillows in the Santiago region (Supplementary Data 1.1; Images DR368-1502, 1520, 1524).

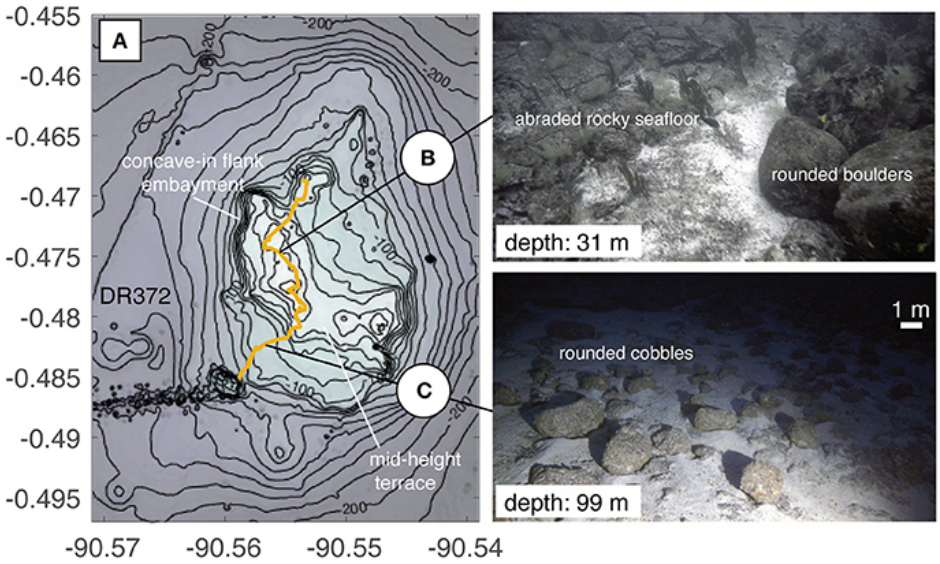

Figure 1.6. Map of DR372 seamount. (A) Bathymetric contour interval is 10 m. Gold line shows dive track for seamount DR372. This seamount is highly irregular in shape, with a N-S trending elongation at it's base and NW-SE elongation near it's summit. The seamount has steep upper flanks and is adorned by multiple irregular summit features. There are multiple terraces on this seamount, which are flanked by steep sides with flank embayments. ENE-WSW striking linear feature SW of the seamount is a data artifact. (B) Rounded boulder on smoothed bedrock material constituting the seamount's terrace. The left portion of the image shows bulbous/rounded basaltic lava flow bedrock and the right side shows rounded basaltic boulders of a similar size and roundness. (C) Field of rounded cobble-boulder sized clasts on flat lying bedrock, which is mostly obscured by fine sediment. Depths in photos indicate the depth of the seafloor at the point of image capture.

Floreana Seamounts

Similar features to those observed in the Santiago region were observed surrounding Floreana (Figure 1.7A). Terraces are present at water depths of 100–600 m and have a shallow mode at 150 m and a secondary mode at 250 m (Figure 1.7B), with minor modes at greater depths. Thinly bedded laminar deposits are observed at depths between 100 and 400 m (e.g., Figure 1.8C). Rounded cobbles are present at water depths up to 300 m (Figures 1.8B,D). These deep cobbles are similar in size and roundness to

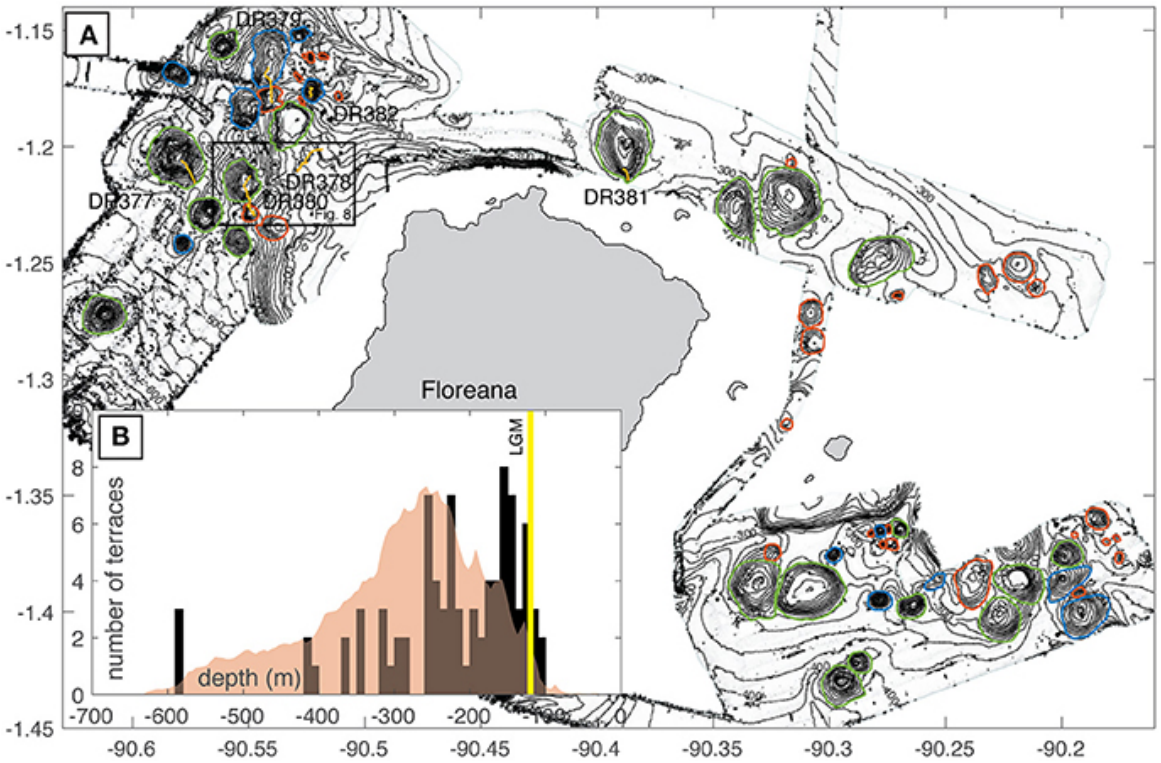

Figure 1.7. (A) Bathymetric map of the Floreana seamounts. Gray polygons locate islands. Bathymetric contour interval is 20 m. Green lines indicate footprints for seamounts > 100 m of relief that have identified terraces. Blue lines indicate other mapped seamounts > 100 m. Red lines indicate mapped seamounts, which are < 100 m in relief. Gold lines indicate dive tracks. Location of Figure 1.8 is indicated by a black box. (B) Black/gray bars are histogram of depths of all identified terraces. Semi-transparent red polygon shows the probability distribution of all depths within the mapped seamount footprints. Yellow bar indicates the depth of the last glacial maximum sea-level lowstand.

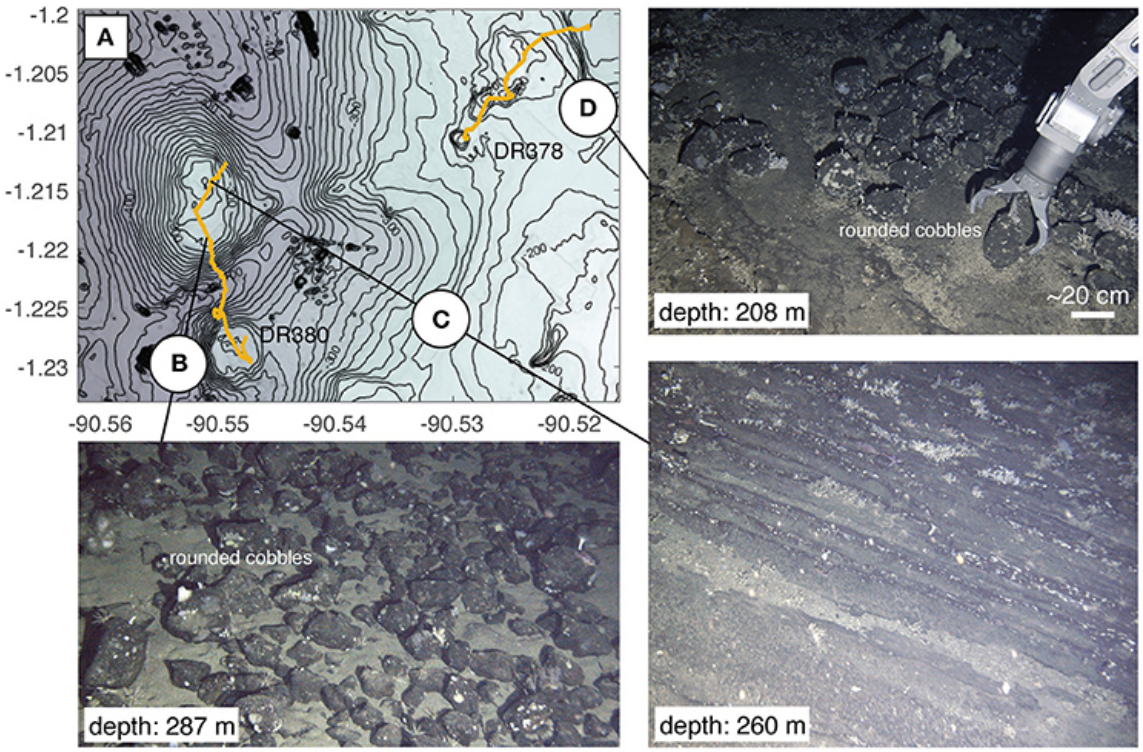

Figure 1.8. Map of DR378 and DR380 seamounts. (A) Bathymetric contour interval is 10 m. Gold lines shows dive tracks for seamounts DR378 and DR380. The two seamounts visited on seamount DR380 have terraced/flat summits. The northernmost of the two is irregular in plan view, with small embayments on the western flank and has a small summit spire. The southernmost is round with no irregular summit features, except for its flat top, and resembles seamounts found in the Fernandina region (Figure 1.9) (B) Field of rounded cobble-boulder sized clasts setting on a flat surface obscured by fine sediment. (C) Near vertical outcrop of sub-horizontally bedded volcaniclastic material. (D) Collection of rounded cobble from top of terrace. Depths in photos indicate the depth of the seafloor at the point of image capture.

those observed at shallower depths and in the Santiago region (Figures 1.6B, 1.8D). Of note, the cobbles at 287 m water depth shown in Figure 1.8B were observed on a terrace at the seamount summit, excluding the possibility of downslope transport. Similar bathymetric features to those observed in the Santiago region are also observed in the Floreana region, including steep cliffs with scalloped and complex contour patterns (Figures 1.7, 1.8). Of the seven seamounts visited by HOV, all but one showed evidence of exposure to wave abrasion in the form of rounded cobbles or other abrasional surfaces.

Of these six seamounts, five have summit terraces, and two of those five had mid-height terraces. Similar to the Santiago region, the only seamount with a morphologically-identified terrace that showed no obvious evidence for erosional features from direct seafloor observations (DR380 southern seamount), only had a summit terrace and had what appeared to be intact pillow lavas at its summit (Supplementary Data 1.1; Images DR380-1500).

Fernandina Seamounts

Terraces in the Fernandina region are observed at depths from 600 to 1,100 m, with no obvious depth modes. Terraces occur as circular and stepped semicircular features. As opposed to the terraces visited in the Santiago and Floreana regions, deep terraces in the Fernandina region were associated with pillow lavas (Figures 1.9A,B). Pillows were typically observed as intact, flat deposits (Figure 1.9C) and mounds as well as incised cliffs and associated talus slopes (Figure 1.9D). Talus slopes originating from these constructions contain sub-meter sized clasts with remnant outer pillow surfaces. These clasts are easily identified as pillow fragments, as opposed to reworked cobbles, due to their presence as steep deposits at the base of intact pillow cliffs and their polygonal and blocky sides. Other lava features are observed including columnar jointed flow interiors. No observations of laminar pyroclastic deposits, wave base erosional surfaces, or rounded clasts were observed in the Fernandina region.

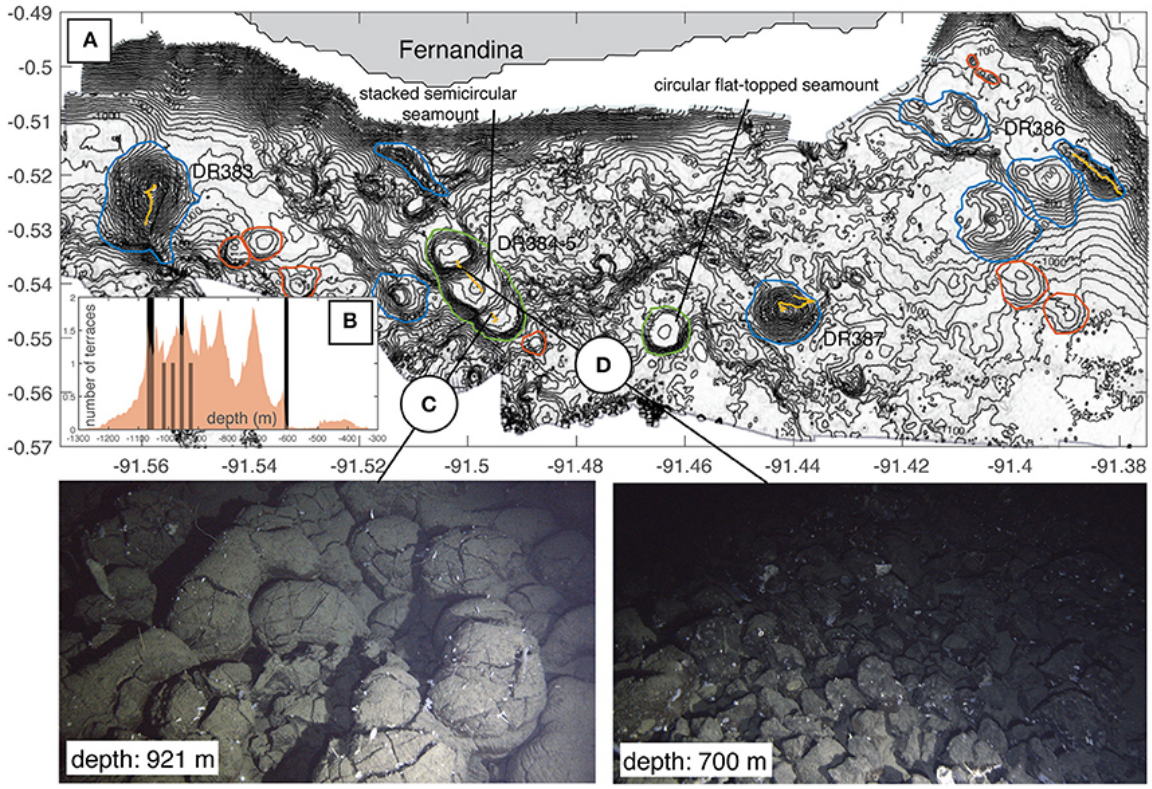

Figure 1.9. (A) Bathymetric map of the Fernandina seamounts. Gray polygon indicates island location. Bathymetric contour interval is 20 m. Green lines indicate footprints for seamounts > 100 m of relief that have identified terraces. Blue lines indicate other mapped seamounts > 100 m. Red lines indicate mapped seamounts, which are < 100 m in relief. Gold lines indicate dive tracks. (B) Histogram of depths of identified terraces. Semi-transparent red polygon shows the probability distribution of all depths within the mapped seamount footprints. (C) Pillow lavas, which serve as the bedrock for the lowermost terrace on this seamount. (D) Steep talus pile on the seamount's flank. Talus is comprised of pillow fragments retaining some of the curved sides of the original pillows and more blocky/polygonal interiors.

Framework for Identifying Erosional Terraces

From our combined bathymetric analyses and direct seafloor observations we have developed a binary framework to delineate erosional terraces from those created from other processes (Figure 1.10). The seafloor observations and their relationships to terraces and flank embayments serve as the training dataset for the binary framework. The 21 visited seamounts (Table 1) are ultimately used to evaluate our interpretations

(e.g., identify false positives and negatives). Visited seamounts with terraces constituting the training datasets (N = 14; Table 1) represent nearly half of all seamounts with terraces (N = 34), which we deem adequate for confidently assessing the accuracy of our classification scheme.

We take a conservative approach in our classification relying primarily on terrace characteristics (e.g., summit vs. mid-height terrace) in order to reduce false positives and the effect of human interpretation biases. We note that only 11 of the 14 seamounts visited by HOV with direct observations indicating erosion at or near the sea surface (e.g., beach cobbles), have identified terraces. This leads to an initial false negative rate of 21%. However, without direct seafloor observations the absence of bathymetrically identifiable terraces (e.g., Figure 1.3) for the remaining unvisited seamounts is an impasse that excludes further identification (N = 42; Figure 1.10A). Thus, all seamounts without bathymetrically identified terraces are excluded from analysis of island subsidence and paleogeography. Interestingly, seamounts with no terraces identified, but show direct seafloor evidence for erosion (N = 3; false negatives), are of comparable size and depth to the seamounts that are positively identified by both metrics. This may suggest that some seamounts are too young to have experienced the same lowstands as nearby seamounts, or that variations in lithology between seamounts may be a primary control on the formation and preservation of terraces.

When present, seamount terraces occur on summits (N = 10), or at mid-level on the seamount in the presence or absence of a summit terrace (N = 24; Figure 1.10B). If the seamount only has a summit terrace and the seamount does not possess any obvious

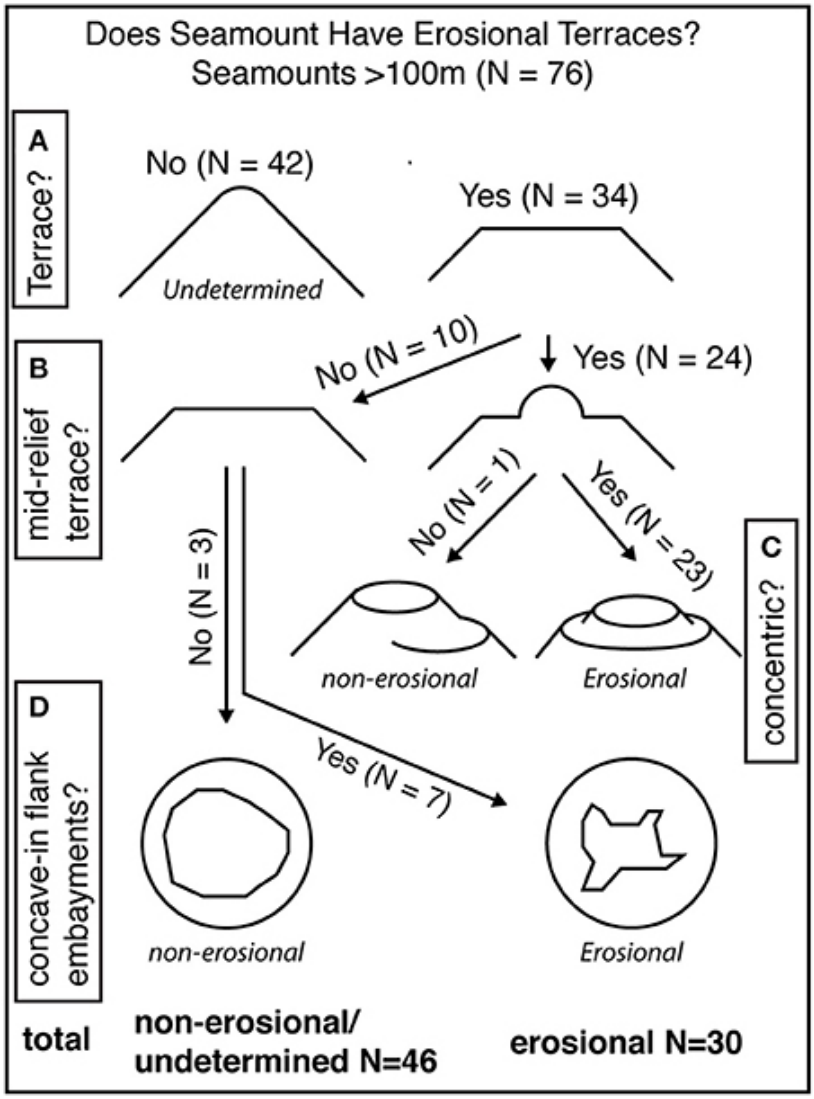

Figure 1.10. Flow chart for extrapolating mapped terraces as erosional terraces indicating observations leading to, and the number of seamounts within, each classification step. See section Framework for Identifying Erosional Terraces for more detailed description of each classification step and discussion of false positives and negatives. (A) Initially seamounts are discriminated by the presence of bathymetrically identified terraces. Seamounts without bathymetrically identified terraces (left) cannot be positively identified as erosional. (B) Seamounts terraces occur on summits (left) or at mid-level on the seamount +/− a summit terrace (right). (C) Of seamounts with mid-level terraces, terraces can either occur non-concentrically (left) or concentrically (right) about the seamount's summit. Seamounts with non-concentric terraces are classified as non-erosional, whereas seamounts with concentric terraces are classified as erosional. (D) For seamounts with summit terraces only seamounts are manually discriminated by the absence (left) or presence (right) of concave-in flank embayments. The former are classified as non-erosional and the later as erosional.

erosional features such as concave-in scalloped flanks, then it cannot be positively identified as erosional (Figure 1.10D). Three seamounts with only summit terraces and lacking erosional features are observed and are found in all three mapping regions (Table 1) and include DR368 (Figure 1.4) and DR380 (southern seamount; Figure 1.8). Flat-topped seamounts are commonly observed seafloor features (e.g., Chaytor et al., 2007). These features are thought to form from the ponding of lavas at seamount summits, similar to subaerial volcanoes in the Galápagos (Clague et al., 2000; Naumann and Geist, 2000), or due to spreading of pyroclastic material due to shallow eruption processes without direct interaction with waves (Mitchell et al., 2012; Casalbore et al., 2015). Both of these mechanisms should result in circular seamounts with relatively gentle summit slopes (Clague et al., 2000; Mitchell et al., 2012). Both DR368 and DR380 only have summit terraces and do not show morphological or seafloor evidence for erosion. In fact, irregularities in extent of the summit of DR380 are convex-out, which more likely indicate volcanic constructional processes (e.g., Geist et al., 2006). There are no false positives or negatives identified in our training dataset for this classification step.

By contrast, we assert that summit terraces, on seamounts with concave-in, scalloped flanks, or steep upper slopes are most likely created by coastal erosional processes (N = 7; Figure 1.10D). Seven seamounts, which have only summit terraces, are accompanied by complex summit shapes as well as steep and scalloped flanks that lead up to terraces (Figure 1.10D). The seamounts that we mapped are all < 1 km in relief and thus should not be gravitationally unstable and therefore not have been significantly modified by large scale mass wasting (Mitchell, 2001). Similarly, these features would not be expected to result from lateral spreading of pyroclastic material or submarine lava

ponding for volcanoes of this size (Clague et al., 2000; Mitchell et al., 2002, 2012). Direct seafloor observations of all seamounts in this group (N = 3; Table 1) indicate exposure at the sea surface, leading to no false positives or negatives.

Twenty-four seamounts have mid-level terraces (Figure 1.10B). These mid-level terraces occur either concentrically about the same mid-point (e.g., Figure 1.3) or non-concentrically (e.g., DR384-5; Figure 1.9A). If the seamount has a mid-level terrace, but the terraces do not occur concentrically (N = 1; Figure 1.10C) then the terrace may not be erosional. The most obvious example of non-concentric terracing is in the Fernandina region, where multiple overlapping flat-topped seamounts are built on a slope producing series of steps (e.g., DR384-5; Figure 1.9A). Seamounts with this morphology have been observed on the flanks of Hawaii at depths where there is no evidence for exposure (e.g., Clague et al., 2000). In addition, prevalent intact pillow lavas are observed on the Fernandina seamounts (e.g., Figure 1.9C), which are deeper than 600 m. These observations, as opposed to observations indicating coastal exposure, make sense, as it would be unreasonable to infer more than 500 m of subsidence for these seamounts, given their close proximity to the hotspot center.

If the mid-level terraces are predominately concentric about the summit of the seamount, then this provides evidence that the seamount has likely been affected by coastal erosional processes, such as the formation of insular shelves (N = 23; Quartau et al., 2010, 2014, 2015, 2016; Ramalho et al., 2013). This claim is supported unanimously by our training data set, where all seamounts with multiple, concentric terraces show direct seafloor evidence for modification by erosion near to the sea surface (Table 1). Based on the lack of false positives, we conclude that the presence of multiple concentric

terraces alone is enough to positively identify a seamount as being modified by coastal processes. Of note however, all seamounts but one that we observed with mid-level terraces are also accompanied by concave-in scalloped flanks and irregular summit shapes (e.g., Figures 1.4C, 1.5, 1.6, 1.8). These observations could be used in tandem to strengthen the identification of erosional seamounts. However, we choose to end classification of these erosional seamounts at this stage because this further classification would require additional manual discrimination (e.g., summit shape), which may result in errors (Figure 1.10C).

After applying our classification to all of the newly mapped seamounts, and including those that we directly observed by HOV, we are able to positively identify 30 of the 74 as having erosional characteristics. This constitutes ~90% of all terraced seamounts (N = 34) in the study region. It would be expected that terraces formed from constructional processes should be randomly distributed about the depths within the seamount footprints, and correlated only with the summit heights of the seamounts. Although the data is sparse, this is what is observed at Fernandina (Figure 1.9B). In this region, there are no preferential depths of terraces, which support the interpretation that they are formed by constructional processes. By contrast, terraces formed through erosional processes should be clustered at similar water depths (i.e., paleo-sea level) and independent of seamount depths. This is observed in terrace depth distributions in both the Santiago and Floreana regions, which show prominent peaks in terrace depth and are skewed toward much shallower depths compared to seamount depth distributions (Figures 1.4B, 1.7B).

Discussion

Seamount Exposures and Terrace Formation During the Last Glacial Maximum

Early observations of features created by island vertical motions combined with sea-level fluctuations were identified in echosounder profiles of guyots and seamounts and coupled with observations of beach cobbles and gravels at the summits of these features (e.g., Carsola and Dietz, 1952; Schwartz, 1972; Lambeck, 1984). Similar terraces have been mapped on the upper 200 m of continental shelves in echosounder profiles, with the prevalence of terraces at a given depth taken to reflect the relative duration of stillstands at that level (e.g., Pratt and Dill, 1974; Wagle et al., 1994). However, uncertainty in sea level fluctuations at the time of these studies limited the appeal of using submarine terraces for reconstructing subsidence rates and/or sea level given the known instability of the oceanic lithosphere, foundering due to thermal contraction with time, and ambiguities arising from primary volcanic terraces (e.g., Chaytor et al., 2007). With established paleo-sea level reconstructions for the past 1,000 ka (e.g., Bintanja et al., 2005) along with improved dating methods and models of subsidence, this approach has been revisited (e.g., Kim et al., 2013; Romagnoli et al., 2018).

Sea-level curves for the past 500 ka have been well established from multiple methods and in various ocean basins (e.g., Shackleton, 1987; Siddall et al., 2003). This record has recently been extended to 1,000 ka by coupling sediment core and ice volume models (Bintanja et al., 2005). Over this interval there have been at least eight glacial and interglacial cycles, which have resulted in sea level lowstands comparable to that of the last glacial maximum (>100 m; Figure 1.11). Depth of shelf edge below −130 m has also been used by Quartau et al. (2014, 2015, 2016) to infer subsidence rates assuming that

insular shelves formed immediately after the end of the volcanic phase and subsided afterwards. For ocean island systems that have not experienced uplift, we hypothesize that terraces formed during these lowstands and were preserved on seamounts by removal from wave action due to subsidence. We visited 10 seamounts with summit depths < 130 m and all show evidence for exposure at the sea surface. Further, five seamounts with summit depths of 130–300 m show evidence for exposure. These features include rounded beach cobbles that range in size from decimeter to meter scale. Thinly bedded deposits, which appear to be primarily pyroclastic in origin (Figures 1.5D, 1.8C), are observed at depths up to but no deeper than 300 m. Bedrock textures on summit terraces include smoothed lava flow surfaces (Figure 1.6B) and shorter wavelength undulating surfaces and cavities (Figures 1.5B,C). These are likely secondary textures due to abrasion at or within tens of meters of the sea surface (e.g., Santos et al., 2010; Romagnoli and Jakobsson, 2015). However, we assert that erosive conditions tend to be most vigorous at the sea surface (Quartau et al., 2010; Ramalho et al., 2013), and decrease significantly at depths greater than 20 m for rocky surfaces. These combined observations confirm that these terrace surfaces now 20–300 m deep must have once been at or near the sea surface.

The intersection of a seamount and the sea surface produces erosional terraces, the depth of these terraces is dependent on the vertical motions of the seamount (e.g., uplift, subsidence) and sea level changes since formation. In the absence of major vertical movements and on islands that have experienced at least one glacial/interglacial eustatic cycle, terrace depths should range from present sea level up to 120 m water depth (Quartau et al., 2010), assuming that similar eustatic conditions existed in the Galápagos.

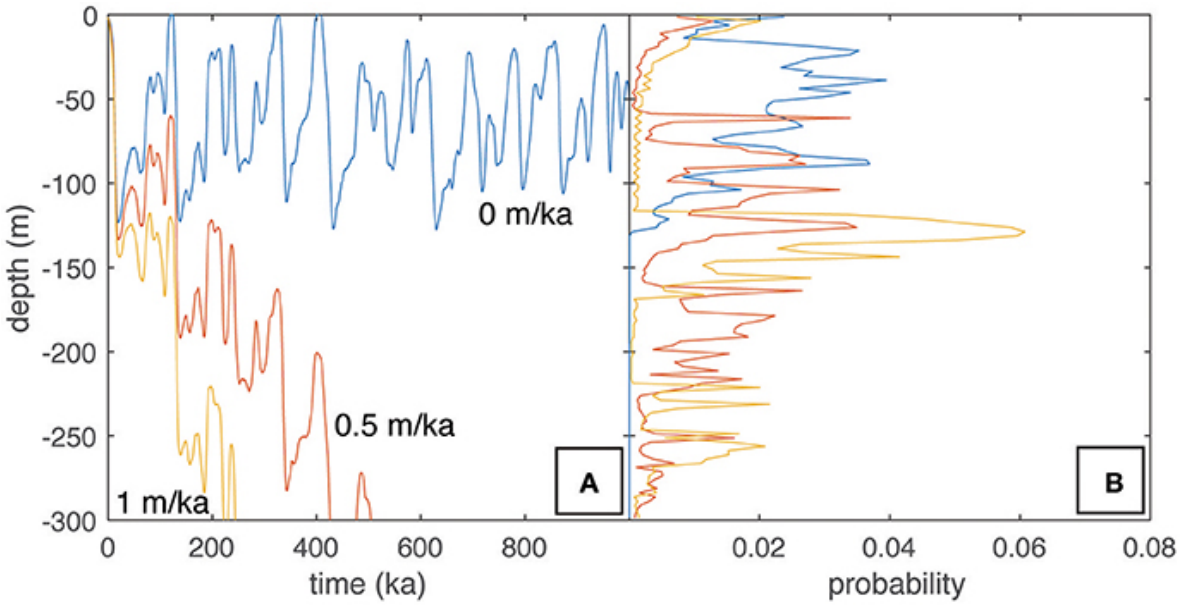

Figure 1.11. Examples of subsidence normalized sea level depth integrations. (A) Sea level as a function of time for the past 1,000 ka. Blue curve shows sea level assuming no subsidence (Bintanja et al., 2005). Red curve shows the same sea level data adjusted for a subsidence rate of 0.5 m/ka, representing relative sea level change at this rate. Orange curve shows the same sea level data adjusted for a subsidence rate of 1 m/ka, representing relative sea level change at this rate. (B) Probability distributions representing the time integrated durations of sea level at all depths for each subsidence rate. Colors shown as defined in (A).

Thus, seamounts with terraces at these depths were present during the LGM at ~20 ka and have likely only experienced minor subsidence or uplift since that time. There is a prevalent peak in the number of terraces at both Santiago (Figure 1.4B) and Floreana (Figure 1.7B) around the depth of sea level during the LGM. These LGM terraces are nearly all associated with directly observed erosional features.

For terraces and erosional features at depths > 130 m, seamounts must be older than 20 ka and must have subsided since their exposure at the sea surface (Quartau et al., 2014, 2015, 2016). From the lack of terraces above 120 m water depth, despite the presence of numerous seamounts within that depth range, the formation of a terrace during a non-lowstand is much less prevalent (Figures 1.4B, 1.7B). This is most likely

due to greater rates of sea level change (i.e., lack of stillstands) during non-lowstand periods. Nevertheless, it is reasonable to assume that erosional terraces occurring at depths > 130 m have either been exposed during earlier sea level still or lowstands and have been subsequently transported to their present depths. Evaluating the mechanism and timing of terrace formation for terraces deeper than 130 m will be discussed in the following section.

Evaluating Subsidence Rates and Paleogeography

Since Darwin's visit to the Galápagos in 1835, the archipelago has played a pivotal role in forming and testing the theory of evolution by natural selection (e.g., Darwin, 1859; Ali and Aitchison, 2014). The archipelago is in a geographical nexus ~1,000 km west of South America, which effectively isolates it from most biologic communication with the continental landmass, but is close enough to enable colonization by non-aquatic, non-volant vertebrates (e.g., Wyles and Sarich, 1983; Rassmann, 1997; Caccone et al., 2002). The Galápagos Islands are also far enough apart to isolate species and promote endemism (e.g., Ricklefs and Bermingham, 2007). Recent evolutionary models have been proposed that link speciation events with glacial maxima where, at extreme sea level lowstands, the islands have presumably been connected, allowing cross-colonization (e.g., Ali and Aitchison, 2014). However, sea level oscillations over the past 1,000 ka alone (< 130 m; Bintanja et al., 2005) cannot explain speciation trends between all of the major islands in the Galápagos that are separated by submarine bridges, which are presently > 300 m below sea level (Figure 1.1A).

We have confirmed the presence of erosional terraces at depths of 290 m through direct observations of beach cobbles and secondary bedrock morphologies, indicative of

abrasion driven erosion by wave action (Figure 1.8B; e.g., Ramalho et al., 2013). We have expanded the observation of these terraces beyond those visited by HOV to include all terraces with similar morphologies (Figures 1.4C, 1.10). From this dataset it is clear that there are several depth ranges with significant terrace abundances that are deeper than sea level has reached in the past 1,000 ka. It is hypothesized that terrace width should be proportional to the duration of wave base erosion at a given depth (e.g., Pratt and Dill, 1974; Menard, 1983; Quartau et al., 2010). For any subsiding archipelago this duration is a function of the sea-level curve as well as the subsidence rate. Thus, with terraces present at the appropriate depths, within the range of predicted sea level variations, the distribution of the terraces provides an independent means by which to test proposed subsidence rates in the Galápagos. The appropriate depth range will be different for all archipelagos, and requires the formation and transport of seamounts for some duration of time appropriate for the subsidence rate. In summary, to relate the terrace distribution on seamounts to subsidence, seamounts must be produced somewhat continuously at the appropriate depth range in order to have a record of these processes.

Based on the emergence ages of Santiago (1 Ma), Santa Cruz and Floreana (2.3 Ma) and the range of ages of lavas on those islands we predict that the seamounts are also on the order of 1 Ma (Geist et al., 2014). Further, we assume that individual seamounts were produced over a relatively short time period, and thus have not been “repaved” and represent unobscured records of exposure since their formation (Chapter 2). Assuming an average subsidence rate of 0.4 m/ka, which is the inferred value for the Galápagos in the vicinity of the seamounts (Geist et al., 2014) we predict that the oldest (~1 Ma) and thus deepest possible terraced seamounts, which may have formed during sea level lowstands

of ~100 m could now have terraces at depths of ~600 m. Terraces that we positively identify as erosional range in depth from 0 to 300 m. This depth range is half that of the maximum expected depth range for terraces and thus should provide sufficient information on subsidence rates over at least the past 500 ka. Since we do not have independent age control on any of the erosional terraces we suggest that by using the combined seamount terrace depth distribution we should be able to assess subsidence rates.

In order to assess subsidence rates, we have combined all bathymetric data within the seamount footprints, which have been positively identified as erosional (Figure 1.10) and determined the relative proportion of data with slopes < 5° at all depths as a proxy for the terrace distribution (Figure 1.3). Although the subsidence rates vary spatially over the archipelago, we assert that the study areas are aligned almost perpendicular to plate motion and have correspondingly similar emergence ages (Geist et al., 2014), so have similar loading histories. Moreover, the submarine platform that underlies Santiago and Floreana makes up a majority of the erupted volume of the archipelago is likely the largest contribution to the gravitational load and was presumably constructed simultaneously for both regions (Geist et al., 2008). We evaluate the subsidence modified sea-level curve that best reproduces the observed terrace distributions (Figure 1.11). This is done by comparing the terrace depth distribution to sea level depth distributions, which are first offset at a constant rate between 0 and 1 m/ka, which is reasonable for the archipelago of 1–2 Ma in age (Figure 1.12; Geist et al., 2014). These depth distributions are then time integrated to represent the probability that sea level has reached a given depth over the past 1 Ma. Similarity between the actual terrace depth distribution and that

predicted from sea level history with an imposed subsidence rate are assessed using the Kullback-Leibler Divergence (D_{KL}), which is a metric for assessing the amount of information that is lost by substituting the terrace distribution for the subsidence adjusted sea-level curve at each subsidence rate (Figures 1.12A,B). The lowest D_{KL} is attained when the substituted distribution most closely matches that of the original distribution. The D_{KL} is calculated from the following equation:

$$D_{KL}(p||q) = \sum xp(x)\cdot \log p(x)q(x) \quad (1)$$

where x is depth in 1 m intervals, $p(x)$ is the terrace depth distribution and $q(x)$ is the distribution produced by the integration of the sea-level curve. We discretize depth in 1 m intervals. The summation is an approximation of the integral definition of the D_{KL} (see MacKay (2003) for more details). In addition to the D_{KL} we compare the cumulative density functions for the subsidence-corrected sea level distributions and terrace distributions using a Kilinogorov-Smirnov (k-s test), using the MATLAB function kstest2 to assess the similarity of the curves. The k-s test provides a p-value, which indicates the similarity of the curves; a p-value > 0.05 indicates that the curves are indistinguishable at the 95% confidence interval (Figures 1.12A,C). From the D_{KL} for each subsidence rate there is a clear trend and minima at 0.2 m/ka. Similarly, the results from the k-s test indicate that the two cumulative probability density curves are indistinguishable between 0.2 and 0.4 m/ka. These subsidence rates are slightly lower than, but on the same order as estimates by other researchers (0.4–0.5 m/ka; Geist et al., 2014).

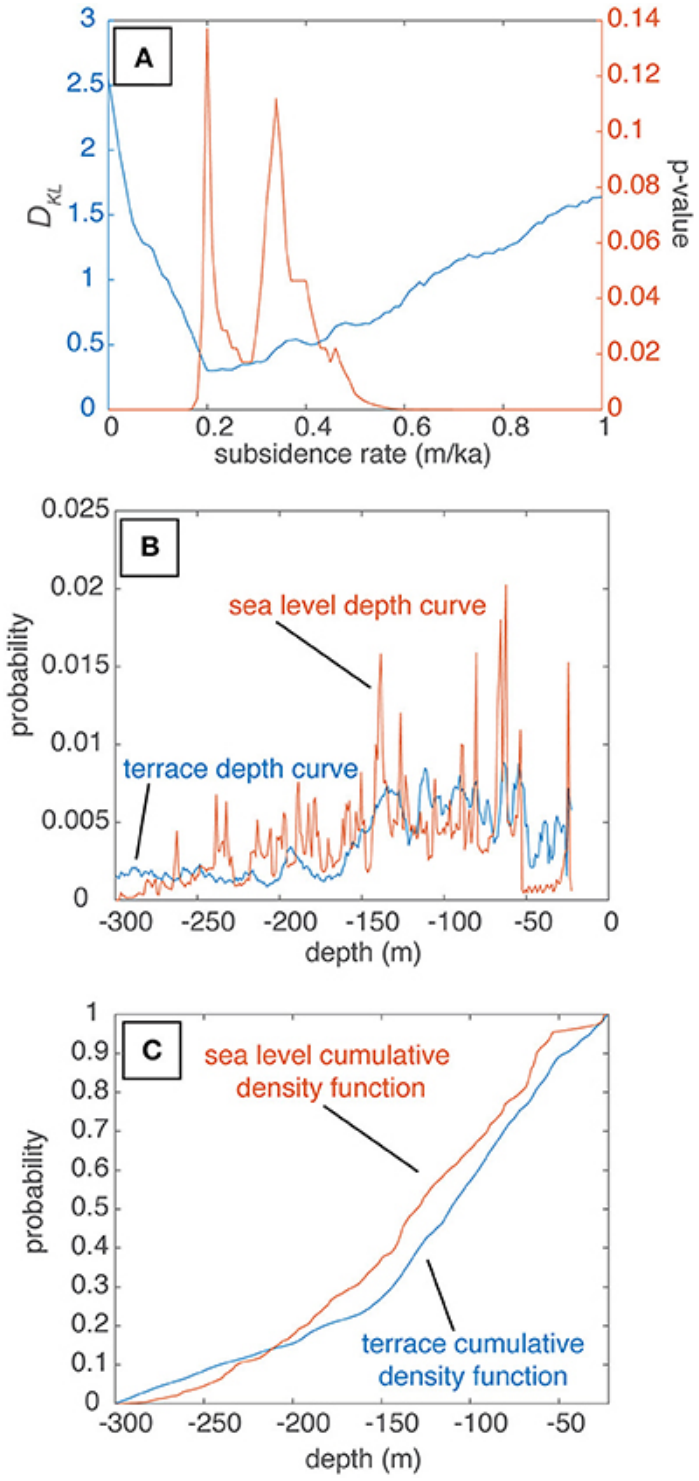

Figure 1.12. Comparison of sea level data with terrace depths at various subsidence rates. (A) Kullback-Leibler Divergence (D_{KL}; blue line) and k-s test (red line) results comparing terrace to sea level distributions adjusted by subsidence rates between 0 and 1 m/ka. The minimum D_{KL} between the two distributions is 0.2 m/ka, and the cumulative distribution function of the curves are indistinguishable at the 2-sigma confidence interval between about 0.2 and 0.4 m/ka. (B) Comparison of probability density functions for terrace distribution (blue line) and time integrated sea level distribution adjusted for a subsidence rate of 0.2 m/ka (red line) used for calculating the D_{KL}. (C) Comparison of cumulative density functions for terrace distribution (blue line) and time integrated sea level distribution adjusted for a subsidence rate of 0.2 m/ka (red line) used for performing the k-s test.

Our calculated rate of subsidence of 0.2 m/ka is an order of magnitude faster than what is predicted for transport beyond a hotspot swell similar to that of Hawaii for young lithosphere (0.04 m/ka; Detrick and Crough, 1978), thus is more likely due to loading or aging of the underlying lithosphere. The subsidence rates are nearly identical to those determined for Ascension Island near the Mid-Atlantic Ridge (0.3 m/ka; Minshull et al., 2010), which is on similarly aged lithosphere (~6–10 Ma; Minshull and Brozena, 1997; Villagómez et al., 2007), and of approximately the same age (2–3 Ma; Minshull et al., 2010) as the islands of Floreana and Santiago. Minshull et al. (2010) invoke viscoelastic relaxation in response to loading of the volcanic edifice as the only mechanism able to produce the observed subsidence rates. Given that we only observe 200 m of subsidence in our dataset, it is possible that elastic loading (110 m; Minshull et al., 2010), and/or cooling of the lithosphere away from the Galápagos spreading center over the past 2 Ma (e.g., Marty and Cazenave, 1989) could together produce the observed subsidence (~150 m; Kane and Hayes, 1994). It is out of the scope of this study to determine the mechanisms of subsidence, but it seems likely that volcanic loading is important in the evolution of the Galápagos Archipelago.

We have mapped the area that would be exposed at two time-intervals based on the sea-level curves of Bintanja et al. (2005) modified using our derived subsidence rates. Land between Isabela and Santa Cruz could be connected as early as the LGM (Figure 1.13A), but additional mapping is needed to prove this given that significant changes may

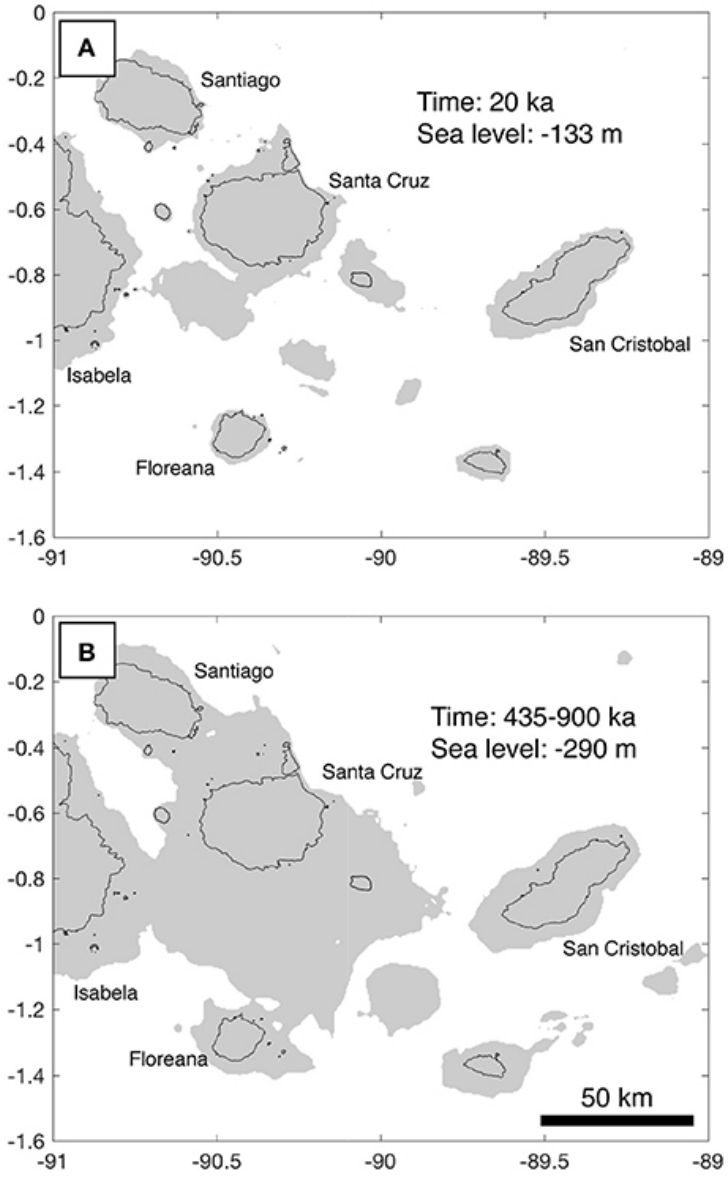

Figure 1.13. Map of DR372 seamount. (A) Bathymetric contour interval is 10 m. Gold line shows dive track for seamount DR372. This seamount is highly irregular in shape, with a N-S trending elongation at it's base and NW-SE elongation near it's summit. The seamount has steep upper flanks and is adorned by multiple irregular summit features. There are multiple terraces on this seamount, which are flanked by steep sides with flank embayments. ENE-WSW striking linear feature SW of the seamount is a data artifact. (B) Rounded boulder on smoothed bedrock material constituting the seamount's terrace. The left portion of the image shows bulbous/rounded basaltic lava flow bedrock and the right side shows rounded basaltic boulders of a similar size and roundness. (C) Field of rounded cobble-boulder sized clasts on flat lying bedrock, which is mostly obscured by fine sediment. Depths in photos indicate the depth of the seafloor at the point of image capture.

have occurred in island volume due to volcanic activity over the past 20 ka. Further, given the current data, we have provided evidence that the central Galápagos Archipelago areas that are now at 290 m water depth were in the past at < 130 m water depth. This evidence includes rounded cobbles atop a terrace at that depth in the Floreana region (Figure 1.8) and seamounts with scalloped upper flanks and terraces resembling those exposed during the last glacial maximum in the Santiago region (Figure 1.4C). We estimate based on the range of subsidence rates that we determined (0.2–0.4 m/ka) that at 435–900 ka, these surfaces were at sea level during the lowstands (Figure 1.13B). Using the previously accepted value of 0.5 m/ka (Geist et al., 2014), these terraces were at lowstand sea levels of ~130 m water depth at 350 ka. During sea level lowstands in this time period it is conceivable that all islands in the central archipelago could be connected by present day bathymetric highs. This prediction hinges on limited modification of the potential bridges due to sedimentation, which at this point cannot be determined due to the lack of seismic data in the Galápagos. Future work should be targeted toward these drowned land bridges in search of evidence for their exposure history to confirm this speculation and search for evidence of deeper features that show evidence for exposure at the sea surface. These observations would provide a means to more rigorously assess the spatial and temporal variations in subsidence rate across the archipelago. Further, direct dating of terraces through micropaleontology or dating of sparse carbonates buried by beach cobbles on the deepest terraces may provide further age-depth relationships.

Conclusion

Through direct seafloor observations of seamounts and correlation with bathymetric data we have confirmed that the modern archipelago has experienced significant subsidence over the past ~1 Ma. We observed rounded cobbles and boulders in addition to other bedrock features, which we interpret to represent exposure of many seamounts at the sea surface. Bathymetric features, including submarine terraces, are correlated with direct seafloor observations of erosional features, which we use to create a framework to identify seamounts, which have experienced exposure at the sea surface. Seamounts with rounded cobble deposits and with similar morphologic features are observed to depths of 300 m in both the Santiago and Floreana regions. These are the first direct observations that indicate all islands in the central archipelago have subsided around ~200 m and could have been at least intermittently connected in the past. Without independent age data on the seamount terraces we are able to use their distribution and established sea-level curves to assess subsidence rates, and thus obtain approximate timing of potential inter-island connections. The comparison of these distributions leads us to conclude that since the formation of the seamounts the archipelago has been subsiding between 0.2 and 0.4 m/ka. We infer from these subsidence rates that the deepest observed terraces were formed between 435 and 900 ka during or within close proximity to lowstands. Extending this record to greater depths (and ages), will impact the interpretation of inter-island migration and speciation in the Galápagos. Combined seafloor observation and use of seamount terrace depth distributions have the potential to provide a more complete and robust understanding of paleogeography in ocean island

systems. As the resolution of the timing and nature of sea level fluctuations increases, the interpretations resulting from terrace depth distributions on seamounts will only improve.

Acknowledgements

We would first like to thank the captain and crew of the M/V *Alucia* for their hard work during the cruise upon which the data for this project were acquired. Further, we would like to acknowledge the skilled HOV pilots for their dedication to the safety and success of the dive operations over the course of the cruise. We acknowledge the Galápagos National Park directorate for permission to map and collect submarine rock samples (PC-44-15), and our colleagues at the Charles Darwin Foundation for facilitating scientific collaboration in the Galápagos. We are grateful to the Government of Ecuador and INOCAR for permission to operate in their territorial waters and marine protected areas. We thank Dan Fornari, Mark Richards, Pelayo Salinas de León for their assistance in data acquisition and scientific input on the cruise, as well as Hannah Bercovici for assistance with rock sample preparation and data processing. We appreciate Neil Mitchell, Rui Quartau and Daneiele Casalbore for their detailed and thoughtful reviews, which greatly improved the manuscript. This project was carried out with financial support from the NSF (OCE-1634685 to SS and OCE-1634952 to VW) and the Dalio Explore Fund.

References

Ali, J. R., and Aitchison, J. C. (2014). Exploring the combined role of eustasy and oceanic island thermal subsidence in shaping biodiversity on the Galápagos. J. Biogeogr. 41, 1227–1241. doi: 10.1111/jbi.12313

Allan, J. F., and Simkin, T. (2000). Fernandina volcano's evolved, well-mixed basalts: Mineralogical and petrological constraints on the nature of the Galápagos plume. J. Geophys. Res. 105, 6017–6041. doi: 10.1029/1999JB900417

Bintanja, R., van de Wal, R. S. W., and Oerlemans, J. (2005). Modelled atmospheric temperatures and global sea levels over the past million years. Nature 437, 125–128. doi: 10.1038/nature03975

Bohnenstiehl, D. R., Howell, J. K., White, S. M., and Hey, R. N. (2012). A modified basal outlining algorithm for identifying topographic highs from gridded elevation data, Part 1: motivation and methods. Comput. Geosci. 49, 308–314. doi: 10.1016/j.cageo.2012.04.023

Caccone, A., Gentile, G., Gibbs, J. P., Fritts, T. H., Snell, H. L., Betts, J., et al. (2002). Phylogeography and History of Giant Galápagos Tortoises. Evolution 56, 2052–2066. Available online at: http://www.jstor.org/stable/3094648

Campbell, J. F. (1984). Rapid subsidence of Kohala Volcano and its effect on coral reef growth. Geo Mar. Lett. 4, 31–36. doi: 10.1007/BF02237971

Carey, S., Fisher, C. R., de Leon, P. S., Roman, C., Raineault, N. A., Suarez, J., et al. (2016). Exploring the undersea world of the Galápagos Islands. Ocean. Mag. 29, 32–34.

Carsola, A. J., and Dietz, R. S. (1952). Submarine geology of two flat-topped northeast Pacific seamounts. Am. J. Sci. 250, 481–497. doi: 10.2475/ajs.250.7.481

Cas, R. A. F. (1992). Submarine volcanism: eruption styles, products, and relevance to understanding the host-rock successions to volcanic-hosted massive sulfide deposits. Econ. Geol. 87, 511–541. doi: 10.2113/gsecongeo.87.3.511

Casalbore, D. (2018). Volcanic Islands and Seamounts. Submarine Geomorphology Springer Geology. Cham: Springer, 333–347.

Casalbore, D., Falese, F., Martorelli, E., Romagnoli, C., and Chiocci, F. L. (2017). Submarine depositional terraces in the Tyrrhenian Sea as a proxy for paleo-sea level reconstruction: problems and perspective. Quat. Int. 439, 169–180. doi: 10.1016/j.quaint.2016.02.027

Casalbore, D., Romagnoli, C., Pimentel, A., Quartau, R., Casas, D., Ercilla, G., et al. (2015). Volcanic, tectonic and mass-wasting processes offshore Terceira Island (Azores) revealed by high-resolution seafloor mapping. Bull. Volcanol. 77:24. doi: 10.1007/s00445-015-0905-3

Chaytor, J. D., Keller, R. A., Duncan, R. A., and Dziak, R. P. (2007). Seamount morphology in the Bowie and Cobb hot spot trails, Gulf of Alaska. Geochem. Geophys. Geosyst. 8, 1–26. doi: 10.1029/2007GC001712

Christie, D. M., Duncan, R. A., McBirney, A. R., Richards, M. A., White, W. M., Harpp, K. S., et al. (1992). Drowned islands downstream from the Galápagos hotspot imply extended speciation times. Nature 355, 246–248. doi: 10.1038/355246a0

Clague, D. A., Moore, J. G., and Reynolds, J. R. (2000). Formation of submarine flat-topped volcanic cones in Hawai'i. Bull. Volcanol. 62, 214–233. doi: 10.1007/s004450000088

Couce, E., Ridgwell, A., and Hendy, E. J. (2012). Environmental controls on the global distribution of shallow-water coral reefs. J. Biogeogr. 39, 1508–1523. doi: 10.1111/j.1365-2699.2012.02706.x

Darwin, C. (1859). The Origin of Species by Means of Natural Selection. London.

Detrick, R. S., and Crough, S. T. (1978). Island subsidence, hot spots, and lithospheric thinning. J. Geophys. Res. Solid Earth 83, 1236–1244.

Geist, D. (1984). On the emergence and submergence of the Galápagos islands. Not. Galápagos 56, 5–9.

Geist, D., Diefenbach, B. A., Fornari, D. J., Kurz, M. D., Harpp, K., and Blusztajn, J. (2008). Construction of the Galápagos platform by large submarine volcanic terraces. Geochem. Geophys. Geosyst. 9, 1–27. doi: 10.1029/2007GC001795

Geist, D. J., Fornari, D. J., Kurz, M. D., Harpp, K. S., Adam Soule, S., Perfit, M. R., et al. (2006). Submarine Fernandina: Magmatism at the leading edge of the Galápagos hot spot. Geochem. Geophys. Geosyst. 7, 1–27. doi: 10.1029/2006GC001290

Geist, D., Snell, H., Snell, H., Goddard, C., and Kurz, M. D. (2014). A Paleogeographic Model of the Galápagos Islands and Biogeographical and Evolutionary Implications. Galápagos Nat. Lab. Earth Sci. Am. Geophys. Union, Washington DC, 145–166.

Harpp, K., and Geist, D. (2002). Wolf-Darwin lineament and plume-ridge interaction in northern Galápagos. Geochem. Geophys. Geosyst. 3, 1–19. doi: 10.1029/2002GC000370

Harpp, K. S., Fornari, D. J., Geist, D. J., and Kurz, M. D. (2003). Genovesa Submarine Ridge: A manifestation of plume-ridge interaction in the northern Galápagos Islands. Geochem. Geophys. Geosyst. 4, 1–27. doi: 10.1029/2003GC000531

Huppert, K. L., Royden, L. H., and Perron, J. T. (2015). Dominant influence of volcanic loading on vertical motions of the Hawaiian Islands. Earth Planet. Sci. Lett. 418, 149–171. doi: 10.1016/j.epsl.2015.02.027

Kane, K. A., and Hayes, D. E. (1994). A new relationship between subsidence rate and zero-age depth. J. Geophys. Res. Earth 99, 21759–21777. doi: 10.1029/94JB01747

Kim, G. B., Yoon, S. H., Sohn, Y. K., and Kwon, Y. K. (2013). Wave-planation surfaces in the mid-western East Sea (Sea of Japan): indicators of subsidence history and paleogeographic evolution of back-arc basin. Mar. Geol. 344, 65–81. doi: 10.1016/j.margeo.2013.07.008

Kleypas, J. A., Mcmanus, J. W., and Menez, L. A. B. (1999). Environmental limits to coral reef development : where do we draw the line? Am. Zoo. 39, 146–159. doi: 10.1093/icb/39.1.146

Kokelaar, B. P., and Durant, G. P. (1983). The submarine eruption and erosion of Surtla (Surtsey), Iceland. J. Volcanol. Geotherm. Res. 19, 239–246. doi: 10.1016/0377-0273(83)90112-9

Kurz, M. D., and Geist, D. (1999). Dynamics of the Galápagos hotspot from helium isotope geochemistry. Geochim. Cosmochim. Acta 63, 4139–4156. doi: 10.1016/S0016-7037(99)00314-2

Kurz, M. D., Rowland, S. K., Curtice, J., Saal, A. E., and Naumann, T. (2014). "Eruption rates for fernandina volcano: a new chronology at the galápagos hotspot center," in The Galápagos: A Natural Laboratory for the Earth Sciences, eds K. S. Harpp, E. Mittelstaedt, N. d'Ozouville, and D. W. Graham (Washington, DC), 41–54. doi: 10.1002/9781118852538.ch4

Lambeck, K. (1984). Subsidence of a guyot west of Flores, Azores. Can. J. Earth Sci. 21, 960–963. doi: 10.1139/e84-100

Ludwig, K. R., Szabo, B. J., Moore, J. G., and Simmons, K. R. (1991). Crustal subsidence rates off Hawaii determined from 234U/238 ages of drowned coral reefs. Geology 19, 171–174. doi: 10.1130/0091-7613(1991)019<0171:CSROHD>2.3.CO;2

MacKay, D. J. C. (2003). Information Theory, Inference and Learning Algorithms. Cambridge: Cambridge University Press.

Marty, J. C., and Cazenave, A. (1989). Regional variations in subsidence rate of oceanic plates: a global analysis. Earth Planet. Sci. Lett. 94, 301–315. doi: 10.1016/0012-821X(89)90148-9

McBirney, A. R., and Williams, H. (1969). Geology and petrology of the Galápagos Islands. Geol. Soc. Am. Mem. 118, 1–197. doi: 10.1130/MEM118-p1

Menard, H. W. (1983). Insular erosion, isostasy, and subsidence. Science 220, 913–918. doi: 10.1126/science.220.4600.913

Menard, H. W., and Ladd, H. S. (1963). Oceanic islands, seamounts, guyots and atolls. Sea 3, 365–385.

Minshull, T. A., and Brozena, J. M. (1997). Gravity anomalies and flexure of the lithosphere at Ascension Island. Geophys. J. Int. 131, 347–360. doi: 10.1111/j.1365-246X.1997.tb01227.x

Minshull, T. A., Ishizuka, O., and Garcia-Castellanos, D. (2010). Long-term growth and subsidence of Ascension Island: constraints on the rheology of young oceanic lithosphere. Geophys. Res. Lett. 37, 3–7. doi: 10.1029/2010GL045112

Mitchell, N. C. (2001). Transition from circular to stellate forms of submarine volcanoes. J. Geophys. Res. Solid Earth 106, 1987–2003. doi: 10.1029/2000JB900263

Mitchell, N. C., Masson, D. G., Watts, A. B., Gee, M. J. R., and Urgeles, R. (2002). The morphology of the submarine flanks of volcanic ocean islands: a comparative study of the Canary and Hawaiian hotspot islands. J. Volcanol. Geotherm. Res. 115, 83–107. doi: 10.1016/S0377-0273(01)00310-9

Mitchell, N. C., Stretch, R., Oppenheimer, C., Kay, D., and Beier, C. (2012). Cone morphologies associated with shallow marine eruptions: east Pico Island, Azores. Bull. Volcanol. 74, 2289–2301. doi: 10.1007/s00445-012-0662-5

Mittelstaedt, E., Soule, S., Harpp, K., Fornari, D., McKee, C., Tivey, M., et al. (2012). Multiple expressions of plume-ridge interaction in the Galápagos: volcanic lineaments and ridge jumps. Geochem. Geophys. Geosyst. 13:Q05018. doi: 10.1029/2012GC004093

Moore, J. G. (1970). Relationship between subsidence and volcanic load, Hawaii. Bull. Volcanol. 34, 562–576. doi: 10.1007/BF02596771

Moore, J. G., Clague, D. A., and Normark, W. R. (1982). Diverse basalt types from Loihi seamount, Hawaii. Geology 10, 88–92. doi: 10.1130/0091-7613(1982)10<88:DBTFLS>2.0.CO;2

Moore, J. G., and Fornari, D. J. (1984). Drowned reefs as indicators of the rate of subsidence of the island of Hawaii. J. Geol. 92, 752–759. doi: 10.1086/628910

Naumann, T., and Geist, D. J. (2000). Volcano, Isabela Island, Galµpagos : implications for the development. Bull. Volcanol. 61, 497–514. doi: 10.1007/s004450050001

Passaro, S., Ferranti, L., and de Alteriis, G. (2011). The use of high-resolution elevation histograms for mapping submerged terraces: tests from the Eastern Tyrrhenian Sea and the Eastern Atlantic Ocean. Quat. Int. 232, 238–249. doi: 10.1016/j.quaint.2010.04.030

Pratt, R. M., and Dill, R. F. (1974). Deep eustatic terrace levels: Further speculations. Geology 2, 155–156. doi: 10.1130/0091-7613(1974)2<155:DETLFS>2.0.CO;2

Quartau, R., Hipólito, A., Romagnoli, C., Casalbore, D., Madeira, J., Tempera, F., et al. (2014). The morphology of insular shelves as a key for understanding the geological evolution of volcanic islands: insights from Terceira Island (Azores). Geochem. Geophys. Geosyst. 15, 1801–1826. doi: 10.1002/2014GC005248

Quartau, R., Madeira, J., Mitchell, N. C., Tempera, F., Silva, P. F., and Brandão, F. (2015). The insular shelves of the Faial-Pico Ridge: a morphological record of its geologic evolution (Azores archipelago). Geochem. Geophys. Geosyst. 16, 1401–1420. doi: 10.1002/2015GC005733

Quartau, R., Madeira, J., Mitchell, N. C., Tempera, F., Silva, P. F., and Brandão, F. (2016). Reply to comment by Marques et al. on “The insular shelves of the Faial-Pico Ridge (Azores archipelago): A morphological record of its evolution.” Geochem Geophys Geosyst. 17, 633–641. doi: 10.1002/2015GC006180

Quartau, R., Trenhaile, A. S., Mitchell, N. C., and Tempera, F. (2010). Development of volcanic insular shelves: insights from observations and modelling of Faial Island in the Azores Archipelago. Mar. Geol. 275, 66–83. doi: 10.1016/j.margeo.2010.04.008

Ramalho, R. S., Quartau, R., Trenhaile, A. S., Mitchell, N. C., Woodroffe, C. D., and Ávila, S. P. (2013). Coastal evolution on volcanic oceanic islands: a complex interplay between volcanism, erosion, sedimentation, sea-level change and biogenic production. Earth Sci. Rev. 127, 140–170. doi: 10.1016/j.earscirev.2013.10.007

Rassmann, K. (1997). Evolutionary age of the Galápagos iguanas predates the age of the present Galápagos Islands. Mol. Phylogenet. Evol. 7, 158–172. doi: 10.1006/mpev.1996.0386

Ricklefs, R. E., and Bermingham, E. (2007). The causes of evolutionary radiations in archipelagoes: passerine birds in the lesser antilles. Am. Nat. 169, 285–297. doi: 10.1086/510730

Romagnoli, C., Casalbore, D., Ricchi, A., Lucchi, F., Quartau, R., Bosman, A., et al. (2018). Morpho-bathymetric and seismo-stratigraphic analysis of the insular shelf of Salina (Aeolian archipelago) to unveil its Late-Quaternary geological evolution. Mar. Geol. 395, 133–151. doi: 10.1016/j.margeo.2017.10.003

Romagnoli, C., and Jakobsson, S. P. (2015). Post-eruptive morphological evolution of island volcanoes: surtsey as a modern case study. Geomorphology 250, 384–396. doi: 10.1016/j.geomorph.2015.09.016

Rubin, K. H., Fletcher, C. H., and Sherman, C. (2000). Fossiliferous Lana'i deposits formed by multiple events rather than a single giant tsunami. Nature 408, 675–681. doi: 10.1038/35047008

Santos, R. S., Tempera, F., Colaço, A., Cardigos, F., and Morato, T. (2010). Spotlight 11: Dom João de Castro Seamount. Oceanography 23, 200–201. doi: 10.5670/oceanog.2010.83

Schwartz, D. M., Wanless, V. D., Berg, R., Jones, M., Fornari, D. J., Soule, S. A., et al. (2018). Petrogenesis of alkalic seamounts on the Galápagos Platform. Deep Sea Res. Part II Top. Stud. Oceanogr. 150, 170–180. doi: 10.1016/j.dsr2.2017.09.019

Schwartz, M. (1972). Seamounts as sea-level indicators. Geol. Soc. Am. Bull. 83, 2975–2979. doi: 10.1130/0016-7606(1972)83[2975:SASI]2.0.CO;2

Shackleton, N. J. (1987). Oxygen isotopes, ice volume and sea level. Quat. Sci. Rev. 6, 183–190. doi: 10.1016/0277-3791(87)90003-5

Siddall, M., Rohling, E., Almogi-Labin, A., Hemleben, C., Meischner, D., Schmelzer, I., et al. (2003). Sea-level fluctuations during the last glacial cycle. Nature 423, 853–858. doi: 10.1038/nature01690

Sinton, C. W., Harpp, K. S., and Christie, D. M. (2014). A preliminary survey of the northeast seamounts, galápagos platform. Galápagos A Nat. Lab. Earth Sci. 335–362. doi: 10.1002/9781118852538.ch16

Smith, W. H. F., and Sandwell, D. T. (1997). Global sea floor topography from satellite altimetry and ship depth soundings. Science 277, 1956–1962. doi: 10.1126/science.277.5334.1956

Trenhaile, A. S. (1987). The Geomorphology of Rock Coasts. Oxford: Oxford University Press.

Trenhaile, A. S. (2000). Modeling the development of wave-cut shore platforms. Mar. Geol. 166, 163–178. doi: 10.1016/S0025-3227(00)00013-X

Villagómez, D. R., Toomey, D. R., Geist, D. J., Hooft, E. E. E., and Solomon, S. C. (2014). Mantle flow and multistage melting beneath the Galápagos hotspot revealed by seismic imaging. Nat. Geosci. 7, 151–156. doi: 10.1038/ngeo2062

Villagómez, D. R., Toomey, D. R., Hooft, E. E. E., and Solomon, S. C. (2007). Upper mantle structure beneath the Galápagos Archipelago from surface wave tomography. J. Geophys. Res. 112:B07303. doi: 10.1029/2006JB004672

Wagle, B. G., Vora, K. H., Karisiddaiah, S. M., Veerayya, M., and Almeida, F. (1994). Holocene submarine terraces on the western continental shelf of India; Implications for sea-level changes. Mar. Geol. 117, 207–225. doi: 10.1016/0025-3227(94)90016-7

Watts, A. B., and Ten Brink, U. S. (1989). Crustal structure, flexure, and subsidence history of the Hawaiian Islands. J. Geophys. Res. Solid Earth 94, 10473–10500. doi: 10.1029/JB094iB08p10473

Weatherall, P., Marks, K. M., Jakobsson, M., Schmitt, T., Tani, S., Arndt, J. E., et al. (2015). A new digital bathymetric map of the world's oceans. Earth Space Sci. 2, 331–345. doi: 10.1002/2015EA000107

Werner, R., Hoernle, K., Barckhausen, U., and Hauff, F. (2003). Geodynamic evolution of the Galápagos hot spot system (Central East Pacific) over the past 20 m.y.:

Constraints from morphology, geochemistry, and magnetic anomalies. Geochem. Geophys. Geosyst. 4. doi: 10.1029/2003GC000576

White, W. M., McBirney, A. R., and Duncan, R. A. (1993). Petrology and geochemistry of the Galápagos Islands: Portrait of a pathological mantle plume. J. Geophys. Res. Solid Earth 98, 19533–19563. doi: 10.1029/93JB02018

Wyles, J. S., and Sarich, V. M. (1983). “Are the Galápagos iguanas older than the Galápagos? Molecular evolution and colonization models for the archipelago,” in Patterns of Evolution in Galápagos Organisms, eds R. I. Bowman, M. Berson, and A. E. Levinton (San Francisco, CA: American Association for the Advancement of Science, Pacific Division), 177–185.

Zecchin, M., Ceramicola, S., Lodolo, E., Casalbore, D., and Chiocci, F. L. (2015). Episodic, rapid sea-level rises on the central Mediterranean shelves after the Last Glacial Maximum: a review. Mar. Geol. 369, 212–223. doi: 10.1016/j.margeo.2015.09.002

CHAPTER TWO: PETROGENESIS OF ALKALIC SEAMOUNTS ON THE GALÁPAGOS PLATFORM

This chapter was published by Elsevier in the journal *Deep Sea Research Part II* and should be referenced appropriately as below.

Schwartz, D. M., Wanless, V. D., Berg, R., Jones, M., Fornari, D. J., Soule, S. A., Lytle, M., Carey, S. (2018). Petrogenesis of alkalic seamounts on the Galápagos Platform. Deep Sea Research Part II: Topical Studies in Oceanography, 150, 170-180.

Abstract

In the hotspot-fed Galápagos Archipelago there are transitions between volcano morphology and composition, effective elastic thickness of the crust, and lithospheric thickness in the direction of plate motion from west to east. Through sampling on the island scale it is unclear whether these transitions are gradational or sharp and whether they result in a gradational or a sharp boundary in terms of the composition of erupted lavas. Clusters of interisland seamounts are prevalent on the Galápagos Platform, and occur in the transition zone in morphology between western and eastern volcanoes providing an opportunity to evaluate sharpness of the compositional boundary resulting from these physical transitions. Two of these seamounts, located east of Isabela Island and southwest of the island of Santiago, were sampled by remotely operated vehicle in 2015 during a telepresence supported E/V *Nautilus* cruise, operated by the Ocean Exploration Trust. We compare the chemistries of these seamount lavas with samples erupted subaerially on the islands of Isabela and Santiago, to test whether seamounts are formed from melt generation and storage similar to that of the western or eastern volcanoes, or transitional between the two systems. There are no systematic variations between the two seamounts and variability in all samples can be related through<10% fractional crystallization at 500–900 MPa. Both seamounts are interpreted to represent a single magmatic episode and eruptive event. Trace element compositions indicate they formed downstream of the hotspot center. The calculated extents of melting are consistent with generation of magmas sourcing the seamounts beneath lithosphere of intermediate thickness (~ 56 km). The seamount lavas have compositions that are nearly identical to a subset of lavas erupted subaerially on Santiago Island, suggesting lateral

magma transport on the order of 10 km from their source region prior to eruption. The compositional characteristics and, in particular, depth of crystallization suggest that although seamount magmas have a transitional melting signature, they are discretized on the island scale, through homogenization in the lithospheric mantle and redistributed by vertical and horizontal diking in the shallow crust. Due to this homogenization, it remains unclear whether the variation in erupted lava chemistries from west to east are representative of sharp or gradual changes in mantle composition and structure across the archipelago.

Introduction

The lifespan of hotspot sourced volcanic islands is controlled by the interplay between volcano growth (i.e., eruption rate), subsidence and erosion (e.g., Geist, 1996; Geist et al., 2014a). These processes are modulated by the transport of the islands away from a fixed “plume” source by plate motion (e.g., Morgan, 1972). The archetypal example of this process is the Hawaiian Island chain. The Hawaiian Islands form a linear, age-progressive, volcanic succession parallel to the direction of absolute plate motion, where large, young islands become progressively smaller, older and more dissected to the northwest (e.g., Clague and Dalrymple, 1987). This general progression is less clear for other plume-sourced intraplate volcanic systems, including the Galápagos Archipelago, which is the subject of this study (Figure 2.1).

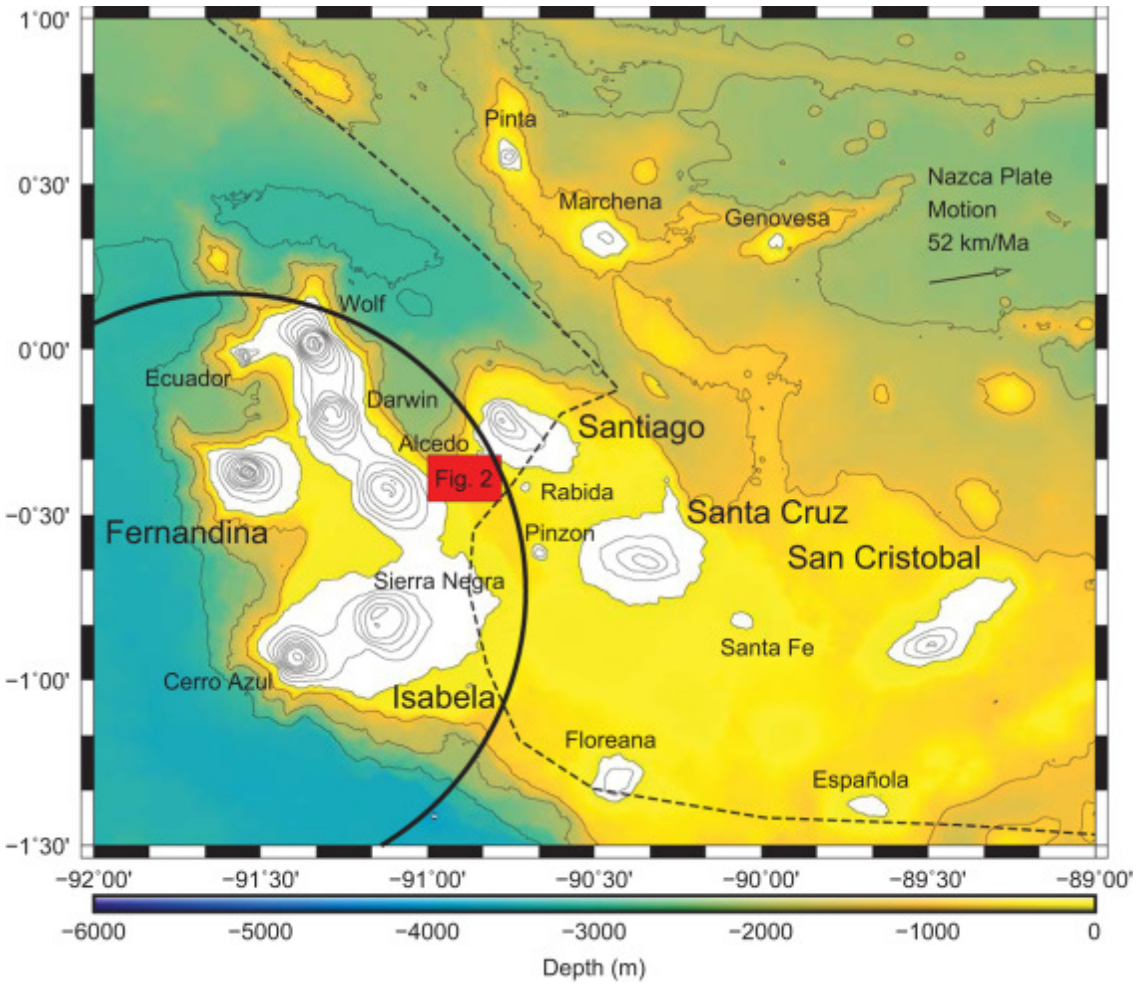

Figure 2.1. Map of the Galápagos Archipelago. The western islands (Isabela, Fernandina) are typified by steep upper flanks and central calderas, eastern islands (Santiago, Santa Cruz, San Cristobal) have shallow slopes and are characterized by dispersed linear volcanic vent systems. Subaerial contours show elevations at 200 m intervals. Submarine contours show bathymetry at 500 m intervals. Solid black circle indicates boundary of anomalously thin mantle transition zone, inferred as plume upwelling region centered below Fernandina (Hooft et al., 2003). Dashed line shows boundary between high (12 km to the west) and low (6 km to the east) effective elastic thickness of the crust (Feighner and Richards, 1994), which correlates with the boundary of thick and thin mantle lithosphere (Villagómez et al., 2007). Location of seamounts sampled in this study is shown by the red region, and in more detail in Figure 2.2. (For interpretation of the references to color in this figure legend, the reader is referred to the web version of this article).

The Galápagos consists of 13 major volcanic islands and numerous smaller islands, and volcanic seamounts in the eastern equatorial Pacific (Figure 2.1; McBirney and Williams, 1969; Christie et al., 1992). Most of the islands rise from a large (~ 3500 km2), shallow volcanic platform that stands ~ 3000 m above the surrounding seafloor (Geist et al., 2008a). The center of plume upwelling in the Galápagos lies southwest of Fernandina Island, the westernmost and most active volcano (Allan and Simkin, 2000). The position of the plume source has been inferred based on a locally thin mantle transition zone (Figure 2.1; Hooft et al., 2003), low shear-wave velocities (Villagómez et al., 2007, Villagómez et al., 2011), and geochemical enrichment (e.g., Kurz and Geist, 1999). Although there is a general age progression akin to that of Hawaii (White et al., 1993), the Galápagos differs from Hawaii in the persistence of volcanic activity up to 250 km away from the inferred plume center (e.g., Geist et al., 1986), and a wide distribution of islands and seamounts towards the Galápagos Spreading Center, attributed to plume ridge interaction (Harpp and Geist, 2002, Harpp et al., 2003). Despite continued volcanism away from the locus of mantle upwelling, there are clear differences in the magmatic plumbing systems between the western and eastern volcanoes in the Galápagos.

The Galápagos Archipelago displays a unique, systematic variation in morphology between the volcanoes in the west compared to those in the east. The western islands (Fernandina and Isabela; Figure 2.1) are typified by the presence of large and multicyclic summit calderas, surrounded by circumferential fissures near the summits and radial vents on the flanks (Chadwick and Howard, 1991), which are indicators of the presence of persistent shallow (~ 2 km; Yun et al., 2006; Geist et al., 2008b, Geist et al.,

2014b) magma chambers and periodic eruption cycles (Chadwick and Dieterich, 1995). The western volcanoes typically erupt homogenous tholeiitic lavas, resulting from primarily shallow (200 MPa; Geist et al., 1998) crystal fractionation (< 7% MgO; e.g., Saal et al., 2007). By contrast, older islands to the east (Santiago, Santa Cruz, San Cristobal, Floreana, and satellite islands; Figure 2.1) are broad shields that generally lack calderas, and are dominated by flank eruptions, spatter or cinder cones, and elongate rift zones that extend from the island summit to the lower subaerial flanks (e.g., Swanson et al., 1974; Geist and Harpp, 2009). The lavas erupted on the eastern islands and in the central archipelago (e.g., Santiago; Santa Cruz) are highly variable in composition, with rock types ranging from picrites to trachytes (McBirney and Williams, 1969, Swanson et al., 1974, Saal et al., 2007, Herbert et al., 2009, Gibson et al., 2012, Wilson, 2013) and have signatures of deep crystal fractionation (600–900 MPa; Geist et al., 1998).

This transition between western and eastern volcano morphology is mirrored by a transition in both the effective elastic thickness of the crust from 12 km in the west to 6 km in the east (Feighner and Richards, 1994) and lithospheric thickness from 70 km in the west to 40 km in the east (Villagómez et al., 2007). The change in lithospheric thickness ultimately affects the total extent of mantle melting and therefore magma compositions produced in each region (Figure 2.1; Gibson and Geist, 2010). However, because sampling has been restricted primarily to the subaerial islands, it is unclear whether the crustal and lithospheric thickness variations and resulting geochemical signals are abrupt or gradational across the archipelago.

In 2015, we explored and sampled two seamounts that lie between Isabela in the west and Santiago, which presently erupt as caldera-forming and dispersed styles. The

seamounts are within the transition between thin and thick lithosphere (e.g., Villagómez et al., 2007) to determine if there are systematic changes in lava compositions that correlate with geophysical transitions. Specifically, the seamounts are located between Isabela in the west and Santiago in the eastern region of the archipelago (Figure 2.1). We present the first suite of geochemical data from these seamounts with twelve samples collected by the remotely operated vehicle (ROV) Hercules. Analyses of these samples (major and trace element concentrations and volatile contents) provide the first direct measurements of interisland volcanic activity in the modern archipelago. We use these samples to 1) determine depths of crystallization and compositional heterogeneity beneath the seamounts, 2) compare the chemical characteristics of the seamounts to those of the adjacent western and eastern volcanic islands, and 3) test whether the seamounts are formed through magma delivery from a distinct deep magmatic source directly below the seamounts, or from a magma reservoir that also feeds an adjacent volcanic island.

Remotely Operated Vehicle (ROV) Dives and Sample Collection

Rock samples were collected in collaboration with the Ocean Exploration Trust on the E/V *Nautilus* cruise NA064 in July 2015 using the ROV Hercules (Bell et al., 2016). Dive planning and sample collection was coordinated via telepresence from the Woods Hole Oceanographic Institution's Exploration Command Center. Instructions to the onboard team of engineers and scientists were provided via satellite link using both voice, text-based chat, and video links, with real-time data transmitted from the ROV. The dive traversed two unnamed seamounts southwest of Santiago (Figure 2.2) and collected 15 rock samples (seven analyzed from the northern seamount and five analyzed from the southern seamount; Table 1), in addition to extensive high definition video

footage and digital still imagery (Carey et al., 2016). While nearby seamounts observable in the existing Galápagos multibeam bathymetry are nearly conical in shape (Figure 2.2), both seamounts explored during this cruise are more complex, consisting of a central dome of pillow lavas flanked by a semicircular ring of volcaniclastic sediment and talus.

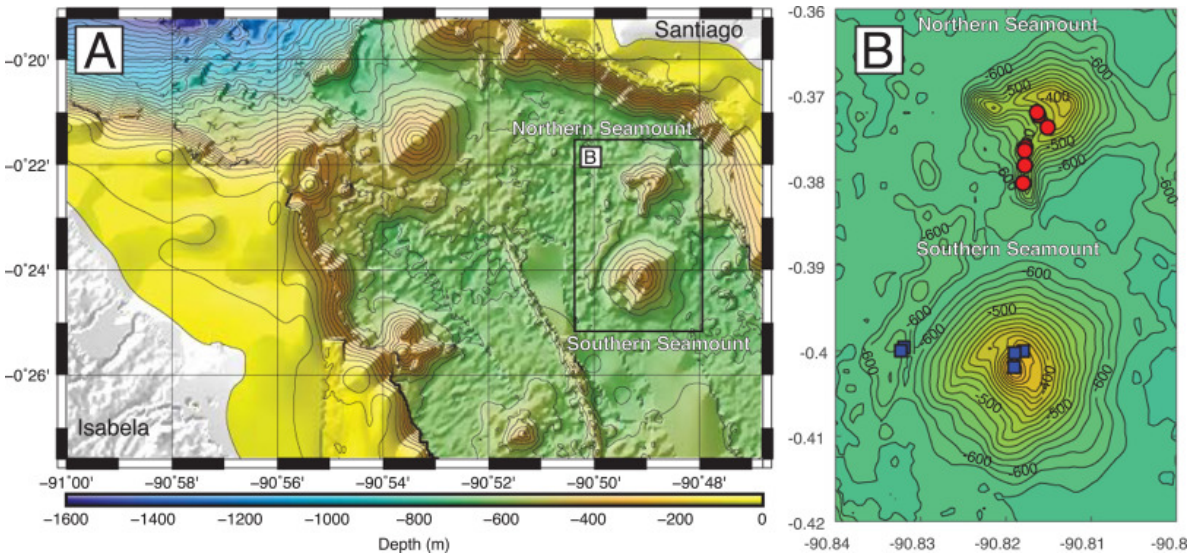

Figure 2.2. A) Bathymetric map of the northern and southern seamount region The seamounts are in the central Galápagos and are on top of the Galápagos platform with basal depths ~ 600 m. Contour interval is 50 m. The nearest islands are Santiago, 5 km to the northeast, and Isabela, 10 km to the west. Black box shows location of inset map. B) Inset Map of Seamounts Colored symbols show sample locations. Colormap is the same as in A, contour interval is 20 m. (For interpretation of the references to color in this figure legend, the reader is referred to the web version of this article).

Northern Seamount Description

The northern seamount has a diameter of 1.6 km is 263 m tall, and has a volume of 0.14 km^3 (Figure 2.2). The base of the seamount lies at 645 m depth and the shallowest point on the eastern summit is at 381 m depth. The summit consists of a horseshoe shaped crater rim, open to the west, composed predominately of volcaniclastic sediment,

Table 2.1 Sample Names and Locations

sample	long	lat	elev. (m)
Northern Seamount			
NA064-114	-90.81503	-0.37395	-422
NA064-115	-90.81612	-0.37255	-439
NA064-116	-90.81627	-0.37220	-420
NA064-120	-90.81763	-0.37630	-450
NA064-123	-90.81772	-0.37668	-445
NA064-127	-90.81770	-0.37840	-469
Southern Seamount			
NA064-129	-90.81792	-0.38047	-472
NA064-131	-90.81907	-0.40192	-265
NA064-132	-90.81797	-0.40003	-329
NA064-133	-90.81900	-0.40025	-325
NA064-134	-90.83197	-0.39960	-588
NA064-135	-90.83233	-0.39998	-587

with a small summit depression containing a lava dome or flow in its center. A N-S linear volcanic ridge extends south from the seamount.

The outer slopes of the seamount are comprised predominately of unconsolidated, tan sediment at the base of the seamount with increasing proportions of, volcaniclastic, black sediment towards the top. The seamount has upper flank slopes that average 23°, with sparse cobbles or boulders of volcanic rock that increase in size with shallower depths. No *in situ* lava flows were observed or sampled on the volcano flanks, but two loose rocks, heavily coated with biological material, were collected from the upper third of the exterior (NA064-113) and interior (NA064-114) slopes. Within the summit depression a small dome or lava flow stands ~ 20 m above the surrounding seafloor. The dome flow is composed almost entirely of basaltic lava, lightly dusted with sediment. The

morphology of the flow ranges from intact and broken pillows to hackly or jumbled lava. Two *in situ* samples were collected from this outcrop (NA064-115 and 116).

The linear volcanic ridge extending south of the crater is ~ 0.5 km long and consists of three small mounds (decreasing in elevation to the south). The tops of the three mounds are composed of relatively large intact pillow lavas, while the lower slopes consist of lavas and sediment. The linear ridges connecting the mounds are composed of smaller pillow tubes with minor volcanic sediment. Lava samples NA064-120 and NA064-123 were collected from the first mound and samples NA064-127 and NA064-129 were collected from the top of the two smaller mounds to the south (Figure 2.2). voice, text-based chat, and video links, with real-time data transmitted from the ROV. The dive traversed two unnamed seamounts southwest of Santiago (Figure 2.2) and collected 15 rock samples (seven analyzed from the northern seamount and five analyzed from the southern seamount; Table 1), in addition to extensive high definition video footage and digital still imagery (Carey et al., 2016). While nearby seamounts observable in the existing Galápagos multibeam bathymetry are nearly conical in shape (Figure 2.2), both seamounts explored during this cruise are more complex, consisting of a central dome of pillow lavas flanked by a semicircular ring of volcaniclastic sediment and talus.

Southern Seamount Description

The larger southern seamount has diameter of ~ 3 km, a height of 388 m, and a volume of 0.34 km3 (Figure 2.2). The base of the seamount lies at 653 m depth and the shallowest point is at 265 m depth. The summit is located at the center of the seamount and is composed of spatter and pillow lavas. Upper flank slopes average ~ 18° and are

composed of unconsolidated sediment and a few sparse cobbles. The semi-circular flank is open to the southwest.

The slopes and crater rim of the seamount are composed almost entirely of tan sediment, with very sparse boulders of volcanic rock. One loose sample was collected from the northern rim of this seamount (NA064-132). The central peak is composed of loose pebble- to cobble-sized basaltic material, which bears resemblance to subaerial spatter (Sample NA064-131). The only intact lava observed on this seamount is a pillow and hackly lava flow that originates near the peak of the central dome and flows downslope to the north. One sample of this lava flow was collected (NA064-133). Two samples (NA064-134 and 135) were collected from heavily sedimented seafloor west of the seamount.

Geochemical Methods

Samples were crushed using a mechanical jaw crusher at Boise State University. Crushed rock chips were rinsed in an ultrasonic bath using a 1% hydrogen peroxide solution, followed by DI water until clean. Approximately 1–2 mm-sized cleaned chips were handpicked using a binocular microscope, avoiding phenocrysts and alteration. Oxidized surfaces were unavoidable on two heavily altered samples (115 and 120).

Whole rock major and select trace element contents were analyzed using a Thermo-ARL automated X-ray Fluorescence (XRF) spectrometer at Washington State University (Table 2). Clean chips (25–50 g) were powdered using a ring mill with tungsten carbide surfaces and fused with Li-tetraborate into glass beads for analyses,

Table 2.2 XRF derived major and trace element concentrations for seamount lavas, and SIMS derived volatile concentrations for sample NA064-114. Analytical precision is reported in Johnson et al. (1999).

NA-064-	114		115	116	120	123	127	129	131	132	133	134	135
Major Element Concentrations (wt%)													
SiO2	44.64	44.44	44.26	46.72	46.24	46.54	45.27	46.61	46.48	46.33	45.07	46.65	46.80
TiO2	2.238	2.178	2.167	2.248	2.324	2.380	2.386	2.318	2.253	2.368	2.372	2.438	2.342
Al2O3	15.31	15.18	15.16	16.07	15.76	15.89	15.68	16.03	15.56	15.76	15.80	15.73	15.71
FeO*	11.52	14.42	14.27	11.69	12.06	12.45	12.85	12.21	11.35	11.51	11.69	11.81	11.66
MnO	0.175	0.190	0.188	0.191	0.209	0.185	0.190	0.212	0.176	0.177	0.161	0.185	0.180
MgO	8.64	8.36	8.34	8.10	8.88	8.17	8.36	8.99	9.42	8.87	7.74	8.77	8.70
CaO	11.95	9.10	9.06	10.81	10.20	10.34	10.10	10.08	10.59	10.53	11.49	10.23	10.35
Na2O	2.78	2.52	2.52	2.85	2.88	2.90	2.82	2.84	2.75	2.93	2.66	2.96	2.85
K2O	0.39	0.61	0.61	0.37	0.38	0.42	0.42	0.39	0.36	0.34	0.40	0.38	0.46
P2O5	0.257	0.489	0.485	0.277	0.283	0.282	0.326	0.266	0.247	0.254	0.775	0.258	0.258
Sum	97.90	97.48	97.06	99.32	99.21	99.56	98.40	99.95	99.18	99.07	98.16	99.41	99.30
LOI %	1.74	2.16	2.16	0.00	0.00	0.00	0.76	0.00	0.00	0.00	1.38	0.00	0.00
Trace Element Concentrations (ppm)													
Ni	173	176	178	142	178	158	163	179	192	168	182	163	162
Cr	239	282	282	244	246	229	247	247	334	284	358	231	276
Sc	27	28	27	31	30	29	27	29	30	30	31	28	29
V	250	249	245	277	268	283	267	265	275	279	282	278	275
Ba	66	65	70	65	72	72	72	75	68	70	62	74	68
Rb	7	11	10	5	7	7	7	7	6	5	8	7	8
Sr	717	352	350	311	319	315	387	313	318	327	400	335	323
Zr	147	144	143	148	151	155	157	152	146	152	148	154	154
Y	27	27	26	28	28	30	29	28	27	27	31	28	27
Nb	12.5	11.1	11.4	12.3	12.5	13.3	12.4	13.0	12.1	13.3	12.9	13.6	12.3
Ga	19	17	16	20	19	19	19	20	19	19	18	20	20
Cu	61	55	57	71	61	54	60	59	68	67	51	66	66
Zn	97	108	114	101	108	108	110	114	104	184	175	134	114
Pb	1	1	1	2	1	1	2	1	1	1	3	1	1
La	12	9	10	11	9	13	16	15	12	10	14	12	12
Ce	29	25	24	30	29	30	30	27	25	32	26	33	28
Th	2	2	1	1	1	1	2	1	0	1	2	2	1
Nd	18	16	17	20	20	19	18	19	19	20	20	20	19
U	2	9	7	1	2	2	2	1	1	2	4	1	3

Volatile Element Concentrations (ppm)

NA064-	H2O	CO2	S	Cl	F
114	8700	135	1636	210	891

following methods of Johnson et al. (1999). Sample NA064-115 was run with a repeat bead to assess procedural reproducibility, which is ≤ 1% difference for all elements. Trace element concentrations for each sample are reported as the mean of three individual analyses, the precision is reported as the standard deviation of these analyses (Supplementary Data Tables 2.3).

Whole rock trace element contents were analyzed by solution ICP-MS at Boise State University following the procedures of Kelley et al. (2003) and Lytle et al. (2012) (Table 3). Approximately 50 mg of each sample were digested in closed 23 mL Savillex Teflon beakers in 3 mL of 8 N HNO3 and 1 mL of HF. Sealed capsules containing sample-acid solution were placed on a hot plate at ≤ 100 °C overnight (~ 12 h) until no trace of solids remained. Dissolved samples were then evaporated to dryness, uncapped on a hot plate, keeping surface temperature ≤ 100 °C, and then re-dissolved in 3 mL of 8 N HNO3 and 3 mL of ultra-pure de-ionized H_2O in sealed capsules on a hot plate at ≤ 100 °C for ~ 12 h. The dissolved samples were transferred into 125 mL HDPE bottles for a 2500× ultra-pure water dilution and sonicated for 30 min to ensure dissolution of all precipitates. Trace element concentrations were measured using a Thermo Electron X-Series II Quadrupole Inductively Coupled Plasma Mass Spectrometer (ICP-MS) coupled with an ESI SC-FAST autosampler. Samples were corrected using an internal standard solution containing In, blank corrected using a procedural blank, drift corrected using Geological Survey of Japan (GSJ) standard JB-3, dilution weight corrected, calibrated using US Geological Survey (USGS) standards, GSJ standards, and internal laboratory standards: BHVO-2, BIR-1, DNC-1, W-2 (USGS), JB-3 (GSJ), and 2392-9 (University of Florida in-house standard; Goss et al., 2010). Trace element concentrations for each

Table 2.3 ICPMS derived trace element contents for seamount lavas; all concentrations are reported in ppm. Analytical precision is reported in the Supplementary Data Tables 2.3.

NA-064-	114	115	116	120	123	127	129	131	132	133	134	135
Li	6.11	5.51	5.39	5.57	5.83	6.06	5.48	6.67	6.28	5.54	5.89	5.15
Sc	27.9	27.8	31.5	27.6	29.1	28.0	26.7	32.1	29.0	29.9	26.3	28.7
V	240	238	264	243	253	244	232	278	255	256	239	245
Cr	235	184	184	201	184	196	188	270	220	287	218	219
Co	57.6	48.2	48.3	56.6	49.5	51.3	56.8	48.1	52.5	51.3	51.0	52.0
Ni	200	139	113	189	126	149	217	124	165	196	153	167
Cu	76.6	63.8	73.2	78.6	59.8	62.5	57.9	83.9	72.5	65.8	62.0	64.5
Zn	117	120	123	111	113	114	110	115	295	115	111	107
Ga	12.9	12.5	13.4	12.6	13.4	13.0	12.7	13.3	13.3	12.8	13.5	12.9
Rb	6.53	6.03	6.32	6.03	6.52	6.42	6.06	6.25	5.49	8.20	5.23	6.76
Sr	312	296	306	301	317	308	303	337	319	342	344	314
Y	27.4	26.1	29.1	27.1	28.5	27.8	26.2	29.5	27.8	28.1	26.3	26.6
Zr	167	147	151	146	155	156	145	170	159	155	150	151
Nb	14.3	12.6	13.8	13.8	14.4	14.1	13.4	14.7	14.7	13.7	14.5	14.2
Cs	0.06	0.07	0.06	0.06	0.07	0.06	0.06	0.06	0.05	0.22	0.05	0.07
Ba	60.2	56.5	60.2	60.1	63.1	63.3	58.8	63.9	65.0	56.3	64.0	60.9
La	10.5	9.4	10.3	10.2	10.6	10.5	9.9	11.0	10.9	10.2	11.0	10.5
Ce	27.1	24.4	26.8	26.4	27.6	27.4	25.1	28.2	27.9	26.3	27.9	26.7
Pr	3.94	3.58	3.93	3.86	4.07	3.96	3.69	4.19	4.15	3.93	4.11	3.85
Nd	17.8	16.2	17.9	17.5	18.5	18.1	16.8	19.3	18.9	17.9	18.7	18.2
Sm	4.65	4.34	4.77	4.63	4.87	4.78	4.46	5.06	4.83	4.65	4.86	4.68
Eu	1.62	1.50	1.65	1.58	1.66	1.65	1.54	1.74	1.72	1.63	1.67	1.62
Gd	5.33	4.98	5.54	5.29	5.64	5.55	5.11	5.74	5.56	5.38	5.44	5.28
Tb	0.92	0.85	0.94	0.90	0.96	0.92	0.87	0.97	0.92	0.91	0.90	0.89
Dy	5.19	4.84	5.37	5.10	5.29	5.26	4.76	5.54	5.10	5.13	5.02	4.97
Ho	0.99	0.95	1.05	0.98	1.01	1.02	0.94	1.08	1.01	1.02	0.98	0.99
Er	2.60	2.52	2.79	2.53	2.69	2.65	2.45	2.82	2.65	2.64	2.52	2.53
Tm	0.38	0.37	0.42	0.38	0.40	0.39	0.36	0.42	0.39	0.39	0.36	0.37
Yb	2.28	2.17	2.45	2.23	2.31	2.32	2.13	2.44	2.25	2.31	2.16	2.15
Lu	0.34	0.32	0.37	0.33	0.34	0.34	0.32	0.36	0.33	0.34	0.31	0.32
Hf	3.91	3.63	3.99	3.86	4.04	4.01	3.73	4.11	4.05	3.91	3.95	3.91
Ta	1.04	0.84	0.92	0.92	0.96	0.96	0.87	0.94	0.96	0.91	0.97	0.93
Pb	1.87	0.86	0.97	1.06	1.21	0.78	0.71	2.63	1.17	1.09	1.22	0.91
Th	0.89	0.76	0.83	0.84	0.88	0.86	0.80	0.86	0.87	0.80	0.92	0.84
U	0.31	0.61	0.47	0.71	0.80	0.32	0.33	0.33	0.29	1.74	0.28	0.57

sample are reported as the mean of three individual analyses, the precision is reported as the standard deviation of these analyses (Supplementary Data Tables 2.3).

Only one sample had glass suitable for volatile analyses. Volatile contents were measured on a glass chip from sample NA064-114 using the Cameca 1280 Secondary Ion Mass Spectrometer at Northeast National Ion Microprobe Facility (NENIMF) at the Woods Hole Oceanographic Institution, using a Cs+ beam with a 30 µm raster size, field aperture of 1250 µm and entry slit of 81 µm, following methods by Hauri et al. (2002, Table 2). The glass fragment was hand-polished using a range of grits on silica carbide sandpaper, mounted in indium, and polished at 6, 3, and 1 µm diamond polish and 1 µm alumina grit for 5–30 min each. Volatile standard 519-4-1 (Hauri et al., 2002) was measured routinely throughout the session to monitor for instrumental drift. Measurements were calibrated with a known set of standard glasses provided by the NENIMF.

Results

Samples from both seamounts have vesicularities on the order of 50%. All samples contain 1–3%, ~ 1 mm plagioclase and olivine phenocrysts, with the exception of sample 131, which has ~ 7% olivine phenocrysts that are up to 2 mm. Major element contents are reported in Table 2. All of the samples are relatively mafic basalts, with MgO contents ranging from 7.74 to 9.42 wt% (Figure 2.3). The degree of alteration observed in hand samples correlates with high loss on ignition (LOI; Table 2). Samples with LOI > 1% greatly increase the variability of major elements including FeO_T, P_2O_5, CaO and Na_2O (Figure 2.3). Excluding sample 115, which is the most pervasively altered

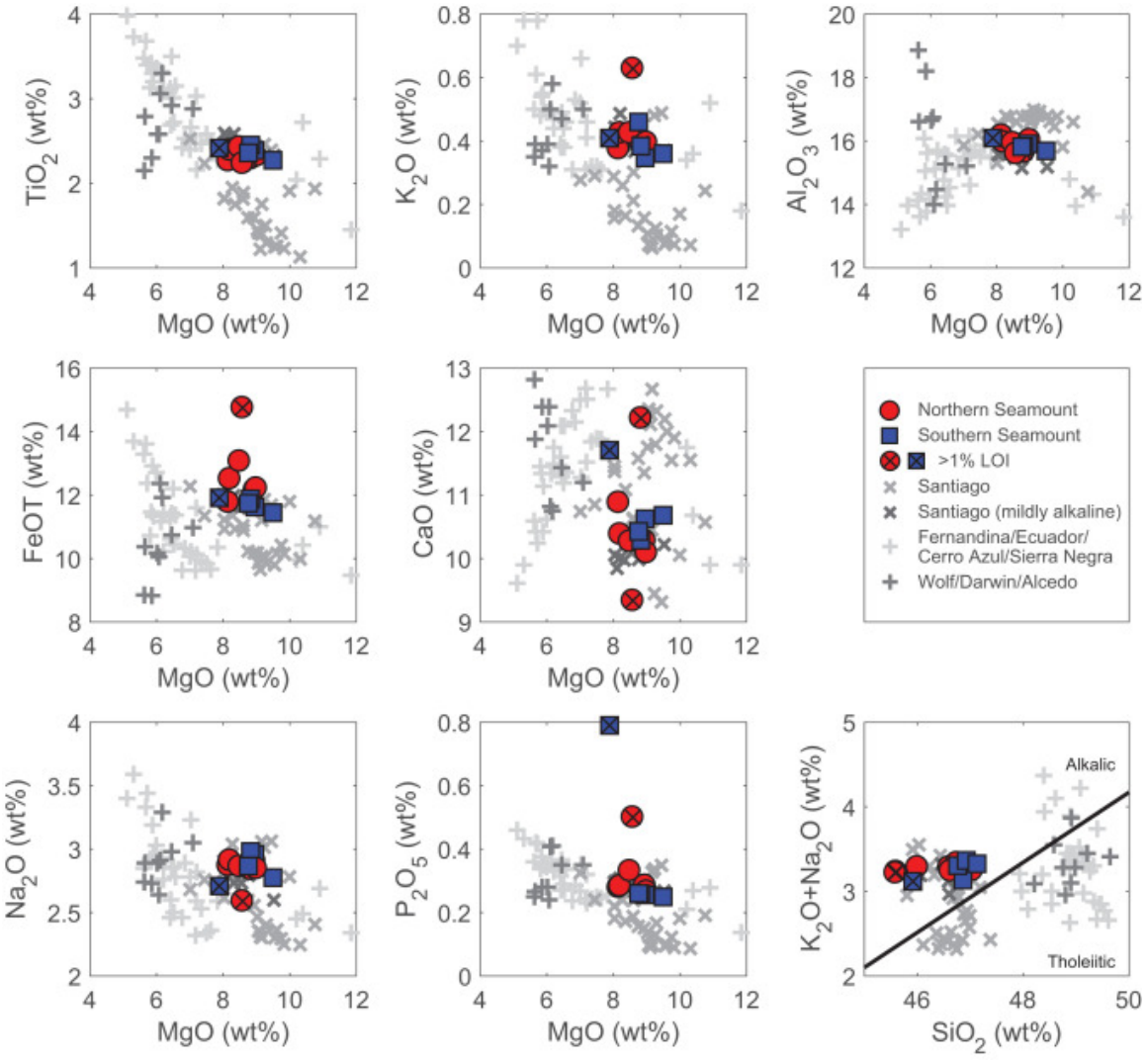

Figure 2.3. Major element variations of seamount lavas. Outlined colored markers show data from this study. Samples with loss on ignition (LOI) > 1 wt% are indicated with black "X". Grey markers show representative lavas from nearby Galápagos volcanoes (Fernandina, Ecuador, Cerro Azul, Sierra Negra, Wolf, Darwin, Alcedo; Saal et al., 2007; Santiago; Gibson et al., 2012). Where not visible, dark grey exes indicating the mildly alkaline Santiago compositions are plotted directly beneath seamount data points. (For interpretation of the references to color in this figure legend, the reader is referred to the web version of this article).

(2.38 wt% LOI), most of the major elements have relatively limited variability, with Al_2O_3 ranging from 15.31 to 16.07 wt%, TiO_2 from 2.18 to 2.44 wt%, Na_2O from 2.52 to 2.96 wt%, and K_2O from 0.34 to 0.46 (Figure 2.3). There is slightly higher variability in CaO (9.10–11.95 wt%) and FeO_T (11.35–12.85 wt%). CaO/Al_2O_3 ratios range from 0.60 to 0.78 (Figure 2.4). The basalts are all mildly alkalic, with total alkali contents (Na_2O+K_2O) ranging from 3.06 to 3.35 and SiO_2 contents of 44.6–46.8 wt% (Figure 2.3).

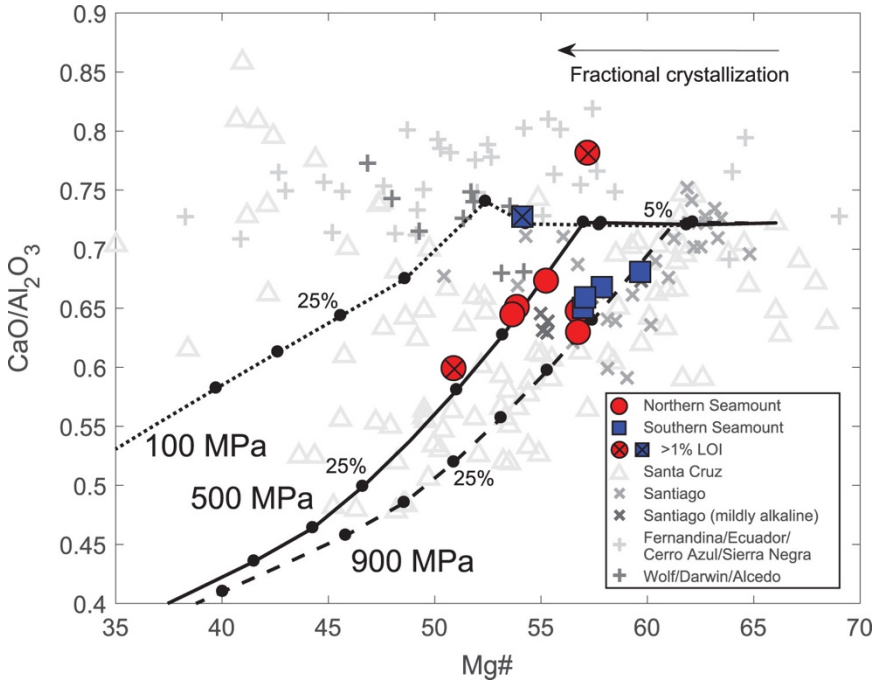

Figure 2.4. Variation of CaO/Al_2O_3 as a function of Mg#. Mg# is defined as molecular $MgO/(MgO+FeO_T)*100$. Black lines show isobaric fractional crystallization trends at 100, 500 and 900 MPa, black dots along lines indicate 5% increments of crystal fractionation by mass. Fractional crystallization is modeled from alphaMELTS software (see text for model descriptions). Outlined colored markers show data from this study. Samples with loss on ignition (LOI) > 1 wt% are indicated with black "X". Grey markers show representative lavas from nearby Galápagos volcanoes (Fernandina, Ecuador, Cerro Azul, Sierra Negra, Wolf, Darwin, Alcedo; Saal et al., 2007; Santiago; Gibson et al., 2012; Santa Cruz; Wilson, 2013). (For interpretation of the references to color in this figure legend, the reader is referred to the web version of this article).

Trace element contents are reported in Table 3, uncertainties are reported in Supplementary Data Tables 2.3. Samples from both seamounts span a narrow range in incompatible trace element concentrations (e.g., 13–15 ppm Nb, 56–65 ppm Ba; Figure 2.5). Despite the slight variations in concentration, the samples have low variability in CI chondrite normalized (McDonough and Sun, 1995) trace element ratios (e.g., $[La/Nb]_N$ 0.74–0.77; Figure 2.6). REE patterns are nearly uniform for all samples, with a negative slope at increasing atomic mass and slight concave down pattern in light REEs (Figure 2.7). REE ratios are also similar (e.g., $[La/Sm]_N$ 1.3–1.4$[Sm/Yb]_N$ 2.1–2.5; Figure 2.8). All samples show a broad increase in primitive mantle normalized trace element concentrations with increasing incompatibility, save for the most incompatible elements, Rb and Ba, which are depleted relative to more compatible Th and Nb (Figure 2.5).

Glass from sample NA064-114 was measured for H_2O, CO_2, Cl, F, and S. The sample has a H_2O concentration of 0.87 wt%, a CO_2 concentration of 135 ppm, Cl concentration of 210 ppm, F concentration of 891 ppm, and S concentration of 1636 ppm (Table 2). All samples have high vesicularities, on the order of 50%, so significant degassing likely occurred prior to eruption.

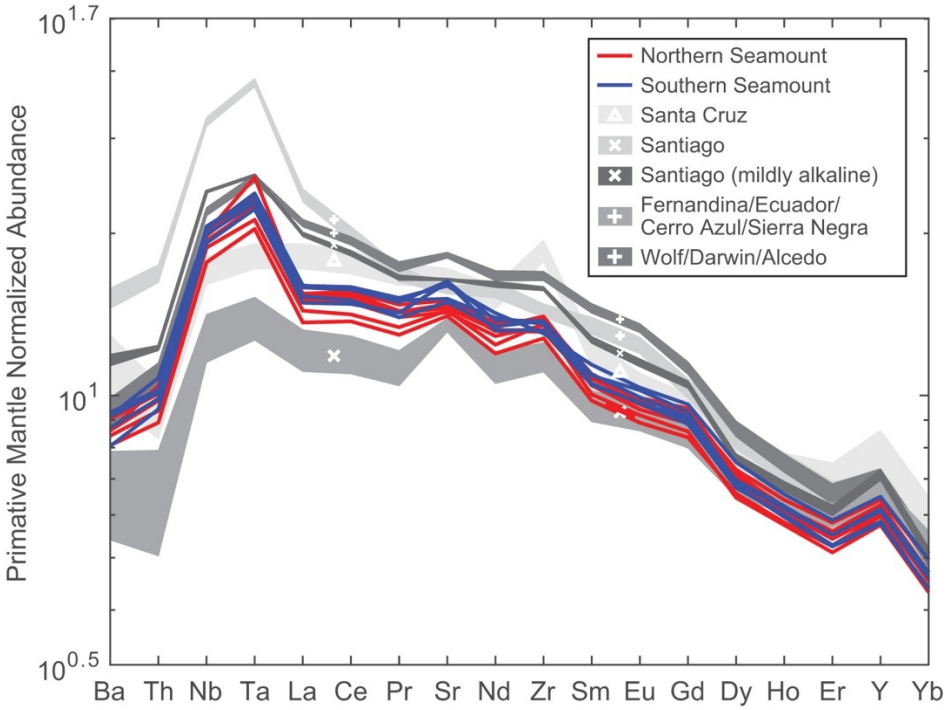

Figure 2.5. Trace element diagram comparing the seamount samples to averaged Galápagos Lavas. Elements are listed in order of increasing compatibility and normalized to the primitive mantle (McDonough and Sun, 1995). Colored lines show data from this study. Grey fields show mean value and 2σ range for representative lavas from nearby Galápagos volcanoes (symbols are consistent with previous figures; data sources as indicated in Figure 2.4). (For interpretation of the references to color in this figure legend, the reader is referred to the web version of this article).

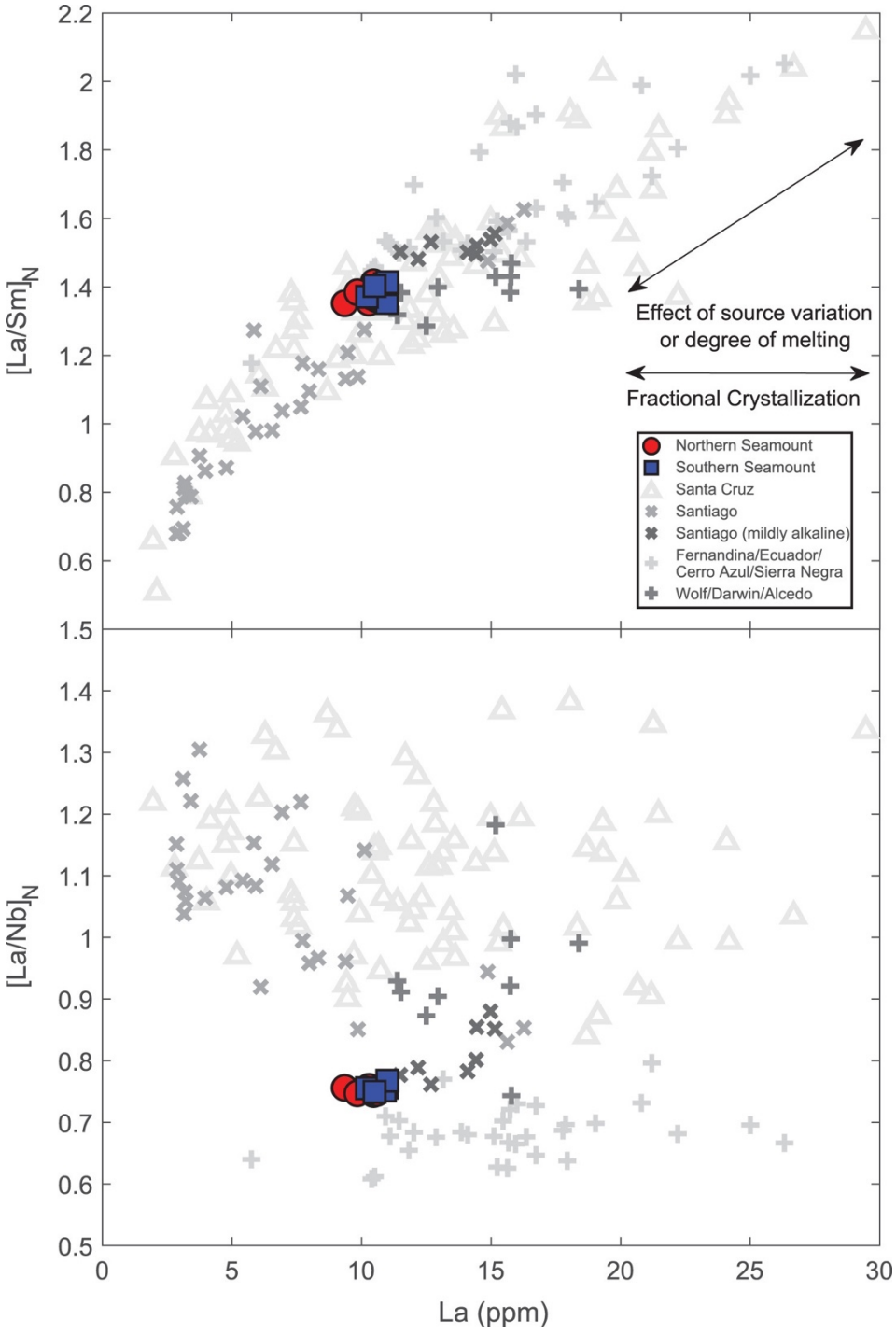

Figure 2.6. Variation of $[La/Sm]_N$ and $[La/Nb]_N$ as a function of La concentration. Trace element ratios are normalized to CI (McDonough and Sun, 1995). Outlined colored markers show data from this study. Grey markers show representative lavas from nearby Galápagos volcanoes (data sources as indicated in Figure 2.4). (For interpretation of the references to color in this figure legend, the reader is referred to the web version of this article).

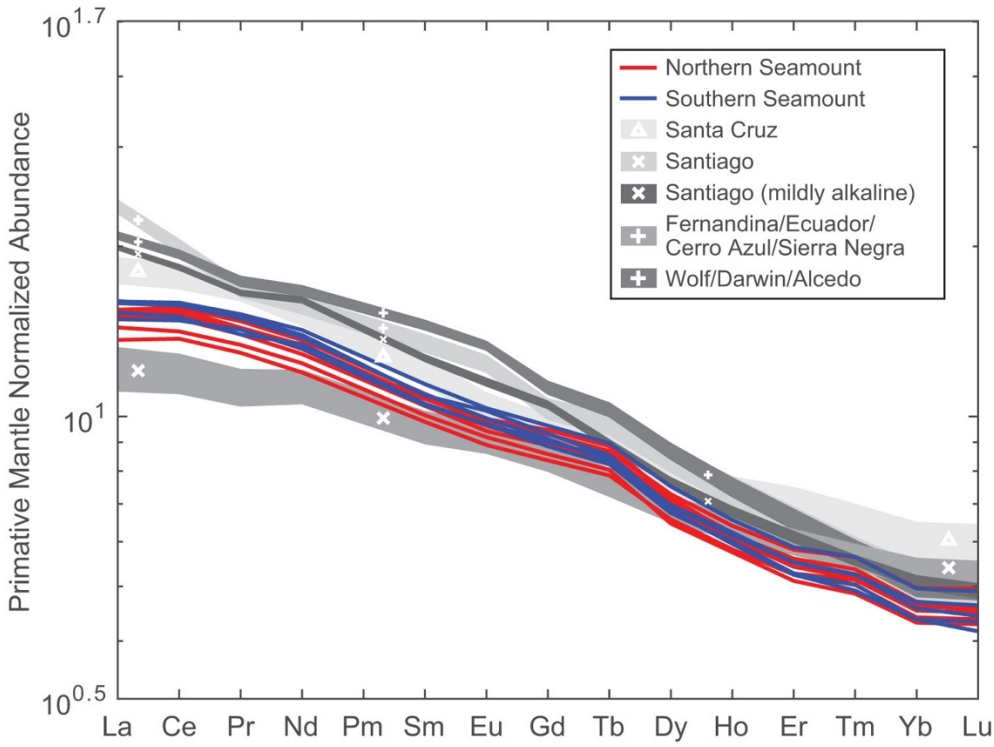

Figure 2.7. REE diagram comparing the seamount samples to averaged Galápagos Lavas. Elements are normalized to the primitive mantle (McDonough and Sun, 1995). Colored lines show data from this study. Grey fields show mean value and 2σ range for representative lavas from nearby Galápagos volcanoes (symbols are consistent with previous figures; data sources as indicated in Figure 2.4). (For interpretation of the references to color in this figure legend, the reader is referred to the web version of this article).

Petrogenesis

Major element variability and slight negative slopes in incompatible minor elements (TiO_2, K_2O, P_2O_5) with MgO (Figure 2.3) suggest all seamount lavas sampled from these seamounts are related through small extents of fractional crystallization. To test this hypothesis and assess the mean depth of crystallization, we modeled fractional crystallization using alphaMELTS (Ghiorso and Sack, 1995, Asimow and Ghiorso, 1998, Smith and Asimow, 2005). Crystallization models were run at 100, 500 and 900 MPa, QFM buffered, log ΔfO_2 offset of −0.83 (average Galápagos basalt; Rilling, 2005), primitive starting composition (taken from Santa Cruz; Wilson, 2013) and water contents

of 0.87 wt% (based on volatile contents in quenched glass from sample NA064-114). This water content is near the upper limit for submarine basaltic glasses analyzed in the Galápagos (0.098–1.15 wt% H_2O; Peterson et al., 2013) but is likely a lower bound given the high vesicularities in these samples.

Results of the petrologic models suggest that the range of major element compositions at both seamounts can be explained by < 10% crystallization of olivine+clinopyroxene from a similar parental magma (Figure 2.4), and that the majority

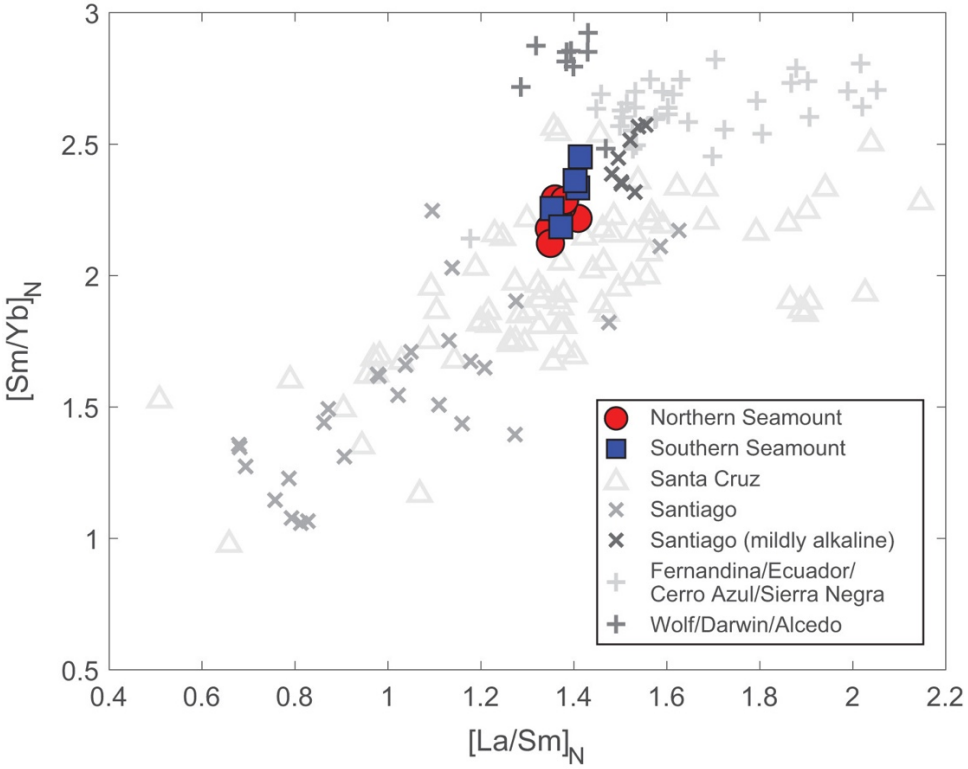

Figure 2.8. Variation of $[Sm/Yb]_N$ as a function of $[La/Sm]_N$. Trace element ratios are normalized to CI (McDonough and Sun, 1995). Outlined colored markers show data from this study. Grey markers show representative lavas from nearby Galápagos volcanoes (data sources as indicated in Figure 2.4). (For interpretation of the references to color in this figure legend, the reader is referred to the web version of this article).

of lavas are related by ~ 4% fractional crystallization. Notably, sample NA064-115 is offset from many of the crystallization trends (FeO_T, K_2O, and P_2O_5), which likely results from significant alteration (LOI = 2.38%) of the whole rock. The best-fit trends were produced from crystallization at pressures between 500–900 MPa. Crystallization paths between the north and south seamounts are offset in CaO/Al_2O_3 as a function of Mg# (molecular $MgO/(MgO+FeO_T) \times 100$), which may indicate magma storage and crystallization at variable depths prior to eruption or crystallization during ascent (Figure 2.4). In either case, these models suggest that the seamount lavas underwent storage and minor crystallization in a deep (17–35 km) magma chamber. This is significantly shallower than the inferred base of the lithosphere in the region (~ 55 km; Villagómez et al., 2007; Gibson et al., 2012), but is deeper than crustal thickness estimates for the central archipelago (~ 16 km; Feighner and Richards, 1994; Toomey et al., 2001). Thus, these depths imply crystallization in the lithospheric mantle.

Lavas from both seamounts show slight variations in trace element concentrations (e.g., 9.38–10.99 ppm La; Figure 2.6). These variations can be produced by fluctuations in extents of partial melting (Shaw, 1970), source variation (e.g., Weaver, 1991), or fractional crystallization (Shaw, 1970). Variations in extents of partial melting or mantle sources with different trace element concentrations will result in differences in trace element ratios (e.g., low extents of melting or mixing with an enriched source will produce high La concentrations and high $[La/Sm]_N$ ratios or low $[La/Nb]_N$ ratios; e.g., Kurz and Geist, 1999). By contrast, limited extents of fractional crystallization, such as those indicated by major element variations (< 10%; Figure 2.4) will result in nearly equal enrichments of all incompatible trace elements, preserving trace element ratios.

Despite limited variations in trace element concentrations at both seamounts, there are only minor variations in $[La/Sm]_N$ and no variation in $[La/Nb]_N$ (Figure 2.6, Figure 2.8), indicating that the lavas may be produced by only slight variations in degree of melting of a similar source. The nearly uniform trace element ratios (Figure 2.6, Figure 2.8) and REE patterns (Figure 2.7) are consistent limited fractional crystallization during the evolution of magmas at both seamounts.

White et al. (1993) noted a downstream depletion in highly incompatible trace elements from the center of plume upwelling, attributed to progressive dilution of the mantle plume with entrained upper mantle material. The primitive component of the Galápagos mantle plume has can be identified by high $^3He/^4He$ isotopic ratios (~ 30 Ra, Kurz and Geist, 1999; Kurz et al., 2009), which correlates with elevated Ti, Ta and Nb, relative to elements of similar compatibilities (Kurz and Geist, 1999, Jackson et al., 2008). This dilution trend is manifested as extremely low $[La/Nb]_N$ ratios in lavas erupted at Fernandina compared to nearby Wolf, Darwin and Alcedo volcanoes on Isabela Island (Figure 2.6; mean $[La/Nb]_N$ 0.67 and 0.97, respectively), despite similar degrees of melting predicted for this region (Gibson and Geist, 2010). The downstream change in these ratios allows us to assess the lateral position of melt generation that produced the seamounts relative to the plume center. Seamount lavas have mean $[La/Nb]_N$ 0.75 (Figure 2.6), which is higher than that of lavas erupted at Fernandina. This suggests that the seamounts did not form over the plume center and migrate eastward with plate motion, but instead erupted relatively recently downstream of the plume center.

The dissolved CO_2 concentration measured in sample NA064-114 (135 ppm) is ~ 95% less than presumably undegassed Galápagos melt inclusion contents (up to 5821

ppm CO_2; Koleszar et al., 2009). This concentration is also much lower than the range of CO_2 (4200–5600 ppm) predicted from CO_2/Nb for undegassed mid-ocean ridge basalts (300; Saal et al., 2002) and Gálapagos lavas (400; Peterson et al., 2013) using mean Nb values of the seamount samples (14 ppm). By contrast, S (1636 ppm) is comparable to that of S measured in undersaturated submarine glasses collected at greater water depths (1599 ppm; Peterson et al., 2010). Despite evidence for extensive degassing (high vesicularites), the CO_2 contents are still greater than predicted for their eruption depths. Any excess volatile concentrations, relative to experimentally derived solubility curves, likely result from rapid ascent and quenching with insufficient time for degassing (e.g., Dixon et al., 1988; le Roux et al., 2006). We use the dissolved CO_2 and H_2O concentrations measured in NA064-114 (135 ppm and 0.87 wt%, respectively) to yield a vapor saturation pressure of 36 MPa, which is equivalent to ~ 1.2 km below seafloor (Dixon and Stolper, 1995, Newman and Lowenstern, 2002). Thus, we suggest that the exsolution of CO_2 and H_2O, within a magmatic system at > 1.2 km depth drove rapid magma ascent, vesiculation and fragmentation. Fragmentation may also be enhanced by seawater interaction, common for submarine volcanoes at depths between 200 and 1300 m (Allen and McPhie, 2009). This is consistent with pyroclastic activity forming a majority of the volume of each seamount edifice, followed by limited extents of effusive volcanism associated with crater filling pillow lava and flows.

The similarity between the two seamounts in major elements (Figure 2.3), trace element contents (Figure 2.5) and ratios (Figure 2.6, Figure 2.8) indicates that they were either produced from the same mantle source and evolved under similar conditions or shared the same batch of magma and were erupted over a short duration. Similarity in

morphological features between the two seamounts, including outer slope angles and southwestward breaching, indicates similarity in vent conditions and ocean currents during eruption (e.g., Settle, 1979). Combined with the spatial proximity of the two seamounts, we suggest that, together, the seamounts were produced during a single eruptive event or closely timed events originating from the same magma batch. Individual seamount volumes (0.14–0.36 km3) are on the order of other single lava flows observed in the Galápagos (0.12 km3; Rowland, 1996), and combined are less than the total volume for single eruptive events described for multiple events at Fernandina (2 km3; Simkin and Howard, 1970; 2.3 km3; Rowland, 1996), thus it is conceivable that both were produced from a single monogenic basaltic eruption.

Comparison of Seamounts to the Western and Eastern Volcanic Systems on the Galápagos Platform

Extents of Melting and Lithospheric Thickness

The mean extent of melting experienced by the upwelling mantle beneath a hotspot volcano is controlled by the depth difference between the solidus and the base of the lithosphere (e.g., McKenzie and Bickle, 1988). In the Galápagos, there is a change in lithospheric thickness from 70 km in the west to 40 km in the east (Villagómez et al., 2007). As a result, western volcanoes undergo lower mean extents of melting than those in the east (Gibson and Geist, 2010), despite a deeper onset of melting resulting from higher excess temperatures (Villagómez et al., 2007) and chemical enrichment (White et al., 1993). Mean extents of melting for magmas of a similar source composition can be assessed from the ratios of REEs or slopes in primitive mantle normalized REE diagrams (e.g., Gibson and Geist, 2010). At low extents of melting, light REEs will be fractionated

into the melt to greater extents than heavy REEs, creating relatively steep patterns and elevated trace element ratios. The depth to the top of the melting column (serving as a proxy for mean extent of melting) can be calculated from empirical relationships between both $[La/Sm]_N$ and $[Sm/Yb]_N$, which are derived from REE inversion modeling (Eqs. (1), (2) in Gibson and Geist (2010)).

Determining relative extents of melting across the Galápagos is complicated by mantle source heterogeneities, which also vary from west to east across the archipelago (e.g., White et al., 1993). Lower negative slopes in REEs are predicted with increasing distance from the plume due to decreasing extent of "plume" material in the source (White et al., 1993). Fortunately, the degree of source enrichment can be evaluated independently of melting processes through the use of radiogenic isotopes (e.g., Gibson et al., 2012). While we have not measured radiogenic isotope ratios in the seamount lavas, there is little variation in 87Sr/86Sr and 206Pb/207Pb in lavas with $[La/Nb]_N < 0.9$ from volcanoes adjacent to the seamounts (Wolf and Darwin; Western Santiago), suggesting similar mantle sources (Gibson et al., 2012). Seamount lavas have $[La/Nb]_N$ ranging from 0.74 to 0.77, thus we assume a similar source composition between seamounts and lavas erupted at nearby islands. Additionally, to minimize the impact of this assumption, we choose to only evaluate depth to the top of the melting column using $[Sm/Yb]_N$, which is less sensitive to source variation than $[La/Sm]_N$ (Gibson and Geist, 2010).

The mean REE slope of the western volcanoes is greater than that of the eastern volcanoes, suggesting lower mean extents of melting, and consistent with a thicker lithosphere (Figure 2.7). The nearest western volcanoes to the seamounts (Wolf, Darwin

and Alcedo on Isabela Island) have mean $[Sm/Yb]_N$ of 2.55, attributed to a depth to the top of the melting column at 57 km (Gibson and Geist, 2010). By comparison, eastern volcanoes (Santiago and Santa Cruz Islands) have lower mean $[Sm/Yb]_N$ of 1.55, which equates to a shallower depth to the top of the melting column of 53 km. Notably however, there is a break in $[Sm/Yb]_N$ from W-E across the island of Santiago (56 km vs. 53 km, respectively; Gibson et al., 2012) suggesting that the transition between thick and thin lithosphere is relatively sharp and dissects the island into a western and eastern volcanic system, assuming melts ascend vertically from their source. The seamount REE patterns (Figure 2.7) and ratios (Figure 2.8) are intermediate between western and eastern volcanoes, suggesting that magmas producing the seamounts were generated from intermediate mean extents of melting. Seamount lavas have an average $[Sm/Yb]_N$ of 2.3 (Figure 2.8), corresponding to a depth to the top of the melting column of 56 km (Eq. (1) in Gibson and Geist (2010)). This depth falls between that of the western and eastern volcanoes on average, but is more consistent with the thicker lithosphere of the western volcanoes and is identical to that of western Santiago.

Crystallization and Melt Storage

The seamounts are located within a major transition in volcano morphology and magma storage depth between the western and eastern volcanic provinces on the Gálapagos Platform. Lavas erupted at western Galápagos volcanoes are produced by relatively high extents of fractional crystallization (average MgO of 6.79 wt%; e.g., Saal et al., 2007) in shallow crustal magma chambers (~ 200 MPa; Geist et al., 1998). By contrast, lavas erupted at eastern volcanoes undergo less fractional crystallization

(average of 8.34 wt% MgO; Gibson et al., 2012; Wilson, 2013) at greater depths (~ 600 MPa; Geist et al., 1998).

All of the seamount lavas are relatively mafic, with MgO contents > 7.7 wt%, suggesting limited crystallization prior to eruption. These MgO contents are higher than the narrow range that is typically observed on the western islands of Fernandina and Isabela (Figure 2.3; e.g., Saal et al., 2007), but fall within the range of the eastern volcanoes (Figure 2.3; e.g., Gibson et al., 2012; Wilson, 2013). Petrologic modeling indicates that crystallization depths of ~ 17–30 km (equivalent to 500–900 MPa; Figure 2.4), consistent with deeper magmatic plumbing systems at eastern volcanoes of ~ 21 km (Santa Cruz, Santiago, San Cristobal; 600 ± 100 MPa; Geist et al., 1998). Thus trace element patterns and ratios of the seamount lavas share melting characteristics similar to western Santiago and Wolf, Darwin and Alcedo volcanoes on Isabela, while the magma storage conditions closely resemble those associated with the eastern volcanoes.

Shared Seamount Magma Plumbing with Santiago?

The closest island to the two seamounts is Santiago (Figure 2.2), which is 5 km to the northeast, near the northern edge of the Galápagos Platform (Figure 2.1). The island has morphological characteristics of the eastern volcanoes, lacking a large central caldera and having lower eruption rates compared to the more active western volcanoes (Figure 2.1; Geist et al., 2008b). Santiago remains volcanically active, with historical eruptions occurring on the eastern side of the island in 1906 and on the western side in ~ 1754 (Siebert et al., 2011). Lavas erupted on Santiago are highly variable, with rock types ranging from picrites to trachytes (McBirney and Williams, 1969, Saal et al., 2007, Herbert et al., 2009, Gibson et al., 2012). Geochemical analyses of subaerial basalts

indicate variable major and trace element compositions (tholeiitic, transitional, and alkalic) that are spatially distributed across the island (Gibson et al., 2012). The western portion of the island is dominated by eruption of mildly alkaline basalts, while the eastern portion of the island has erupted both tholeiitic and transitional basalts. This compositional zonation from west to east is thought to occur due to an abrupt change in the lithospheric thickness directly below Santiago (Gibson et al., 2012).

Trace element patterns in mildly alkaline lavas on western Santiago are interpreted to result from melting directly beneath that side of the island, where thicker lithosphere truncates the melting column at greater depths (Gibson et al., 2012). The seamount lavas are compositionally similar to the mildly alkaline series and in particular, a subset of lavas erupted subaerially on the western flank of Santiago (hereon referred to as the Western Mildly Alkaline (WMA) lavas; Gibson et al., 2012). WMA lavas are distinguished from other mildly alkalic lavas on the western side of the island by low $[La/Ba]_N$ ratios and similar trace element patterns. Both the seamounts and WMA lavas have undergone similar degrees of crystallization (means of 8.68 and 8.79 wt% MgO, respectively) at similar storage depths of 17–35 km (interpreted from similar mean CaO/Al_2O_3 of 0.67 and 0.65, respectively). Moreover, similar mantle source and degrees of melting are inferred for seamount and WMA lavas based on REE abundances (10 and 11 mean ppm La, respectively) and mean $[La/Sm]_N$ ratios (1.38 and 1.51, respectively). Similar depths to the top of the melting column are inferred from mean $[Sm/Yb]_N$ (2.26 and 2.35 respectively). The similarities between seamounts and WMA lavas are even recognizable in the most nuanced variations in trace elements, including negative Ba anomaly and slightly positive Sr and Zr anomalies (Figure 2.9).

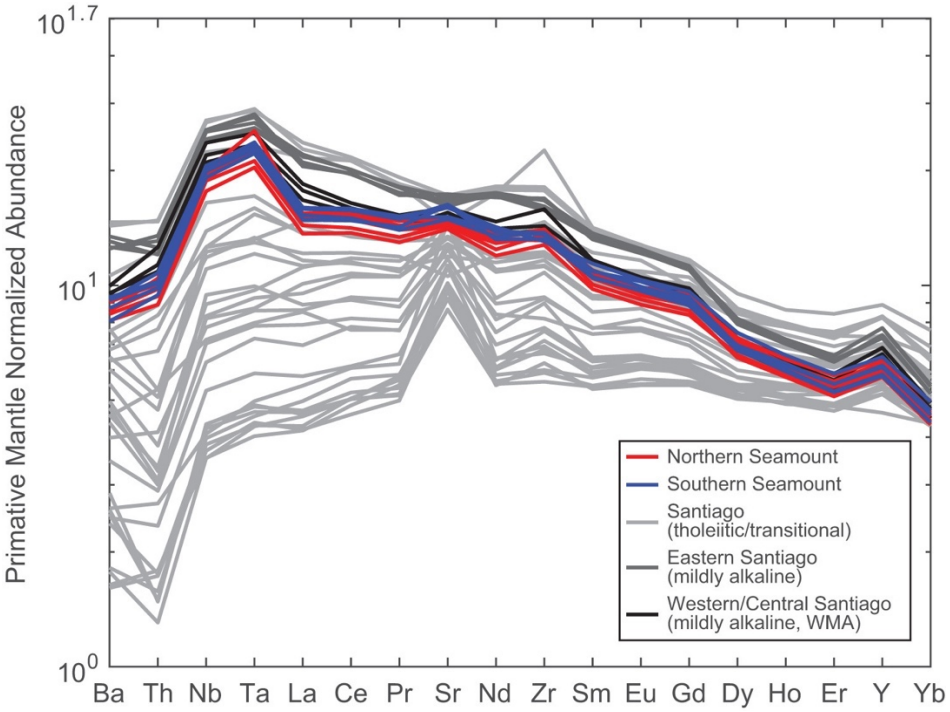

Figure 2.9. Trace element diagram comparing the seamount samples to Santiago Lavas. Elements are listed in order of relative compatibility and normalized to the primitive mantle (McDonough and Sun, 1995). Colored lines show data from this study. Grey lines show Santiago lava compositions simplified from Gibson et al. (2012). (For interpretation of the references to color in this figure legend, the reader is referred to the web version of this article).

Based on these geochemical similarities, the seamount and WMA lavas are either produced from a single magmatic event or two separate events, under nearly identical conditions. If the seamounts were produced in a separate magmatic event, their chemical similarities, outlined above, would require that they underwent the same degree of melting of the same source, with similar transport and crystallization histories as the WMA lavas. We assert that it is much simpler to assume that lavas for both seamounts were produced in a single batch, and passed through the same magma plumbing system. Thus, we conclude that the seamount and WMA lavas are sourced from the same central reservoir in the lithospheric mantle (500–900 MPa; Figure 2.10) beneath Santiago and erupted over a relatively short time period. The distribution of WMA and seamount lavas implies that, in the absence of shallow magma reservoirs in the eastern archipelago, magmas stored deep in the crust can be transported laterally on the order of 10 km in subsurface dikes prior to eruption (Figure 2.10). We propose that lateral magma migration begins between the transition into the elastic crust at 6–12 km (Feighner and Richards, 1994) and depths derived from CO_2 and H_2O vapor saturation pressures at 1.2 km (Section 5; Figure 2.10). In Hawaii, similar dike dimensions (15–25 km lateral extent by 4–8 km vertical extent) have been inferred from limits of seismic swarms during emplacement events (Rubin and Pollard, 1988). This finding differs from that of Gibson et al. (2012), who, based on the geochemistry of the subaerial sample suite suggest that there is limited lateral transport of magmas during ascent through the lithosphere. This highlights the importance of investigating submarine features around the main islands on the platform in order to better understand the complexities of melt generation and construction of the archipelago.

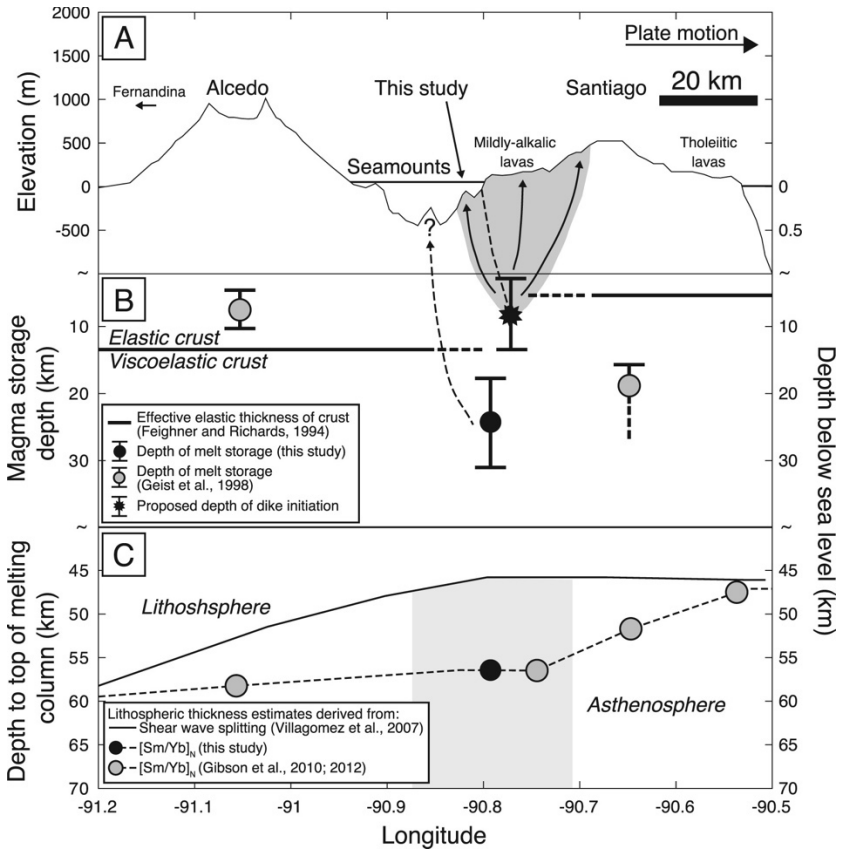

Figure 2.10. Schematic cross-section depicting seamount genesis. A) Thin black line is an elevation profile from W-E across the Galápagos Platform, from Alcedo Volcano on Isabela Island to Santiago Island. Thick black horizontal line shows sea level. Dark grey region is the proposed extent of shallow diking, resulting in distribution of mildly alkalic lavas from seamounts to central Santiago. Dashed line within the diking region indicates a separation between the seamount lavas from those erupted subaerially. Solid arrows indicate rapid melt transport in elastic crust evidenced by limited shallow degassing of lavas (Section 5). Dashed arrow shows potential melt transport pathway for other unexplored seamounts. B) Solid line is the effective elastic thickness of crust (Feighner and Richards, 1994). Black circle indicates range of melt storage and crystallization depths for seamount lavas, derived from CaO/Al2O3 ratios (Section 5). Grey circles indicate range of melt storage depths for Alcedo and Santiago (Geist et al., 1998). Black decagram indicates depth of dike initiation constrained by transition into the elastic crust (6–12 km) and depths derived from CO_2 and H_2O vapor saturation pressures (1.2 km; Section 5). C) Solid black line indicates lithospheric thickness derived from shear wave splitting data (Villagómez et al., 2007). Black circle indicates top of the melting column calculated from average $[Sm/Yb]_N$ values of seamount samples from this study. Grey circles indicate top of the melting column calculated from average $[Sm/Yb]_N$ values from Alcedo (Gibson and Geist, 2010) and Santiago (Gibson et al., 2012). Black dashed line is the lithospheric thickness derived from the combined $[Sm/Yb]_N$ calculations. Light grey region indicates the potential melting region for seamount lavas.

Given the transitional nature and compositional similarity of the lavas from the two seamounts and WMA lavas, in both maximum depths and extents of melting, we prefer a model where melts may be generated in the mantle over a wide region between Alcedo and Santiago (~ 50 km wide; Figure 2.10), but are channeled through and homogenized within the deep magmatic system associated with western Santiago prior to their redistribution in the shallow crust. In this case, even if mantle heterogeneity or lithospheric thickness undergo gradual changes across the archipelago, the variations are discretized in the nearest island's complex plumbing system. Further geochemical and morphological investigations of seamounts throughout the Galápagos Platform, and comparisons to nearby volcanoes would help determine the extent to which the major volcano magmatic systems control the geochemistry of intra-island seamounts.

Conclusion

Similarities in major and trace element concentrations and ratios suggest that lavas erupted from two seamounts between the islands of Isabela and Santiago in the Galápagos Archipelago are from the same parental magma. The seamounts were likely produced by rapid magma ascent from depths > 1.2 km, resulting in the construction of the main edifices by both explosive and effusive volcanism. Magma supplied to the seamounts were generated away from the plume center and underwent storage and minor crystallization in a chamber located in the lithospheric mantle (17–35 km; Figure 2.4, Figure 2.10).

Total extents of melting, as indicated by intermediate average REE patterns, and $[Sm/Yb]_N$ are transitional between the western and eastern regions of the archipelago (Figure 2.7, Figure 2.8; Gibson and Geist, 2010), and closely resemble those of the

nearby western volcanoes of Wolf, Darwin and Alcedo on Isabela Island, as well as western Santiago, in average trace element contents (Figure 2.5). These data suggest that seamount magmas were generated above a lithosphere of intermediate thickness similar conditions beneath eastern Isabela and western Santiago. Despite this, seamount magmas appear to have a transport and storage history more akin to that of the eastern volcanoes (e.g., low extents of fractional crystallization, Figure 2.3; deep storage, Figure 2.4), reflecting lower magma supply and deeper crystallization. These compositional characteristics signify that, although seamount magmas have a transitional melting signature, their crustal signature suggests they are parasitic to Santiago and pass through a shared plumbing system that has also erupted subaerial lavas (Figure 2.10).

Given the transitional nature of the seamount lavas, in both maximum depths and extents of melting, between that of the western and eastern volcanoes, we prefer a model where melts are generated over a ~ 50 km wide region beneath the seamounts and the island, but are homogenized in the lithospheric mantle and are channeled through western Santiago's crustal plumbing system and transported laterally on the order of 10 km in subsurface dikes prior to eruption on the shallow submarine platform (Figure 2.10). The Galápagos Platform is studded with numerous clusters and lineaments of small seamounts adjacent to the islands, most of which have never been sampled. Further detailed geological and geochemical investigations of these seamounts and their relationship to adjacent volcanoes would enable a better assessment of the extent of magma partitioning between subaerial and submarine systems' relationship to seamount and subaerial morphologies as well as the origins of the magmas in both settings.

Acknowledgements

We thank the Ocean Exploration Trust, and the crew of the E/V *Nautilus* for facilitating the mapping and sample collection for this project. Thank you to the NOAA Office of Exploration and Research for funding the E/V *Nautilus* Exploration Program (NA15OAR0110220). Additionally, we are grateful to the Galápagos National Park directorate for allowing the collection of submarine rock samples through joint permit (PC-45-15) in collaboration with the Charles Darwin Research Foundation. We also gratefully recognize the Government of Ecuador via the Ecuadorian Navy for permission to operate in their territorial waters and marine protected areas. We appreciate the WSU Geoanalytical Facility and WHOI Ionprobe Facility for XRF and volatile analysis, respectively. Work for this project was carried out with support provided by the NSF (OCE-1634952 to VDW, OCE-1634685 to SAS) and the Dalio Explore Fund and Investment in Science Fund at WHOI. We also thank Bill Chadwick and an anonymous reviewer for their comments and suggestions, which greatly improved the final manuscript.

References

Allan, J.F., Simkin, T., 2000. Fernandina Volcano's evolved, well-mixed basalts: mineralogical and petrological constraints on the nature of the Galápagos plume. J. Geophys. Res. 105, 6017.http://dx.doi.org/10.1029/1999JB900417.

Allen, S.R., McPhie, J., 2009. Products of Neptunian eruptions. Geology 37, 639–642.

Asimow, P.D., Ghiorso, M.S., 1998. Algorithmic modifications extending MELTS to calculate subsolidus phase relations. Am. Mineral. 83, 1127–1132.

Bell, K.L.C., Brennan, M.L., Flanders, J., Raineault, N.A., Wagner, K., 2016. New Frontiers in Ocean Exploration: The E/V *Nautilus* and NOAA Ship *Okeanos Explorer*, 2015 Field Season.

Carey, B.S., Fisher, C.R., Leon, P.S. De, Roman, C., Raineault, N.A., Suarez, J., Smart, C., Kane, R., Tüzün, S., Balcanoff, J., Lubetkin, M., Jones, M., Schwartz, D., Fornari, D., Soule, A., Wanless, D., Watling, L., Ballard, R.D., 2016. Exploring the Undersea World of the Galápagos Islands Exploring the Undersea World of the Galápagos Islands.

Chadwick, W.W., Dieterich, J.H., 1995. Mechanical modeling of circumferential and radial dike intrusion on Galápagos volcanoes. J. Volcanol. Geotherm. Res. 66, 37–52.

Chadwick, W.W., Howard, K.A., 1991. The pattern of circumferential and radial eruptive fissures on the volcanoes of Fernandina and Isabela islands, Galápagos. Bull. Volcanol. 53, 259–275. http://dx.doi.org/10.1007/BF00414523.

Christie, D.M., Duncan, R.A., McBirney, A.R., Richards, M.A., White, W.M., Harpp, K.S., Fox, C.G., 1992. Drowned islands downstream from the Galápagos hotspot imply extended speciation times. Nature 355, 246–248. http://dx.doi.org/10.1038/355246a0.

Clague, D.A., Dalrymple, G.B., 1987. The Hawaiian-emperor volcanic chain. Part I. Geologic evolution. Volcanism Hawaii 1, 5–54.

Dixon, J.E., Stolper, E.M., 1995. An experimental study of water and carbon dioxide solubilities in mid-ocean ridge basaltic liquids. Part II: applications to degassing. J. Petrol. 36, 1633–1646.

Dixon, J.E., Stolper, E.M., Delaney, J.R., 1988. Infrared spectroscopic measurements of CO_2 and H_2O in Juan de Fuca Ridge basaltic glasses. Earth Planet. Sci. Lett. 90, 87–104. http://dx.doi.org/10.1016/0012-821X(88)90114-8.

Feighner, M.A., Richards, M.A., 1994. Lithospheric structure and compensation mechanisms of the Galápagos Archipelago. J. Geophys. Res. 99, 6711–6729.

Geist, D., 1996. On the emergence and submergence of the Galápagos Islands. Not. Galápagos 56, 5–9.

Geist, D., Harpp, K., 2009. Galápagos Islands: Geology. Encycl. Islands.

Geist, D., Naumann, T., Larson, P., 1998. Evolution of Galápagos magmas: mantle and crustal fractionation without assimilation. J. Petrol. 39, 953–971.

Geist, D., Diefenbach, B.A., Fornari, D.J., Kurz, M.D., Harpp, K., Blusztajn, J., 2008a.Construction of the Galápagos platform by large submarine volcanic terraces. Geochemistry. Geophys. Geosyst. 9. http://dx.doi.org/10.1029/2007GC001795.

Geist, D., Snell, H., Snell, H., Goddard, C., Kurz, M.D., 2014a. A paleogeographic model of the Galápagos Islands and biogeographical and evolutionary implications. In: Harpp, Karen S., Mittelstaedt, Eric, d'Ozouville, Noémi, Graham, D.W. (Eds.), The Galápagos: A Natural Laboratory for the Earth Sciences, Geophysical Monograph 204. John Wiley & Sons, Inc, pp. 145–166.

Geist, D.J., McBirney, A.R., Duncan, R.A., 1986. Geology and petrogenesis of lavas from San Cristobal Island, Galápagos Archipelago. Geol. Soc. Am. Bull. 97, 555. http://dx.doi.org/10.1130/0016-7606(1986)97<555:GAPOLF>2.0.CO;2.

Geist, D.J., Harpp, K.S., Naumann, T.R., Poland, M., Chadwick, W.W., Hall, M., Rader, E.,2008b. The 2005 eruption of Sierra Negra volcano, Galápagos, Ecuador. Bull. Volcanol. 70, 655–673. http://dx.doi.org/10.1007/s00445-007-0160-3.

Geist, D.J., Bergantz, G., Chadwick, W.W., 2014b. Galápagos magma chambers. In: Harpp, Karen S., Mittelstaedt, Eric, d'Ozouville, Noémi, Graham, D.W. (Eds.), The Galápagos: A Natural Laboratory for the Earth Sciences, Geophysical Monograph 204.John Wiley & Sons, Inc, Washington, DC, pp. 55–70.

Ghiorso, M.S., Sack, R.O., 1995. Chemical mass transfer in magmatic processes IV. A revised and internally consistent thermodynamic model for the interpolation and extrapolation of liquid-solid equilibria in magmatic systems at elevated temperatures and pressures. Contrib. Mineral. Petrol. 119, 197–212.

Gibson, S., Geist, D., 2010. Geochemical and geophysical estimates of lithospheric thickness variation beneath Galápagos. Earth Planet. Sci. Lett. 300, 275–286. http://dx.doi.org/10.1016/j.epsl.2010.10.002.

Gibson, S., Geist, D.J., Day, J., Dale, C.W., 2012. Short wavelength heterogeneity in the Galápagos plume: evidence from compositionally diverse basalts on Isla Santiago. Geochem. Geophys. Geosyst. 13, Q09007. http://dx.doi.org/10.1029/2012GC004244.

Goss, A.R., Perfit, M.R., Ridley, W.I., Rubin, K.H., Kamenov, G.D., Soule, S.A., Fundis, A., Fornari, D.J., 2010. Geochemistry of lavas from the 2005–2006 eruption at the East Pacific Rise, 9°46′N-9°56N: implications for ridge crest plumbing and decadal changes in magma chamber compositions. Geochem., Geophys. Geosyst. 11, 1–35. http://dx.doi.org/10.1029/2009GC002977.

Harpp, K., Geist, D., 2002. Wolf–Darwin lineament and plume–ridge interaction in northern Galápagos. Geochem. Geophys. Geosyst. 3, 1–19.

Harpp, K.S., Fornari, D.J., Geist, D.J., Kurz, M.D., 2003. Genovesa submarine Ridge: amanifestation of plume-ridge interaction in the northern Galápagos Islands. Geochem. Geophys. Geosyst. 4.

Hauri, E., Wang, J., Dixon, J.E., King, P.L., Mandeville, C., Newman, S., 2002. SIMS analysis of volatiles in silicate glasses 1. Calibration, matrix effects and comparisons with FTIR. Chem. Geol. 183, 99–114. http://dx.doi.org/10.1016/S0009-2541(01)00375-8.

Herbert, S., Gibson, S., Norman, D., Geist, D.J., Estes, G., Grant, T., Miles, A., 2009. In to the field again: re-examining Charles Darwin's 1835 geological work on Isla Santiago (James Island) in the Galápagos Archipelago. Earth Sci. Hist.

Hooft, E.E.E., Toomey, D.R., Solomon, S.C., 2003. Anomalously thin transition zone beneath the Galápagos hotspot. Earth Planet. Sci. Lett. 216, 55–64.

Jackson, M.G., Hart, S.R., Saal, A.E., Shimizu, N., Kurz, M.D., Blusztajn, J.S., Skovgaard, A.C., 2008. Globally elevated titanium, tantalum, and niobium (TITAN) in ocean island basalts with high 3He/4He. Geochem. Geophys. Geosyst. 9. http://dx.doi.org/10.1029/2007GC001876.

Johnson, D.M., Hooper, P.R., Conrey, R.M., 1999. XRF analysis of rocks and minerals for major and trace elements on a single low dilution Li-tetraborate fused bead. Adv. X-ray Anal. 41, 843–867.

Kelley, K.A., Plank, T., Ludden, J., Staudigel, H., 2003. Composition of altered oceanic crust at ODP Sites 801 and 1149. Geochem. Geophys. Geosyst. 4.Koleszar, A.M., Saal, A.E., Hauri, E.H., Nagle, A.N., Liang, Y., Kurz, M.D., 2009. The volatile contents of the Galápagos plume; evidence for H_2O and F open system behavior in melt inclusions. Earth Planet. Sci. Lett. 287, 442–452.

Kurz, M., Geist, D., 1999. Dynamics of the Galápagos hotspot from helium isotope geochemistry. Geochim. Cosmochim. Acta 63, 4139–4156.

Kurz, M.D., Curtice, J., Fornari, D., Geist, D., Moreira, M., 2009. Primitive neon from the center of the Galápagos hotspot. Earth Planet. Sci. Lett. 286, 23–34. http://dx.doi.org/10.1016/j.epsl.2009.06.008.

Lytle, M.L., Kelley, K.A., Hauri, E.H., Gill, J.B., Papia, D., Arculus, R.J., 2012. Tracing mantle sources and Samoan influence in the northwestern Lau back-arc basin. Geochem. Geophys. Geosyst. 13.

McBirney, A.R., Williams, H., 1969. Geology and petrology of the Galápagos Islands. Geol. Soc. Am. Mem. 118, 1–197.

McDonough, W.F., Sun, S.S., 1995. The composition of the Earth. Chem. Geol. 120,223–253.

McKenzie, D., Bickle, M.J., 1988. The volume and composition of melt generated by extension of the lithosphere. J. Petrol. 29, 625–679.

Morgan, W.J., 1972. Deep mantle convection plumes and plate motions. Am. Assoc. Pet.Geol. Bull. 56, 203–213.

Newman, S., Lowenstern, J.B., 2002. Volatile Calc: a silicate melt–H_2O–CO_2 solution model written in Visual Basic for Excel. Comput. Geosci. 28, 597–604.

Peterson, M., Saal, A.E., Hauri, E.H., Werner, R., Hauff, S.F., Kurz, M.D., Geist, D., Harpp, K.S., 2010. Sources of volatiles in basalts from the Galápagos

Archipelago: deep and shallow evidence. In: Proceedings of the AGU Fall Meeting Abstracts.

Peterson, M., Saal, A., Hauri, E., Kurz, M., Werner, R., Hauff, F., Geist, D., Harpp, K., 2013. Volatile budget of the Galápagos Plume. In: Proceedings of the Goldschmidt2013 Conference Abstract 1956.

Rilling, S.E., 2005. Oxygen fugacities of lavas from the Galápagos islands and the Galápagos spreading center. In: Proceedings of the AGU Fall Meeting Abstracts.

le Roux, P.J., Shirey, S.B., Hauri, E.H., Perfit, M.R., Bender, J.F., 2006. The effects of variable sources, processes and contaminants on the composition of northern EPRMORB (8–10 N and 12–14 N): Evidence from volatiles (H_2O, CO_2, S) and halogens(F, Cl). Earth Planet. Sci. Lett. 251, 209–231.

Rowland, S.K., 1996. Slopes, lava flow volumes, and vent distributions on Volcan Fernandina, Galápagos Islands. J. Geophys. Res. Solid Earth 101, 27657–27672.

Rubin, A.M., Pollard, D.D., 1988. Dike-induced faulting in rift zones of Iceland and Afar.G eology 16, 413–417.

Saal, A.E., Hauri, E.H., Langmuir, C.H., Perfit, M.R., 2002. Vapour Undersaturation in Primitive Mid-ocean-ridge Basalt and the Volatile Content of Earth's Upper Mantle. 41.

Saal, A.E., Kurz, M.D., Hart, S.R., Blusztajn, J.S., Blichert-Toft, J., Liang, Y., Geist, D.J., 2007. The role of lithospheric gabbros on the composition of Galápagos lavas. Earth Planet. Sci. Lett. 257, 391–406.

Settle, M., 1979. The structure and emplacement of cinder cone fields. Am. J. Sci., 279, pp.1089-1107.

Shaw, D.M., 1970. Trace element fractionation during anatexis. Geochim. Cosmochim. Acta 34, 237–243.

Siebert, L., Simkin, T., Kimberly, P., 2011. Volcanoes of the World. Univ of California Press, Berkeley; Los Angeles; London.

Simkin, T., Howard, K.A., 1970. Caldera collapse in the Galápagos Islands, 1968. Science (80) 169, 429–437.

Smith, P.M., Asimow, P.D., 2005. Adiabat_1ph: a new public front-end to the MELTS, pMELTS, and pHMELTS models. Geochem. Geophys. Geosyst. 6.

Swanson, F.J., Baitis, H.W., Lexa, J., Dymond, J., 1974. Geology of Santiago, Rábida, and Pinzón Islands, Galápagos. Geol. Soc. Am. Bull. 85, 1803–1810.

Toomey, D.R., Hooft Toomey, E.E., Hooft Toomey, E.E., Detrick, R.S., 2001. Crustal thickness variations and internal structure of the Galápagos Archipelago In: Proceedings of the AGU Fall Meeting Abstracts.

Villagómez, D.R., Toomey, D.R., Hooft, E.E.E., Solomon, S.C., 2007. Upper mantle structure beneath the Galápagos Archipelago from surface wave tomography. J. Geophys. Res. 112, B07303. http://dx.doi.org/10.1029/2006JB004672.

Villagómez, D.R., Toomey, D.R., Hooft, E.E.E., Solomon, S.C., 2011. Crustal structure beneath the Galápagos Archipelago from ambient noise tomography and its implications for plume-lithosphere interactions. J. Geophys. Res. Solid Earth 116, 1–20. http://dx.doi.org/10.1029/2010JB007764.

Weaver, B.L., 1991. The origin of ocean island basalt end-member compositions: trace element and isotopic constraints. Earth Planet. Sci. Lett. 104, 381–397.

White, W.M., McBirney, A.R., Duncan, R.A., 1993. Petrology and geochemistry of theGalápagos Islands: portrait of a pathological mantle plume. J. Geophys. Res. SolidEarth 98, 19533–19563.

Wilson, E.L., 2013. The Geochemical Evolution of Santa Cruz Island, Galápagos Archipelago. University of Idaho, Moscow (ID).

Yun, S., Segall, P., Zebker, H., 2006. Constraints on magma chamber geometry at Sierra Negra Volcano, Galápagos Islands, based on InSAR observations. J. Volcanol. Geotherm. Res. 150, 232–243. http://dx.doi.org/10.1016/j.jvolgeores.2005.07.00

CHAPTER THREE: PETROGENESIS OF MONOGENETIC NEAR-ISLAND SEAMOUNTS ON THE GALÁPAGOS PLATFORM: ASSESSING A PREDOMINANTLY ISLAND BASED SAMPLING BIAS

Abstract

The Galápagos Archipelago is a hotspot derived volcanic island chain sourced from a deeply seated mantle plume. From previous work it appears that the Galápagos Archipelago does not undergo the same systematic evolution as is predicted by hotspot theory. Further, there is a complicated pattern of geochemistry recorded in lavas that comprise the major islands, which has been related to multicomponent gradational zonation of the Galápagos plume source. To date, a majority of sampling in the modern archipelago has previously targeted the subaerial portion of the archipelago or large volume lava flows constituting their base. Sampling restricted to these large volcanic features may result in a biased view of magmatic and source processes. We investigate whether finer scale sampling of satellite volcanoes surrounding the major islands can be used to constrain the evolution of volcanoes as they pass over the hotspot and their mantle source. Seamounts were targeted that surround islands representing the three primary geochemical endmembers of the plume. In all regions, seamounts appear to be monogenetic, but seamount fields are emplaced from multigenerational magmatic episodes. This study finds that the seamounts show greater geochemical variability than the islands they surround but have isotopic and trace element signatures that resemble their respective nearby islands. Seamounts may have their source in the base of the

magmatic systems, which supply the islands. Variations in seamount chemistry support the concept that islands along the center of the hotspot track may undergo early evolutionary phases predicted by plume theory. Seemingly random patterns of geochemical and isotopic enrichment of seamounts within each region do not support the model of gradational zonation of mantle components.

Introduction

The Galápagos Archipelago is located on the Nazca Plate, approximately 200 km south of the Galápagos Spreading Center and 1000 km off the west coast of South America (Figure 3.1). The Galápagos consists of thirteen volcanic islands and numerous satellite constructions and seamounts (Figure 3.1; McBirney and Williams, 1969; Chapter 1 and Chapter 2). Geophysical observations indicate that the center of the Galápagos is underlain by anomalously hot asthenosphere with an excess temperature of 30-150°C, attributed to the underlying Galápagos hotspot (gravity anomalies; Hooft et al., 2003; seismic tomography: Villagomez et al., 2007; 2014). Many basalts erupted in the Galápagos carry a chemical signature characteristic of a deep mantle reservoir ($^{3}He/^{4}He$ > 30 R/R_A; Graham et al., 1993; Kurz and Geist, 1999; Kurz et al., 2009). Thus, the hotspot is likely the result of upwelling and melting of a deeply seated mantle plume (Courtillot et al., 2003).

Galápagos Islands are most volcanically active on the western edge of the archipelago, near the center of plume upwelling (e.g., Allan and Simkin, 2000) and increase in age with the direction of plate motion to the east (Geist et al., 2014), consistent with their construction over a fixed source (White et al., 1993; 51 km/Ma to the east; Argus et al., 2010). Despite this general aging trend, islands remain volcanically

active much longer than is predicted by hotspot theory alone, with historic eruptions distributed over an ~200 km-wide area on Fernandina, Floreana, Santiago and San Cristobal (Siebert et al., 2011). This prolonged volcanic activity has been explained by changes in lithospheric thickness across the archipelago that is not observed in Hawaii (Feighner and Richards, 1994; Gibson and Geist, 2010), and interaction of the hotspot with a mid-ocean ridge to the north as the archipelago has evolved, which may enhance volcanic activity downstream from the center of upwelling (Harpp and Geist, 2002, Harpp et al., 2003; Mittelstaedt et al., 2012; Harpp and Geist, 2018).

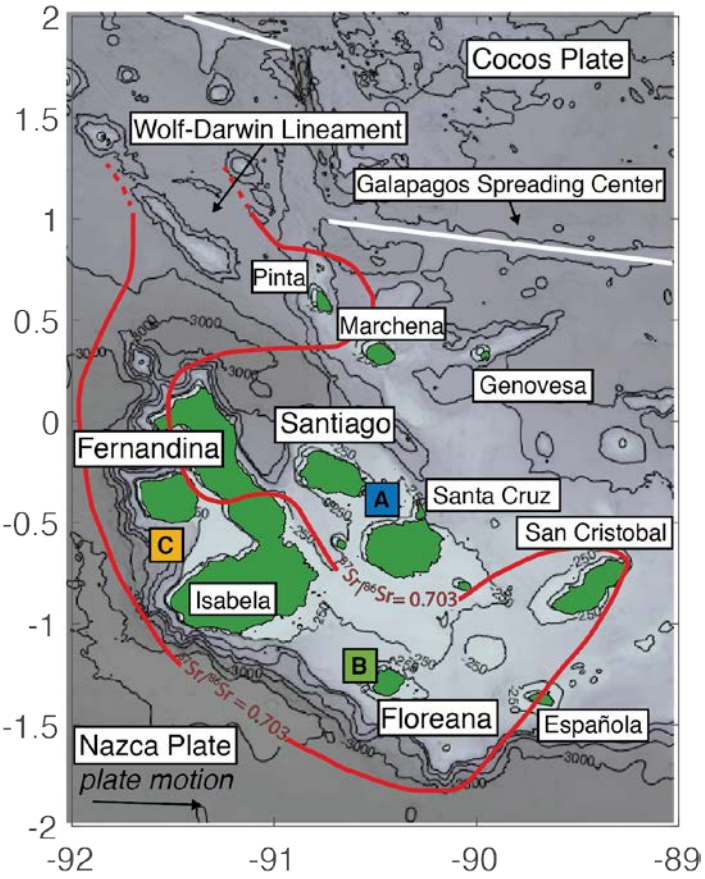

Figure 3.1. Map of the Galápagos Archipelago. Islands are shown in green, sit atop the Nazca Plate, with hotspot relative plate motion ~50km/Ma east (Argus et al., 2010). The location of the Galápagos Spreading Center is indicated by white lines. Bathymetric contour interval is 500 m except the shallowest index at 250 m. Colored squares indicate the respective locations of panels A, B and C in Figure 2. Nazca Plate motion, relative to the fixed hotspot reference frame is nearly due east and is shown as a black arrow in the bottom left of the map (Argus et al., 2010). Red line indicates $^{87}Sr/^{86}Sr$ isotopic contour derived from island and platform data (Harpp and White, 2001).

Unlike many other ocean island systems, the islands in the modern Galápagos Archipelago are underlain by a large, shallow submarine platform, constructed by the terracing of voluminous basaltic lava flows (Geist et al., 2006 and 2008). The platform has nearly 4000 m of vertical relief on its leading edge in the west and represents a vast majority of the volume of erupted material in the archipelago. Platform construction is thought to have occurred through eruption of large volume tholeiitic lava flows that precede island formation at the leading edge of the hotspot. If true, this suggests that the earliest phase of volcanism in the Galápagos differs significantly from that of prototypical hotspot evolution, where initial island building begins with low volume, pre-shield building, alkalic magmatism. The lack of a clear linear age progression and absence of a defined pre-shield alkalic phase at the leading edge of the hotspot track call into question whether the evolution of the Galápagos Archipelago is controlled on first order by traditional hotspot theory (Harpp and Geist 2018). However, recent investigations of samples collected *in situ* from distinct lava flows at the leading edge of the platform to the west of the archipelago have a greater diversity of composition that are consistent with the presence of an alkalic low volume leading edge phase of volcanism, as is observed in Hawaii (Anderson et al., 2018). In this model, the low volumes of alkalic magmatism and presence of the Galápagos platform may largely obscure the early alkalic stages of magmatism at the leading edge of the Galápagos plume.

Adding to the complexity, the Galápagos shows a complicated pattern of chemical and isotopic enrichments compared to other plume sourced hotspot provinces, despite their all being sourced from the lower mantle (White et al., 1993). Since its impingement

on the pacific basin, resulting in the formation of the Caribbean Large Igneous Province (~90 Ma; Hauff et al., 2000; Hoernle et al., 2000), the Galápagos mantle plume appears to have produced lavas of at least three geochemical and isotopic domains with the same isotopic geography reflected at the surface for >70 Ma (White et al., 1993; Hoernle et al. 2000; Werner et al., 2003; Harpp et al., 2014a; Trela et al., 2015; Gazel et al., 2018). In general, individual islands, seamounts, and submarine lava flows are typified by eruption of relatively limited lava compositions compared to the diversity observed on the archipelago scale (White et al., 1993).

Based primarily on radiogenic isotope ratios, the zonation of the Galápagos mantle plume is commonly described as a horseshoe with an enriched periphery ("C" shaped, with respect to north) and a depleted interior (Figure 3.1). In the modern archipelago, these domains are commonly referred to as PLUME, FLO and DUM, and WDL (Harpp and White, 2001). The unique zonation pattern consisting of enriched PLUME and FLO to the north and south and DUM to the east, has been attributed to entrainment of upper mantle into a gradationally zoned plume during ascent (White et al., 1993; Harpp and White, 2001), plume-ridge interaction (Ito and Bianco., 2014), or tapping of a complexly zoned or striped plume (Geist et al., 1988; White et al., 1993; Hoernle et al., 2000; Werner et al., 2003; Gazel et al., 2018; Harpp et al., 2014a). Regardless of the exact origins of this heterogeneity, almost all models (excluding Gibson et al., 2012; Harpp et al., 2014b) invoke extensive mantle endmembers that grade (or mix) evenly between islands to produce the observed geochemical patterns.

The interpretations of Galápagos evolution and its mantle source are predominately based on geochemical analyses of lavas erupted on the subaerial volcanic

islands (e.g., White et al., 1993 and references therein), expansive lava flows that form the platform terraces (Geist et al., 2006; 2008), or dredging of massive seamounts offset from the currently active volcanic platform (Christie et al., 1992; Werner et al., 1999; Hoernle et al., 2000; Harpp and White, 2001; Werner et al., 2003; Sinton et al., 2014). Thus, the above interpretations may be the result of a sampling bias that traditionally focused on the main volcanic centers. These larger features may pave over early phases volcanism and obscure the true scales mantle heterogeneity as a result of melting and mixing on the island scale. We evaluate the severity of this bias by investigating the distribution and geochemical heterogeneity of near-island seamounts located throughout the modern archipelago.

Background

Because ocean island basalts (OIBs) show the most extreme compositional variation of all ocean basin lavas, they are often used to investigate mantle heterogeneity. Chemical variations in OIBs reflect a combination of shallow and deep magmatic processes; however, isotopic variations are thought to represent longstanding heterogeneities in the mantle from which they are sourced (Hart et al., 1992; Hofmann, 1997). Isotopic variations on the surface are often interpreted to represent the length scales and relative distributions of deeply seated mantle source reservoirs. For instance, longstanding temporal variations at single ocean island archipelagos leads to schematic cartoons of the mantle, where reservoirs are simplified into distinct domains, hundreds of kilometers in scale (Hawaii; e.g., Abouchami et al., 2005; Galápagos; e.g., Gazel et al., 2018). Geographic isotopic patterns at the surface are explained via tapping of various reservoirs represented by numerous components, often called the “mantle zoo” (Hart et

al., 1992), each sequestered somewhere in the mantle (Hofmann, 1997). Bilaterally asymmetric patterns in radiogenic isotope ratios, in particular, have been linked to seismic anomalies observed at the core mantle boundary in the Pacific (Castillo, 1988; Weis et al., 2011; Harpp et al., 2014a) and Atlantic Ocean basins (Hoernle et al., 2015). Other models invoke mixing of endmember components originating from shallower boundary layers in the mantle (Mazza et al., 2019). However, as global sampling increases, it has been called into question if the persistent isotopic signals in the ocean island record can be representative of source variations or are only apparent given the nature of melting at ocean islands themselves (Bianco et al., 2008 and 2011; Ito and Bianco, 2014; Jones et al., 2016; Jones et al., 2017).

Ocean islands form as a consequence of the intermittent eruption of lavas in a localized area as the Earth's lithosphere moves over a hotspot source. Thus, a single island or seamount contains an integrated history of repeated eruptions through time. Together, ocean island and seamount chains record hotspot activity occurring for tens of millions of years, providing a window into the evolution of hotspots and mantle heterogeneity in general. However, due to the difficulty in accessing the submarine portions of these systems, a majority of the sampling of OIB is from the subaerial edifices. This is potentially an issue since the extreme endmembers of the OIB source are modified as melts mix (Stracke and Bourdon, 2009), evolve and react during ascent and storage in the lithosphere prior to eruption at ocean islands (e.g., Saal et al., 2007; Peterson et al., 2014 and Peterson et al., 2017). Further, ocean islands, being polygenetic in nature, are continuously repaved, largely overprinting any variations that arise through time. Mixing in the mantle and crust and repaving at the surface are at the highest

efficiency during the main stage of ocean island volcanism, where high magma supply favors the formation of shallow magma reservoirs and high effusion rates (e.g., Geist et al., 2014). As a consequence, these highly processed lavas may dominate our sampling leading to a potential observational bias that we refer to as the “island effect”.

If the island effect is significant, we can establish a series of hypotheses that predict (1) all plume derived ocean islands undergo the same evolutionary sequence predicted by hotspot theory, with gaps that represent only a sampling bias towards the main stage of formation, and (2) the length scales and magnitudes of mantle heterogeneity are shorter/more extreme than what is preserved in OIB due to magma mixing during ascent and storage in shallow magma chambers. The efficiency of this effect will be dependent on combined plume strength (i.e., completeness of repaving), mantle geography and plate motion (e.g., Jones et al., 2016), and will be accentuated at ocean islands that are not extensively dissected by erosion. Further, we note that melting systematics may play a key role in the geographic distribution of geochemical endmembers at hotspots, which is tangentially related to the bias introduced by studying the mantle through ocean islands (e.g., Stracke and Bourdon, 2009; Ito and Bianco, 2014). As such, in order to understand the evolution of hotspot systems, the spatial structure of chemical domains in the mantle, and the endmember compositions that exist in the mantle prior to melt transport and mixing, sampling must be done on finer scales and away from the large volcanic centers that promote shallow mixing. Further, targeting features that might be preserved through mainstage volcanism.

Monogenetic volcanoes surrounding larger volcanic edifices in all tectonic settings provide a punctuated record of source and storage conditions in a magmatic

system (Wood, 1979). Smaller monogenetic cones are common features surrounding larger point source volcanoes, which generally show considerable chemical variability relative to one another and compared to the larger edifice they surround (Brenna et al., 2011; Smith and Nemeth, 2017). In ocean island systems these features can be satellite cones or fissures on a volcanoes flanks or small seamounts on the submerged periphery of the volcanic island. Although the former is commonly targeted for sampling, the seamounts on the flanks of an ocean island volcano might originate from a less shallow or centralized reservoir, providing a different perspective on the deeper magmatic system. Thus, one approach to evaluating ocean island evolution and mantle heterogeneity on a finer scale is to systematically sample lavas from near-island seamounts, which are preserved through mainstage volcanism. Targeting these features, as opposed to the polygenetic volcanoes that they surround, may provide a less biased insight into the magnitudes and length scales of mantle heterogeneity.

Here, we utilize recently sampled seamounts in the Galápagos Archipelago that surround the islands of Fernandina, Santiago and Floreana. Lavas collected from the islands in each location are sourced from three end-member isotopic reservoirs that have persisted over the Galápagos plume's history (e.g., Hoernle et al, 2000). We first compare the lava compositions observed in each seamount region to the volcanic islands that they surround to evaluate relationship between the seamounts s and the main magmatic system. From this framework we then assess how seamount sampling improves the understating of chemical and isotopic geography, how this geography relates to the evolution of the Galápagos hotspot system, and the nature of heterogeneities in the Galápagos mantle source.

Methods

Seamount Mapping, Sampling and Initial Sample Preparation

In 2015, two research cruises on the E/V *Nautilus* and M/V *Alucia* mapped >100 seamounts on the top of the Galápagos Platform, most of which were previously undiscovered (Carey et al., 2016; Chapters 1 and 2). Approximately 150 rock samples were collected from the seamounts using the Ocean Exploration Trust's remotely operated vehicle *Hercules* and the Dalio Foundation's manned submersibles *Deep Rover 2* and *Nadir*. Seamounts around three islands were targeted: south and southeast of Santiago, northwest of Floreana, and south of Fernandina (Figure 3.1; Table 3.1). These regions were chosen based on satellite altimetry derived bathymetry that suggested the presence of seamounts (Smith and Sandwell, 1994), and because these regions represent three primary geochemical endmembers (central, eastern, and southern) in the archipelago (e.g., Hoernle et al., 2000).

The seamounts were mapped at 10 m spatial resolution by shipboard multibeam (Chapter 1; Figure 3.2). Once mapped, seamounts were targeted that displayed variable morphology (e.g., elongation direction, aspect ratio; surface roughness, volume), which were taken to be a product of eruption from variable stress conditions, and thus separate events. Post-cruise morphological characteristics were quantified using seamount footprints and bathymetric data (Chapter 2). Seamount volume was calculated as the difference between the mean depth of the pixels within each seamount and mean base depth of each seamount, converted to volume by multiplying this value by the number of pixels comprising the seamount and individual pixel area. Similarly, the volume of the subaerial portion of Santiago, Floreana and Fernandina islands were calculated for

reference with a global multiresolution topography grid (Ryan et al., 2008), using the mean elevation of each island. Aspect ratio is calculated as the length divided by normally oriented width of each seamount (L/W), in the orientation that maximized this value. The direction of the long axis in the aspect ratio measurement was further recorded as the elongation direction.

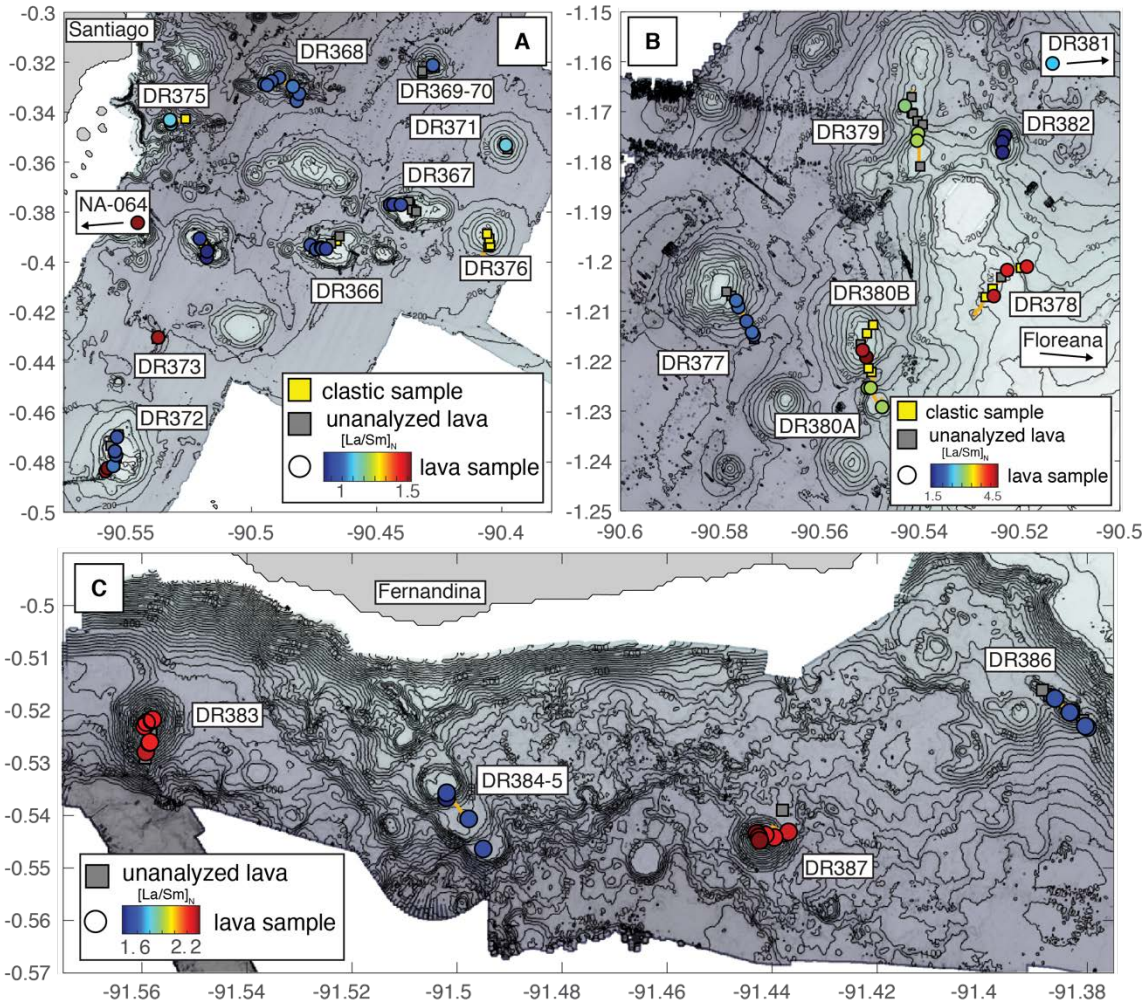

Figure 3.2. Map of seamount samples for Santiago (A), Floreana (B) and Fernandina regions (C). Labels indicate HOV dive names. Gold lines show HOV dive track. Clastic samples are shown as yellow squares. Lavas that were not analyzed because of high degrees of alteration are shown as grey squares. All other samples are shown as colored circles, with color representing $[La/Sm]_N$.

Submersible dives typically began at the base of each seamount and collected samples up the seamount's stratigraphy to assess the chemical variability within a single cone. Upon recovery, samples were rinsed and cleaned of biological residue and air dried. At Boise State University (BSU) rock samples were further crushed by sledge and ceramic plate jaw crusher to 1-10 mm diameter chips. Chips were sonicated 3x in an ultrasonic bath of ultrapure milliq-H_2O to remove contaminants, leached in the ultrasonic bath for 20 mins with 1% peroxide, and finally rinsed 3x with milliq H_2O to remove alteration products and surficial seawater contamination.

Major and Trace Element Analysis

Whole rock major elements were collected by X-ray Fluorescence (XRF) for all basaltic samples, where unaltered and carbonate free material was available. Fresh chips, devoid of alteration, were hand-picked under binocular microscope for analysis, typically from the 5-10 mm size fraction. Cleaned chips (10-20 g) were powdered at Washington State University (WSU) Geoanalytical Facility using swing mill with tungsten carbide surfaces. Powders were double fused with Li-tetraborate into a glass bead for analysis. XRF analysis was carried out in four sessions using a Thermo-ARL automated XRF spectrometer at WSU under the methods of Johnson et al. (1999). Reproducibility of major elements was assessed by repeat measurements of unknowns, which was between 0.25 and 1% for all oxides except K_2O (2.8%). We report all trace element results from XRF measurements. Loss on ignition (LOI) was measured for all samples. High LOI is taken as an indication of high degrees of alteration or significant adhering carbonates. Samples with LOI >1% are not interpreted with the rest of the major element data and are

flagged with an “X” in the major element diagrams and subsequently described trace element results.

For all samples analyzed for major elements, an additional 50 mg of material was handpicked from the 1-2 mm size fraction for solution ICPMS trace element analysis. Care was taken to select chips without obvious phenocrysts, alteration, or adhering carbonates. Picked separates were further sonicated in milliq H_2O for 20-minute intervals, with fines decanted in between, until clear. Samples were dissolved following the procedure of Kelley et al. (2003) and Lytle et al. (2012), as modified and summarized in Chapter 2. Of note, 15 mL Teflon Savillex beakers were used in the digestion steps.

Trace element concentrations were measured in three sessions on 2500X dilution aliquots of dissolved samples and standards over the course of a year, using a Thermo Electron X-Series II Quadrupole ICPMS coupled with an ESI SC-FAST solution autosampler at BSU. Concentrations were calibrated from the instrumental raw-counts using GeoRem preferred values for United States Geological Survey standards BHVO-2, BIR-1, DNC-1, W-2 (Jochum et al., 2016), and Geological Survey of Japan standard JB-3 (GeoREM accepted value), tied at the y-intercept to a total procedural blank measurement. Individual analyses (30 seconds) were adjusted to a uniform sensitivity using a 20 ppb In internal standard solution. Final concentrations were determined by the average of three analyses, and analytical precision was determined from the standard deviation of these runs (Supplementary Data Table 3.4). All data reduction to this point was carried out using PlasmaLab software. Repeat measurements of JB-3 were made every 5-10 analyses to monitor and correct for instrumental drift (averaged percent

relative deviation of JB-3 drift measurements from initial calibration value, calculated block by block; <1% correction on average for all blocks).

Accuracy of the ICPMS data is given by the reproducibility of geologic standards (and repeat measurements of samples) measured before and after each session (Supplementary Table 3.6). These uncertainties are typically 2-5% for all elements >0.5 ppm, which is comparable to the internal precision of the three averaged analyses (Supplementary Table 3.5). Of note, reproducibility of high abundance transition metals for our XRF analyses is a factor of 5 greater than on the ICPMS (1%; Ni, Cr, V), and comparable for lower abundance elements (2-4%; Sc, Ga, Cu, Zn). Thus, we prefer these XRF derived measurements for these elements over the ICPMS values.

Radiogenic Isotope Analysis

Splits of the chipped samples, previously prepared for major and trace element analysis, were leached in 6 M HCl to remove the effect of seawater contamination and alteration on the isotopic ratios. To assess the effects of alteration and contamination on the measured isotopic ratios, samples were leached using two methods, the first was a gentle approach and involved the repeat leaching of samples in an ultrasonic bath (e.g., Nobre Silva et al., 2009); the second was more aggressive, where samples were leached for two three-hour periods in 150℃ 6M HCl, followed by repeated 20 min sonication in milliq-H_2O and decanting until clear of fines. Leached rock chips were dissolved using standard procedures and separated into their chemical species using ion exchange chromatography, under standard procedures practiced at the BSU Isotope Geology Laboratory (IGL; Fisher et al., 2011; Sousa et al., 2013) as adapted from Korkisch (1989). All isotope ratios were measured on the IsotopX Phoenix X62 TIMS at the IGL.

Strontium isotope ratios were measured on single Re filaments in a three-sequence dynamic routine utilizing five Faraday cups (e.g., Kurz et al., 2017). Samples were loaded using 2 uL Ta gel emitter solution following standard loading procedures. Samples and standards were run maintaining 2-4V ^{88}Sr beam for 150 cycles. Internal precisions of analyses are typically 3-6 ppm for $^{87}Sr/^{86}Sr$ (Table 3.3). Mass dependent fractionation is corrected using an exponential law and $^{86}Sr/^{88}Sr$ of 0.1194, and bias corrected relative to the certificate value for NBS-987 of 0.710248. Running mean of NBS-987 $^{87}Sr/^{86}Sr$ measured on the Phoenix at BSU since put into operation is 0.710248 ± 5 (6 ppm, 1-sigma).

Neodymium isotope ratios were measured using a triple filament setup, with sample loaded on a single side filament and ionized from a high temperature center filament (Thirlwall, 1982). Analysis was made, using a three-sequence dynamic routine utilizing five Faraday cups (e.g., Kurz et al., 2017). Samples were loaded as 3 uL aliquots. Samples and standards were run maintaining ≥2V ^{144}Nd beam for 150 cycles. Internal precisions of analyses are 10 ppm on average for $^{143}Nd/^{144}Nd$ (1-sigma internal standard error; Table 3.3). Mass dependent fractionation is corrected using an exponential law and $^{146}Nd/^{144}Nd = 0.7219$, and bias corrected relative to the certificate value for JNdi-1 of 0.512110. Running mean of Jndi-1 $^{143}Nd/^{144}Nd$ measured on the Phoenix at BSU since put into operation is 0.512104 ± 2 (7 ppm, 1-sigma); remarkably, this is consistently less than the internal precision of analyses for these analytical sessions.

<u>He isotope Analysis</u>

Olivine grains used for He isotopic analysis were handpicked under a binocular microscope, typically from the 500-1000 µm sieve fractions from the original crushed

and cleaned samples. Picked olivine for each sample were crushed and melted at Woods Hole Oceanographic Institute (WHOI) to permit helium extraction and measurement. Crushing sample releases He contained in melt and fluid inclusions, which is representative of the inherited component and measured as $^{3}He/^{4}He$ (Kurz 1986a), and reported as the $^{3}He/^{4}He$ relative to the present day atmosphere (R/R_a). Melting the crushed fraction in a single step releases the remaining gas, yielding total concentrations of ^{3}He and ^{4}He. Samples melted to assess the presence of a cosmogenic component, related to subaerial sample exposure (e.g., Chapter 2), are also reported here. We assume that the inherited He ratio does not change due to the radiogenic production of ^{4}He from the decay of Th and U. This assumption is valid due to the low concentration of U and Th in the samples (<1ppm; Supplementary Table 3.4). Samples were analyzed using the rock analysis mass spectrometer system (MS2) at WHOI, consisting of a 90° magnetic sector noble gas mass spectrometer and a quadrupole mass spectrometer. We carried out the analyses following the analytical procedure described by Kurz and Geist (1999), Kurz (1986b), and Kurz et al. (1996).

Results

Summaries of the seamount spatial statistics, including rose diagrams of seamount elongations and histograms for the seamount volume and aspect ratio for each region, are shown in Figure 3.3. A total of 145 rock samples were recovered from 21 seamounts. Many of the collected lavas are variably altered and contaminated by adhering carbonates on outer surfaces and in vesicles. From the Santiago and Floreana regions, 20 samples were volcaniclastic (termed “clastic”) and are not evaluated further (Figure 3.2). Only lavas reasonably clean of alteration and adhering carbonates were analyzed for major and

trace elements (N = 81), and subsequent isotopic analysis (N=31). We include in our discussion 12 samples collected on the R/V *Nautilus* (Chapter 2), two of these samples were analyzed for isotopes and are presented in this study. Trace elements from that study have been reprocessed using updated standard values and reported here, so they can be compared directly with our data.

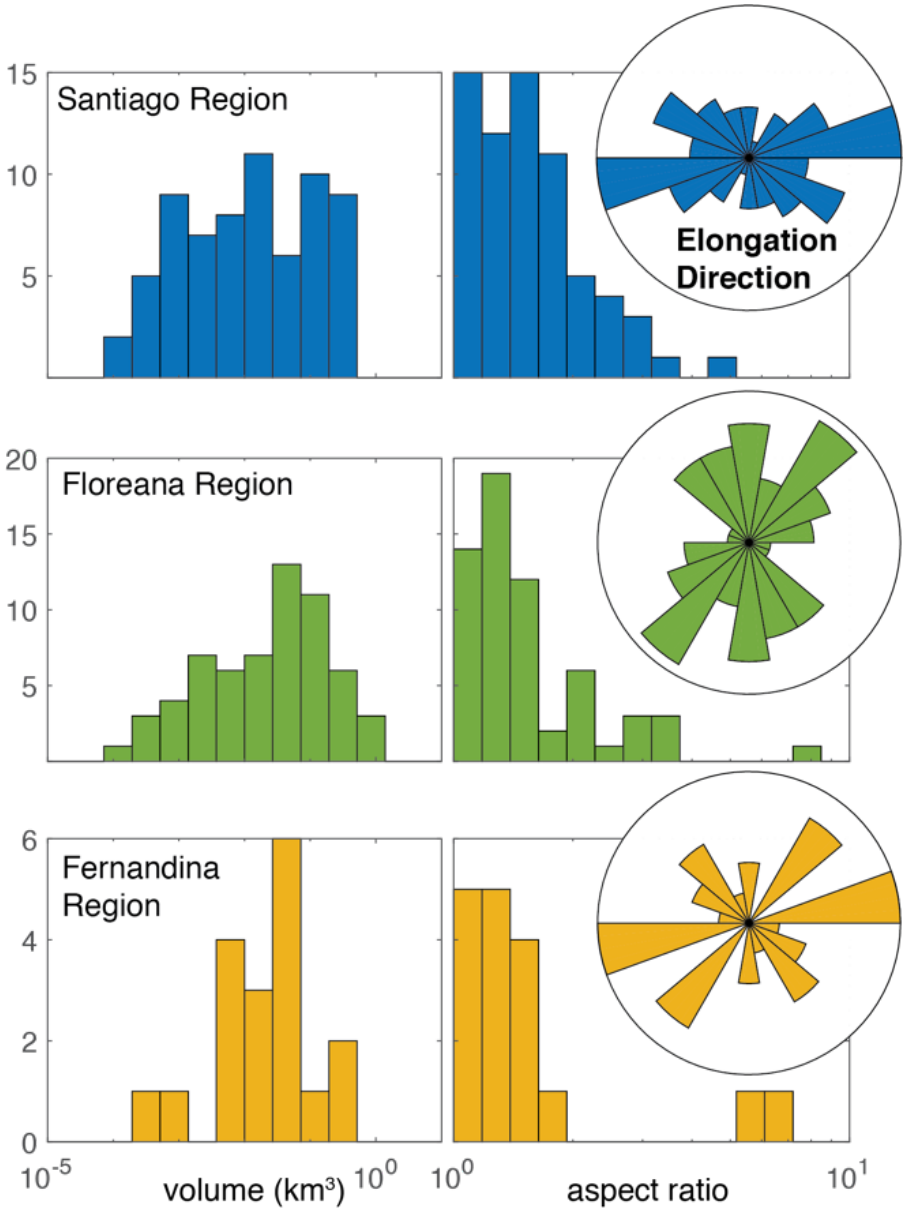

Figure 3.3. Spatial statistics of mapped seamounts size and shape summarized by region.

Table 3.1 Summary of geochemical and morphological data by seamount

seamount	volume (km3)	L/W	elong. dir.	MgO	K_2O+ Na2O	$[La/Sm]_N$	%RSD	$^{87}Sr/^{86}Sr$	$^{143}Nd/^{144}Nd$	$^{3}He/^{4}He$
Santiago										
DR367	0.39	2.0	90	8.98	2.63	0.82	1.1	0.7026521	0.5130815	-
DR371	0.11	1.1	138	9.12	2.97	1.07	-	0.7027170	0.5130810	10.4
DR375	0.024	1.1	90	8.66	3.08	1.05	0.5	0.7027458	0.5130780	-
DR369-70	0.13	1.2	100	8.95	2.63	0.93	-	0.7027086	0.5130700	11.9
DR368	0.35	1.5	118	9.74	2.54	0.93	2.2	0.7028265	0.5130560	9.03
DR373	-	-	-	5.11	3.63	1.56	-	0.7028885	0.5130560	-
DR366	0.35	1.7	82	9.25	2.65	0.87	3.8	0.7027873	0.5130540	-
DR374	0.35	1.5	126	10.5	2.38	0.77	3.0	0.7028460	0.5130530	10.1
DR372	0.38	1.4	1	7.74	2.80	1.13	30	0.7028699	0.5130470	-
HERC1	0.30	1.3	57	8.50	3.22	1.47	1.5	0.7029960	0.5130040	-
HERC2	0.60	1.1	5	8.70	3.22	1.49	1.9	0.7029168	0.5130010	-
Floreana										
DR382	0.043	1.4	0	9.62	2.75	1.46	2.3	0.7033207	0.5129945	-
DR377	0.56	1.1	152	8.00	2.55	2.22	2.1	0.7032962	0.5129630	12.4
DR381	0.50	1.3	179	10.5	3.44	2.49	4.7	0.7033279	0.5129570	-
DR379	0.043	1.5	39	9.31	2.21	3.26	2.5	0.7034294	0.5129535	15.1
DR380	0.15	1.2	160	10.6	3.41	4.21	21	0.7034390	0.5129465	14.6
DR378	0.18	1.4	179	10.7	3.55	4.70	1.5	0.7035724	0.5129395	14.4
Fernandina										
DR383	0.44	1.4	5	6.65	5.27	2.21	0.8	0.7032393	0.5129740	-
DR387	0.14	1.1	88	6.05	4.84	2.25	1.4	0.7032580	0.5129710	-
DR384-5	0.22	1.1	90	6.44	3.04	1.68	1.9	0.7032410	0.5129440	23.6
DR386	0.020	6.6	123	5.24	3.11	1.74	0.5	0.7032710	0.5129310	-

Excluding samples with LOI >1%, all samples analyzed are tholeiitic to mildly alkalic basalts (MgO = 4.88-13.4 and SiO_2=43.4-50.0; Table 3.1 and Figure 3.4), with total alkali (TA; Na_2O+K_2O) contents ranging from 2.14-5.39 wt%. Given that we will compare the isotopic and trace element signatures of the lavas to mantle sources, all trace element ratios are reported relative to the primitive mantle (PM; McDonough and Sun, 1995). The seamounts are characterized by differences in light to middle rare Earth element ratios (LREE/MREE), large ion lithophile to LREE (LILE/LREE) and highly

incompatible high field strength element (HFSE) to similarly incompatible LREE enrichments (e.g., $[Nb/La]_N$), and depletion in some HFSEs to similarly compatible REEs (e.g., $[Hf/Nd]_N$) (Figure 3.5), and variable Pb anomalies, which are summarized along with their major element and isotopic characteristics by region below. For reference, results are summarized by seamount in Table 3.1.

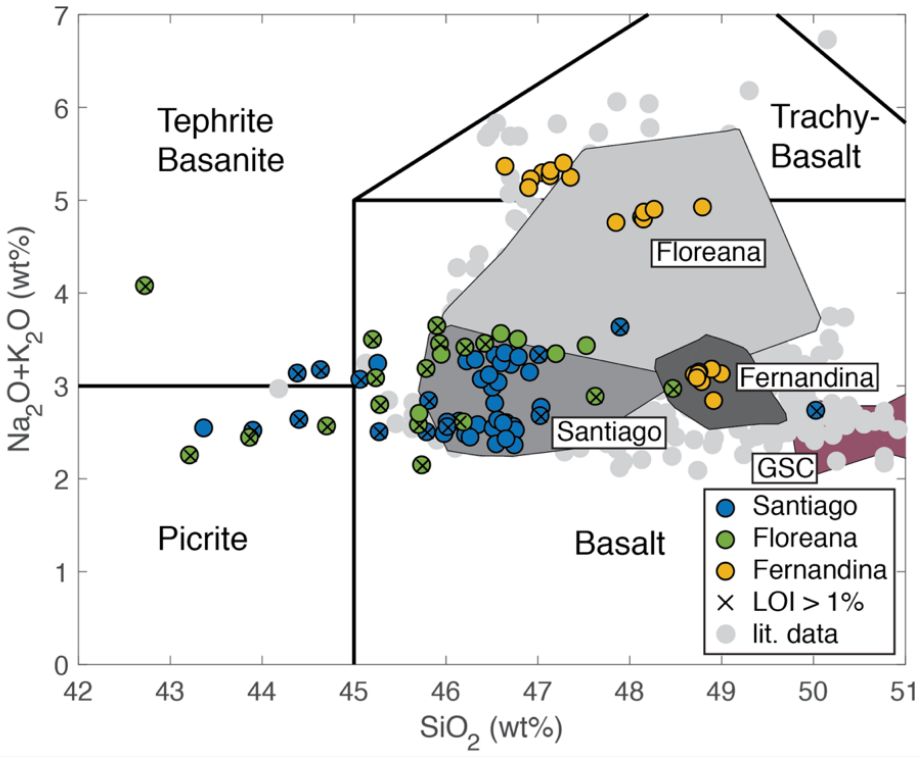

Figure 3.4. Total alkali contents as a function of silica for seamount samples compared to previously collected data. Seamount samples are shown as colored circles. Samples with black X's had LOI >1%. Grey circles show compiled literature data (Regional: White et al., 1993; Harpp and White, 2001; Saal et al., 2007; Santiago: Gibson et al., 2012; Santa Cruz: Wilson, 2013; Floreana: Harpp et al., 2014; Terrace lavas: Geist et al., 2008; Peterson et al., 2017; Anderson et al., 2018). Variably shaded grey fields have been drawn around literature data for the three islands nearest to the seamounts sampled (light: Floreana, medium: Santiago, dark: Fernandina). Mauve field surrounds data from the GSC, >750 km from the Galápagos hotspot (Gale et al., 2013 and references therein).

Santiago Region

Based on bathymetric data, 22 seamounts were identified in the Santiago region (Chapter 1). Integrating the volume within the footprints of each of these mapped seamounts results in a total seamount volume of 6.4 km^3, which is 6% of the subaerial volume of Santiago Island (99 km^3). The average seamount volume is 0.07 km^3, which is the median of the three regions (Figure 3.3). The Santiago seamounts are clustered spatially into two primary regions, the first is off of the southwestern flank of Santiago and the second to the east-southeast (Figure 3.2A). The cluster off the southeastern flank harbors a majority of mapped seamounts (Figure 3.2A). These seamounts form multiple lineaments and are variably elongate (mean aspect ratio = 1.7; Figure 3.3) subparallel to linear seamount clusters (mean elongation direction = 96°; Figure 3.3), and to the strike of the elliptical island of Santiago (Figure 3.1) and its elongate volcanic vents (see Gibson et al., 2012). By comparison there are only two, relatively conical seamounts in the southwestern region as first described in Chapter 2. Generally, seamounts furthest from Santiago are the most conical, which includes the two seamounts on the southeastern flank of the island.

We analyzed forty-five samples from eleven of the seamounts (and one platform sample; DR373) southwest (NA-064; Chapter 2) and east-southeast (DR366-DR376) of Santiago. The seamounts are composed of relatively mafic (MgO = 6.52-10.9; Table 3.1 Supplementary Figure 3.1), tholeiitic to mildly alkaline (K2O+Na2O = 2.35-3.34 wt%) basalts (Figure 3.4). Although the most alkalic samples are located off the southwest coast of Santiago, mildly alkalic lavas are also sourced from low aspect ratio, conical vents on both the southwestern and eastern seamount regions. Lavas from each individual

seamount have different trace element concentrations and ratios (Figure 3.2; e.g., $[La/Sm]_N$ = 0.757–1.59). However, all the lavas erupted at an individual seamounts are characterized by nearly uniform trace element ratios ($[La/Sm]_N$ < 4 %RSD; Table 3.1), with the exception of one seamount, which spans nearly the entire range of chemical variability observed in the region (DR372). The Santiago seamount lavas have the lowest $[Rb/La]_N$ and $[Ba/La]_N$ values (max. of 0.82 and 0.61 respectively) of the three regions (Figure 3.5). In contrast to the other seamount regions, Santiago samples show almost no $[Nb/La]_N$ enrichments (max. of 1.2) or $[Hf/Nd]_N$ depletions (min. of 0.92). Of note, Santiago samples have the highest Pb concentrations relative to similarly compatible Th ($[Pb/Th]_N$= 0.36-2.3). Isotope ratios form two linear trends in bivariate isotope space (Figure 3.6). The two trends are pinned on the more depleted isotopic endmember but diverge towards two more radiogenic compositions in Sr-Nd isotopic space (Figure 3.6). The Santiago seamounts have the most depleted compositions of all lavas recovered and are more depleted compared to subaerial lavas erupted on Santiago Island (e.g., min. $^{87}Sr/^{86}Sr$ = 0.702639 and max. $^{143}Nd/^{144}Nd$ = 0.513085). Helium isotopic compositions for the Santiago samples are all greater than the average MORB value of ~8.5 R/Ra (Anderson, 2000) and range from 8.49-10.4 R/Ra (Table 3.1). Neither major or trace element contents directly correlate with isotopic enrichments of the seamounts, which is also true for He isotopes (Table 3.1).

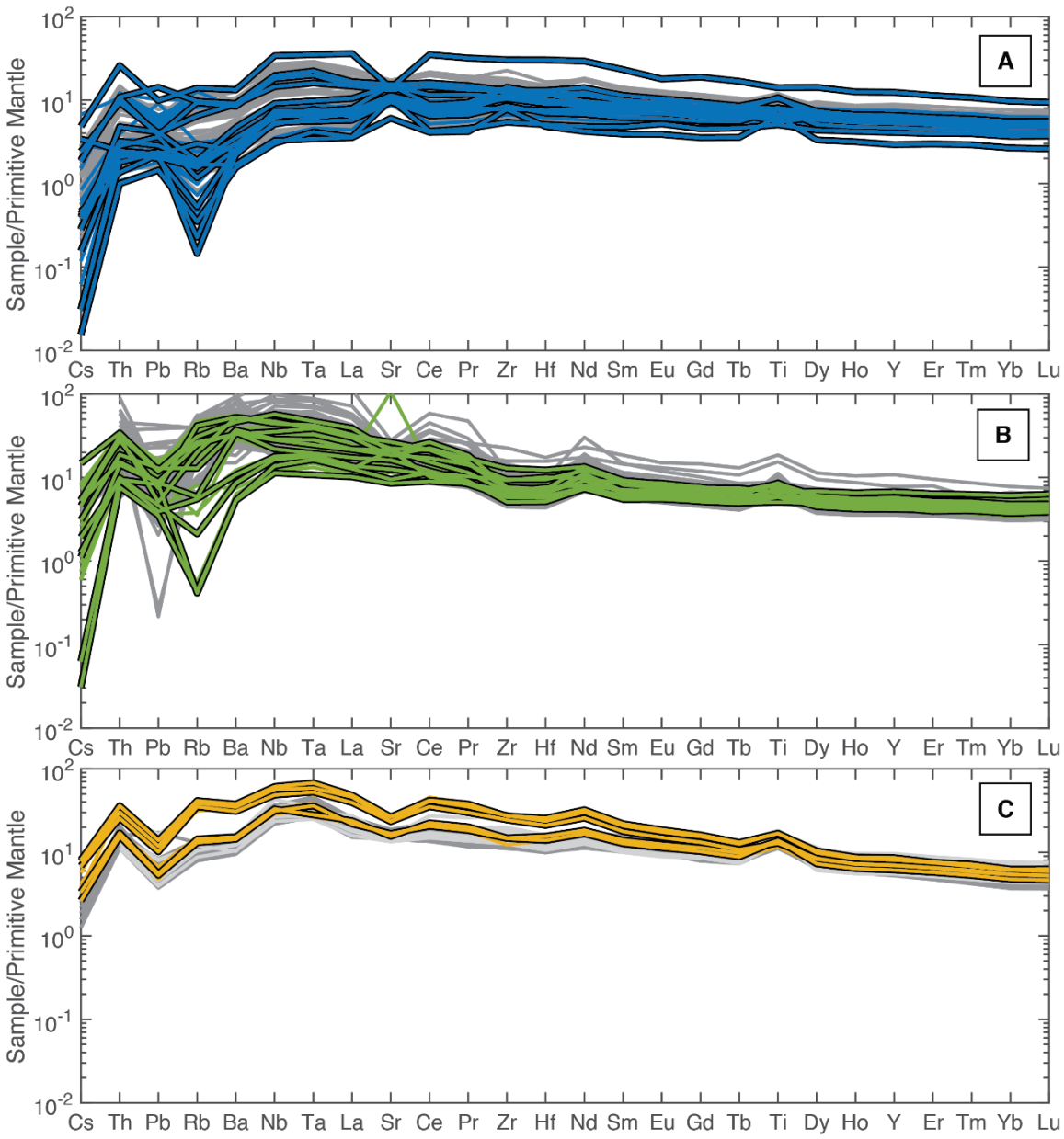

Figure 3.5. Spider diagrams showing trace element variability for each seamount region compared to representative data from each nearby island (A) Santiago; B) Floreana; C) Fernandina). Trace elements are ordered from most incompatible to least incompatible based on bulk partition coefficients for a basaltic melt from a peridotite (57% ol, 13% clinopyroxene 28% low calcium pyroxene and 2% spinel). Partition coefficients for each mineral are averages of all values for each mineral from the GERM database. Colored lines are data from this study. Colored lines outlined in black are those with isotopes analyzed. Grey lines in back are literature data (see Figure 3.3 for references).

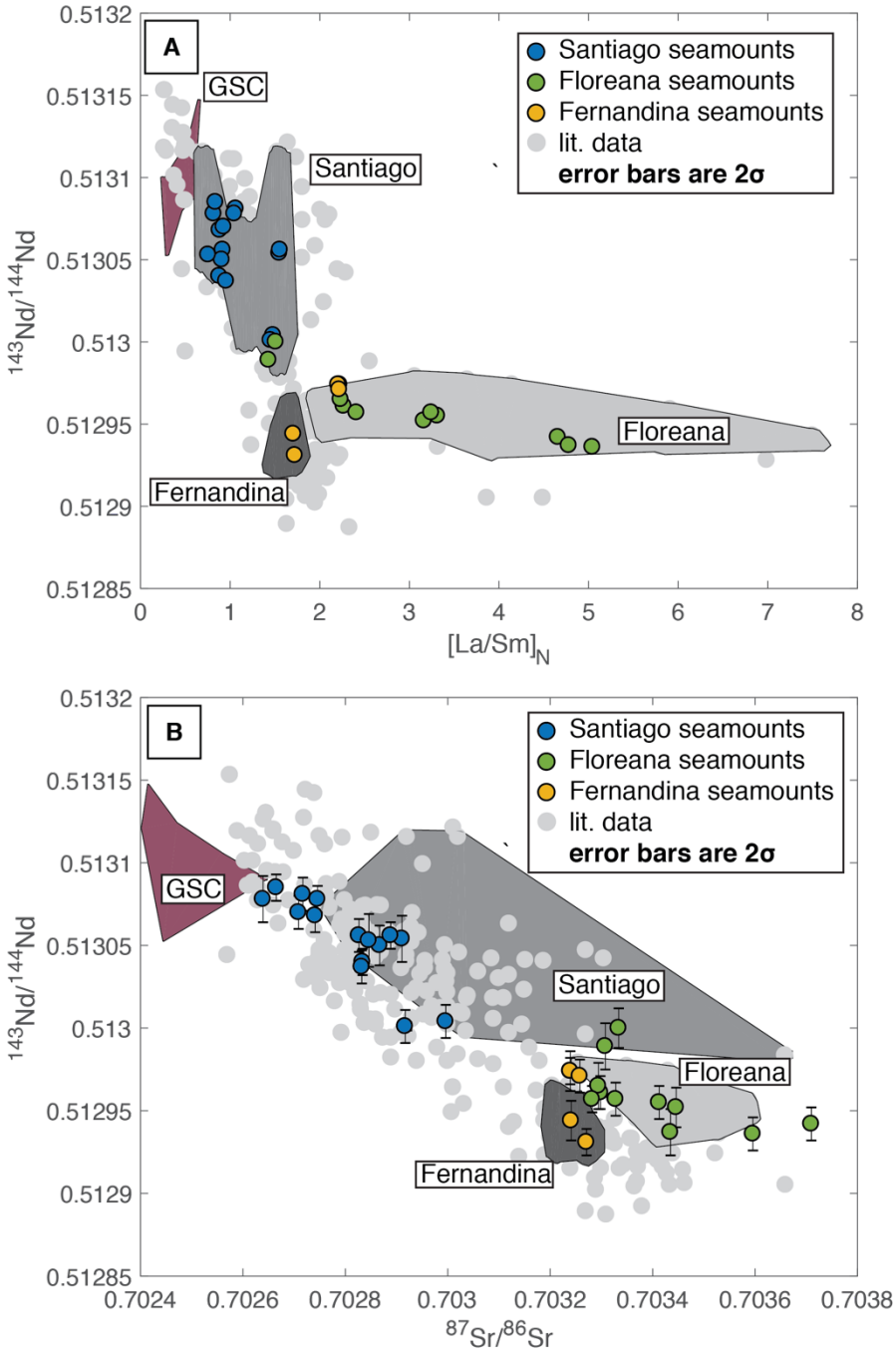

Figure 3.6. Trace element and Isotopic variation of seamounts compared to previously published data. Seamount samples are shown as colored circles. Grey circles show compiled literature data (see Figure 3.3 for references). Variably shaded grey fields have been drawn around literature data for the three islands nearest to the seamounts sampled (light: Floreana, medium: Santiago, dark: Fernandina). Mauve field surrounds data from the GSC, >750 km from the Galápagos hotspot (Gale et al., 2013 and references therein).

Floreana Region

A total of 61 seamounts were identified in the Floreana region (Chapter 1). The seamounts are located on the eastern, northern and western flanks of the island, but predominantly are located on the island's northeastern (Figure 3.2B) and western flanks (Chapter 1). The Floreana seamounts are the largest on average (0.09 km^3) and represent the greatest proportion relative to the subaerial volcano at 23% (seamount volume = 5.7 km^3; Floreana subaerial volume = 26 km^3). Of note, a previously unrecognized prominent NW striking submarine volcanic rift zone emanating from Floreana island is observed in bathymetric maps (Figure 3.2B).

We measured twenty-eight lavas from seven seamounts west of the Island of Floreana. Similar to the Santiago seamounts, lavas from a single seamount are generally more homogenous than the seamount region as a whole ($[La/Sm]_N$= 1.4–4.7 for all seamounts; Figures 3.2 and 3.6; $[La/Sm]_N$ < 5 %RSD for 5 out of 6 seamounts; Table 3.3.1). Volcanic features with greater chemical variability are cones with complicated morphologies (e.g., DR380). Floreana seamount lavas are distinguished from the other seamount compositions by concave up LREE patterns (Figure 3.8). Floreana lavas have the highest $[Rb/La]_N$ and $[Ba/La]_N$ values (max. of 1.4 and 2.0 respectively) of the three regions with coupled $[Nb/La]_N$ enrichments (max. of 1.48). The trace element patterns also exhibit the lowest $[Hf/Nd]_N$ (0.54) and Pb relative to Th ($[Pb/Th]_N$= 0.36-0.86). All lavas form a linear, albeit scattered array in Nd-Sr isotope space (Figure 3.6). Floreana lavas are characterized by the most extreme radiogenic Sr compositions (e.g., max. $^{87}Sr/^{86}Sr$ = 0.702639, with intermediate $^{143}Nd/^{144}Nd$ (0.512936-0.513000; Figure 3.6B).

Similar to Santiago, there are no clear trends in major and trace element data with seamount morphology or geography.

Like the lavas previously analyzed on Floreana Island, seamount lavas show unsystematic isotopic and trace element enrichment patterns (e.g., $[La/Sm]_N$; Figures 3.2 and 3.6; e.g., Harpp et al., 2014b). In general, seamount lavas are similar to lavas that have been erupted on Floreana Island (Figure 3.5). However, two seamounts have isotopic ratios that more closely resemble Santiago/Fernandina lavas than anything else yet observed in the area (DR377, DR382; Figure 3.6). These samples have less radiogenic isotopic signatures and are similar to the most enriched samples at Santiago. These samples still have concave up REE patterns, however, have less pronounced LILE enrichment and higher Hf relative to Nd (Figure 3.5). Floreana samples have intermediate He isotopic ratios between 12.4 and 15.1 R/R_a, which do not directly correlate with other isotopic ratios (Table 3.1).

Fernandina Region

From bathymetric data, eighteen seamounts were identified in the Fernandina region, all of which were mapped on the island's southern flank (Chapter 1). The seamounts have an average volume of 0.06 km^3, which is the smallest of the three regions (Figure 3.3). Correspondingly, the mapped seamounts volume (1.2 km^3) accounts for the lowest absolute volume and lowest percentage of the subaerial island volume of Fernandina (<1%), which is 191 km^3. In total, the seamount volume is on the order of what is estimated for single subaerial eruptions on Fernandina (1-2 km^3; Simkin and Howard; 1970). Seamounts are either conical (e.g., DR383 and DR387), are elongate ridges oriented radially about Fernandina (e.g., DR386), or occur as stepped – flat topped

features resembling an off centered stack of coins (e.g., Clague et al., 2000), also oriented N-S toward Fernandina (Figure 3.2C).

We analyzed twenty-two lavas from four seamounts south of Fernandina (Figure 3.2C). Unlike the previously described seamount regions, these lavas form two distinct, but tightly clustered chemical domains (mildly alkalic, DR383, DR387 and tholeiitic DR384-5 and DR386; Figure 3.4). All seamounts from both groups show very little internal variation (%RSD of $[La/Sm]_N$ <2%; Table 3.1). These domains are unique in major elements (Figure 3.4), which correspond to differences in trace element ratios (e.g., high TA samples have higher TE contents; Figure 3.5 and higher $[La/Sm]_N$; Figure 3.6A). Lavas with compositions most similar to those erupted subaerially at Fernandina (tholeiitic) are from the elongate NW-SE trending vents and the NW-SE trending series of flat-topped stepped seamounts (Table 3.1; Figure 3.2). By contrast, the more alkalic lavas were collected from circular, point source seamounts and are chemically similar to two deep-water (~4000 m) lava flows located on the seafloor at the western leading edge of the Galápagos Platform (Anderson et al., 2018; Figure 3.5). Both suites of Fernandina seamount lavas have the most similar $[Rb/La]_N$ values (max $[Rb/La]_N$ = 0.90; Figure 3.5) of the three regions relative to PM and is the only region to have a relative depletion in $[Ba/La]_N$ (max of 0.79). Unlike the other regions, Fernandina seamounts have positive Nb anomalies (max for $[Nb/La]_N$ = 1.44) that are not coupled with LILE enrichment (Figure 3.5). Similar to Floreana, the Fernandina seamount trace element patterns are characterized by depletion in Hf relative to Nd (min. for $[Hf/Nd]_N$ = 0.77; Figure 3.5). Fernandina samples have the lowest $[Pb/Th]_N$ ratios of the three seamount regions (0.30-0.39; Figure 3.5). Isotopically, samples are intermediate in Sr isotopes ($^{87}Sr/^{86}Sr$ =

0.703239-0.703271; Figure 3.6), with the most radiogenic $^{143}Nd/^{144}Nd$ (0.512931; Figure 3.6) and highest Helium isotopic composition of 23 R/Ra (Table 3.1). Notably, lavas show very little variation in Sr isotope ratios, with variation in Nd isotopes, which is different than the other seamount region mixing arrays. Nd isotopes negatively correlate with trace element enrichment, where alkalic samples have more radiogenic isotopic compositions (Figure 3.6A).

Discussion

Formation of the Seamount Fields

Lavas erupted at individual seamounts within the Santiago region have limited major element contents and trace element ratios (e.g., RSD of $[La/Sm]_N$ at 10 of the 11 seamounts < 4%; Table 3.1), suggesting that they are monogenetic (i.e., formed from a single magma batch) and each likely formed from a single or a series of closely timed eruptions. However, based on variability in isotopic ratios (Figure 3.6B) and trace element ratios that are invariant to fractionation for small degrees of crystallization (e.g., $[La/Sm]_N$; Figure 3.6B), it is clear that the Santiago seamount field as a whole must have formed through multiple episodes of volcanism sourced from different magma batches.

Similar to Santiago, seamounts in the Floreana region show much less variability at individual seamounts in comparison to the seamount region as a whole (Table 3.1; Figure 3.2). Thus, we suggest that the Floreana seamounts are also monogenetic in their construction, or at least produced from the same batch of magma, erupted over a short time interval. However, the isotopic and trace element differences between individual Floreana seamounts suggest that they are produced by separate magmatic events with different source compositions (Figure 3.5 and Figure 3.6). Furthermore, seamounts in the

Fernandina region show the least intra-seamount variability of the three regions (RSD of $[La/Sm]_N$ <2%; Table 3.1), again suggesting that the seamounts are monogenentic in their construction. Fernandina seamounts form two clear groups based on geochemistry and morphology (Figure 3.2), including an alkalic and tholeiitic group that could either be formed through source or melting variability.

Combined, the difference between seamount intra- and inter-variability for all three regions suggests that the formation of seamounts on the top of the Galápagos Platform is a part of the long-term growth of the subaerial volcano and not the result of a single magmatic event. The greater volume of seamounts observed in the downstream (Santiago) or periphery (Floreana) of the archipelago (Figure 3.3) either indicate that seamounts are preserved as the islands age or that the emplacement mechanism for the seamounts is favored during later stages of growth of the island forming volcanoes.

Seamount Heterogeneity and Relationship to Surrounding Islands

Although the platform makes up a majority of the submarine volume of the Galápagos Archipelago, our bathymetric data clearly shows that seamounts represent a significant volume relative to the subaerial islands (Table 3.1; Figure 3.3). We have already shown that the seamounts are primarily monogenetic in their construction. At monogenetic volcanic fields, magma is either focused through the central volcano's magmatic plumbing system and then redirected from the central volcanic system via lateral dikes (Walker, 2000; Muirhead et al., 2016), or emplaced through the vertical ascent of magmas that bypass the magmatic plumbing system of the central edifice (e.g., Needham et al., 2011). In the former case, there may be little variability in the compositions of the submarine and subaerial lavas as magmas are mixed within the

shallow system prior to eruption. In the latter case, there may be significant chemical variations among monogenetic volcanoes themselves that may provide insights into the length scale and structural heterogeneity in the mantle or small-scale variations in melting systematics (e.g., LeCorvec et al., 2013; Rasoazanamparany et al., 2015).

In this section we evaluate the origins of the geochemical heterogeneity of each seamount region relative to the islands that they surround. Previous works in the Galápagos show that variations in the degrees of melting (Gibson and Geist 2010; Gibson et al., 2012), reactive melt transport in the mantle (Saal et al., 2007; Peterson et al., 2014; Gibson et al., 2016) and storage within the crust (Geist et al., 1988) result in variable chemical and isotopic signatures across the archipelago (White et al., 1993). Thus, we assess the elemental and isotopic characteristics of each geochemical endmember sampled by the seamounts and discuss the possibilities for their origins specifically related to melting and source.

Santiago Region

The island of Santiago is composed of two geochemical domains, which makes it unique for a Galápagos volcano (Swanson et al., 1974). The island erupts alkalic and isotopically enriched lavas in the west and tholeiitic, isotopically depleted lavas to the east. Partly based on this observation, it has been suggested that the island sits above an abrupt change in lithospheric thickness (Gibson and Geist 2010) that allows for a change in the total extents of melting and, therefore, the chemical composition of erupted lavas (Gibson et al., 2012). Further, the preservation of this signal suggests little lateral transportation of melt and no homogenization in a centralized shallow magma reservoir prior to eruption (Gibson et al., 2012).

Although the Santiago seamount lavas are not the most depleted in the archipelago (e.g., Sinton et al., 2014), several lavas are the most depleted of the seamounts sampled and fall outside the field for the subaerial Santiago, particularly in the extreme depletion of the most highly incompatible trace elements (Figure 3.5) and unradiogenic Sr-Nd isotopes (Figure 3.6). The depleted component in the Galápagos source has been explained by entrainment of depleted upper mantle into the upwelling plume (Geist et al., 1988; White et al., 1993; DUM; Harpp and White, 2001; DGM; Gibson et al., 2012) or as an incompatible trace element depleted component intrinsic to the Galápagos plume (e.g., Hoernle et al., 2000; Werner et al., 2003; Gazel et al., 2018). Since the seamount lavas are more depleted than the island lavas from which these original hypotheses were postulated, we take the opportunity to reevaluate its origin. To do this we compare the seamounts to average global MORB (Gale et al., 2013), and the far-field GSC (>750 km from the Galápagos hotspot; compiled by Gale et al., 2013), which we take to represent the ambient depleted upper mantle (Gale et al., 2013). The Santiago seamount lavas have slightly higher $[La/Sm]_N$ than average MORB and GSC lavas presumably beyond the influence of the Galápagos plume (Figure 3.7). If the seamount lavas are of a primarily MORB or GSC source then the relative $[La/Sm]_N$ enrichment must result from lower extents of melting compared to the GSC lavas. It would then follow that they should be equally enriched in the most highly incompatible trace elements compared to the REEs (e.g., high $[Th/La]_N$). This would produce negative-linear or concave up trace element patterns compared to MORB, which is not observed (Figure 3.7). Instead, the Santiago lavas have concave down highly incompatible trace element patterns and lower $[Th/La]_{N\text{-}MORB}$ (Figure 3.7). In short, the simultaneous

elevation of $[La/Sm]_{N\text{-}MORB}$ and depression of $[Th/La]_{N\text{-}MORB}$ can only occur if the Santiago source is more depleted than the GSC or MORB source. Therefore, we suggest that the depleted component of the Galápagos plume is not the result of entrainment of the ambient upper mantle but is of a source that is more depleted in highly incompatible trace elements than the ambient upper mantle (i.e., a depleted-depleted mantle; DDM) and is intrinsic to the plume itself. This conclusion is consistent with geophysical observations (Villagomez et al., 2014), and numerical models, which suggest limited coupling between plume and ambient mantle (Ito et al., 2014).

Despite the fact that Santiago seamount lavas typify the most depleted of the seamount array they converge towards both the Floreana and Fernandina enriched isotopic endmembers (Figure 3.6). Together these observations indicate mixing between three source endmembers over relatively short spatial scales. However, given that trace element ratios related to enrichment (e.g., high $[La/Sm]_N$) do not directly correlate with isotopic ratios (Figure 3.6A; Table 3.1), the chemical variability likely result from both variations in melting extent and heterogeneity in mantle source. The seamounts generally conform to the broad spatial chemical zonation of the island, where the most alkalic lavas are erupted at the western seamounts and the more tholeiitic lavas erupted in the east (Figure 3.2). Further, many of the seamounts in the east have elongate or linear vents that are oriented towards Santiago and aligned with its subaerial vent structures (Figures 3.2 and 3.3; Swanson et al., 1974; Gibson et al., 2012), suggesting that the seamounts may be an extension of the subaerial magmatic system. Tholeiitic lavas in the eastern seamount province have the same TE patterns as the island tholeiites (Figure 3.5A). Similarly, a detailed investigation of lavas erupted at the two western seamounts (Chapter 2) shows

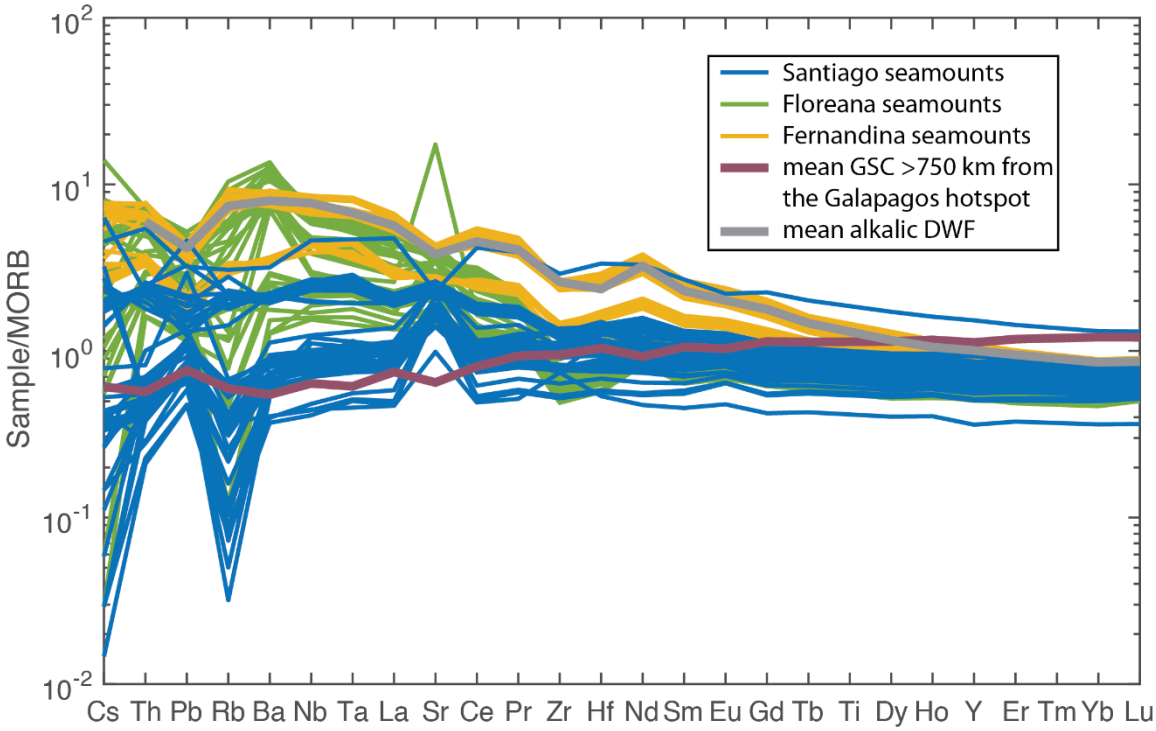

Figure 3.7. Spider diagram showing difference between seamount samples and average MORB (Gale et al., 2013). Solid colored lines show data from this study. Mauve line shows average GSC trace element content for samples located >750 km from the Galápagos Hotspot (Gale et al., 2013). Grey line shows average deep-water lava flow (DWF) sampled *in situ* at the leading edge of the Galápagos platform (Anderson et al., 2018).

they are nearly compositionally identical to a subset of subaerially erupted lavas, suggesting that the magmas were transported laterally from the central magmatic system onto the submarine flanks. Combined, these observations indicate that the seamount lavas in this region likely passed through Santiago's centralized plumbing system prior to being redistributed out towards its flanks onto the seafloor via lateral diking.

Interestingly, Santiago and the nearby satellite islands of Rabida and Pinzon have all erupted lavas, which are much more evolved than what is observed in the Santiago seamount dataset (Swanson et al., 1974). Given the absence of more evolved samples in the seamount suite it is possible that emplacement of seamount lavas may only occur during the early stages of magma storage beneath the island or that they are sourced from

a deeper part of the magmatic plumbing system compared to subaerial eruptions, similar to lavas erupted on the submarine rift of Fernandiana (Geist et al., 2014). Thus, despite not fully bypassing Santiago's magmatic system, the seamounts still provide greater insights into the more extreme chemical and isotopic heterogeneity of magmas prior to further mixing and evolution occurring beneath the island. This would explain the more extreme variations observed in the seamounts than what is preserved on the island.

Floreana Region

There is an unsystematic geographic enrichment pattern of the Floreana lavas erupted both subaerially and submarine (Harpp et al., 2014b). This suggests that there is likely no steady state magma reservoir beneath Floreana, working to centralize or homogenize lavas (Harpp et al., 2014b). In isotopic space, the Floreana seamount lavas generally have the most enriched signatures of all the seamount lavas (Figure 3.6). Despite this, a geochemical evolution from Fernandina-like lavas to what typifies the island today, is suggested by studies of cumulate xenoliths entrained in Floreana lavas (Lyons et al., 2007; Vidito et al., 2013; Harpp et al., 2014b) but have not been directly observed in erupted lavas. The seamounts preserve more heterogeneity than is observed subaerially (Figure 3.6A). In particular, the seamounts have compositions that are isotopically (Figure 3.6B) and geochemically (Figure 3.6A) similar to Fernandina or Santiago. Thus, the seamounts provide complimentary evidence that Floreana lavas have undergone significant source variation during its evolution by tapping a source more similar to the central or eastern islands.

The extreme enriched isotopic endmember expressed in both submarine and subaerial Floreana lavas has been linked to recycling and melting of fluid element

enriched oceanic crust (OC) based on LILE enrichment that is coupled with Sr-Nd-Pb systematics (Harpp et al., 2014b). In general, these observations of subaerial lavas are consistent with characteristics of the seamount lavas (e.g., highest $[Ba/Th]_N$; Figure 3.9; highest $^{87}Sr/^{86}Sr$; Figure 3.6B). Thus, we accept that the enrichment characteristics of the Floreana endmember are likely a product of fluid interaction. However, we speculate on the need for oceanic crust in the Floreana source. When considering only trace element abundances, the most striking difference between the Floreana samples and other seamount regions is their LREE enrichments, with a concave up pattern on REE diagrams (Figure 3.8). This pattern could be due to the melting of OC into the source or shallow melt production outside of the garnet stability field (Harpp et al., 2014b). However, Santiago lavas and MORB lavas (Gale et al., 2013), which have also experienced melting outside the garnet stability field and have similar $[Sm/Yb]_N$ as Floreana lavas, do not have the same concave REE pattern (Figure 3.7). Thus, this pattern is not produced by variations in melting systematics alone (Figure 3.5). Further, melting of a source, which is the enriched product of a melting event such as OC, should produce positive $[Hf/Nd]_N$, which is not observed (Figure 3.9A). Instead, it is likely intrinsic to the Floreana mantle source and either acquired through mixing with a REE enriched reservoir (e.g., CC), or sourced from a mantle component with an exotic lithology (e.g., plagioclase enrichment; Phillpotts and Schnetzler; 1968), a component that has evaded previous depletion in trace elements (e.g., PM), or a component that has been re-enriched in trace elements since depletion. LILE enrichment, coupled with Sr-Nd-Pb systematics are inconsistent with either PM or CC source (Harpp et al., 2014b). Furthermore, mantle melting models of using PM (McDonough and Sun, 1995) and CC (modeled as a 2% melt of the primitive

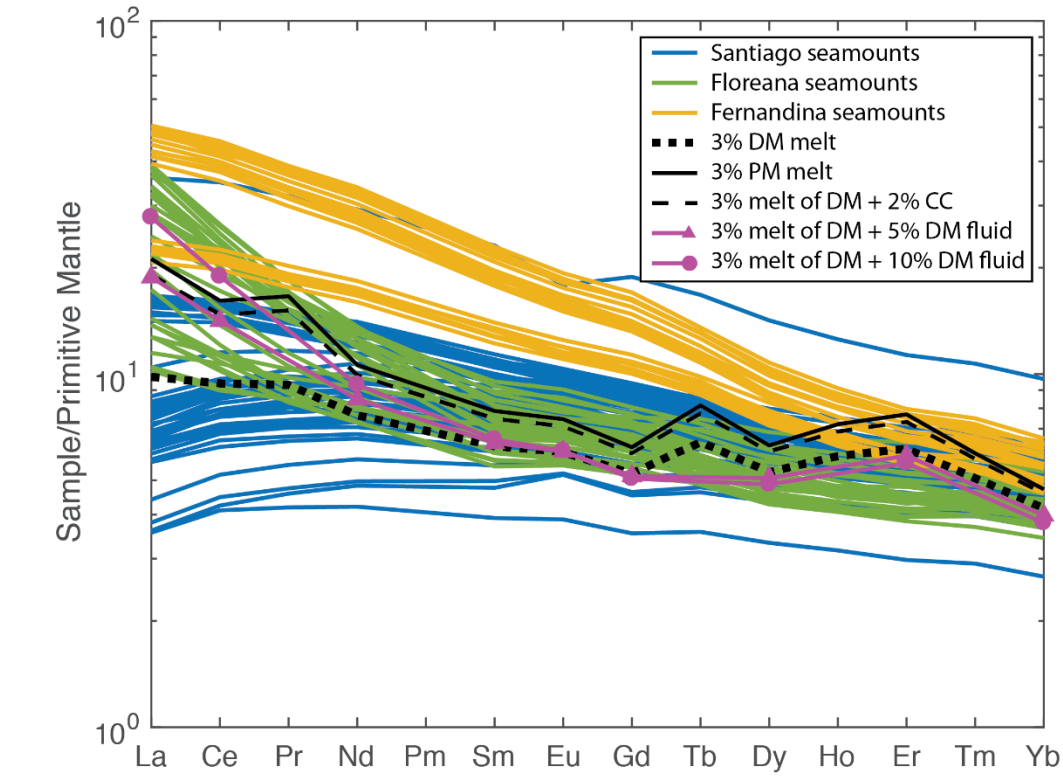

Figure 3.8. Rare Earth element diagram showing variability between seamounts. Solid colored lines show data from this study. Other lines show modeled REE patterns of melts (3% continuous melting with 1% melt retained; Zou, 1998) from various source endmembers. Sources are as follows, thick dotted black line: depleted mantle (DM); solid black line: primitive mantle; dashed black line: DM mixed with 2% continental crust (CC); magenta line with triangle markers: DM with the addition of 5% fluid derived from the same DM composition; magenta line with circle markers: DM with the addition of 10% fluid of the same composition as previous model. Fluid compositions are calculated using partition coefficients for an 800C fluid at 4 Gpa (Kessel et al., 2005).

mantle) fail to produce the extreme La enrichments compared to MREE and HREE abundances (Figure 3.8). Plagioclase is the only common mantle mineral that could impart a positive REE pattern upon melting (Supplementary Table 3.9). However, lack of extreme major (Al_2O_3; Supplementary Figure 3.1) and trace element (Eu) anomalies (Figure 3.8), rules out this lithology as a possible source for the REE patterns.

Given that the Floreana source has elevated LILE elements that have been previously ascribed to effects of dehydration (Harpp et al., 2014b), it is likely that the concave up pattern in REE may be imparted by the same process. Experimental studies show that supercritical fluids strongly partition LREE/HREE (Kessel et al., 2005) and the degree of partitioning increases non-linearly as an inverse function of atomic number. Therefore, the addition of hot (>300C) fluids from a previously depleted source can impart a concave up trace element pattern (Gammons et al., 1996). Metasomatic fluids are also expected to partition REE to HFSE ($[Hf/Nd]_N$; e.g., Keppler, 1996; Kessel et al., 2005), which would normally have similar incompatibilities in magmas (Figure 3.9A). To determine the extent of metasomatism required to produce the observed trace element patterns, we model the mixing of a 3% DM melt (using average partition coefficients from GERM database; Supplementary Data Table 3.9) with a fluid derived from the same DM composition, using partition coefficients from Kessel et al. (2005). The DM composition is derived from PM (McDonough and Sun, 1995) as the residue of 2% continuous melt extraction (1% retained; Zou, 1998). Coupled LREE/HREE and LREE/HFS indicates that <5% addition of this metasomatic fluid can produce the observed enrichment exemplified by the Floreana endmember (Figures 3.8 and 3.9).

While the majority of the lavas fall within the range of known subaerial Floreana lavas, several have compositions that lie outside of this field and are closer in composition to Santiago or Fernandina lavas (Figure 3.6A). Non-linear isotopic mixing trends in the Floreana seamount dataset (Figure 3.6B) suggest that the Floreana lavas require at least three sources (two depleted sources and an enriched component typified by the Floreana seamounts themselves).

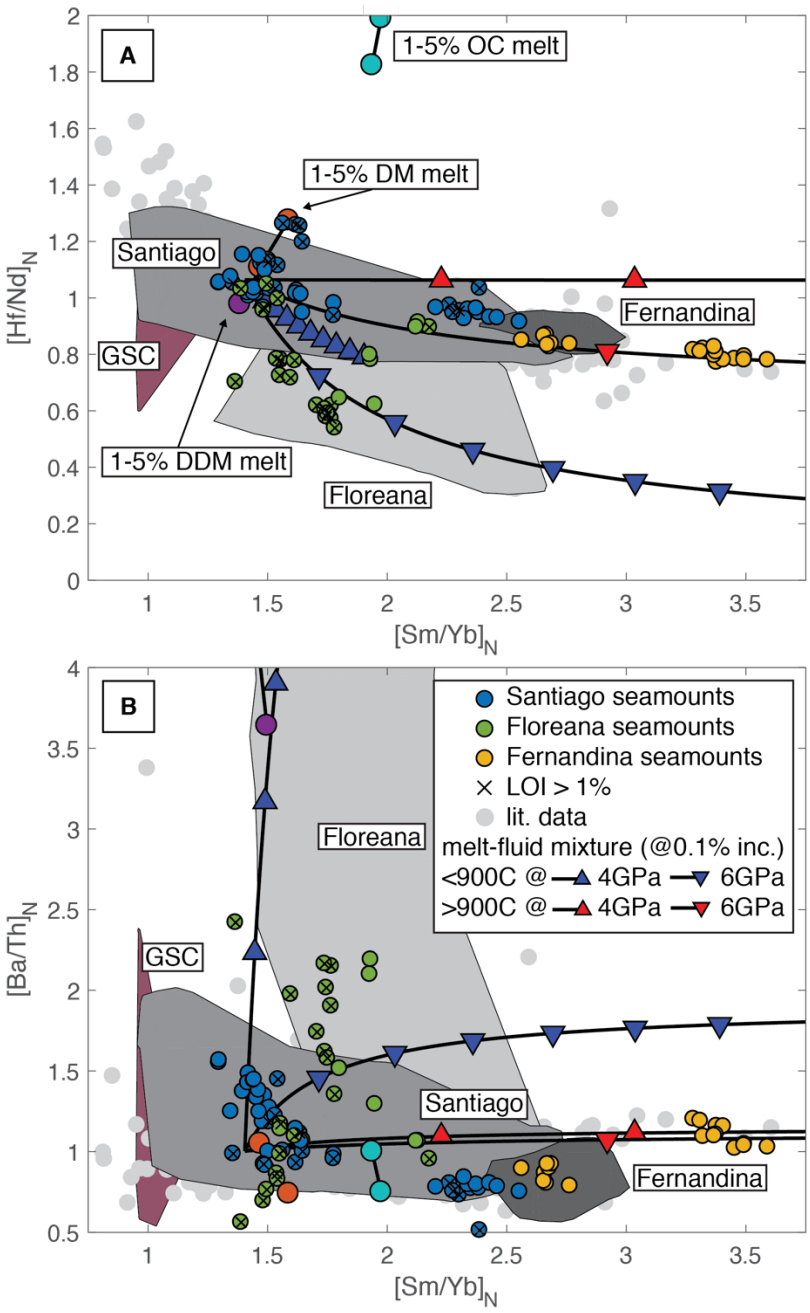

Figure 3.9. Variations in REE and fluid mobile/immobile ratios. Symbology of data the same as Figure 3. Barbell symbols bracket 1-5% melting of various source compositions to indicate the direction of magmatic trace element fractionation, particularly on the y-axis. Lines connected with triangles are modeled mixtures between a magma and metasomatic fluid. The metasomatic fluid is modeled using the experimentally derived partition coefficients of Kessel et al. (2005) at various P-T conditions (see legend) from modeled OC trace element composition (3% continuous melt of DM; Zou, 1998). Triangles indicate 0.1% mixing increments.

Fernandina Region

Fernandina erupts the most monotonic tholeiitic lavas in the archipelago (Saal et al., 2007; Geist et al., 2014). The tholeiitic seamount lavas have major (Figure 3.4), trace element and isotopic compositions that closely resemble subaerially erupted Fernandina lavas (Figure 3.5 and Figure 3.6). By contrast, the alkalic lavas have higher trace element abundances (Figure 3.5) and more steeply sloped PM normalized trace element and REE patters than the tholeiitic lavas from the region (Figure 8). Additionally, the alkalic seamount lavas have slightly more radiogenic Nd isotopic compositions for a given Sr isotopic compositions (Figure 3.6B).

As opposed to Floreana, radiogenic isotope enrichment of the Fernandina lavas is not accompanied by an extreme enrichment of LILEs (Figure 3.9). Thus, the Fernandina source is not likely a product of metasomatic enrichment. Fernandina seamount lavas have the highest $^{3}He/^{4}He$ (up to 23.4 R/Ra; Table 3.1), and are characterized by intermediate isotopic compositions, and positive highly incompatible HFSE anomalies (Figure 3.5). These characteristics are observed globally in ocean islands (Jackson et al., 2008) and have been attributed to melting of an eclogitic mantle component formed from recycling of OC that experienced melt extraction in the rutile stability field during subduction (referred to as the TITAN reservoir; Jackson et al., 2008). The HFS elements Nb, Ta and Ti are all compatible in rutile. Thus, melting in the presence of rutile will lead to a magma that is depleted in the HFS elements and a complementary residue enriched in these elements. If the residue is then melted, outside of the stability field for rutile, then this HFS enrichment will be imparted onto the new melt.

High He isotope ratios in the TITAN component is attributed to a sequestered undegassed portion of depleted upper mantle (Jackson et al., 2008). Although not intrinsically related, the primitive He and HFSE enrichment are linked due to melting systematics at the leading edge of plumes, where hydrated eclogite is the most fusible so imparts its trace element and isotopic signature, while the more depleted components simultaneously degas He, imparting this signature (Jackson et al., 2008; Villagomez et al., 2014). If this is the case, the maximum observed Helium isotopic ratios of ~23 R/Ra (Table 3.1) reflect the values for an undegassed depleted mantle component that has been isolated for 1-2 Ga (Jackson et al., 2008). Although the source of the Fernandina lava signature has been historically ascribed to be a PM component (Geist et al., 1988; White et al., 1993; Hart et al., 1992; Harpp and White, 2001), the depletion of highest incompatibility trace elements (Cs, Ba) is more consistent with a previously depleted origin. Thus, we prefer a recycled origin for the Fernandina endmember source.

Variations in geochemistry and isotopic composition between the two seamount groups (alkalic and tholeiitic) are either due to dilution of the Fernandina source with other source compositions or resultant from variable extents of melting or both. Alkalic lavas have higher $[La/Sm]_N$ (Table 3.1) which is consistent with their being formed from lower degrees of melting of a similar mantle source compared to the tholeiitic magmas. These lavas have more radiogenic Nd isotopic compositions (i.e., highly incompatible trace element depleted; Figure 3.6A), which is the opposite of what is expected if the alkalic lavas are low degree melts from the most fusible (i.e., time integrated trace element enriched) source. Variations in isotopic composition would typically be interpreted to represent variations in source (e.g., Hart et al., 1992). However, the

enrichments in Nd isotopic are not coupled with variations in Sr isotopes, which have parent and daughter isotopes which are expected to be fractionated similarly for both magmatic and fluid related processes (e.g., Kessel et al., 2005). Combined, these observations suggest that source variation does not likely contribute to the Nd isotopic variation at all. This leads us to seek another explanation for the isotopic variation between the alkalic and tholeiitic lavas. The trace element enrichment of the alkalic lavas is accompanied by extreme enrichments in middle to heavy REEs (e.g., high $[Sm/Yb]_N$; Figure 3.9). This enrichment is predicted for melts originating in the garnet stability field, due to the relative compatibility of HREEs compared to MREEs in garnet (Supplementary Data Table 3.9). These enrichments are observed elsewhere in the Galápagos (White et al., 1993). Given this REE compatibility, garnet would also favor Sm over Nd, which would result in more radiogenic Nd values in garnet integrated over long timescales. However, due to the inverse relationship between compatibility and enrichment during partial melting, garnet preferably releases Nd relative to Sm into a melt, which leads to the more highly radiogenic "garnet Nd" (i.e., apparent depleted) signatures of the alkalic lavas (Figure 3.6A). This is further evidence that garnet is in fact in the source region of some, if not all Galápagos lavas and that lithology and degree of melting at least partially controls the isotopic composition of samples in the absence of chemical or isotopic source variations. In the case of the Fernandina source perhaps this signal is intensified owing to its apparently eclogitic origins further supporting the TITAN source hypothesis.

The seamount alkalic lavas are identical to alkalic deep water lava flows (DWFs), sampled *in situ* on the seafloor at the leading edge of the Galápagos platform (Figure 3.7;

Anderson et al., 2018). The DWF alkalic lavas form primarily through lower degree partial melting of a Fernandina mantle source compared to the tholeiitic lavas (Anderson et al., 2018). Given that the alkalic seamounts have similar trace element concentrations and patterns, we conclude that a majority of the chemical variations between the alkalic and tholeiitic lavas erupted on the submarine flanks of Fernandina is likely derived from the same magmatic process. One characteristic of subaerial Fernandina is the presence of numerous radial vents surrounding the central caldera (e.g., Chadwick and Howard, 1991). The seamount tholeiitic lavas are all erupted from N-S oriented vents similar to the subaerial vents. The similarity in orientation and chemistry of the submarine and subaerial vents suggests that the seamounts are the submarine extension of the same volcanic plumbing system. Thus, we interpret that all the tholeiitic lavas are sourced from the same centralized magma chamber. The alkalic seamounts on the other hand, are conical, point source volcanic features. Further, there are no known subaerial alkalic lavas erupted on Fernandina. Combined, this suggests that the alkalic magmas bypass Fernandnina's present day shallow magma reservoir, similar to the petrogenesis of the alkalic DWFs (Anderson et al., 2018).

Implications of Seamount Heterogeneity on the Interpretation of Ocean Island Evolution and Mantle Zonation in the Galápagos

On the whole, we have shown that almost all individual seamounts are chemically homogeneous, especially when compared to the overall variation in chemistry between seamounts within any given region (Figure 3.2; Table 3.1). This similarity in composition suggests that most seamounts are monogenetic and erupted during the same magmatic event or under similar magmatic conditions (Smith and Nemeth, 2017). Variations in

major, trace element and particularly isotopic ratios between seamounts in each region result from magmas produced from slightly different mixtures of the same sources and variations in extents of melting. This suggests that seamounts are generally generated from discreet magmatic events, but the geochemical fields are generated from multiple events in all three regions. Some seamounts have lavas that appear to directly relate to subaerially erupted lavas, particularly in Santiago (Chapter 2), and tholeiitic lavas around Fernandina (Figure 3.3). Nevertheless, there is clearly more chemical diversity erupted at the seamounts compared to the islands, suggesting that some seamount lavas bypass mixing in the main magmatic system or that the seamounts preserve more discrete magmatic events than are observed on the islands. This suggests that seamounts can provide a wider window into mantle processes compared to the islands themselves.

It is commonly thought that the Galápagos archipelago does not undergo the same evolutionary sequence that is predicted by plume theory (e.g., Harpp and Geist, 2018). However, the observation of alkalic lava flows at the leading edge of the submarine platform provides some evidence that there may be a pre-shield building phase (Anderson et al., 2018). More alkalic lavas, which are not accounted for by source variation alone at both Fernandina and Santiago. The presence of alkalic lavas high up in the volcanic stratigraphy in Fernandina is strong evidence that the Galápagos does produce low degree melts at its leading edge. The lack of an obvious progression on the southern edge of the archipelago may indicate that degree of melting is more strongly controlled by mantle fertility, as was suggested by Harpp et al., (2014).

In the Galápagos, the monogenetic seamounts generally have geochemical characteristics similar to those of the islands that they surround (Figures 3.5 and 3.6).

However, some Santiago and Floreana seamounts are geochemically distinct, with less radiogenic (i.e., trace element depleted) signatures compared to the island lavas (Figure 3.6). For the Santiago and Floreana regions, mixing must occur between multiple endmembers to produce the spread in isotopic data (Figure 3.6B). The geochemical and isotopic data are consistent with mixing of three sources originating from a very depleted component (DDM), a component of oceanic crust, and a component sourced from metasomatized mantle. These endmembers are most strongly represented at Santiago, Fernandina and Floreana, respectively. However, within a given seamount region mixing between these endmembers has no spatial coherency (Figure 3.3). Further, all endmembers are potentially being sampled in a single seamount region (e.g., Santiago; Figure 3.6B).

Together the above observations do not support the idea a gradational zonation of the Galápagos source. In order to tap these heterogeneities in such close proximity, the length scales of the isotopic domains in the mantle must be shorter (<1 km based on seamount spacing; e.g., Gibson et al., 2012) than is suggested by some models (>100 km zones e.g., Hoernle et al., 2000). Further, a recycling origin of all endmember composition does not support models of progressive depletion by entrainment of upper mantle (e.g., Geist et al., 1988). As an alternative to large geochemical zonation in the mantle, it is possible that consistent broad patterns of geochemical heterogeneity can be brought about through melting processes and relatively consistent homogenization (e.g., Jones et al., 2017).

Despite the expanded variability of the seamount dataset, the evolution from purely Fernandina like compositions to those of Floreana or Santiago to Fernandina is not

observed. This either indicates that this endmember evolution does not occur, or that despite increasing sampling resolution, repaving efficiently erases early evolutionary history of the subaerial and submarine portion of ocean islands. Perhaps the odds of preservation of all stages of a volcano's history are vanishingly small compared to mainstage volcanic phases at each of the islands. Moreover, lower relative volumes of seamounts at the leading edge of the plume (Fernandina 1% seamounts relative to subaerial volume) relative to the periphery suggest that the mechanism for seamount creation may not be favored in the early in the evolutionary history of an island but favored later in its development (Santiago 6% seamounts relative to subaerial volume) or on the archipelago's periphery (Floreana; 23% seamounts relative to subaerial volume). This may exacerbate the lack of preservation of early stages of growth. Thus, in order to fully evaluate geochemical evolution outside of main stage volcanism at ocean islands, high sampling resolution is always likely a requirement.

Acknowledgements

Thanks to the crew of the M/V *Alucia* for skilled data and sample collection, and the Dalio Foundation for supporting the data and sample collection effort. We also thank the science party on the M/V *Alucia* cruise including Dan Fornari and Meghan Jones who assisted with data collection and post cruise data processing. We acknowledge the Dalio Foundation and the Ocean Exploration Trust for use of their assets as well as partial funding for post cruise research. We thank the Darwin Foundation for Facilitating research in the Galápagos and the Galápagos National Park and Ecuadorean Navy (INOCAR) for permission to operate in marine protected waters. We appreciate Josh Curtice for his analytical expertise in the He isotope lab at Woods Hole Oceanographic

Institute, and the technical staff at the Peter Hooper Geoanalytical Facility at Washington State University for their assistance with the XRF analyses and data reduction. We thank Marion Lytle for her assistance in collecting trace element data at the Boise State Geoanalytical facility. Finally, this work could not have been completed if it were not for the help of Emma McCully, Hannah Bercovici and Cecelia Wheeler for their assistance in sample preparation for various geochemical analyses. This work was carried out with funding from NSF (OCE-1634952 to VDW, OCE-1634685 to SAS).

References

Abouchami, W., Hofmann, A.W., Galer, S.J.G., Frey, F.A., Eisele, J., Feigenson, M., 2005. Lead isotopes reveal bilateral asymmetry and vertical continuity in the Hawaiian mantle plume. Nature 434, 851.

Allan, J.F., Simkin, T., 2000. Fernandina Volcano's evolved, well-mixed basalts: Mineralogical and petrological constraints on the nature of the Galápagos plume. J. Geophys. Res. 105, 6017.

Anderson, M., Wanless, V.D., Schwartz, D.M., McCully, E., Fornari, D.J., Jones, M.R., Soule, S.A., 2018. Submarine Deep-Water Lava Flows at the Base of the Western Galápagos Platform. Geochemistry, Geophys. Geosystems 19, 3945–3961.

Argus, D.F., Gordon, R.G., Heflin, M.B., Ma, C., Eanes, R.J., Willis, P., Peltier, W.R. and Owen, S.E., 2010. The angular velocities of the plates and the velocity of Earth's centre from space geodesy. Geophysical Journal International, 180, 913-960.

Bianco, T.A., Ito, G., van Hunen, J., Ballmer, M.D., Mahoney, J.J., 2008. Geochemical variation at the Hawaiian hot spot caused by upper mantle dynamics and melting of a heterogeneous plume. Geochemistry, Geophys. geosystems 9.

Bianco, T.A., Ito, G., van Hunen, J., Ballmer, M.D., Mahoney, J.J., 2011. Geochemical variations at intraplate hot spots caused by variable melting of a veined mantle plume. Geochemistry, Geophys. Geosystems 12.

Brenna, M., Cronin, S.J., Nemeth, K., Smith, I.E.M., Sohn, Y.K., 2011. The influence of magma plumbing complexity on monogenetic eruptions, Jeju Island, Korea. Terra Nov. 23, 70–75.

Carey, B.S., Fisher, C.R., Leon, P.S. De, Roman, C., Raineault, N.A., Suarez, J., Smart, C., Kane, R., Tüzün, S., Balcanoff, J., Lubetkin, M., Jones, M., Schwartz, D., Fornari, D., Soule, A., Wanless, D., Watling, L., Ballard, R.D., 2016. Exploring the Undersea World of the Galápagos Islands Exploring the Undersea World of the Galápagos Islands 32–34.

Castillo, P., 1988. The Dupal anomaly as a trace of the upwelling lower mantle. Nature 336, 667.

Chadwick, W.W., Howard, K.A., 1991. The pattern of circumferential and radial eruptive fissures on the volcanoes of Fernandina and Isabela islands, Galápagos. Bull. Volcanol. 53, 259–275.

Christie, D.M., Duncan, R.A., McBirney, A.R., Richards, M.A., White, W.M., Harpp, K.S., Fox, C.G., 1992. Drowned islands downstream from the Galápagos hotspot imply extended speciation times. Nature 355, 246–248.

Clague, D.A., Moore, J.G., Reynolds, J.R., 2000. Formation of submarine flat-topped volcanic cones in Hawai'i. Bull. Volcanol. 62, 214–233.

Courtillot, V., Davaille, A., Besse, J., Stock, J., 2003. Three distinct types of hotspots in the Earth's mantle. Earth Planet. Sci. Lett. 205, 295–308.

Feighner, M.A., Richards, M.A., 1994. Lithospheric structure and compensation mechanisms of the Galápagos Archipelago. J. Geophys. Res. 99, 6711–6729.

Fisher, C.M., McFarlane, C.R.M., Hanchar, J.M., Schmitz, M.D., Sylvester, P.J., Lam, R., Longerich, H.P., 2011. Sm–Nd isotope systematics by laser ablation-multicollector-inductively coupled plasma mass spectrometry: Methods and potential natural and synthetic reference materials. Chem. Geol. 284, 1–20.

Gale, A., Dalton, C.A., Langmuir, C.H., Su, Y., Schilling, J., 2013. The mean composition of ocean ridge basalts. Geochemistry, Geophys. Geosystems 14, 489–518.

Gazel, E., Trela, J., Bizimis, M., Sobolev, A., Batanova, V., Class, C., Jicha, B., 2018. Long-Lived Source Heterogeneities in the Galápagos Mantle Plume. Geochemistry, Geophys. Geosystems 19, 2764–2779.

Geist, D., Snell, H., Snell, H., Goddard, C., Kurz, M.D., 2014. A paleogeographic model of the Galápagos Islands and biogeographical and evolutionary implications. Galápagos a Nat. Lab. Earth Sci. Am. Geophys. Union, Washingt. DC, USA 145–166.

Geist, D.J., Bergantz, G., Chadwick, W.W., 2014. Galápagos Magma Chambers. In: Karen S. Harpp, Eric Mittelstaedt, Noémi d'Ozouville, and D.W.G. (Ed.), The Galápagos: A Natural Laboratory for the Earth Sciences, Geophysical Monograph 204. John Wiley & Sons, Inc., pp. 55–70.

Geist, D.J., Fornari, D.J., Kurz, M.D., Harpp, K.S., Adam Soule, S., Perfit, M.R., Koleszar, A.M., 2006. Submarine Fernandina: Magmatism at the leading edge of the Galápagos hot spot. Geochemistry, Geophys. Geosystems 7.

Geist, D.J., White, W.M., McBirney, A.R., 1988. Plume-asthenosphere mixing beneath the Galápagos archipelago. Nature 333, 657–660.

Geist, D., Diefenbach, B.A., Fornari, D.J., Kurz, M.D., Harpp, K., Blusztajn, J., 2008. Construction of the Galápagos platform by large submarine volcanic terraces. Geochemistry, Geophys. Geosystems 9.

Gibson, S. a., Geist, D.G., Day, J. a., Dale, C.W., 2012. Short wavelength heterogeneity in the Galápagos plume: Evidence from compositionally diverse basalts on Isla Santiago. Geochemistry Geophys. Geosystems 13, Q09007.

Gibson, S. a., Geist, D., 2010. Geochemical and geophysical estimates of lithospheric thickness variation beneath Galápagos. Earth Planet. Sci. Lett. 300, 275–286.

Gibson, S.A., Dale, C.W., Geist, D.J., Day, J.A., Brügmann, G., Harpp, K.S., 2016. The influence of melt flux and crustal processing on Re–Os isotope systematics of ocean island basalts: Constraints from Galápagos. Earth Planet. Sci. Lett. 449, 345–359.

Graham, D.W., Christie, D.M., Harpp, K.S., Lupton, J.E., 1993. Mantle plume helium in submarine basalts from the Galápagos platform. Science (80-.). 262, 2023–2026.

Harpp, K., Fornari, D., Geist, D.J., Kurz, M.D., 2014b. The geology and geochemistry of Isla Floreana, Galápagos: a different type of late stage ocean island volcanism. Galápagos Nat. Lab. Earth Sci. AGU Monogr 204, 71–118.

Harpp, K.S., Fornari, D.J., Geist, D.J., Kurz, M.D., 2003. Genovesa Submarine Ridge: A manifestation of plume-ridge interaction in the northern Galápagos Islands. Geochemistry, Geophys. Geosystems 4.

Harpp, K.S., Geist, D.J., 2018. The Evolution of Galápagos Volcanoes: An Alternative Perspective. Front. Earth Sci. 6, 50.

Harpp, K.S., Hall, P.S., Jackson, M.G., 2014a. Galápagos and Easter: A tale of two hotspots. Galápagos A Nat Lab Earth Sci 204, 27–40.

Harpp, K.S., White, W.M., 2001. Tracing a mantle plume: Isotopic and trace element variations of Galápagos seamounts. Geochemistry, Geophys. Geosystems 2.

Harpp, K., Geist, D., 2002. Wolf–Darwin lineament and plume–ridge interaction in northern Galápagos. Geochemistry, Geophys. Geosystems 3, 1–19.

Hart, S.R., Hauri, E.H., Oschmann, L.A., Whitehead, J.A., 1992. Mantle plumes and entrainment: isotopic evidence. Science (80-.). 256, 517–520.

Hauff, F., Hoernle, K., Tilton, G., Graham, D.W., Kerr, A.C., 2000. Large volume recycling of oceanic lithosphere over short time scales: geochemical constraints from the Caribbean Large Igneous Province. Earth Planet. Sci. Lett. 174, 247–263.

Hoernle, K., Werner, R., Morgan, J.P., Garbe-Schönberg, D., Bryce, J., Mrazek, J., 2000. Existence of complex spatial zonation in the Galápagos plume. Geology 28, 435–438.

Hoernle, K., Rohde, J., Hauff, F., Garbe-Schönberg, D., Homrighausen, S., Werner, R., Morgan, J.P., 2015. How and when plume zonation appeared during the 132 Myr evolution of the Tristan Hotspot. Nat. Commun. 6, 7799.

Hofmann, A.W., 1997. Mantle geochemistry: the message from oceanic volcanism. Nature 385, 219.

Hooft, E.E.E., Toomey, D.R., Solomon, S.C., 2003. Anomalously thin transition zone beneath the Galápagos hotspot. Earth Planet. Sci. Lett. 216, 55–64.

Ito, G., Bianco, T., 2014. Patterns in Galápagos magmatism arising from the upper mantle dynamics of plume-ridge interaction. Wiley Online Library.

Jackson, M.G., Hart, S.R., Saal, A.E., Shimizu, N., Kurz, M.D., Blusztajn, J.S., Skovgaard, A.C., 2008. Globally elevated titanium, tantalum, and niobium (TITAN) in ocean island basalts with high 3He/4He. Geochemistry, Geophys. Geosystems 9.

Jochum, K.P., Weis, U., Schwager, B., Stoll, B., Wilson, S.A., Haug, G.H., Andreae, M.O., Enzweiler, J., 2016. Reference values following ISO guidelines for frequently requested rock reference materials. Geostand. Geoanalytical Res. 40, 333–350.

Johnson, D.M., Hooper, P.R., Conrey, R.M., 1999. XRF analysis of rocks and minerals for major and trace elements on a single low dilution Li-tetraborate fused bead. Adv. X-ray Anal. 41, 843–867.

Jones, T.D., Davies, D.R., Campbell, I.H., Wilson, C.R., Kramer, S.C., 2016. Do mantle plumes preserve the heterogeneous structure of their deep-mantle source? Earth Planet. Sci. Lett. 434, 10–17.

Jones, T.D., Davies, D.R., Campbell, I.H., Iaffaldano, G., Yaxley, G., Kramer, S.C. and Wilson, C.R., 2017. The concurrent emergence and causes of double volcanic hotspot tracks on the Pacific plate. Nature, 545, 472.

Kelley, K.A., Plank, T., Ludden, J., Staudigel, H., 2003. Composition of altered oceanic crust at ODP Sites 801 and 1149. Geochemistry, Geophys. Geosystems 4.

Kessel, R., Schmidt, M.W., Ulmer, P., Pettke, T., 2005. Trace element signature of subduction-zone fluids, melts and supercritical liquids at 120–180 km depth. Nature 437, 724.

Korkisch, J., Worsfold, P.J., 1990. Handbook of ion exchange resins: their application to inorganic analytical chemistry: Volume 1, CRC Press, Boca Raton, FL, 1989 (ISBN 0-8493-3191-9). 301 pp. Price£ 100.50.

Kurz, G.A., Schmitz, M.D., Northrup, C.J., Vallier, T.L., 2017. Isotopic compositions of intrusive rocks from the Wallowa and Olds Ferry arc terranes of northeastern Oregon and western Idaho: Implications for Cordilleran evolution, lithospheric structure, and Miocene magmatism. Lithosphere 9, 235–264.

Kurz, M.D., 1986b. Cosmogenic helium in a terrestrial igneous rock. Nature 320, 435.

Kurz, M.D., 1986a. *in situ* production of terrestrial cosmogenic helium and some applications to geochronology. Geochim. Cosmochim. Acta 50, 2855–2862.

Kurz, M.D., Curtice, J., Fornari, D., Geist, D., Moreira, M., 2009. Primitive neon from the center of the Galápagos hotspot. Earth Planet. Sci. Lett. 286, 23–34.

Kurz, M.D., Geist, D., 1999. Dynamics of the Galápagos hotspot from helium isotope geochemistry. Geochim. Cosmochim. Acta 63, 4139–4156.

Kurz, M.D., Kenna, T.C., Lassiter, J.C., DePaolo, D.J., 1996. Helium isotopic evolution of Mauna Kea Volcano: First results from the 1-km drill core. J. Geophys. Res. Solid Earth 101, 11781–11791.

Le Corvec, N., Menand, T., Lindsay, J., 2013. Interaction of ascending magma with pre-existing crustal fractures in monogenetic basaltic volcanism: an experimental approach. J. Geophys. Res. Solid Earth 118, 968–984.

Lyons, J., Geist, D., Harpp, K., Diefenbach, B., Olin, P., Vervoort, J., 2007. Crustal growth by magmatic overplating in the Galápagos. Geology 35, 511–514.

Lytle, M.L., Kelley, K.A., Hauri, E.H., Gill, J.B., Papia, D., Arculus, R.J., 2012. Tracing mantle sources and Samoan influence in the northwestern Lau back-arc basin. Geochemistry, Geophys. Geosystems 13.

Mazza, S.E., Gazel, E., Bizimis, M., Moucha, R., Béguelin, P., Johnson, E.A., McAleer, R.J. and Sobolev, A.V., 2019. Sampling the volatile-rich transition zone beneath Bermuda. Nature, 569, 398.

McBirney, A.R., Williams, H., 1969. Geology and petrology of the Galápagos Islands. Geol. Soc. Am. Mem. 118, 1–197.

McDonough, W.F., Sun, S.-S., 1995. The composition of the Earth. Chem. Geol. 120, 223–253.

Mittelstaedt, E., Soule, S., Harpp, K., Fornari, D., McKee, C., Tivey, M., Geist, D., Kurz, M.D., Sinton, C., Mello, C., 2012. Multiple expressions of plume-ridge interaction in the Galápagos: Volcanic lineaments and ridge jumps. Geochemistry Geophys. Geosystems 13, Q05018.

Muirhead, J.D., Van Eaton, A.R., Re, G., White, J.D.L., Ort, M.H., 2016. Monogenetic volcanoes fed by interconnected dikes and sills in the Hopi Buttes volcanic field, Navajo Nation, USA. Bull. Volcanol. 78, 11.

Needham, A.J., Lindsay, J.M., Smith, I.E.M., Augustinus, P. and Shane, P.A., 2011. Sequential eruption of alkaline and sub-alkaline magmas from a small monogenetic volcano in the Auckland Volcanic Field, New Zealand. Journal of Volcanology and Geothermal Research, 201, 126-142.

Nobre Silva, I.G., Weis, D., Barling, J. and Scoates, J.S., 2009. Leaching systematics and matrix elimination for the determination of high-precision Pb isotope compositions of ocean island basalts. Geochemistry, Geophysics, Geosystems, 10.

Peterson, M.E., Saal, A.E., Kurz, M.D., Hauri, E.H., Blusztajn, J.S., Harpp, K.S., Werner, R., Geist, D.J., 2017. Submarine basaltic glasses from the Galápagos Archipelago: determining the volatile budget of the mantle plume. J. Petrol. 58, 1419–1450.

Peterson, M.E., Saal, A.E., Nakamura, E., Kitagawa, H., Kurz, M.D., Koleszar, A.M., 2014. Origin of the “ghost plagioclase”signature in Galápagos melt inclusions: new evidence from Pb isotopes. J. Petrol. 55, 2193–2216.

Philpotts, J.A., Schnetzler, C.C., 1968. Europium anomalies and the genesis of basalt. Chem. Geol. 3, 5–13.

Rasoazanamparany, C., Widom, E., Valentine, G.A., Smith, E.I., Cortés, J.A., Kuentz, D., Johnsen, R., 2015. Origin of chemical and isotopic heterogeneity in a mafic,

monogenetic volcanic field: A case study of the Lunar Crater Volcanic Field, Nevada. Chem. Geol. 397, 76–93.

Ryan, W.B.F., Carbotte, S.M., Coplan, J.O., O'Hara, S., Melkonian, A., Arko, R., Weissel, R.A., Ferrini, V., Goodwillie, A., Nitsche, F., 2009. Global multi-resolution topography synthesis. Geochemistry, Geophys. Geosystems 10.

Saal, A.E., Kurz, M.D., Hart, S.R., Blusztajn, J.S., Blichert-Toft, J., Liang, Y., Geist, D.J., 2007. The role of lithospheric gabbros on the composition of Galápagos lavas. Earth Planet. Sci. Lett. 257, 391–406.

Simkin, T., Howard, K.A., 1970. Caldera collapse in the Galápagos Islands, 1968. Science (80). 169, 429–437.

Siebert, L., Simkin, T., Kimberly, P., 2011. Volcanoes of the World. Univ of California Press.

Sinton, C.W., Harpp, K.S., Christie, D.M., 2014. A preliminary survey of the northeast seamounts, galápagos platform. Galápagos A Nat. Lab. Earth Sci. 204, 335.

Smith, I.E.M., Németh, K., 2017. Source to surface model of monogenetic volcanism: a critical review. Geol. Soc. London, Spec. Publ. 446, 1–28.

Smith, W.H.F., Sandwell, D.T., 1994. Bathymetric prediction from dense satellite altimetry and sparse shipboard bathymetry. J. Geophys. Res. Solid Earth 99, 21803–21824.

Sousa, J., Kohn, M.J., Schmitz, M.D., Northrup, C.J., Spear, F.S., 2013. Strontium isotope zoning in garnet: implications for metamorphic matrix equilibration, geochronology and phase equilibrium modelling. J. Metamorph. Geol. 31, 437–452.

Stracke, A., Bourdon, B., 2009. The importance of melt extraction for tracing mantle heterogeneity. Geochim. Cosmochim. Acta 73, 218–238.

Swanson, F.J., Baitis, H.W., Lexa, J., Dymond, J., 1974. Geology of Santiago, Rábida, and Pinzón Islands, Galápagos. Geol. Soc. Am. Bull. 85, 1803–1810.

Thirlwall, M.F., 1982. A triple-filament method for rapid and precise analysis of rare-Earth elements by isotope dilution. Chem. Geol. 35, 155–166.

Trela, J., Vidito, C., Gazel, E., Herzberg, C., Class, C., Whalen, W., Jicha, B., Bizimis, M., Alvarado, G.E., 2015. Recycled crust in the Galápagos Plume source at 70 Ma: Implications for plume evolution. Earth Planet. Sci. Lett. 425, 268–277.

Vidito, C., Herzberg, C., Gazel, E., Geist, D., Harpp, K., 2013. Lithological structure of the Galápagos Plume. Geochemistry, Geophys. Geosystems 14, 4214–4240.

Villagómez, D.R., Toomey, D.R., Geist, D.J., Hooft, E.E.E., Solomon, S.C., 2014. Mantle flow and multistage melting beneath the Galápagos hotspot revealed by seismic imaging. Nat. Geosci. 7, 151.

Villagómez, D.R., Toomey, D.R., Hooft, E.E.E., Solomon, S.C., 2007. Upper mantle structure beneath the Galápagos Archipelago from surface wave tomography. J. Geophys. Res. Solid Earth 112.

Walker, G.P.L., 2000. Basaltic volcanoes and volcanic systems. Encycl. Volcanoes 283–289.

Weis, D., Garcia, M.O., Rhodes, J.M., Jellinek, M., Scoates, J.S., 2011. Role of the deep mantle in generating the compositional asymmetry of the Hawaiian mantle plume. Nat. Geosci. 4, 831.

Werner, R., Hoernle, K., Barckhausen, U., Hauff, F., 2003. Geodynamic evolution of the Galápagos hot spot system (Central East Pacific) over the past 20 my: Constraints from morphology, geochemistry, and magnetic anomalies. Geochemistry, Geophys. Geosystems 4.

Werner, R., Hoernle, K., van den Bogaard, P., Ranero, C., von Huene, R., Korich, D., 1999. Drowned 14-my-old Galápagos archipelago off the coast of Costa Rica: implications for tectonic and evolutionary models. Geology 27, 499–502.

White, W.M., McBirney, A.R., Duncan, R.A., 1993. Petrology and geochemistry of the Galápagos Islands: Portrait of a pathological mantle plume. J. Geophys. Res. Solid Earth 98, 19533–19563.

Wood, C.A., 1979. Monogenetic volcanoes of the terrestrial planets. In: Lunar and Planetary Science Conference Proceedings. pp. 2815–2840.

Zou, H., 1998. Trace element fractionation during modal and nonmodal dynamic melting and open-system melting: a mathematical treatment. Geochim. Cosmochim. Acta 62, 1937–1945.

CHAPTER FOUR: CALIBRATION OF ^{207}Pb-^{204}Pb DOUBLE SPIKE: DS74

Abstract

The double spike technique is commonly applied to correct Pb isotope measurements for mass dependent fractionation occurring upon ionization. We mix and calibrate a ^{207}Pb-^{204}Pb double spike for the Isotope Geology Laboratory and Boise State University. We provide calculators in Excel and MATLAB, which utilize previously derived equations (Hamelin et al., 1985), to produce double-spike corrected Pb isotope ratios and propagated uncertainties from pairs of spiked and unspiked analyses. We present isotope data for 152 individual TIMS analyses of standard reference materials used for calibration and validation. We show that, TIMS analyses exhibit predictable mass dependent fractionation behavior and can be successfully corrected using a double spike. We calibrate our spike against the certificate value of NBS982 and prove the quality of calibration through multiple analyses of NBS981 and BCR-2 at variable sample-spike proportion. From sample spike pairs which are within 50% of the ideal mixing proportion we derive isotopic compositions for NBS981 ($^{206}Pb/^{204}Pb = 16.9413 \pm 0.0013$ 1σ, $^{207}Pb/^{204}Pb = 15.5010 \pm 0.0012$; $^{207}Pb/^{204}Pb = 36.7331 \pm 0.0032$; errors of 78, 80 and 86 ppm respectively), NBS982 ($^{206}Pb/^{204}Pb = 36.7429 \pm 0.0033$, $^{207}Pb/^{204}Pb = 17.1635 \pm 0.0020$; $^{207}Pb/^{204}Pb = 36.7573 \pm 0.0052$; errors of 90, 117 and 142 ppm), BCR-2 ($^{206}Pb/^{204}Pb = 18.8033 \pm 0.0022$ 1σ, $^{207}Pb/^{204}Pb = 15.6278 \pm 0.0020$; $^{207}Pb/^{204}Pb = 38.8388 \pm 0.0054$; errors of 117, 130 and 140 ppm) and BHVO-2 ($^{206}Pb/^{204}Pb = 18.6472$

± 0.0028 1σ, $^{207}Pb/^{204}Pb$ = 15.4944 ± 0.0028; $^{207}Pb/^{204}Pb$ = 38.2219 ± 0.0071; errors of 151, 181 and 185 ppm). The greater uncertainty in the measurements of geologic materials over commonly used NBS981 highlights the need to use geologic standards, which closely match those of unknows to determine between run reproducibility and provide a benchmark for accuracy.

Introduction

There are four naturally occurring Pb isotopes, three of which are radiogenic. Patterns of ingrowth and variability of Pb isotopes are produced by the decay of ^{238}U and ^{235}U with differing decay constants and one from ^{232}Th. Thus, the three radiogenic isotopes, ^{206}Pb, ^{207}Pb and ^{208}Pb can be used together to delineate the timing and nature of chemical differentiation of the Earth (e.g., Stacey and Kramers, 1975; Vervoort et al., 1994). This makes Pb unique among the terrestrial elements. Used collectively with other long lived radiogenic isotope ratios (Sr-Nd-Hf-Os), the daughter products of short-lived nuclides (e.g., ^{142}Nd, ^{182}W), noble gas ($^{3}He/^{4}He$, $^{20}Ne/^{22}Ne$), and stable isotope ratios (e.g., $\delta^{2}H$, $\delta^{18}O$), Pb isotopes can be used to holistically study the origins and distribution of geochemical reservoirs of the Earth, including the hydrosphere (Goldstein and Hemming, 2003) and the solid Earth (e.g., Hofmann, 1988; Hart et al., 1992; Boyet and Carlson; 2005; Dixon et al., 2017). However, precise measurements of these isotopic ratios are necessary to delineate endmember components in mixing lines or arrays and determine the relative contribution of individual components in all of these systems, or accurately define a slope related to time, in the case of the Pb isotope system, in particular.

The advent of multicollector (MC) thermal ionization and inductively coupled plasma mass spectrometry (TIMS and ICPMS, respectively) has enabled the simultaneous measurement of isotopic ratios (e.g., Sr, Nd, Pb; Todt et al., 1983). This advance, and improvements in loading techniques for TIMS analyses, leading to more efficient ionization (e.g., silica gel - phosphoric acid carrier solution; Manhes et al., 1978), have reduced the uncertainty in the measurement of isotopic ratios, amidst dynamic beam conditions for both source types (Todt et al., 1983). The implementation of peak jumping algorithms (i.e., dynamic MC routines) has further eliminated known uncertainties in the measurement of isotope ratios due to variations in collector efficiencies (Thirlwall, 2000; Richter et al., 2001). Thus, modern precision and accuracy of isotopic measurements by MC-TIMS and MC-ICPMS are largely limited by beam strength (i.e., sample size) and the ability to correct for mass-dependent fractionation occurring during ionization and analysis (e.g., Thirlwall, 2000). For isotope systems with at least two stable, non-radiogenic nuclides (i.e., whose ratios are constant in nature), instrumental fractionation can be removed by correcting measured values against the known ratio of these two nuclides with constant ratio (e.g., Sr, and Nd; Hofmann, 1971). In the absence of this criterium (e.g., the Pb isotope system), a spike constituting two (i.e., double spike) or three (i.e., triple spike) isotopes of the element of interest, in known proportions, can be added to a sample run (i.e., “spiked”) to correct for the effects of mass dependent fractionation on the measured isotope ratios (Dodson, 1963).

In order to correct for instrumental fractionation using a double or triple spike, isotope ratios must be measured in a spiked and unspiked sample run (unless the isotopes used in the spike are not present naturally, which is the case for ^{202}Pb and ^{205}Pb isotopes),

which can be used in tandem to solve for instrumental fractionation assumed to fall along predictable mass dependent, linear, exponential, or Rayleigh fractionation curves (Dodson, 1963; Hamelin et al., 1985). Community use of the double spike technique and double spike mathematics and calibration procedure have both been recently reviewed in detail (Taylor et al., 2015; Klaver and Coath, 2018). We have chosen to implement a ^{204}Pb-^{207}Pb double-spike for the precise measurement of Pb isotopes by MC-TIMS in the Isotope and Geochronology Lab at Boise State University. We prefer the analysis by MC-TIMS over MC-ICPMS due to lower instrumental background, lack of instrument memory, absence of mass interferences (e.g., Hg), and higher instrumental fractionations that must be addressed in MC-ICPMS (Hoffmann et al., 2007).

For this paper we present on techniques used to derive isotope ratios for correcting dynamic multicollector routines for MC-TIMS analyses of Pb isotopes and analysis of standard reference materials, which are used to calibrate the spike and assess precision and accuracy of the double-spike method. We provide calculators (Excel, MATLAB), which utilize the same mathematics to produce double-spike corrected Pb isotope ratios and propagated uncertainties (Hamelin et al., 1985), from pairs of spiked and unspiked analyses. We address data quality issues raised for TIMS Pb analyses and derive a data rejection protocol. We discuss the robustness of the double-spike calibration in terms of calibration method, error magnification due to non-ideal sample spike mixtures, and analysis at non-optimal beam conditions (i.e., low sample volumes and high analysis temperatures).

Methods

The double-spike technique exploits the field-vector behavior of mass-dependent fractionation, where the direction of the fractionation vector in 3D isotope space ($^{206}Pb/^{204}Pb$-$^{207}Pb/^{204}Pb$-$^{208}Pb/^{204}Pb$) is predictable and dependent on the mass difference between the isotope ratios of the analyte and their relative concentrations. In practice, only a single mixing line exists between the fractionation trajectories of the measurements of an unknown isotope concentration (IC), true spike composition and a measured mixture of the two (e.g., Klaver and Coath, 2018). This is regardless of the degree of fractionation of either the IC or mixed runs. The solution for the true (fractionation-corrected) composition of an unknown can be solved for mathematically using linear fractionation law and matrix algebra (e.g., Hamelin et al.,1985). We implement these equations, as well as the error propagation of IC and mixed runs, as an excel workbook and MATLAB functions, which can be found in Supplementary Materials 4.

Reagents and Materials

All dissolutions, subsequent chemical separations and mass spectrometry were carried out in a class 10, cascading positive-pressure, HEPA-filtered clean laboratory. Acids used for cleaning and dissolution are twice distilled to concentrate for purification and have Pb blanks of <0.2 pg/g ppm for HCl and HNO_3. Other reagents (HBr, H_2O_2, H_2PO_5 silica gel) are high purity chemicals from SEASTAR. Water used for cleaning and acid dilutions is from a Millipore Elix/Milli-Q Gradient ultra-clean water system. All containers and dropper bottles used for the double spike procedure were fluxed on a hot plate at 120℃ for >1 week with alternating concentrated HF and HCl acids. After at least

three acid cycles, containers were fluxed overnight with 6M HCl, which were subsequently dried down and analyzed for total Pb concentrations. Additional bottle cleaning cycles and repeat concentration measurements were conducted on individual containers until Pb concentrations were <0.2 pg/g total Pb.

Standards NBS981 and NBS982 (ie., standard reference materials; SRM981 and SRM982) are from the stock solutions commercially available through the National Institute of Standards and Technology (NIST; formerly National Bureau of Standards). A third calibration standard was mixed, which has a wildly different composition to these standards, with the purpose of calibrating the spike independently of any IC runs (Klaver and Coath, 2018). The standard used for this special mixture is NBS983 – which was originally made to represent uranogenic Pb (Catanazaro et al., 1968). This sample has extremely high $^{206}Pb/^{204}Pb$ and relatively high $^{206}Pb/^{208}Pb$. The extremely high ^{206}Pb beam intensity and low ^{204}Pb make it impossible to measure their ratio using a dynamic multicollection routine. Because of this, we have spiked this sample with the same ORNL ^{204}Pb dissolution used to make the BSU double spike, increasing its ^{204}Pb content by ~100X. We refer to this artificially doped standard as NBS983SPECIAL. Due to inconsistent ionization of this sample, as will become apparent in the following sections, we do not discuss the second calibration method further.

United States Geological Survey (USGS) basalt standard BCR-2 and BHVO-2 were chosen as secondary reference materials for use in both the calibration and as the geologic standard for assessing external precision of the entire procedure, leading up to and including the application of the double spike technique in fractionation correcting unknowns. Although we report data for BHVO-2, we only discuss results for BCR-2,

given its previous use as an isotopic standard, and thus, relatively large dataset of modern analysis from which it can be benchmarked (e.g., n=26 from 12 dissolutions; Jweda et al., 2016). Of note however, it has been shown that the fidelity of Pb isotope ratios in BCR-2, and other USGS provided sample powders likely suffer from variable Pb contamination, likely due to addition of grinding materials during the pulverization (Weis et al., 2006; Jweda et al., 2016). Thus, the absolute values for the geologic standards may be different than those previously analyzed for this reason. To mitigate this issue, prior to dissolution, USGS provided rock powders were 3x leached in 6M HCl in an ultrasonic bath for 20 minutes, and finally sonically rinsed 3x in ultra-clean H_2O. Following the leaching procedure, standards were dissolved using standard dissolution steps and purified twice through HBr ion exchange columns prior to loading.

Spike Selection and Preparation

The Pb double spike technique has become pervasive in the correction of mass dependent fractionation of Pb isotope measurements over the past 30 years (Taylor et al., 2015). Since the first successfully calibrated ^{204}Pb-^{207}Pb spikes (Hamelin et al., 1985) there have been four similar spikes calibrated (SBL74, e.g., Baker et al., 2004; VUA Pb DS; Klaver et al., 2016), a single triple spike (^{204}Pb-^{207}Pb-^{206}Pb; Galer and Abouchami, 1998, Galer et al., 1999), two ^{202}Pb-^{205}Pb double spikes (Todt et al., 1996; Amelin and Davis, 2006), and one double spike pair (^{202}Pb-^{204}Pb and ^{207}Pb-^{204}Pb; Kuritani and Nakamura, 2003). These spikes have been mixed for both MC-ICPMS (Thirlwall, 2002; Baker et al., 2004; Taylor et al., 2015) and MC-TIMS isotope facilities (Hamelin et al., 1985; Woodhead et al., 1995; Todt et al., 1996; Galer, 1999; Thirlwall, 2000; Hoernle et al., 2011; Klaver et al., 2016; Taylor et al., 2015).

Spikes can be mixed from nominally pure isotope spikes available from the Oak Ridge National Laboratory (ORNL). The optimal isotope ratio in the spike and the optimal double spike sample mixture can be found where there is the greatest difference between the mass dependent fractionation trajectories for all measured isotope ratios and where the isotope ratios being measured are closest to one (Rudge et al., 2009). However, the ultimate double spike composition and spike to sample ratio varies based upon the composition of the unknown and the error being minimized (e.g., degree of fractionation or isotope ratio; Rudge et al., 2009). We prepared our double spike using ORNL provided ^{204}Pb and ^{207}Pb single spikes, with the goal of optimizing the $^{206}Pb/^{204}Pb$, which results in an ideal elemental molar Pb sample to spike mixing ratio of 63% double spike (Figure 4.1). Of note, the error surfaces optimizing $^{206}Pb/^{204}Pb$, $^{207}Pb/^{204}Pb$ and $^{208}Pb/^{204}Pb$ are nearly identical (ideal mixing ratios between 54 and 63%) and have similar broad, flat minima, making them nearly insensitive to variations in spike to spike mixing proportions +/- >50% of the optimal values (Figure 4.1). This is mainly to due to the effect of dramatically increasing the relative intensity of the ^{204}Pb beam of the mixed run even at very low spike proportions (Rudge et al., 2009).

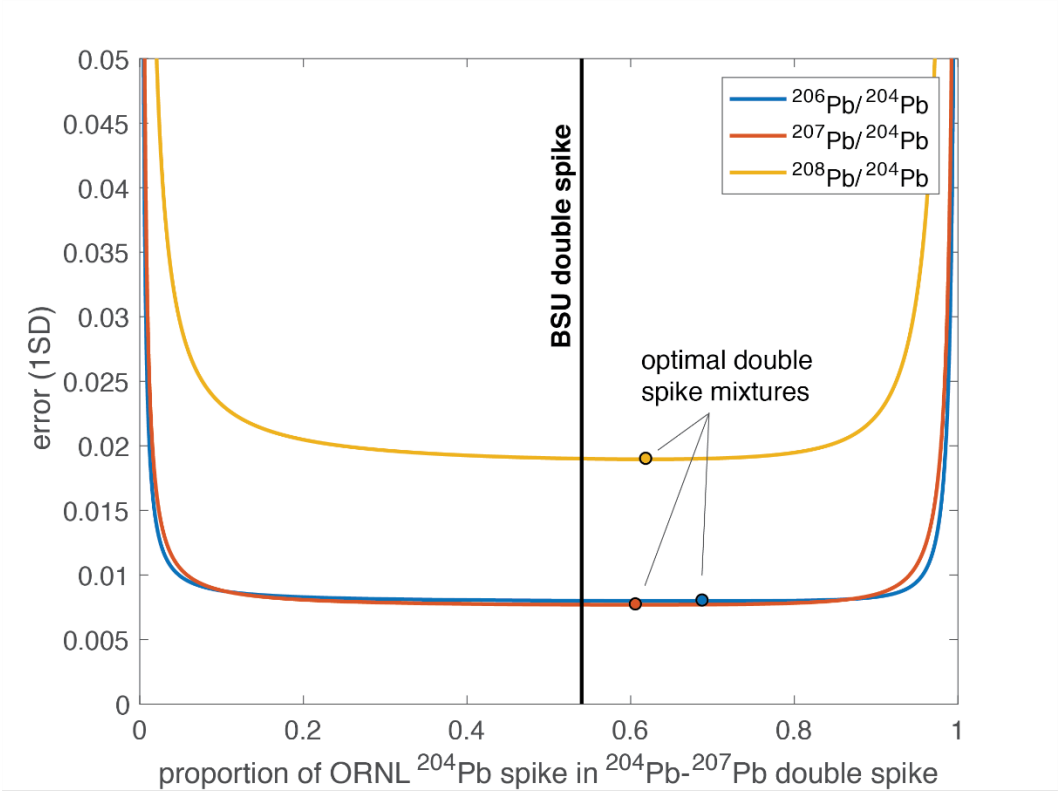

Figure 4.1. Proportion of ORNL ^{204}Pb spike in ^{204}Pb-^{207}Pb double spike, as a function of error in the isotope ratio being optimized, used for determining the BSU double spike composition (vertical black line). Error curves are derived from the Double Spike Toolbox (Rudge et al., 2009). Double spike error curves are calculated assuming an optimum spike-sample proportion for ^{206}Pb/^{204}Pb, ^{207}Pb/^{204}Pb and ^{208}Pb/^{204}Pb (blue orange and gold lines, respectively), 8 second integrations with 10V integrated beam intensity at 300K over 200 ratios. Optimal double spike mixtures are shown for each isotope ratio as colored circles, which are the same as their corresponding error curve.

Single spike powders of ^{204}Pb and ^{207}Pb from ORNL (~1.3 mg Pb carbonate) were dissolved in 200 mL 0.13M HNO_3 acid in separate 500 mL teflon containers. Individual aliquots of each ORNL standard were spiked with a ^{205}Pb-^{233}U-^{235}U solution (BSU-1B; Schmitz and Schoene, 2007) and Pb concentrations were determined via single ID-TIMS analyses of each solution (1.16 M ^{207}Pb and 1.39 M ^{204}Pb). Approximate ideal mixing proportions of the two spikes were determined by stoichiometry from the concentrations

derived from the ^{205}Pb spiked aliquots and values, calculated from the Rudge et al. (2009) ideal mixing proportions, minimizing error on $^{206}Pb/^{204}Pb$. Aliquots of each spike were mixed in a separate double spike container using the calculated proportions and diluted up to 500 mL using the same 0.13M nitric acid, which leads to elemental Pb concentrations in the diluted spike container on the order of 50 ng/g. Although detailed in the results section, the general composition of the BSU double-spike was calculated gravimetrically and has a mixing proportion of ~54% ORNL ^{204}Pb spike (Figure 4.1).

Spiking, Loading and Analytical Procedure

Although the double spike technique for correcting Pb isotope ratios was derived more than half a century ago (Dodson, 1963), early attempts to test the viability of the technique were unsuccessful as a result of high and variable blank values of spiked and unspiked analyses (e.g., Oversby, 1973). Advances in air quality management (e.g., cascading positive pressure HEPA filtered laboratory spaces, laminar flow hoods) and increasing purity of reagents have lowered total procedural blanks, and the development of spiking upon loading have reduced blank variation between spiked and unspiked to acceptable values (1-5 pg Pb; Hamelin et al., 1985; Woodhead et al., 1995; Thirlwall, 2000). Total procedural blanks for the IGL at BSU are on the order of 0.1-0.5 pg Pb, which is an order of magnitude below this nominal required threshold established by previous workers. Therefore, to ensure complete sample-spike equilibration, we prefer to spike samples prior to the final Pb conversion and drydown steps, as opposed to spike addition upon loading. Regardless of the low procedural blanks, by spiking during this step, we isolate the effect of the blank to the final conversions, as opposed to what might be introduced in the columns and dissolutions, which would be intrinsically larger.

To avoid contamination of IC aliquots, spike beakers (5 mL) have been designated and isolated from the normal IC beakers during storage and sample preparation. Sample and sample/spike aliquots of various sizes are taken which result in ~10-50 ng Pb. When spiking, subequal proportions of sample and spike Pb are aliquoted into a double-spike designated beaker, using estimated Pb compositions of the sample and the calculated concentration of the double spike solution. Spiked and unspiked samples are dried down with 3 μL of phosphoric acid, picked up in 30 μL concentrated HNO_3 and H_2O_2 each to liberate organics, dried down and finally picked up and dried down again with 30 μL of 6M HCl. To reduce blanks on loading, pipette tips for each sample are treated with three aliquots of triple distilled 6M HCL. Using the freshly cleaned pipette, sample specks are finally picked up in 2-2.5 μL of silica gel (sonicated for 20 minutes) and loaded onto regular Re filaments, which have first been leached in 6M HCl at 120℃ overnight prior to, and degassed on a DG60 degas bench after, stringing. Filaments are then individually glowed prior to loading into the mass spectrometer. Again, in order to reduce communication between spiked and unspiked samples, spike samples are always dedicated towards the same barrel positions, occupying half of the sample turret. Spent filaments, posts and turret hardware associated with DS runs are stored and cleaned separate to that of normal common Pb runs. Samples were run for 8 blocks of 25 ratios at temperatures ranging between ~1000-1300 C. During ionization, Pb isotope ratios were measured using simultaneous static and dynamic 5-cup multicollector routine (normalized after the fact to mean of the static $^{208}Pb/^{206}Pb$ of the sample; Thirlwall, 2000).

Data Reduction

To assess data quality block statistics were pulled from original Ionvantage files for each run using MATLAB script (DS74_static.m; Supplementary Materials 4). This includes information about each block, including filament temperature $^{207}Pb/^{206}Pb$ and $^{208}Pb/^{206}Pb$ static means for each block. From these we calculate bulk run statistics such as mean run temperature and statistics on fractionation trajectories. Theoretical mass dependent fractionation trajectories are a function of the mass difference between the isotopes being analyzed. In the case of the $^{207}Pb/^{206}Pb$ (mass difference = 1.0014) and $^{208}Pb/^{206}Pb$ (mass difference = 2.0022), there is a resulting theoretical fractionation slope of 0.5002. In turn, for each analysis, we regress a line through the $^{207}Pb/^{206}Pb$ and $^{208}Pb/^{206}Pb$ static means of all blocks for each analysis, with a slope (representing the fractionation trajectory of these combined isotope ratios; which we call *m*). This slope we can directly compare to the theoretical trajectory. From this regression we also calculate an r^2 value, which can be inverted to determine the relative uncertainty of the calculated *m*. For example, a sample with an *m* of 0.5 with an r^2 of 0.95 is assigned an uncertainty in slope of 5%.

Individual analyses were assessed for quality and fractionation through visualization in Tripoli software, prior to decimation for DS inversion. Samples that experienced tortuous-inexplicable ionization were rejected outright. If fractionation trajectories deviated significantly during ionization at high temperatures late in the analysis, we removed the effected blocks. Intermediate blocks were never excluded. Individual ratios were culled at the one-sigma confidence interval for $^{208}Pb/^{206}Pb$ normalized ratios ($^{206}Pb/^{204}Pb$, $^{207}Pb/^{204}Pb$ and $^{207}Pb/^{206}Pb$). Mean ratios and standard

errors for uncorrected IC and DS measurements, along with number of blocks used for the reported ratios for each sample were exported for DS inversion. Of note, despite these steps, all blocks, no cleaning, are shown in the block results.

Results

The calibration and validation dataset of IC and mixed runs consists of 152 individual analyses. Block statistics for all analyses are reported in Supplementary Data Tables 4.1 (Figure 4.2). Most samples generally follow predicted mass dependent fractionation trajectories within error of their calculated slopes; with scatter that is not highly correlated with temperature (Figure 4.3). There is consistent reverse fractionation between the first and second blocks for almost all samples (Figure 4.2). In addition, some samples fractionate consistently for all blocks for all runs (BHVO-2; Figure 4.2). Other samples have runs which display peculiar and erratic fractionation patterns, which can be identified by high standard deviation of the $^{208}Pb/^{204}Pb$ and low r^2 values (Supplementary Data Tables 4.2). In particular, NBS983SPECIAL displays consistently anomalous fractionation (Figure 4.2). However, the only sample rejected was NBS981 IC5, which had erroneous dynamic compared to static ratios, likely resulting from using an incorrect normalization value upon reprocessing. Averaged ratios for IC and mixed runs are presented in Supplementary Data Table 4.1, and are organized by sample, consecutively: NBS981, NBS982, BCR-2, BHVO-2, NBS983SPECIAL and DS74.

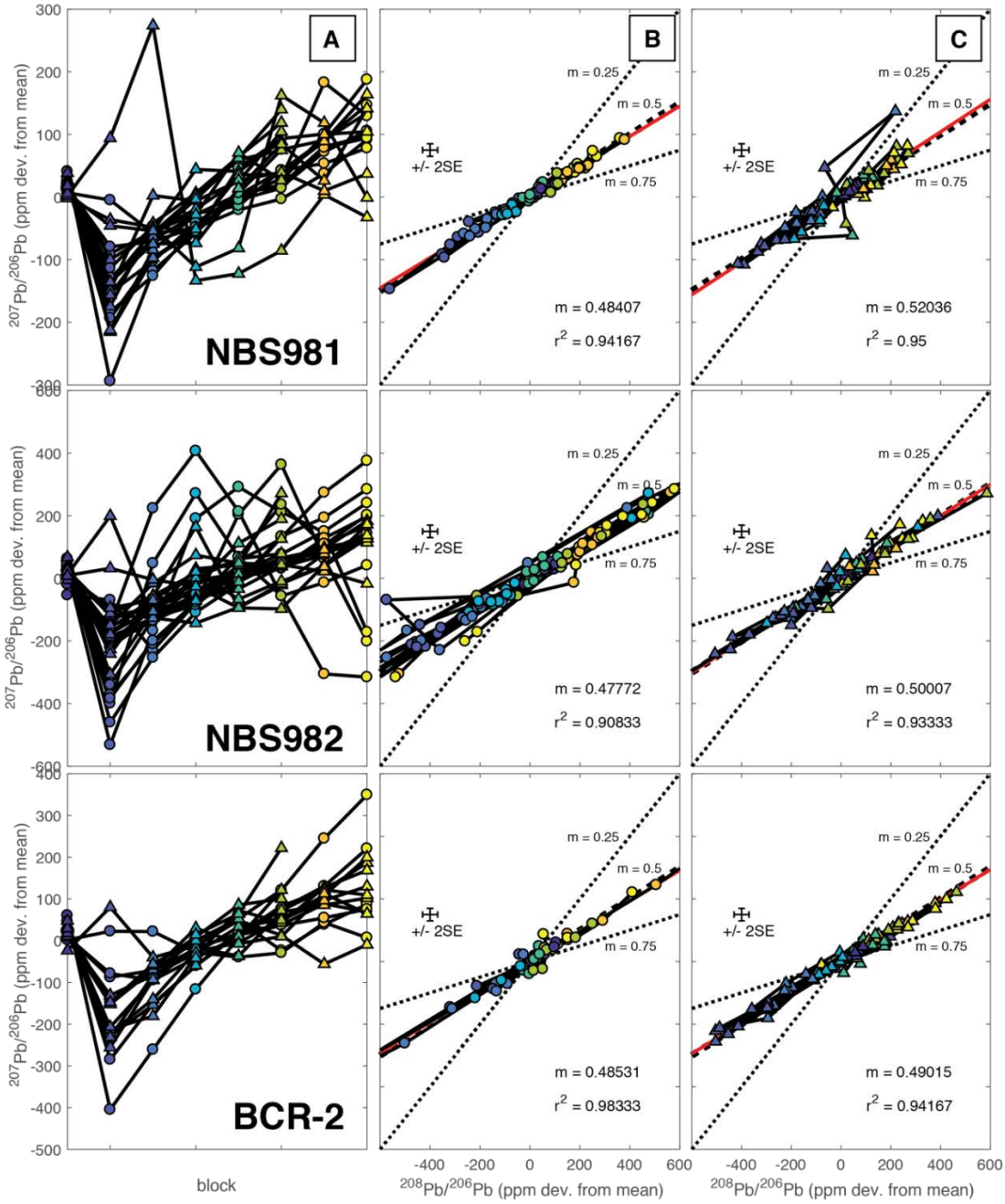

Figure 4.2. Block statistics for BCR-2 spiked and unspiked runs. A) variation in $^{207}Pb/^{204}Pb$ static means as a function of block (25 ratios/block). Symbol color is graded by block number (cool-warm from 1-8, as depicted in A). Ratios from the same run are connected by a solid black line. Most samples show a positive fractionation trend with time; however, a few samples have nearly flat slopes. B) correlated variation in $^{207}Pb/^{204}Pb$ and $^{208}Pb/^{204}Pb$ static means for IC runs colored as a function of block as shown in A. Fractionation trajectories are shown as dotted lines, the theoretical trajectory predicted for the ratios shown is ~0.5 and is shown as a thick dashed line. A linear fit to the samples showing in run variations with r^2 values >0.95 are used to generate a single fractionation trend shown in red. C) DS mixed runs with the same symbology as described in B.

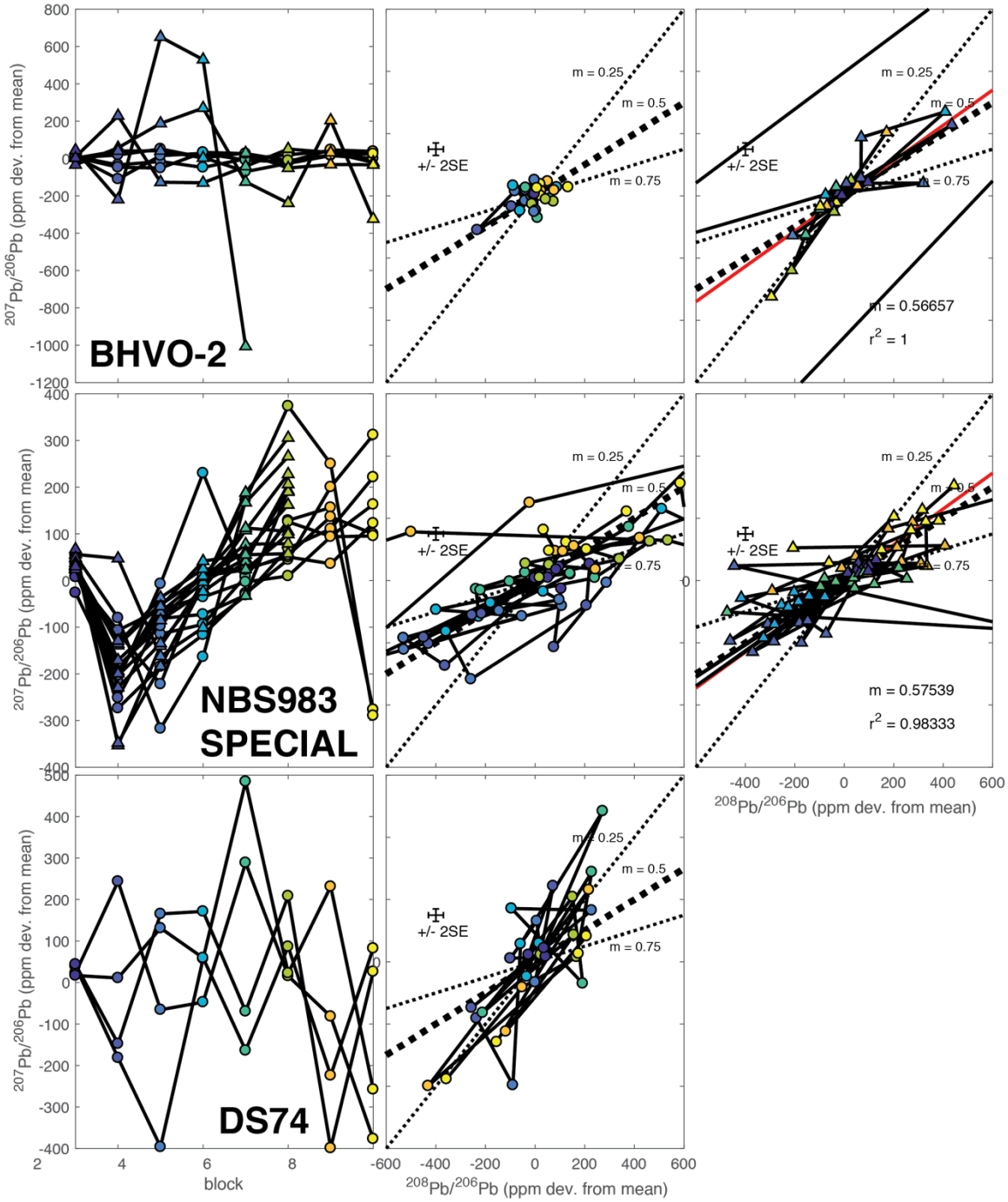

Figure 4.2 Continued.

Assessment of Data Quality and Data Rejection Criteria

Previous in-depth investigation of the fractionation behavior of Pb during TIMS analyses uncovered troublingly anomalous behavior, suggesting that mass independent fractionation is a process that affects the measured isotope ratios at analytical temperatures >1200 C. From a theoretical basis, this fractionation cannot be corrected for using a double spike (Thirlwall, 2000). To address this observation and assess the effects of mass independent fractionation on our analyses, we review the characteristics of the block statistics for NBS981, NBS982 and BCR-2 (Figures 2 and 3).

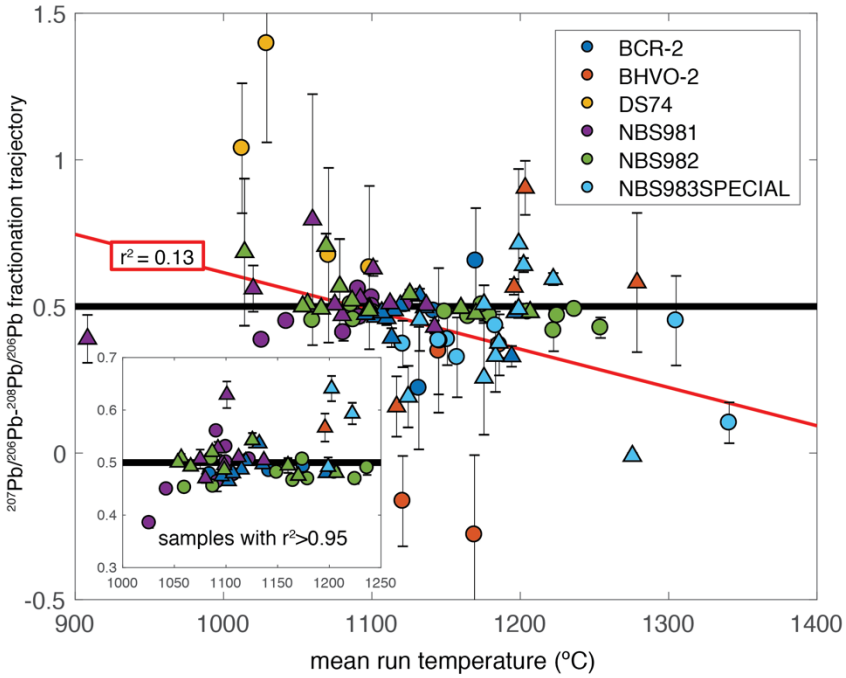

Figure 4.3. Calculated $^{207}Pb/^{206}Pb$-$^{208}Pb/^{206}Pb$ fractionation trajectory (m) as a function of mean run temperature for all analyses. Analyses are colored by sample. IC runs are shown as circles and mixed runs are shown as triangles. Horizontal black bar indicates theoretical mass fractionation slope for the ratios shown. A line is regressed through all data points to show the trend of the data, which is poorly correlated (r^2=0.13). Inset shows the same data for samples that have well defined fractionation slopes.

In short, we observe no systematic correlation between mean run temperature and fractionation trajectory - *m* (Figure 4.3). For samples that followed very linear fractionation paths (R^2 >= 0.95), calculated *m* values are between 0.4 and 0.7, which show no apparent correlation with mean in-run temperature (Figure 4.3). Further, on a sample by sample basis we calculate an average *m* for all analysis for each sample that have consistent fractionation trends (R^2 >= 0.95; Figure 4.2B and C). For samples that have highly correlated *m* values, all have average fractionation slopes between 0.49 and 0.57 (Figure 4.2B and C). Thus, we conclude that run temperature within the bounds tested by our data, plays little role in the fractionation path of TIMS analyses.

Deviations from a linear trajectory over the course of a run appear to be mostly random. We explain these deviations as incomplete ionization and mixing of various fractionating reservoirs on the filament. If this is the case, despite the apparently mass independent fractionation, they are still following mass dependent behavior on average and still be correctable using the double spike technique. One caveat to this is that all isotope ratios are averaged in the same way and intermediate blocks are not removed. Thus, we take a conservative approach to culling data prior to averaging for DS reduction, where all blocks which display sloping fractionation paths are not culled in any way. There are two scenarios where the assumption of mass dependent fractionation may not hold and culling of data will not affect the final results, this is at the beginning and end of an analysis. At first, nearly all samples display a negative *m* between the first and second block (Figure 4.2A). It is possible that this is due to ionization of interfering masses upon sample warm up. Thus, it may be justified to remove the initial blocks of data where this negative fractionation is occurring. However, the $^{207}Pb/^{206}Pb$ from the

first data block is always centered about the mean of the run (Figure 4.2A), thus, the addition of this block does not likely affect the mean value significantly. Second, negative fractionation paths observed at the end of a sample run could be due to the exhaustion of the lowest abundance isotopes, which would constitute mass independent fractionation. Thus, when this behavior is observed, those blocks are rejected prior to averaging for DS inversion.

Typically, visualization of the data series prior to reduction enables the elimination of blocks at either the beginning or end of an analysis, resulting in greater in-run reproducibility, and between run reproducibility of standards. Thus, for the analysis of unknowns, it is our recommendation that these block statistics be compiled and reported for all analyses as a means of assessing data quality (DS74_static.m; Supplementary Materials 4) and culling anomalous blocks at the beginning and end of individual analyses prior to decimation for DS inversion.

"Quadruple-Spike" Calibration and Validation

Arguably, the simplest method for calibrating the DS is to treat DS IC analyses as unknowns, fractionation corrected using mixtures of it and standard with a "known" isotopic composition (Klaver and Coath, 2018). In this case, the standard serves as a "quadruple spike" in the DS inversion and can be solved using the same set of equations set up for the standard DS inversion (e.g., Hamelin et al., 1985). Limitations with this method are the intrinsic assumption of a known isotopic value of the standard, difficulty in precisely measuring the DS IC, which in our case has low ^{206}Pb and ^{208}Pb concentrations, and the effect of a blank at these low isotope concentrations.

In the interest of interlaboratory consistency, we have customarily chosen to calibrate DS74 against the certificate value of NBS982 (Catanazaro et al., 1968). In order to account for the above-mentioned limitations, we take a Monte Carlo approach to solving for the DS composition. We use a random sampling (from a normal distribution within the 1 sigma standard errors of in-run reproducibility) of the five DS74 ICs and DS74-NBS982 mixtures, both selected at random. The mixtures used all have mixing proportions (p) between 0.2 and 0.8 and have been culled using the criteria laid out in the previous section. Together the randomly sampled DS74 IC and mixes are used in the DS inversion (DS74_invert.m; Supplementary Materials 4) to solve for the true DS74 composition. This is done one million times. The results of this inversion are shown in Figure 4.4. The final spike composition, and associated uncertainties are taken as the mean and standard errors of this ensemble and are presented in Table 1.

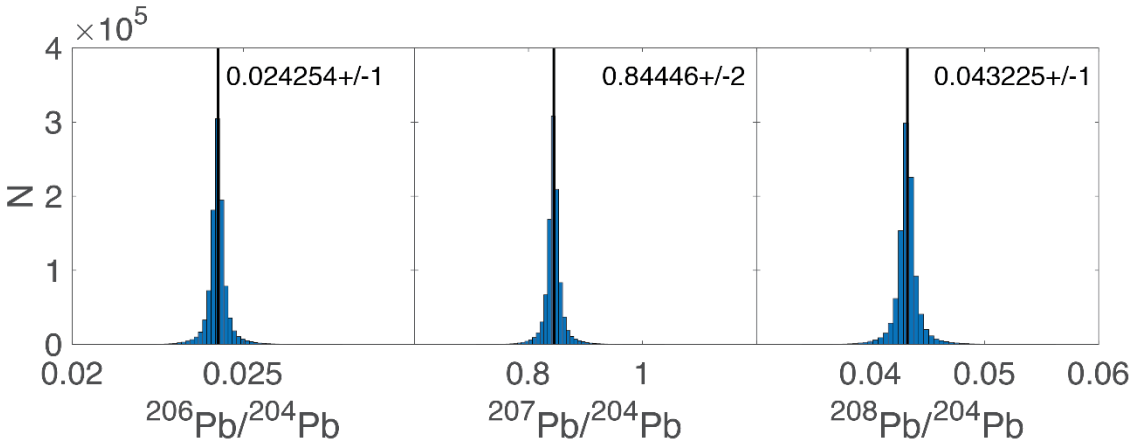

Figure 4.4. Results of the Monte Carlo DS inversion using NBS982 as a quadruple-spike; $^{206}Pb/^{204}Pb$ (left), $^{207}Pb/^{204}Pb$ (middle) and $^{208}Pb/^{204}Pb$ (right).

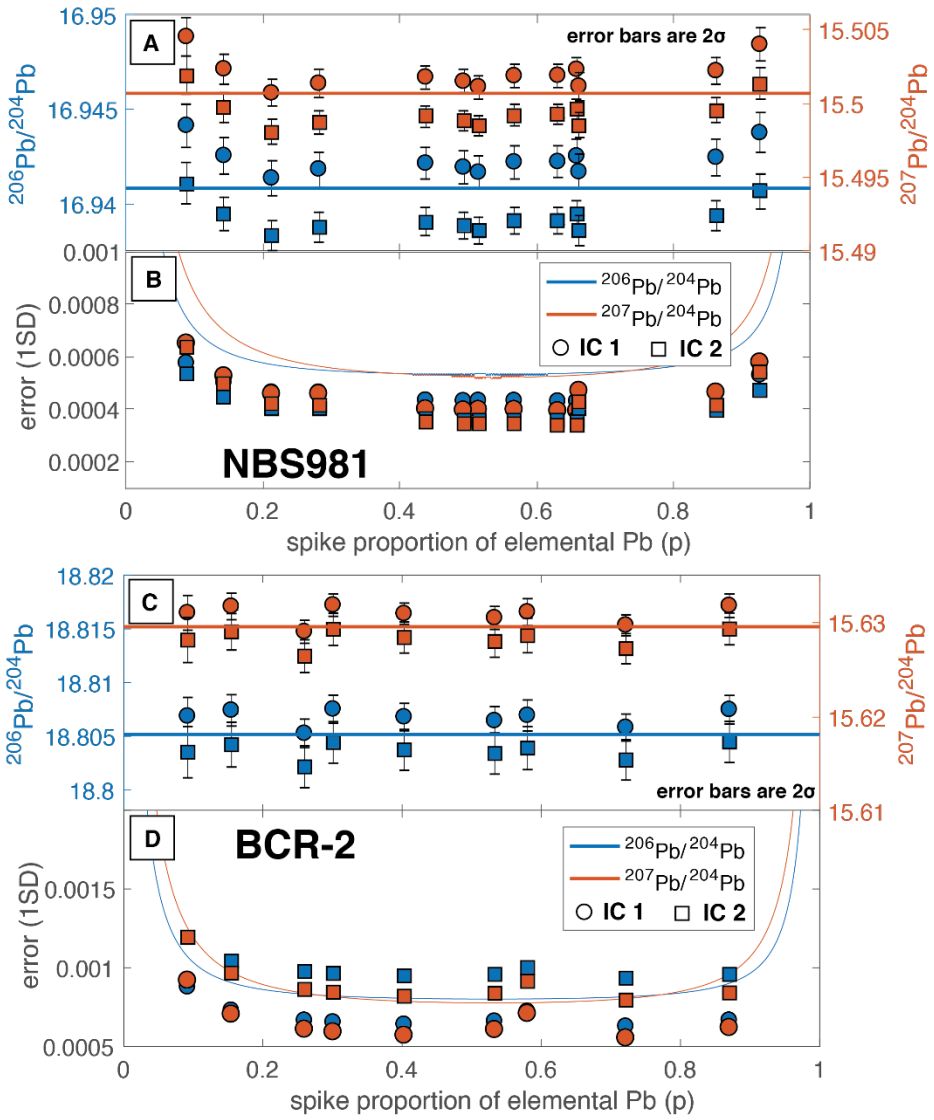

Figure 4.5. Reproducibility of NBS981 and BCR-2, with associated uncertainties as a function of spike proportion. Spike proportion is shown as p, which is the spike proportion of elemental Pb (Rudge et al., 2009). A) Double spike corrected $^{206}Pb/^{204}Pb$ (orange symbols) and $^{207}Pb/^{204}Pb$ (blue symbols) for two IC analyses of NBS981 (squares and circles). Error bars show 2σ uncertainties resulting from the double spike deconvolution. Means for each ratio are shown as horizontal lines. B) Propagated uncertainties from double spike corrected $^{206}Pb/^{204}Pb$ (orange symbols) and $^{207}Pb/^{204}Pb$ (blue symbols) for two IC analyses of BCR-2 (squares and circles). Symbols overlap where not visible. Curves show theoretical error envelopes from Rudge et al. (2009) using the BSU double spike composition and 8 second integrations with total beam intensities of 20V, for 200 ratios at 300 K. C and D are the same as above plots except showing results for two BCR-2 IC runs. For comparison, we note error envelopes use same parameters as B.

When calibrated correctly the recovered double-spike corrected isotope ratios of an unknown will not vary as a function of spike proportion for a series of variably spiked mixed runs. If improperly calibrated, at non-ideal spike-sample proportions the double-spike composition will leverage (i.e. bias) the recovered isotopic ratios of the double spike corrected unknown - toward the true spike composition. Given the lack of correlation between spike-sample proportion for the quadruple spike calibrated DS74 composition for NBS981 and BCR-2 (Figure 4.5), we deem it to be accurately calibrated.

Table 4.1 DS74 composition

	ratio	SE
$^{206}Pb/^{204}Pb$	0.024253914	0.00000030
$^{207}Pb/^{204}Pb$	0.8444605	0.000015
$^{208}Pb/^{204}Pb$	0.04322505	0.0000011

Reproducibility of Unknowns

Using the “quadruple spike” calibrated DS74 composition, we invert for all unknowns to assess the reproducibility of analyses. For each sample dissolution all combinations of sample and spike are inverted to produce an ensemble of DS74 corrected IC measurements which are presented in Supplementary Data Tables 4.3. For each sample, average values and standard deviations are tabulated and presented in Table 2. For BCR-2 and BHVO-2 we calculate the average and standard deviation for all analyses as well as for each individual dissolution. For BCR-2 and NBS981, and NBS982 it is clear that analyses corrected by mixtures outside of the ideal mixing proportions fall outside of the other data points (Figure 4.6); thus, averages and errors exclude these pairs.

In general, there is greater standard deviations for the ensembles that include poor mixtures. Thus, it is ideal to have mixed runs between 0.2 and 0.8. The reproducibility of NBS981 is on the order of 80 ppm for the three ratios presented. Although a relatively small dataset, these reproducibilities are on the order of what are reported from well-established DS laboratories (Thirlwall, 2000; Thirlwall, 2002; Woodhead et al., 1995).

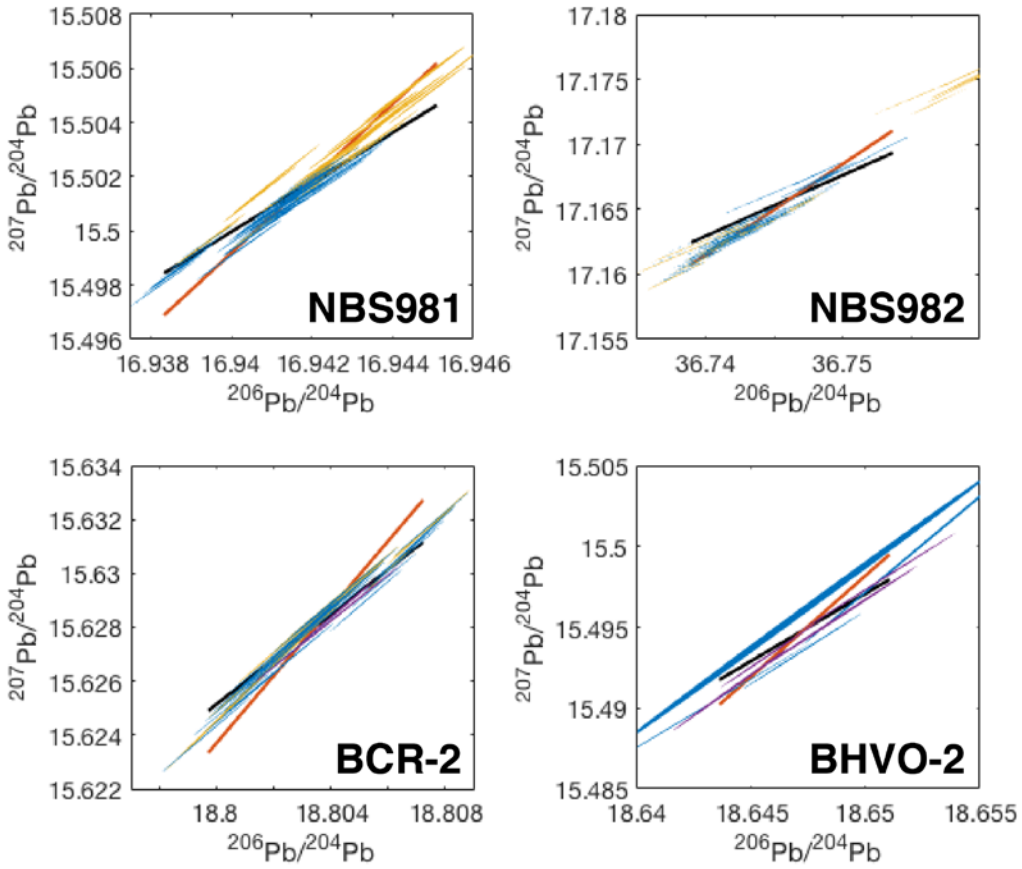

Figure 4.6. Reproducibility of standard reference materials corrected for mass dependent fractionation using DS74. Correlated error ellipses are used to represent individual analyses and their respective 2-sigma errors. Blue ellipses show DS74 corrected data for mixes with sample spike proportions between 0.2 and 0.8, yellow show data outside of that range. For USGS reference materials purple ellipses show second dissolution. Red line indicates mass dependent fractionation trajectory (+/- 0.001) centered about the mean of the data, black line shows the uncertainty in 204Pb (+/- 200 ppm). Lines are the same absolute length for all plots.

Table 4.2 Composition of reference materials and associated uncertainties determined by averaging multiple DS74 corrected sample-spike pairs.

sample	N	$\frac{^{206}Pb}{^{204}Pb}$	σ	ppm	$\frac{^{207}Pb}{^{204}Pb}$	σ	ppm	$\frac{^{208}Pb}{^{204}Pb}$	σ	ppm
NBS981	54	16.9413	0.0013	78	15.5010	0.0012	80	36.7331	0.0032	86
NBS982	80	36.7429	0.0033	90	17.1635	0.0020	117	36.7573	0.0052	142
BCR-2-DS158	24	18.8033	0.0022	117	15.6278	0.0020	130	38.8388	0.0054	140
BCR-2-DS159	4	18.8041	0.0002	12	15.6283	0.0003	18	38.8406	0.0005	14
BHVO-2-DS156	4	18.6473	0.0047	253	15.4949	0.0050	322	38.2232	0.0154	402
BHVO-2-DS157	4	18.6472	0.0028	151	15.4944	0.0028	181	38.2219	0.0071	185
NBS983SPECIAL	56	20.3100	0.3557	17513	1.4457	0.0371	25637	0.2787	0.0077	27644

As reported by Woodhead et al. (1995), we note that the sample spread for DS corrected unknowns does not spread along the fractionation trajectory but is distributed along the error trajectory for ^{204}Pb (Figure 4.6). For geologic materials, ^{204}Pb is by far the lowest abundance isotope (<2%), and thus has the lowest beam intensity upon analysis. This provides a reasonable explanation as to why the primary control on the precision of DS corrected measurements is no longer the ability to correct for fractionation but is related to the uncertainty in the ^{204}Pb peak. There is an almost 2-fold decrease in reproducibility of BCR-2 for the same analytical period. This is the case even when considering the single dissolution of BCR-2. Thus, we conclude that there is greater uncertainty in running geologic materials as opposed to the pure Pb standards. This may be due to residual matrix effects from ion exchange chemistry. Regardless of the cause of this difference, we stress the importance for running repeat measurements of geologic materials – which closely match that of unknowns, in order to assess instrumental reproducibility.

Conclusions

We do not observe anomalous fractionation as a function of increasing ionization temperature (e.g., Thirlwall, 2000). However, anomalous fractionation trajectories can be observed qualitatively by plotting the block statistics for any given run and rejected based on the user's intuition. For instance, the beginning and end of runs often exhibit the most anomalous fractionation, which we recommend be removed before the final decimation of data. If anomalous fractionation is observed in the middle of a run it may be best practice to flag or reject the data outright. Commonly more Pb is available than what is run, so attaining a well ionizing sample is worth the trouble. We have calibrated the double spike using two methods, on samples which appear to follow predictable mass dependent fractionation trajectories. In practice, the accuracy and precision of the double spike correction does not appear to be dependent on the underpinning assumption of the NBS982 composition or affected by the blank of the spike IC. In fact, independent triple unknown calibration reveals values for NBS981 and NBS982 reveal values, which are within uncertainty of the original certificate values. Thus, for future work we use and vet the technique of calibrating against NBS982 to promote the internal consistency of international laboratory comparisons. With this double spike composition and all sample spike mixes that are within ~50% of the ideal 50-50 proportion, reproducibility for all ratios of NBS981 are <90 ppm and leached BCR-2 value <140 ppm. We show that the limiting factor for precision measurements of Pb isotopes is limited by the uncertainty in the ^{204}Pb peak. Higher uncertainty in the geologic standard, which is independent of dissolution, highlights that the reproducibility of samples is no longer a function of sample preparation and blank but on the uncertainty in the final measurement, of which

the more inconstant ionization of geologic materials is of importance. Thus, we stress the use of a secondary reference material, which closely matches that being analyzed as an unknown in order to fully understand the reproducibility of double spike corrected isotope measurements.

Acknowledgements

We thank Michael Mohr for help with preparing the double spike reagents and materials, mixing the double spike analyzing standards and refining the double spike calibration. This work was conducted with the support of NSF grant (OCE-1634952) to VDW.

References

Amelin, Y., Davis, W.J., 2006. Isotopic analysis of lead in sub-nanogram quantities by TIMS using a 202 Pb–205 Pb spike. J. Anal. At. Spectrom. 21, 1053–1061.

Baker, J., Peate, D., Waight, T., Meyzen, C., 2004. Pb isotopic analysis of standards and samples using a 207Pb–204Pb double spike and thallium to correct for mass bias with a double-focusing MC-ICP-MS. Chem. Geol. 211, 275–303.

Boyet, M., Carlson, R.W., 2005. 142Nd evidence for early (> 4.53 Ga) global differentiation of the silicate Earth. Science (80-.). 309, 576–581.

Dixon, J.E., Bindeman, I.N., Kingsley, R.H., Simons, K.K., Le Roux, P.J., Hajewski, T.R., Swart, P., Langmuir, C.H., Ryan, J.G., Walowski, K.J., 2017. Light stable isotopic compositions of enriched mantle sources: Resolving the dehydration paradox. Geochemistry, Geophys. Geosystems 18, 3801–3839.

Dodson, M.H., 1963. A theoretical study of the use of internal standards for precise isotopic analysis by the surface ionization technique: Part I-General first-order algebraic solutions. J. Sci. Instrum. 40, 289.

Galer, S.J.G., Abouchami, W., 1998. Practical application of lead triple spiking for correction of instrumental mass discrimination. Miner. Mag. A 62, 491–492.

Galer, S.J.G., 1999. Optimal double and triple spiking for high precision lead isotopic measurement. Chem. Geol. 157, 255–274.

Goldstein, S.L., Hemming, S.R., 2003. Long-lived isotopic tracers in oceanography, paleoceanography, and ice-sheet dynamics. Treatise on geochemistry 6, 625.

Hamelin, B., Manhes, G., Albarede, F., Allègre, C.J., 1985. Precise lead isotope measurements by the double spike technique: a reconsideration. Geochim. Cosmochim. Acta 49, 173–182.

Hart, S.R., Hauri, E.H., Oschmann, L.A., Whitehead, J.A., 1992. Mantle Plumes and Entrainment : Isotopic Evidence. Science (80-.). 256, 517–520.

Hoernle, K., Hauff, F., Werner, R., van den Bogaard, P., Gibbons, A.D., Conrad, S., Müller, R.D., 2011. Origin of Indian Ocean Seamount Province by shallow recycling of continental lithosphere. Nat. Geosci. 4, 883.

Hoffmann, D.L., Prytulak, J., Richards, D.A., Elliott, T., Coath, C.D., Smart, P.L., Scholz, D., 2007. Procedures for accurate U and Th isotope measurements by high precision MC-ICPMS. Int. J. Mass Spectrom. 264, 97–109.

Hofmann, A., 1971. Fractionation corrections for mixed-isotope spikes of Sr, K, and Pb. Earth Planet. Sci. Lett. 10, 397–402.

Hofmann, A.W., 1988. Chemical differentiation of the Earth: the relationship between mantle, continental crust, and oceanic crust. Earth Planet. Sci. Lett. 90, 297–314.

Jweda, J., Bolge, L., Class, C., Goldstein, S.L., 2016. High precision Sr-Nd-Hf-Pb isotopic compositions of USGS reference material BCR-2. Geostand. Geoanalytical Res. 40, 101–115.

Klaver, M., Coath, C.D., 2019. Obtaining Accurate Isotopic Compositions with the Double Spike Technique: Practical Considerations. Geostand. Geoanalytical Res. 43, 5–22.

Klaver, M., Smeets, R.J., Koornneef, J.M., Davies, G.R., Vroon, P.Z., 2016. Pb isotope analysis of ng size samples by TIMS equipped with a 10 13 Ω resistor using a 207 Pb–204 Pb double spike. J. Anal. At. Spectrom. 31, 171–178.

Kuritani, T., Nakamura, E., 2003. Highly precise and accurate isotopic analysis of small amounts of Pb using 205 Pb–204 Pb and 207 Pb-204 Pb, two double spikes. J. Anal. At. Spectrom. 18, 1464–1470.

Manhes, G., Minster, J.F., Allègre, C.J., 1978. Comparative uranium-thorium-lead and rubidium-strontium study of the Saint Severin amphoterite: Consequences for early solar system chronology. Earth Planet. Sci. Lett. 39, 14–24.

Oversby, V.M., 1973. Redetermination of lead isotopic composition in Canyon Diablo troilite. Geochim. Cosmochim. Acta 37, 2693–2696.

Richter, S., Goldberg, S.A., Mason, P.B., Traina, A.J., Schwieters, J.B., 2001. Linearity tests for secondary electron multipliers used in isotope ratio mass spectrometry. Int. J. Mass Spectrom. 206, 105–127.

Rudge, J.F., Reynolds, B.C., Bourdon, B., 2009. The double spike toolbox. Chem. Geol. 265, 420–431.

Schmitz, M.D., Schoene, B., 2007. Derivation of isotope ratios, errors, and error correlations for U-Pb geochronology using 205Pb-235U-(233U)-spiked isotope dilution thermal ionization mass spectrometric data. Geochemistry, Geophys. Geosystems 8.

Stacey, J.S. t, Kramers, 1JD, 1975. Approximation of terrestrial lead isotope evolution by a two-stage model. Earth Planet. Sci. Lett. 26, 207–221.

Taylor, R.N., Ishizuka, O., Michalik, A., Milton, J.A., Croudace, I.W., 2015. Evaluating the precision of Pb isotope measurement by mass spectrometry. J. Anal. At. Spectrom. 30, 198–213.

Thirlwall, M.F., 2000. Inter-laboratory and other errors in Pb isotope analyses investigated using a 207Pb–204Pb double spike. Chem. Geol. 163, 299–322.

Thirlwall, M.F. and Multicollector, I.C.P.M.S., 2002. analysis of Pb isotopes using a 207Pb-204Pb double spike demonstrates up to 400 ppm/amu systematic errors in Tl-normalization. Chem. Geol, 184, 255-279.

Todt, W., Cliff, R.A., Hanser, A., Hofmann, A.W., 1996. Evaluation of a 202pb _ 205pb Double Spike for High-Precision Lead Isotope Analysis. Earth Process. Read. Isot. code 95, 429.

Todt, W., Dupre, B., Hofmann, A.W., 1983. Pb isotope measurements using a multicollector: applications to standards and basalts. Terra Cogn. 3, 140.

Vervoort, J.D., White, W.M., Thorpe, R.I., 1994. Nd and Pb isotope ratios of the Abitibi greenstone belt: new evidence for very early differentiation of the Earth. Earth Planet. Sci. Lett. 128, 215–229.

Weis, D., Kieffer, B., Maerschalk, C., Barling, J., De Jong, J., Williams, G.A., Hanano, D., Pretorius, W., Mattielli, N., Scoates, J.S., 2006. High-precision isotopic characterization of USGS reference materials by TIMS and MC-ICP-MS. Geochemistry, Geophys. Geosystems 7.

Woodhead, J.D., Volker, F., McCulloch, M.T., 1995. Routine lead isotope determinations using a lead-207–lead-204 double spike: a long-term assessment of analytical precision and accuracy. Analyst 120, 35–39.

CHAPTER FIVE: TESTING A SINGLE RESERVOIR MODEL TO EXPLAIN THE GEOCHEMICAL VARIATION IN THE GALÁPAGOS ARCHIPELAGO USING DOUBLE-SPIKE CORRECTED PB ISOTOPE MEASUREMENTS OF SEAMOUNT LAVAS

Abstract

It is well accepted that ocean islands sample material recycled into the deep Earth through the subduction cycle. Further, the diversity of basalts at ocean islands can be explained in large part by different parts of the oceanic package that is being sampled in a single hotspot province, together representing the global ocean island basalt array in isotopic space (e.g., Pb-Nd-Sr). High precision Pb isotope measurements afforded by the double spike technique provide a means for testing whether these isotopic endmembers can be related through a "single reservoir model", where a single hotspot province is sourced from one mantle domain that is heterogeneous on short length scales. We present the first double spike corrected Pb isotope measurements of basalts sourced from the Galápagos hotspot. The samples are from seamounts, which have chemistries representing the three most prominent geochemical endmembers of the Galápagos Array in Sr-Nd isotopic space. Our results collapse the spread in $^{206}Pb/^{204}Pb$-$^{207}Pb/^{204}Pb$ for the Galápagos onto a single line, with a slope and scatter consistent with their formation from a single differentiation event occurring between 1.5 and 1.75 Ga. In addition, there is a strong linear trend in $^{206}Pb/^{204}Pb$-$^{208}Pb/^{204}Pb$ for the same samples. As opposed to ^{206}Pb and ^{207}Pb, which are only fractionated by time integrated differences in U and Pb, ^{206}Pb

and ^{208}Pb are additionally fractionated by differences in parent-parent ratios (Th/U), which is difficult, if not impossible to produce from reservoirs experiencing differing differentiation histories; this observation favors a single reservoir origin. We model the evolution of the Galápagos Array as three stage melting and metasomatism from a single parent composition. From this model we show that the isotopic and geochemical diversity can be formed from the mixing of compositions resultant from the subduction and recycling of a single oceanic package at ~1.6 Ga, consistent with the Pb isotope results.

Introduction

In a landmark study, Hofmann and White (1982) suggested that the compositional variation in ocean island basalts (OIBs) was linked to the recycling of oceanic crust as a long-term consequence of subduction. This is significant, given that this process would be impossible to directly observe were it not for the fact that OIBs are produced by hotspots that sample the deep Earth (Wilson, 1963; Morgan, 1971; Hofmann, 1997). Since then, it has been hypothesized that the subduction recycling process can impart a wide array of compositional signatures onto OIBs and basalts from mid-ocean ridges, depending on what part of the subducted oceanic package (e.g., sediments, crust, mantle) is being sampled at a hotspot (e.g., Zindler and Hart, 1986; Hofmann et al., 1986). Recent assessments of more cryptic, but common components of the geochemical array indicate that perhaps the vast majority of material erupted at hotspot volcanoes can be attributed to a recycled origin (Stracke et al., 2005; Jackson et al., 2008; Castillo, 2015; Dixon et al., 2017); however, the relationship between and arrangement of these geochemical endmembers in the mantle remains elusive (Hofmann, 1997).

A recycled origin for mantle sources feeding a given hotspot province provides a unique opportunity to test hypotheses related to hotspot domains, specifically, how these endmembers are related in the deeper Earth. Multiple mantle components are invoked to explain the geochemical variability in the basalts erupted in most hotspot provinces (e.g., Zindler and Hart; 1986; Farley et al., 1992; White et al., 1993; Jackson et al., 2014; Harpp et al., 2014a). While the overall distribution of these components in the mantle is not well-constrained, there are broad geographic patterns (geochemical strips) in OIB lavas erupted at a given hotspot over time (e.g., Hoernle et al., 2000; Abouchami et al., 2005) and between multiple hotspot provinces (e.g., Hart, 1984). These observations have led to the suggestion that the geochemical variability of hotspots originates from entrainment of multiple chemically distinct reservoirs in the mantle, be it plume mixing with asthenosphere during ascent (e.g., White et al., 1993; Keller et al., 2000), or tapping of multiple distinct reservoirs at depths as great as the core mantle boundary (e.g., Weis et al, 2011; Gazel et al., 2018). Regardless of the exact depth-origins of these endmembers, the multiple reservoir model is a prevalent explanation for the complex geochemical patterns observed in erupted basalts at ocean islands (Figure 5.1A). However, the need to invoke a range of different components at individual hotspot provinces leads to the question of how all of these endmember sources came to be related to be simultaneously sampled in the first place. An independent test of the multiple reservoir model is to assess, at a single hotspot province, the genesis of each reservoir in relationship to one another (Allègre et al., 1980). If it could be determined that all components are genetically related, then that would instead favor a single reservoir, short-scale heterogeneity model (Figure 5.1B), where the "single reservoir" can be linked

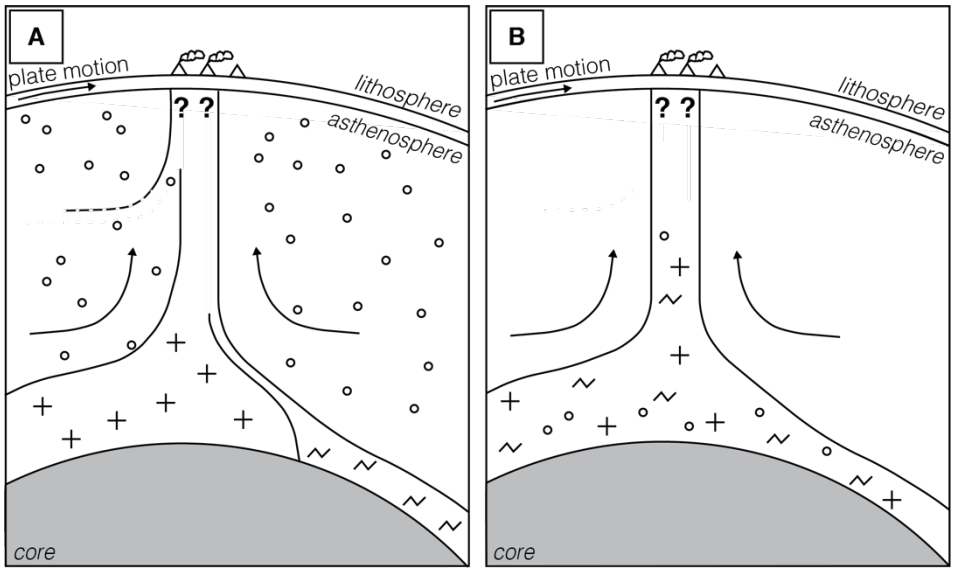

Figure 5.1. Schematic cross sections of multiple reservoir vs single reservoir models explaining the origins of heterogeneity of a single hotspot province. A) Multiple Reservoir Model where geochemical reservoirs are represented by different symbols and are stored separately in the mantle. These reservoirs are tapped – to various degrees and potentially originating from various mantle locations, mix to form the geochemical variability observed in a single hotspot province. B) Single Reservoir Model where the geochemical variability within a single reservoir, representing the same endmembers as A, is tapped and mix to form the geochemical variability observed in a single hotspot province. For simplicity in illustrating, the reservoir models it is assumed that the source of hotspot province volcanism is a vertically ascending plume originating from the core mantle boundary. However, the same concept is applicable to other hotspot sources, with shallower origins. In both models it is unclear how heterogeneity in the deeper source region of the hotspot is manifested geographically on the ocean islands due to uncertainties in mantle flow and dynamic melting associated with plume ascent and plate motion (e.g., Jones et al., 2016 and Jones et al., 2017).

back to a single subducted and recycled package of oceanic lithosphere and associated metasomatized mantle.

Radiogenic Pb isotopes provide a unique perspective on tracing materials into and out of the deep Earth because the three radiogenically produced Pb isotopes (^{206}Pb, ^{207}Pb and ^{208}Pb) originate from three separate parent isotopes (^{238}U, ^{235}U and ^{232}Th, respectively), with a range of decay rates and chemical properties. Thus, the patterns of

ingrowth and variability in Pb isotopes can be used to delineate the time of chemical differentiation and reservoir formation, and subsequent mixing and rehomogenization of chemical and isotopic heterogeneities through time (e.g., Stacey and Kramers, 1975; Vervoort et al., 1994). Hofmann and White (1982) suggested that linearity of Pb isotopes from a given hotspot province on a $^{206}Pb/^{204}Pb$-$^{207}Pb/^{204}Pb$ diagram (i.e., pseudo-isochrons) either mark two-component mixtures of mantle domains with different Pb isotope signatures or are actual isochrons (i.e., produce a Pb-Pb age), with a slope representative of time since a single U/Pb differentiation event (e.g., Stacey and Kramers, 1975). In either case, deviations from linear trends must be a product of mixing between multiple components with different differentiation histories. In other words, linear relationships between more than two endmembers in $^{206}Pb/^{204}Pb$-$^{207}Pb/^{204}Pb$ are difficult to produce, unless they are all genetically linked. On top of this, it should be even more difficult to produce $^{206}Pb/^{204}Pb$-$^{208}Pb/^{204}Pb$ trends between more than two components given that in addition to parent-daughter differentiation (e.g., U/Pb - traditionally defined as $^{206}Pb/^{238}U$ or μ and Th/Pb), there are also variations between parent-parent ratios (i.e., Th/U; commonly κ). Thus, the linearity of multiple component mixing in ^{206}Pb-^{207}Pb-^{208}Pb isotopic space provides a test of the genetic relationship between mantle reservoirs. Further, if Pb isotope ratios are genetically linked, then it follows that the isotopic and trace element patterns should be associated with the storage of various products of recycling for the time that is imposed by the Pb isotope constraints. This hypothesis can be tested using high precision Pb isotope measurements that are fractionation corrected using a double-spike (DS), which is free of sample and instrumental bias (Thirlwall,

2002), coupled with high precision Sr and Nd isotope measurements on the same samples.

Here, we test a single reservoir model for the geochemical endmembers observed at the Galápagos Hotspot. Lavas erupted along the Galápagos hotspot have chemical signatures that require more than three mantle components, which define a pseudo-isochron in Pb-Pb isotopic space (White et al., 1993; Harpp and White, 2001; Hauff et al., 2000). We present the first DS corrected Pb isotope measurements of lavas sourced from seamounts that sample three of the primary endmembers of the Galápagos hotspot (Chapter 3). Using this high precision technique, we show a considerable decrease in scatter of Pb isotopes when viewed in Pb-Pb isotopic space compared to previous studies. This suggests that the Pb isotopic heterogeneity observed in the Galápagos hotspot lavas may largely be attributed to U-Th/Pb fractionation during a single or series of related differentiation events. Based on this hypothesis, we model the formation of the Galápagos hotspot mantle endmembers as a three-stage melting and metasomatism model starting with the differentiation of the core, formation of the continental crust/depleted mantle, and formation and metasomatism of the package of oceanic reservoirs, which are then subducted, recycled, and remelted to reproduce the components preserved in the Galápagos hotspot lavas. Using numerical models and time integrated Pb-isotope systematics, we suggest that the compositional variability observed in the current Galápagos Archipelago can be attributed to melting of a single package of subducted oceanic lithosphere and metasomatized mantle formed at ~1.6 Ga.

Background on Isotopic Endmembers and the Galápagos

The Galápagos Archipelago is a hotspot sourced volcanic island chain located in the equatorial Pacific, 1000 km west of South America (Figure 5.2). The hotspot sourcing the archipelago has been active for >90 Ma (e.g., Gazel et al., 2018), and has erupted lavas with at least three geochemical affinities (commonly separated into a central, southern and eastern domains; Hoernle et al., 2000), more or less continuously, since its impingement on the Pacific Ocean basin (White et al., 1993; Harpp and White; 2001; Horenle et al., 2000; Hauff et al., 2000; Werner et al., 2003; Gazel et al., 2018). The modern Galápagos Archipelago is underlain by anomalously hot, buoyant asthenosphere producing both seismic and gravity anomalies (Villagomez et al., 2007; Villagomez et al., 2014; Hooft et al., 2003). These observations, combined with observations of high primitive Ne (Kurz et al., 2009) and He isotope signatures (Graham et al., 1993; Kurz and Geist, 1999), have been used to link the hotspot source to a deeply seated mantle plume (Courtillot et al., 2003). We review the isotopic and geochemical signatures of the three primary endmembers present in the modern Galápagos Archipelago (i.e., the Galápagos Array) and place them into the context of their potential sources in regard to a single reservoir recycling model (Table 5.1), where a single hotspot province is sourced from one mantle domain that is heterogeneous on short length scales. (Chapter 3; Figure 5.1B).

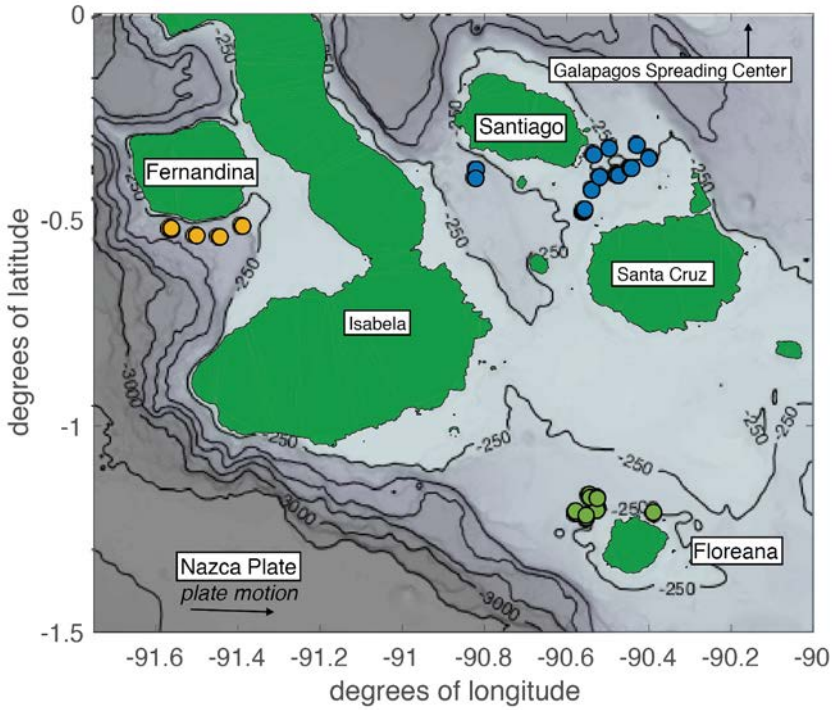

Figure 5.2. Map of the Galápagos Archipelago. Islands are shown in green, sit atop the Nazca Plate, with hotspot relative plate motion ~50km/Ma east (Argus et al., 2010). The Galápagos Spreading Center is north of the map extent. Bathymetric contour interval is 500 m except the shallowest index at 250 m (Smith and Sandwell, 1994). Seamount samples that are measured for Pb isotopes in this study are shown as colored circles.

The geochemical endmember represented by the central domain is expressed most strongly at Fernandina Island (Figure 5.2). Fernandina, located at leading edge of the Galápagos Archipelago, erupts lavas with the least radiogenic $^{143}Nd/^{144}Nd$, and highest $^{3}He/^{4}He$ ratios, followed by the volcanoes on Isabela Island (White et al., 1993; Graham et al., 1993; Kurz and Geist, 1999; Saal et al., 2007; Kurz et al., 2014). Owing to its high $^{3}He/^{4}He$ and near-solar Ne (Kurz et al., 2009), the Fernandina component has been linked to tapping of a primitive mantle component (White et al., 1993; Peterson et al., 2017) and is referred to as the PLUME endmember for the modern Galápagos Archipelago (i.e.,

Table 5.1 Key for linking common terms for mantle components expressed most strongly at each island with its local, regional and global endmember designation. See text for details on citations for endmember names.

Location	Local Name	Regional Name	Most Similar Global Endmember
Santiago	Depleted Upper Mantle (DUM) Depleted Galapagos Mantle (DGM)	Eastern Domain	Depleted MORB Mantle (DMM)
Floreana	FLO	Southern Domain	High-μ
Fernandina	PLUME	Central Domain	Primitive Mantle (PM), FOZO, TITAN

"locally"; Harpp and White, 2001), but more generally as the central domain for work including the Cocos and Carnegie ridges as well as accreted terranes of Central America (i.e., regionally; Hoernle et al., 2000; Gazel et al., 2018). However, trace element characteristics of the central domain, including the seamounts sampled in this study, have highly incompatible high field strength element (HFSE; e.g., Ti, Ta, Nb) enrichments (Harpp et al., 2014b; Chapter 3). High $^{3}He/^{4}He$ isotopic ratios and HFSE enrichment link these lavas to a globally prevalent TITAN reservoir (Jackson et al., 2008). These characteristics have been attributed to remelting of recycled oceanic crust (OC), combined with melting systematics at the leading edge of the plume (Jackson et al., 2008), consistent with the origins of the global FOZO endmember (Stracke et al., 2005).

Lavas erupted at Floreana Island typify the geochemical signature of the southern geochemical domain, with the most radiogenic Pb and $^{87}Sr/^{86}Sr$ and intermediate $^{143}Nd/^{144}Nd$ values. These are distinct from those erupted in the central archipelago (Harpp and White, 2001; Harpp et al., 2014b). High large ion lithophile element (LILE) enrichment over similarly incompatible, but less fluid mobile rare Earth elements (REE; e.g., La) and HFSE elements, as well as light rare Earth element (LREE) enrichments of

the lavas, set these lavas apart from other geochemical endmembers in the Galápagos (Harpp et al., 2014b; Chapter 3), and is commonly referred to locally as FLO (Harpp and White, 2001; Gibson et al., 2012; Peterson et al., 2017), or the southern domain for regional work (e.g., Hoernle et al., 2000; Gazel et al., 2018). These characteristics are all readily explained by interaction between mantle or oceanic crust with high temperature fluids which are expected to have imparted these characteristics during metasomatism (Kessel et al., 2005). Thus, the geochemical signature of the southern Floreana component is most consistent with metasomatic enrichment of either the depleted mantle (MDM; Chapter 3) or oceanic crust (Harpp et al., 2014b), which occurs in the sub-lithospheric mantle or overlying mantle wedge during subduction (Harpp et al., 2014b; Chapter 3).

Islands in the eastern archipelago (e.g., San Cristobal, Santa Cruz, Santiago) have MORB-like depleted mantle signatures with high $^{143}Nd/^{144}Nd$, low $^{87}Sr/^{86}Sr$ and Pb isotopes (White et al., 1993; Wilson, 2013; Harpp and White, 2001; Gibson et al., 2013; Chapter 3). The presence of this depleted endmember has been explained by entrainment of upper mantle that sources the nearby Galápagos spreading center (Geist et al., 1988, White et al., 1993, Harpp and White, 2001) and is referred to as DUM ("depleted upper mantle"; Harpp and White, 2001; DGM; "depleted Galápagos mantle"; Gibson et al., 2012), or by melting of a depleted component, intrinsic to the Galápagos hotspot and referred to as the eastern domain (e.g., Hoernle et al., 2000; Buchs et al., 2016; Gazel et a., 2018). Analysis of the extreme depletion of these lavas in the most highly incompatible trace elements, despite having undergone lower extents of melting to the GSC lavas, is evidence that the eastern domain lavas are of a source more depleted than

that of the MORB GSC source (Depleted-depleted mantle; DDM; Chapter 3). Thus, it is likely that this component is indeed a component of the hotspot itself (Chapter 3). Of note, another domain of isotopic and trace element depleted lavas is observed in the northern portion of the Galápagos along a series of islands and seamounts known as the Wolf-Darwin Lineament (WDL; White et al., 1993). WDL lavas are set apart from the depleted lavas in the eastern domain by their high relative $^{208}Pb/^{204}Pb$ for a given $^{206}Pb/^{204}Pb$ (White et al., 1993). These lavas may reflect mixing with the GSC MORB source (Harpp et al., 2002; Harpp and Geist, 2002; Harpp et al., 2003), and are referred to regionally as the northern domain (Hoernle et al., 2000; e.g., Gazel et al., 2018).

Recently, seamounts in the Galápagos were sampled on two research cruises (E/V *Nautilus* and M/V *Alucia*). Seamounts around three islands were targeted: south and southeast of Santiago, northwest of Floreana, and south of Fernandina (Figure 5.2). These localities erupt lavas that represent the three primary geochemical endmembers in the archipelago, which we refer to as the eastern, southern and central domains, respectively. To avoid confusion, we prefer this nomenclature since it conveniently does not imply origin (e.g., “the upper mantle”). However, we do not mean to suggest that since each of the geochemical endmembers are expressed most strongly in each geographic region that they are not expressed elsewhere in the archipelago, or that this has anything to do with how the endmembers are arranged in the mantle, which a different subject entirely. The geochemistry of these seamounts, as well as high precision Sr and Nd isotopic compositions of these seamounts, is presented in Chapter 3. Here we report Pb isotopes of samples from this study, which we use to test the single reservoir model in the Galápagos.

Methods

Double-Spike Corrected Pb Isotope Ratios by MC-TIMS

Lead isotope ratios were measured on an IsotopX Phoenix X62 magnetic sector multicollector thermal ionization mass spectrometer (MC-TIIMS) at Boise State University Isotope Geology lab. Samples were chosen from three seamount groups, which were previously identified to represent the range in chemical compositions from each geochemical group studied in Chapter 3 (Figure 5.2). Description of the sample preparation for these samples is provided in Chapter 3; Pb isotopic measurements were made on Pb cuts from the same leaches as presented therein. Samples were measured in duplicate as a spiked and unspiked aliquot (Dodson, 1963). The motivation and procedure for the DS correction, as well as overall reproducibility of the DS technique for standards and unknowns is described in detail in Chapter 4. Both isotope concentration (IC) and DS runs were made targeting 20 ng of Pb upon loading. Samples were spiked to achieve 50-50 sample spike proportion (Rudge et al., 2009), using predicted Pb compositions derived from combined ICPMS Pb measurements and assumed Pb loss upon leaching (25-75% based on degree of alteration). DS aliquots were run first, to determine absolute Pb concentration of the samples. If DS proportion was > 30% off of the targeted 50-50 proportion, DS samples were rerun, although there is no observed bias or increased inaccuracy induced by the double spike at high or low proportions well outside of this window (Chapter 4).

Samples and standards were loaded onto 6M-HCl-leached and degassed Re filaments using standard phosphoric acid – silica gel loading techniques (e.g., Manhes et

al., 1978). Samples were run for 8 blocks of 25 ratios at temperatures ranging between 1080 and 1200 C to avoid the possibility of unpredictable isotopic fractionation during analysis at high temperature (Thirlwall, 2000). During ionization, Pb isotope ratios were measured using simultaneous static and dynamic 5-cup multicollector routine (normalized after the fact to mean of the static $^{208}Pb/^{206}Pb$ of the sample; Thirlwall, 2000). Data was visually assessed for quality and fractionation through visualization in Tripoli software, prior to averaging for DS inversion. Samples that displayed poor or inconsistent ionization (largely owing to low Pb upon loading), or that had fractionation trajectories outside of what is predicted by exponential mass dependent fractionation, were reanalyzed, if additional sample was available. The first data block was sometimes removed due to apparent negative fractionation trajectories, which we equate to the loss of interfering masses from impurities or incomplete mixing of reservoirs on the filament at the initial stages of ionization. If fractionation trajectories deviated significantly during ionization at high temperatures late in the analysis, we removed the effected blocks. Intermediate blocks were never excluded. Individual ratios were culled at the one-sigma confidence interval for $^{208}Pb/^{206}Pb$ normalized ratios ($^{206}Pb/^{204}Pb$, $^{207}Pb/^{204}Pb$ and $^{207}Pb/^{206}Pb$). Mean ratios and standard errors for uncorrected IC and DS measurements, along with number of blocks used for the reported ratios for each sample were exported for double spike correction (Supplementary Data Table 5.1).

Means and standard errors for the highest quality sample-spike pairs for each sample were corrected for mass dependent fractionation using a ^{204}Pb-^{207}Pb double spike (DS74). Sample pairs were fractionation corrected using the methods of Hamelin et al. (1985), and BSU DS74 composition of $^{206}Pb/^{204}Pb = 0.024254$, $^{207}Pb/^{204}Pb = 0.84446$ and

$^{208}Pb/^{204}Pb$ = 0.043225 (Chapter 4), errors propagated through the formulation of Rudge et al., (2009), both of which are reported in Supplementary Data Table 5.2. Reproducibility of DS74 corrected NBS981 (N = 54 sample spike pairs) is: $^{206}Pb/^{204}Pb$ = 16.9413 ± 0.0013 1σ, $^{207}Pb/^{204}Pb$ = 15.5010 ± 0.0012; $^{207}Pb/^{204}Pb$ = 36.7331 ± 0.0032; errors of 78, 80 and 86 ppm respectively for the analytical session. Total procedural reproducibility is given by the repeat measurements of BCR-2 and BHVO-2 (Chapter 4).

Results

A total of 104 individual analyses of spiked and unspiked samples (Supplementary Data Table 5.1) were reduced to 31 final sample-spike pairs, which have $^{206}Pb/^{204}Pb$ ranging from 18.4563 to 19.9754, $^{207}Pb/^{204}Pb$ ranging from 15.5107 to 15.6602 and $^{208}Pb/^{204}Pb$ ranging from 38.0509 to 39.7294 (Supplementary Data Table 5.2). In general, samples have Pb isotope ratios falling within the fields representing the islands that the seamounts surround (Figures 3 and 4). However, there is a significant decrease in scatter compared to previous analyses of lavas in each region and overall linearity in $^{206}Pb/^{204}Pb$-$^{207}Pb/^{204}Pb$ space (Figure 5.3) and $^{206}Pb/^{204}Pb$-$^{208}Pb/^{204}Pb$ space (Figure 5.4) between regions compared to the previous island dataset. In particular, the distinctly low $^{207}Pb/^{204}Pb$ compared to $^{206}Pb/^{204}Pb$ of the Fernandina regional field is not observed in the seamount lavas, despite the fact that a subset of these have identical trace element chemistry to some of the island lavas (Chapter 3). Floreana seamounts representing the southern domain are the most radiogenic on average, Santiago (eastern domain) the least radiogenic and Fernandina seamounts (central domain) intermediate (Figures 3 and 4). There are a few seamount lavas in the Santiago and Floreana regions that have less radiogenic populations compared to their respective islands (Figures 3 and

4). Despite nearly linear trends in Pb isotopes, variations between Pb and other radiogenic isotopes (Sr, Nd) are decoupled (Figure 5.5), showing multiple distinct linear trajectories, particularly well visible in Pb-Nd isotopic space (Figure 5.5A).

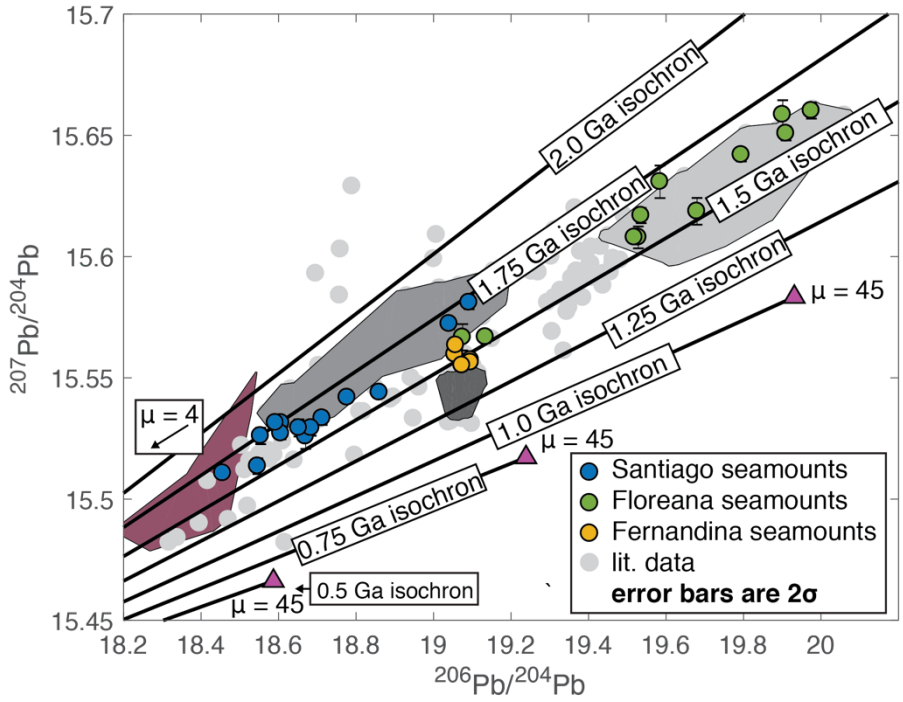

Figure 5.3. $^{206}Pb/^{204}Pb$-$^{207}Pb/^{204}Pb$ isotope variations for the seamount dataset. Seamount samples are shown as colored circles. Grey circles show compiled literature data (Regional: White et al., 1993; Harpp and White, 2001; Saal et al., 2007; Santiago: Gibson et al., 2012; Santa Cruz: Wilson, 2013; Floreana: Harpp et al., 2014b; Terrace lavas: Geist et al., 2008; Peterson et al., 2017; Anderson et al., 2018). Variably shaded grey fields have been drawn around literature data for the three islands nearest to the seamounts sampled (light: Floreana, medium: Santiago, dark: Fernandina). Mauve field surrounds data from the GSC, >750 km from the Galápagos hotspot (Gale et al., 2013 and references therein). Linear spread in $^{206}Pb/^{204}Pb$-$^{207}Pb/^{204}Pb$ modeled as mixing between reservoirs with low and high-μ of the same age. Thick black lines are isochrons between a low and high-μ reservoir (u = 4 and 45 respectively) with a nominal starting composition similar to a modeled depleted mantle at 1.6 Ga, which produces colinear isochrons with the Galápagos dataset (1% melt of 81% of the depleted mantle; see text for further details). Magenta triangles represent modern Pb values for the μ values shown. An alternative isochron is shown with the same slope as a 0.5 Ga isochron from the previously described models but shifted to match the "linear" slope of least radiogenic samples in the seamount dataset.

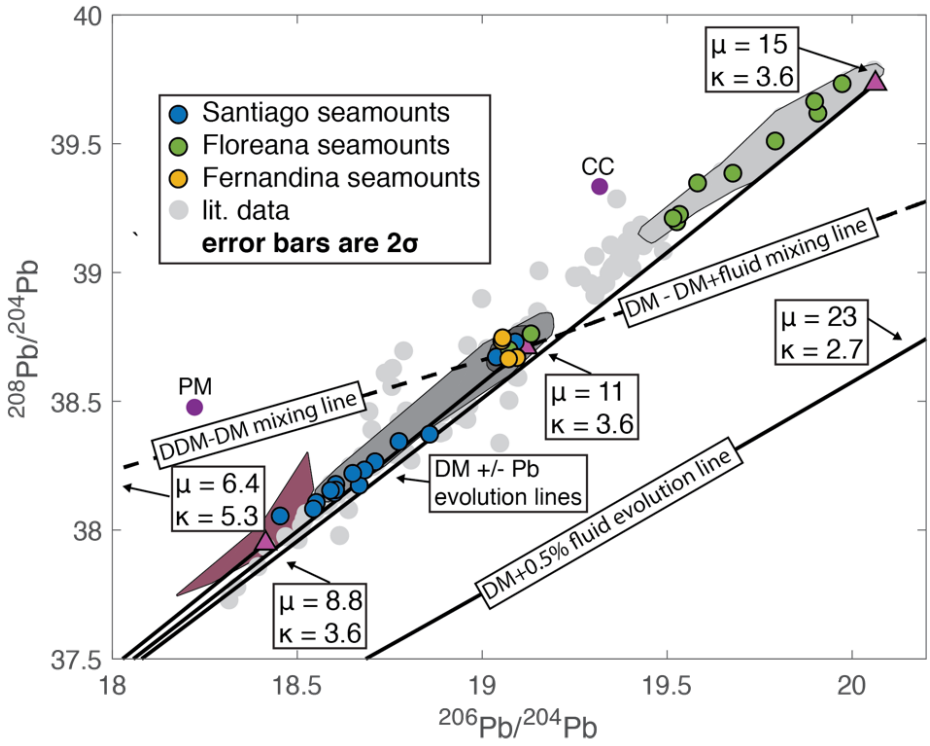

Figure 5.4. $^{206}Pb/^{204}Pb$-$^{208}Pb/^{204}Pb$ isotope variations for the seamount dataset. Symbology of data the same as Figure 5.5. κ and μ for each reservoir are indicated on the Figure. Thick black lines show evolution trajectory from DM at 1.6 Ga. Magenta triangles represent modern Pb values for the μ and κ values shown. Modern Pb isotopic values of modeled PM and CC are shown without evolution lines. Line with μ of 11 and κ of 3.6 in the center of the plot is the modeled DM. Lower μ reservoir is modeled DM with 25% Pb addition at 1.6 Ga and high-μ less 25% Pb at the same time. Combined variations in κ and μ are modeled for DDM derived from melt extraction and mixing of fluid and modeled DM. See discussion for modeling details.

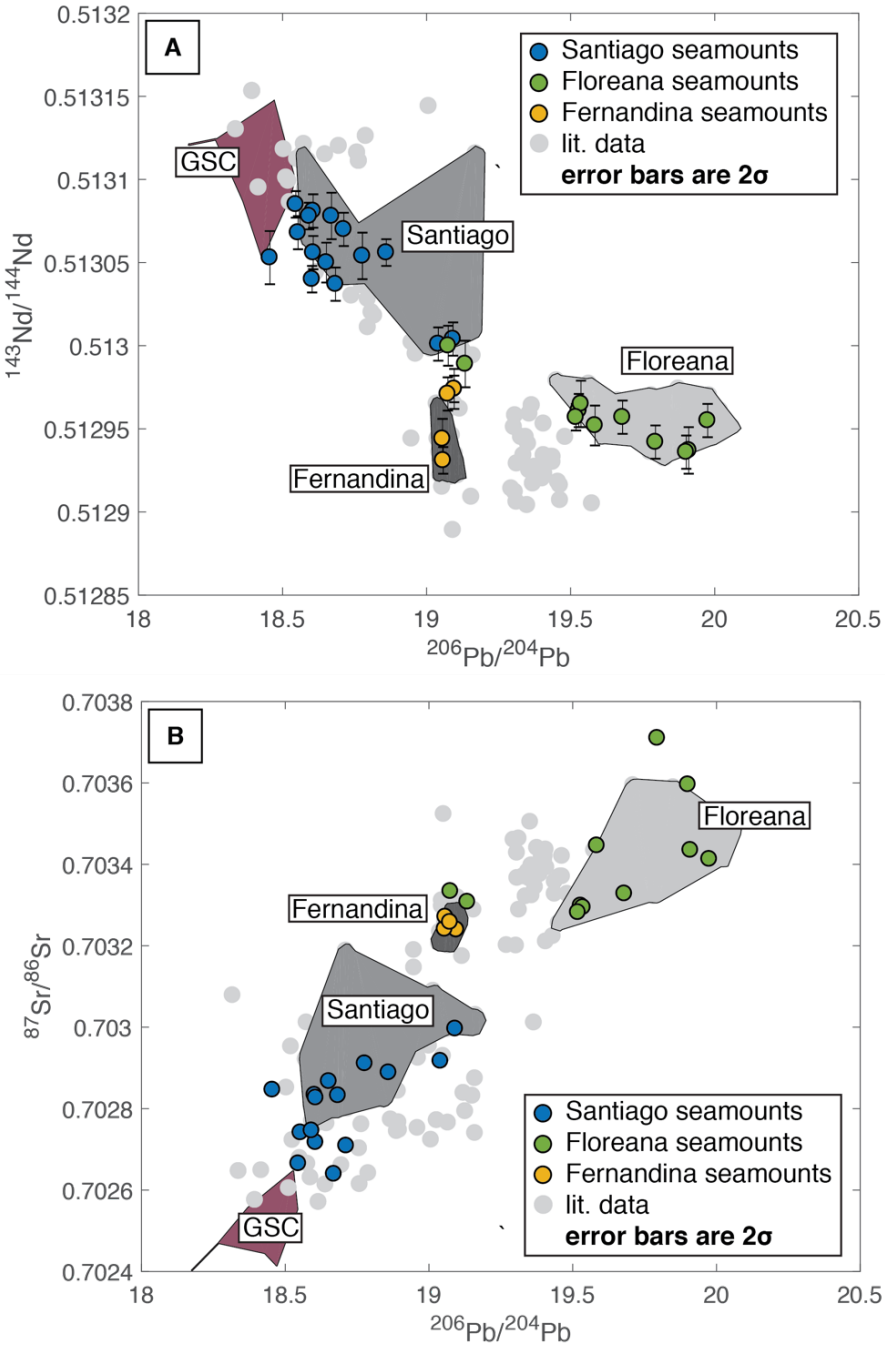

Figure 5.5. Isotopic variation of seamounts compared to previously published data. Seamount samples are shown as colored circles. Grey circles show compiled literature data (see Figure 5.3 for references). Variably shaded grey fields have been drawn around literature data for the three islands nearest to the seamounts sampled (light: Floreana, medium: Santiago, dark: Fernandina). Mauve field surrounds data from the GSC, >750 km from the Galápagos hotspot (Gale et al., 2013 and references therein).

Discussion

Pb Isotopic Constraints on The Relationship Between Geochemical Domains

Deviation of samples from a linear trajectory in $^{206}Pb/^{204}Pb$-$^{207}Pb/^{204}Pb$ space can only result from their formation from differentiation events occurring at different times. The Galápagos seamount lavas have Pb isotopic ratios that are broadly linear in $^{206}Pb/^{204}Pb$ and $^{207}Pb/^{204}Pb$ space, regardless of geochemical domain (Figure 5.3). In fact, the new seamount Pb data shows a more linear relationship than the fields for each geographic region from the literature (Figure 5.3). The variability in $^{207}Pb/^{204}Pb$ relative to $^{206}Pb/^{204}Pb$ observed in previous studies may be analytical artifacts due to difficulties in consistently measuring samples with variable Pb contents and differences between ionization of samples and standards used to correct for mass dependent fractionation in the absence of a DS (Thirlwall, 2002). Regardless, this linearity no longer precludes the necessity for multiple differentiation events in order to produce the geochemical diversity of the Galápagos Array. Despite this, other isotope systems and trace element ratios require at least three mantle components (Figure 5.5 and Chapter 3). It is highly unlikely that the ingrowth trajectory of three reservoirs, with different differentiation histories, would result in them overlapping to form a linear trend in Pb isotopes if they formed during events at separate times. Thus, we explore the simpler explanation.

It is likely that the three Galápagos domains formed at the same event or through closely timed events. However, being formed temporally close does not equate to genetically or spatially related upon formation. Fortunately, $^{206}Pb/^{204}Pb$-$^{208}Pb/^{204}Pb$ systematics provide another angle to view this problem. Unlike ^{206}Pb and ^{207}Pb, ^{208}Pb is thorogenic. Thus, while $^{207}Pb/^{204}Pb$-$^{206}Pb/^{204}Pb$ ratios in a given reservoir can only be

fractionated by time integrated U/Pb (μ), reservoirs with differing Th and U (κ) contents can evolve to form a nonlinear $^{206}Pb/^{204}Pb$-$^{208}Pb/^{204}Pb$ array, regardless of the timing of differentiation. For example, a reservoir depleted by a melt extraction event will have a lower κ than the parent reservoir (e.g., DM, CC; Figure 5.4). Thus, if the three mantle components feeding the three Galápagos domains have different differentiation histories they would likely have distinct μ and κ values, which should produce a triangular array in $^{208}Pb/^{204}Pb$ and $^{206}Pb/^{204}Pb$ space. However, the Galápagos data forms an almost perfectly linear array in $^{208}Pb/^{204}Pb$ and $^{206}Pb/^{204}Pb$ space, meaning they share the same κ value (Figure 5.4). This is remarkable given that in other isotope space, three endmembers are required (Figure 5.5) and that magmatic processes clearly result in endmember compositions that lie off of the $^{208}Pb/^{204}Pb$ and $^{206}Pb/^{204}Pb$ trajectory of the Galápagos data (Figure 5.4). In fact, the ingrowth trajectory of the DM (modeled using the parameters described in the following section) is colinear to the array of Galápagos data (Figure 5.4). This suggests that the relative loss and gain of Pb from a shared source can elegantly explain the entire variation in $^{206}Pb/^{204}Pb$-$^{208}Pb/^{204}Pb$ of the seamount data representing the Galápagos Array (Figure 5.4).

Relative Pb loss and gain can either be explained by Pb mobility or, be apparent due to the coupled enrichment and depletion of Th and U. In the latter case, pelagic sediments, with low Pb and potentially high U and Th have been invoked to explain the spread in radiogenic Pb values of some oceanic basalts (e.g., Castillo, 2015). Hauff et al. (2000) modeled the isotopic data and linearity of Galápagos samples as mixing of oceanic crust and 500 Ma pelagic sediments, prior to isolation and resampling in the Galápagos hotspot. However, U enrichment over Th is expected in sediments due to the

high mobility of U^{6+} compared to U^{4+} (e.g., Keppler and Wyllie, 1990) in an oxidized ocean (Stolper and Keller, 2018). This should leave the reservoir equally depleted in Th relative to U; however, there is no apparent trend in κ with increased radiogenic enrichment of the high-μ like endmember (Figure 5.4). Further, pelagic sediments are not expected to have the same Pb-Pb age as that of the crust that it overlies, given that the ocean contains continentally derived Pb (e.g., Hamelin et al., 1990). Therefore, interaction with pelagic sediments does not likely contribute to the first order variation in Pb isotopes of Galápagos lavas.

Instead, we suggest that variable Pb enrichment and depletion compared to depleted mantle can produce the first order variably of radiogenic isotopes in the Galápagos Array. In this case, the eastern domain endmember, representing DDM, must have gained Pb relative to other trace elements. High relative Pb concentrations have been observed in drill cores from altered oceanic crust and obducted lithospheric mantle, which has not been processed by subduction (Feather River Ophiolite; Li and Lee, 2006). This high Pb could be explained by preferentially leaching from the oceanic crust and transportation into the lithospheric mantle via largescale fluid pathways, like faults, and deposited as sulfides during alteration either at the ridge or during plate bending prior to subduction (Li and Lee, 2006). Thus, the Pb enrichment observed in the Galápagos lavas may result from melting of altered lithospheric mantle. By contrast, the southern domain component must have experienced relative Pb loss.

The southern domain component has been metasomatically altered as indicated by high relative concentrations of LILE elements, concave up, elevated LREE patterns, and low $[Hf/Nd]_N$ ratios (Chapter 3). On its own metasomatism cannot account for the

differentiation between Pb, Th and U, since the have similar compatibilities in low temperature hydrothermal fluids responsible for imparting the chemical characteristics of the southern domain lavas (Chapter 3; Kessel et al., 2005). However, given the extreme enrichments of elements it seems likely that this metasomatism plays a role in the Pb loss of this endmember. This could be accomplished by early Pb loss from the source of the metasomatic fluid that produces the southern domain endmember. This could either be the same Pb loss event that enriches the DDM endmember or a separate Pb loss event, perhaps occurring during progressive metasomatism during subduction (Kelley et al., 2005). It is possible that the Floreana endmember was metasomatized by fluids derived from the same Pb loss event, which contributes to the Pb gain in the DDM endmember. This is supported by the fact that the Santiago and Floreana lavas can be explained by the same enrichment and depletion in Pb from a common parent (25% loss and gain compared to modeled DM; Figure 5.4).

Timing of Domain Differentiation

Coupled U and Th ingrowth trajectories, combined with the fact that all of the reservoirs appear to have the same Pb-Pb age (Figure 5.3), leads us to explore the possibility that the central, southern and eastern domains of the Galápagos Array are related through a single differentiation event. To determine the timing of this event, we model the evolution and mixing of a low and high μ endmember produced from Pb loss and gain from a single source composition at different times. The source composition is the evolving depleted mantle along an approximate Stacey and Kramers (1975) Pb evolution line (initial conditions described in more detail in the following section). High and low-μvalues are obtained through 25% addition and subtraction of Pb from this

parent composition at times ranging between 0.5 and 2 Ga. The slope of the Galápagos Array in $^{207}Pb/^{204}Pb$-$^{206}Pb/^{204}Pb$ is best fit by a Pb-Pb age of the differentiation of the DM to a low and high-μ endmember between 1.5 and 1.75 Ga (Figure 5.3). Consistently, the maximum $^{3}He/^{4}He$ values observed at Fernandina (up to 21 R/Ra; Chapter 3), correspond to the values predicted by a radiogenic ingrowth model beginning with segregation at ~2 Ga (Jackson et al., 2008) as first recognized in the Galápagos by Harpp et al. (2014b). Given that the time window represented by the scatter in $^{207}Pb/^{204}Pb$-$^{206}Pb/^{204}Pb$ (250 Ma) is on the order of the age of the oldest oceanic crust today (>180 Ma; Müller et al., 2008), we suggest that the scatter may be due to age smearing through progressive differentiation between formation and subduction. For simplicity we assign an average Pb-Pb age of ~1.6 Ga to the differentiation event associated with the formation of the Galápagos Array.

Recycling of a Single Package of Altered, Subduction Zone Processed, Oceanic Lithosphere

Mixing between these three components on the archipelago scale results in linear trends in Pb-Pb diagrams (Figures 3 and 4), suggesting they are genetically linked to a differentiation event at ~1.6 Ga. Because of this we suggest that they may all come from a single reservoir sampling an oceanic package created in the same differentiation event. To test this hypothesis, we model a multi-stage isotopic and trace element evolution of multiple reservoirs starting with a single primitive mantle composition (McDonough and Sun, 1995). This PM first undergoes differentiation during core formation, followed by the formation of continental crust, then formation and alteration of oceanic crust and finally, mantle metasomatism during subduction of the altered oceanic crust. For all

melting we use average partition coefficients from GERM database (Supplementary Data Table 4.9) and a peridotite composition representative of the mantle (Workman and Hart, 2005), unless otherwise specified.

The location of the final model compositions in multidimensional isotope space is highly sensitive to initial model conditions (e.g., the timing of core formation, U/Pb ratio of the primitive mantle). We tune our model so that the present day modeled DM composition lies at the center of the Galápagos array, given that it is the hinge pin for the final differentiation stage. We use a starting Pb isotopic composition from the y-intercept of troilites (Blichert-Toft et al., 2010), a chondritic Nd isotopic composition (Bouvier et al., 2008), and Sr from angrites (Hans et al., 2013). The first stage of mantle evolution is modeled as the isotopic evolution of the PM assuming instantaneous core formation at 4.45 Ga with 6% Pb loss to the core (to satisfy the "Pb paradox"; e.g., Wood and Halliday, 2005; Wood and Halliday; 2010). For reference, single stage PM evolution is modeled to the present day and shown on Figure 5.6.

For the second stage we model the effect of the formation of CC resulting in conjugate DM formation, at 3.7 Ga (Stacey and Kramers, 1975). This melting event is modeled as a 1% continuous melt (Zou, 1998) of 81% of the mantle, which is subsequently homogenized with the remaining primitive mantle to create the modeled DM reservoir (e.g., Figure 5.3). The chosen melting degree and proportion of DM to PM results in values that produce the Sr and Nd isotopic composition of the Galápagos

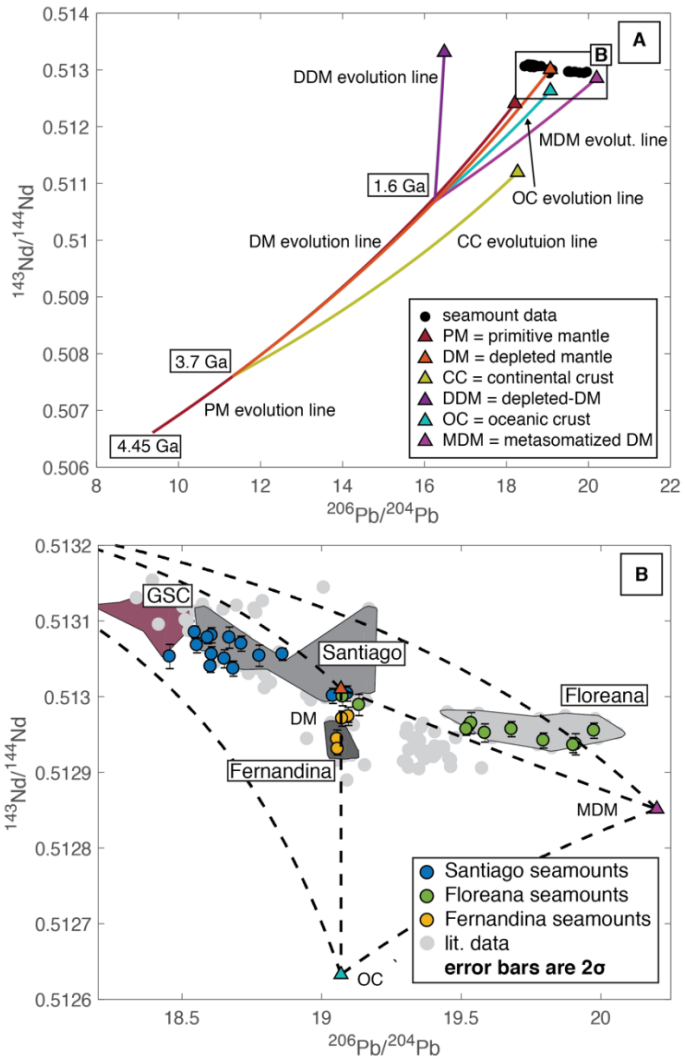

Figure 5.6. $^{206}Pb/^{204}Pb$-$^{143}Nd/^{144}Nd$ isotope modelling results for four component mixture from recycling of subduction zone processed oceanic lithosphere and mantle compared to seamount data. A) Three stage isotope evolution model for Galápagos isotope variations. Isotope evolution lines for various reservoirs are tracked by thick colored lines. Present day values for each modeled reservoir are indicated by colored triangles. Stage one is the evolution of the primitive mantle (McDonough and Sun, 1995) starting at 4.45 Ga. Stage two is the formation of the depleted mantle (DM) and continental crust (CC) at 3.7 Ga (Stacey and Kramers 1975). For reference the undifferentiated PM and modeled CC are allowed to evolve to the present day. The third stage involves the melting of the DM to form an oceanic crust and depleted-DM. This melting is accompanied at the same time by a Pb enrichment in the modeled DDM reservoir and high-pressure high temperature addition to another DM reservoir, which represents subduction related metasomatism of the mantle wedge. This third-stage package is then allowed to evolve to present-day values. B) relationship between present day modeled endmembers and seamount data (same symbology as A). Thick dashed black lines show mixing trends of melts between all four endmembers.

isotopic array (Figure 5.5A) and between what is predicted by mass balance of the continental crust and observed depleted mantle composition of Allègre et al. (1983) and Hofmann (1988). An additional 12.5% Pb and 8% Th are removed from the DM reservoir to satisfy the Pb isotopic composition of the Galápagos array. In other words, without this correction, $^{208}Pb/^{204}Pb$ of the resulting modeled compositions after this stage are unrealistically high compared to $^{206}Pb/^{204}Pb$, in a known paradox referred to as the "kappa conundrum" (e.g., Elliot et al., 1999; Hart and Gaetani, 2006). The disparity can be accounted for uncertainty in mantle lithology and partition coefficients, leading to uncertainty in the differentiation of U and Th upon melting (e.g., Hofmann, 1997).

Following CC differentiation, we model how the DM mantle evolves (DDM) during the formation of oceanic crust (OC), and metasomatism of oceanic crust and mantle reservoirs during subduction (MDM). In this third stage, we produce oceanic crust and conjugate extra depleted "lithospheric" mantle (DDM) as a 3% continuous melt (1% melt retained; Zou, 1998), using the average age of the isochrons derived from the colinear $^{206}Pb/^{204}Pb$ and $^{207}Pb/^{204}Pb$ variation of the Galápagos array (1.6 Ga). If we then follow the oceanic crust through the subduction zone, we can model the Floreana MDM endmember as a DM like lithospheric component that has the addition of 0.1% slab derived fluid derived from the altered OC component (partition coefficients for 900 C fluid at 4 GPa from Kessel et al., 2005; e.g., Chapter 3). The residual DDM endmember, which is considered oceanic lithosphere, has been depleted by 2% continuous melting, and to satisfy the Pb isotope data, Pb is increased by 10X, on the order of what is observed in obducted oceanic lithospheric mantle (Li and Lee, 2006). Unaltered OC is represented as the oceanic crust produced by the melting event at 1.6 Ga.

More realistically however, given the elevated Nb, Ta and Ti, it is likely that this reservoir has experienced at least one prior melt extraction event, thus the true central domain endmember likely lies along a mixing line between the DM like composition and the oceanic crust. This entire subducted package of DDM, OC, and MDM is then recycled back into the mantle during subduction. Finally, these four reservoirs are melted together as a single package of subducted lithosphere to 3%, to mimic trace element enrichments produced by melting of the Galápagos plume and mixed to various extents (Figure 5.1B).

The results of the joint trace element and isotope evolution model can account for the range of compositions erupted in the Galápagos (Figure 5.1B). The model results surround the Galápagos array in Sr-Nd and Pb isotope space (Figure 5.7). The four endmember components that are produced from this single reservoir model are more extreme than what is observed for all in the erupted lavas, which is predicted by numerical simulations of melting and mixing at hotspots (Ito and Bianco., 2014). Seamount data for each geographic region can be explained through binary mixing between all combinations of the modeled reservoirs. The modeled mixing trajectories, which are a function of trace element content of the respective modeled reservoir, match the trends in the data remarkably well. Further, we assert that no exotic recycled materials are required to produce a bulk of the observed variability in the Galápagos Array; including a primitive mantle reservoir or the continental crust. Instead, we have shown that the range of lava compositions erupted on the Galápagos Platform can be explained by melting of a single package of subducted and metasomatized oceanic lithosphere.

Further, our model constrains the approximate timing of oceanic crust formation and subduction to ~1.6 Ga.

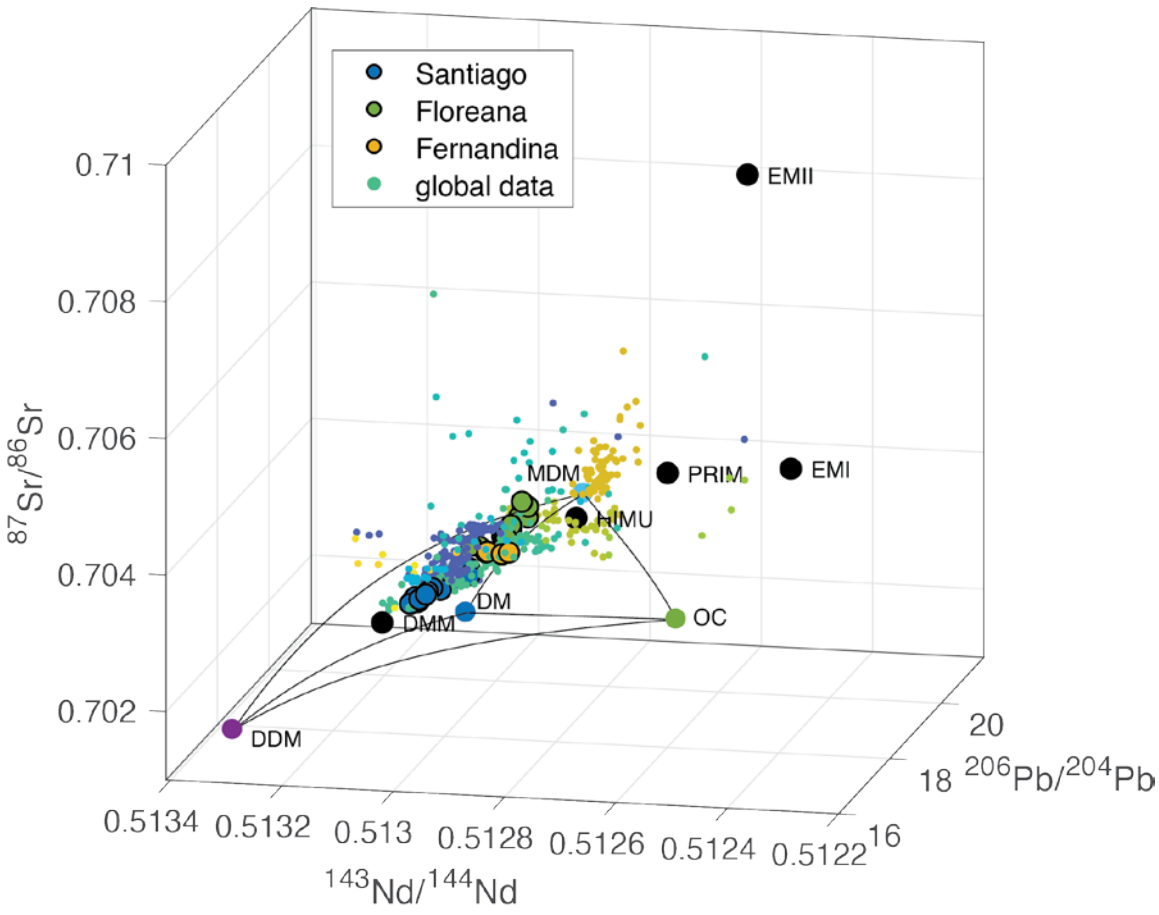

Figure 5.7. Sr-Nd-Pb isotope variation diagram. Galápagos seamount data are shown as outlined colored circles. Small colored data points show global OIB dataset colored by latitude × longitude to depict local isotopic trends (The data were downloaded from the PetDB Database (www.Earthchem.org/petdb) on 7 August 2019, using the following parameters: feature name = ocean island and composition = mafic or intermediate). Modeled endmembers and mixing lines are the same as described in Figure 5.6 but are shown as large colored circles with no outlines for visibility. Black circles show classic mantle endmembers: Depleted Mid-Ocean Ridge Basalt Mantle (DMM), High-μ (HIMU), Enriched Mantle I and II (EMI and EMII) (Hart et al., 1992), and the primitive mantle (McDonough and Sun, 1995). An animated version of this Figure is provided in the supplementary data for this Chapter (Supplementary Figure 5.1).

Implications and Conclusions

Here we show that it is possible to model the trace element and isotopic variations in the Galápagos hotspot province from three stages of melting and metasomatism, linking ocean island basalt compositions to the multistage and long-term evolution of the Earth's mantle. We show that the evolution of the mantle can be modeled from core formation through recycling via subduction zones. From this approach the deep mantle structure can be evaluated through geochemical methods and perhaps linked to geophysical observations of the deep Earth. Many geochemical models of Earth's mantle require multiple components that are spatially ambiguous (e.g., plum pudding; Morgan and Morgan, 1999). However, our results suggest that the endmember components at a single hotspot can be generated from melting of a single recycled slice of subducted lithosphere. If subduction and recycling occur continuously across the globe it is possible that the entire mantle array sampled at hotspots is a result of continuous subduction and resampling of variable extents of differentiation and metasomatic enrichment, occurring throughout Earth's history (e.g., Hart et al., 1992). However, given that different hotspots sample different compositions today, this recycled reservoir is not internally homogeneous, and there are likely multiple reservoirs.

Our results suggest that it is not just dense, altered oceanic crust which makes it to the deep Earth to be stored and sampled by hotspots (Hofmann and White, 1982). Instead, oceanic crust is likely coupled to depleted lower mantle at its base and perhaps the metasomatized mantle wedge above, all of which are stored as separate domains and

sampled on short length scales at individual volcanic islands (Figures 3 and 6B). The spatial proximity of volcanic islands tapping various mixtures of all four components suggests that if the Galápagos hotspot is sourced from a single reservoir, then the length scales of heterogeneity must be relatively small (e.g., Allègre et al., 1980; Gibson et al., 2012) in order to all be sampled simultaneously in the modern archipelago (<200 km in diameter; Figure 5.2). This is not surprising given that the thickness of an ocean basin cross-section is likely less than this prior to subduction (<6 km; Nicolas et al., 1996). Finally, our models also suggest that there is no need for a primitive mantle in the Galápagos hotspot source (e.g., Li et al., 2014), but instead suggests a recycling origin of all components (e.g., Stracke et al., 2005; Jackson et al., 2008; Dixon et al., 2017).

Acknowledgements

We are indebted to the crew of the R/V *Nautilus* and M/V *Alucica* as well as the Dalio Foundation and Ocean Exploration Trust, respectively responsible for multiple sea-going expeditions leading to the discovery and sampling of the features in this study. We thank collaborators at the Darwin Foundation for facilitating research in the Archipelago, and the Galápagos National Park and the Ecuadorian Navy (INOCAR) for allowing research and sampling in marine protected waters. Thanks to Corey Wall for many helpful discussions related to the interpretation of Pb data and improvements to the modelling scheme. We thank Michael Mohr for help in refining the DS method at BSU. Cecelia Wheeler is gratefully acknowledged for help in preparing samples for analysis. This work was carried out with NSF awards to OCE-1634952 to VDW, OCE-1634685 to SAS.

References

Abouchami, W., Hofmann, A.W., Galer, S.J.G., Frey, F.A., Eisele, J., Feigenson, M., 2005. Lead isotopes reveal bilateral asymmetry and vertical continuity in the Hawaiian mantle plume. Nature 434, 851.

Allègre, C.J., Brevart, O., Dupré, B., Minster, J.-F., 1980. Isotopic and chemical effects produced in a continuously differentiating convecting Earth mantle. Philos. Trans. R. Soc. London. Ser. A, Math. Phys. Sci. 297, 447–477.

Allègre, C.J., Hart, S.R. and Minster, J.F., 1983. Chemical structure and evolution of the mantle and continents determined by inversion of Nd and Sr isotopic data, II. Numerical experiments and discussion. Earth and Planet. Sci. Lett., 66, 191-213.

Anderson, M., Wanless, V.D., Schwartz, D.M., McCully, E., Fornari, D.J., Jones, M.R., Soule, S.A., 2018. Submarine Deep-Water Lava Flows at the Base of the Western Galápagos Platform. Geochemistry, Geophys. Geosystems 19, 3945–3961.

Argus, D.F., Gordon, R.G., Heflin, M.B., Ma, C., Eanes, R.J., Willis, P., Peltier, W.R., Owen, S.E., 2010. The angular velocities of the plates and the velocity of Earth's centre from space geodesy. Geophys. J. Int. 180, 913–960.

Blichert-Toft, J., Zanda, B., Ebel, D.S., Albarède, F., 2010. The solar system primordial lead. Earth Planet. Sci. Lett. 300, 152–163.

Bouvier, A., Vervoort, J.D., Patchett, P.J., 2008. The Lu–Hf and Sm–Nd isotopic composition of CHUR: constraints from unequilibrated chondrites and implications for the bulk composition of terrestrial planets. Earth Planet. Sci. Lett. 273, 48–57.

Buchs, D.M., Hoernle, K., Hauff, F., Baumgartner, P.O., 2016. Evidence from accreted seamounts for a depleted component in the early Galápagos plume. Geology 44, 383–386.

Castillo, P.R., 2015. The recycling of marine carbonates and sources of HIMU and FOZO ocean island basalts. Lithos 216, 254–263.

Courtillot, V., Davaille, A., Besse, J., Stock, J., 2003. Three distinct types of hotspots in the Earth's mantle. Earth Planet. Sci. Lett. 205, 295–308.

Dixon, J.E., Bindeman, I.N., Kingsley, R.H., Simons, K.K., Le Roux, P.J., Hajewski, T.R., Swart, P., Langmuir, C.H., Ryan, J.G., Walowski, K.J., 2017. Light stable isotopic compositions of enriched mantle sources: Resolving the dehydration paradox. Geochemistry, Geophys. Geosystems 18, 3801–3839.

Dodson, M.H., 1963. A theoretical study of the use of internal standards for precise isotopic analysis by the surface ionization technique: Part I-General first-order algebraic solutions. J. Sci. Instrum. 40, 289.

Elliott, T., Zindler, A. and Bourdon, B., 1999. Exploring the kappa conundrum: the role of recycling in the lead isotope evolution of the mantle. Earth and Planetary Science Letters, 169(1-2), pp.129-145.

Farley, K.A., Natland, J.H., Craig, H., 1992. Binary mixing of enriched and undegassed (primitive?) mantle components (He, Sr, Nd, Pb) in Samoan lavas. Earth Planet. Sci. Lett. 111, 183–199.

Gale, A., Dalton, C.A., Langmuir, C.H., Su, Y., Schilling, J., 2013. The mean composition of ocean ridge basalts. Geochemistry, Geophys. Geosystems 14, 489–518.

Gammons, C.H., Wood, S.A. and Williams-Jones, A.E., 1996. The aqueous geochemistry of the rare earth elements and yttrium: VI. Stability of neodymium chloride complexes from 25 to 300 C. Geochim. Cosmochim. Acta, 60, 4615-4630.

Gazel, E., Trela, J., Bizimis, M., Sobolev, A., Batanova, V., Class, C., Jicha, B., 2018. Long-Lived Source Heterogeneities in the Galápagos Mantle Plume. Geochemistry, Geophys. Geosystems 19, 2764–2779.

Geist, D., Diefenbach, B. A., Fornari, D. J., Kurz, M. D., Harpp, K., and Blusztajn, J. (2008). Construction of the Galápagos platform by large submarine volcanic terraces. Geochem. Geophys. Geosyst. 9, 1–27. doi: 10.1029/2007GC001795

Geist, D.J., White, W.M. and McBirney, A.R., 1988. Plume-asthenosphere mixing beneath the Galapagos archipelago. Nature, 333(6174), p.657.

Gibson, S., Geist, D.J., Day, J., Dale, C.W., 2012. Short wavelength heterogeneity in the Galápagos plume: evidence from compositionally diverse basalts on Isla Santiago. Geochem. Geophys. Geosyst. 13, Q09007. http://dx.doi.org/10.1029/2012GC004244.

Gibson, S., Geist, D.J., Day, J., Dale, C.W., 2012. Short wavelength heterogeneity in the Galápagos plume: evidence from compositionally diverse basalts on Isla Santiago. Geochem. Geophys. Geosyst. 13, Q09007. http://dx.doi.org/10.1029/2012GC004244.

Graham, D.W., Christie, D.M., Harpp, K.S., Lupton, J.E., 1993. Mantle plume helium in submarine basalts from the Galápagos platform. Science (80). 262, 2023–2026.

Hamelin, B., Grousset, F., Sholkovitz, E.R., 1990. Pb isotopes in surficial pelagic sediments from the North Atlantic. Geochim. Cosmochim. Acta 54, 37–47.

Hans, U., Kleine, T., Bourdon, B., 2013. Rb–Sr chronology of volatile depletion in differentiated protoplanets: BABI, ADOR and ALL revisited. Earth Planet. Sci. Lett. 374, 204–214.

Harpp, K., Fornari, D., Geist, D.J., Kurz, M.D., 2014b. The geology and geochemistry of Isla Floreana, Galápagos: a different type of late stage ocean island volcanism. Galápagos Nat. Lab. Earth Sci. AGU Monogr 204, 71–118.

Harpp, K., Geist, D., 2002. Wolf–Darwin lineament and plume–ridge interaction in northern Galápagos. Geochem. Geophys. Geosyst. 3, 1–19.

Harpp, K.S., Fornari, D.J., Geist, D.J., Kurz, M.D., 2003. Genovesa submarine Ridge: amanifestation of plume-ridge interaction in the northern Galápagos Islands. Geochem. Geophys. Geosyst. 4.

Harpp, K.S., Hall, P.S., Jackson, M.G., 2014a. Galápagos and Easter: A tale of two hotspots. Galápagos A Nat Lab Earth Sci 204, 27–40.

Harpp, K.S., White, W.M., 2001. Tracing a mantle plume: Isotopic and trace element variations of Galápagos seamounts. Geochemistry, Geophys. Geosystems 2.

Harpp, K.S., Wirth, K.R., Korich, D.J., 2002. Northern Galápagos Province: hotspot-induced, near-ridge volcanism at Genovesa Island. Geology 30, 399–402.

Hart, S.R., Hauri, E.H., Oschmann, L.A., Whitehead, J.A., 1992. Mantle plumes and entrainment: isotopic evidence. Science (80-). 256, 517–520.

Hart, S.R., 1984. A large-scale isotope anomaly in the Southern Hemisphere mantle. Nature 309, 753.

Hart, S.R., Gaetani, G.A., 2006. Mantle Pb paradoxes: the sulfide solution. Contrib. to Mineral. Petrol. 152, 295–308.

Hauff, F., Hoernle, K., Tilton, G., Graham, D.W., Kerr, A.C., 2000. Large volume recycling of oceanic lithosphere over short time scales: geochemical constraints from the Caribbean Large Igneous Province. Earth Planet. Sci. Lett. 174, 247–263.

Hoernle, K., Werner, R., Morgan, J.P., Garbe-Schönberg, D., Bryce, J., Mrazek, J., 2000. Existence of complex spatial zonation in the Galápagos plume. Geology 28, 435–438.

Hofmann, A.W., Jochum, K.P., Seufert, M., White, W.M., 1986. Nb and Pb in oceanic basalts: new constraints on mantle evolution. Earth Planet. Sci. Lett. 79, 33–45.

Hofmann, A.W., 1997. Mantle geochemistry: the message from oceanic volcanism. Nature 385, 219.

Hofmann, A.W., 1988. Chemical differentiation of the Earth: the relationship between mantle, continental crust, and oceanic crust. Earth Planet. Sci. Lett. 90, 297–314.

Hofmann, A.W., White, W.M., 1982. Mantle plumes from ancient oceanic crust. Earth Planet. Sci. Lett. 57, 421–436.

Hooft, E.E.E., Toomey, D.R., Solomon, S.C., 2003. Anomalously thin transition zone beneath the Galápagos hotspot. Earth Planet. Sci. Lett. 216, 55–64.

Ito, G., Bianco, T., 2014. Patterns in Galápagos magmatism arising from the upper mantle dynamics of plume-ridge interaction. Wiley Online Library.

Jackson, M.G., Hart, S.R., Konter, J.G., Kurz, M.D., Blusztajn, J., Farley, K.A., 2014. Helium and lead isotopes reveal the geochemical geometry of the Samoan plume. Nature 514, 355.

Jackson, M.G., Hart, S.R., Saal, A.E., Shimizu, N., Kurz, M.D., Blusztajn, J.S., Skovgaard, A.C., 2008. Globally elevated titanium, tantalum, and niobium (TITAN) in ocean island basalts with high 3He/4He. Geochemistry, Geophys. Geosystems 9.

Jones, T.D., Davies, D.R., Campbell, I.H., Wilson, C.R., Kramer, S.C., 2016. Do mantle plumes preserve the heterogeneous structure of their deep-mantle source? Earth Planet. Sci. Lett. 434, 10–17.

Jones, T.D., Davies, D.R., Campbell, I.H., Iaffaldano, G., Yaxley, G., Kramer, S.C. and Wilson, C.R., 2017. The concurrent emergence and causes of double volcanic hotspot tracks on the Pacific plate. Nature, 545, 472.

Keller, R.A., Fisk, M.R., White, W.M., 2000. Isotopic evidence for Late Cretaceous plume–ridge interaction at the Hawaiian hotspot. Nature 405, 673.

Kelley, K.A., Plank, T., Farr, L., Ludden, J., Staudigel, H., 2005. Subduction cycling of U, Th, and Pb. Earth Planet. Sci. Lett. 234, 369–383.

Keppler, H., Wyllie, P.J., 1990. Role of fluids in transport and fractionation of uranium and thorium in magmatic processes. Nature 348, 531.

Keppler, H., 1996. Constraints from partitioning experiments on the composition of subduction-zone fluids. Nature, 380,v.237.

Kessel, R., Schmidt, M.W., Ulmer, P., Pettke, T., 2005. Trace element signature of subduction-zone fluids, melts and supercritical liquids at 120–180 km depth. Nature 437, 724.

Kurz, M.D., Curtice, J., Fornari, D., Geist, D., Moreira, M., 2009. Primitive neon from the center of the Galápagos hotspot. Earth Planet. Sci. Lett. 286, 23–34.

Kurz, M.D., Geist, D., 1999. Dynamics of the Galápagos hotspot from helium isotope geochemistry. Geochim. Cosmochim. Acta 63, 4139–4156.

Kurz, M.D., Rowland, S., Curtice, J., Saal, A. and Naumann, T., 2014. Eruption rates for Fernandina volcano: a new chronology at the Galápagos hotspot center. The Galápagos: A Natural Laboratory for the Earth Sciences. American Geophysical Union, Geophysical Monograph 204, 41-54.

Li, M., McNamara, A.K., Garnero, E.J., 2014. Chemical complexity of hotspots caused by cycling oceanic crust through mantle reservoirs. Nat. Geosci. 7, 366.

Li, Z.-X.A., Lee, C.-T.A., 2006. Geochemical investigation of serpentinized oceanic lithospheric mantle in the Feather River Ophiolite, California: implications for the recycling rate of water by subduction. Chem. Geol. 235, 161–185.

Manhes, G., Minster, J.F., Allègre, C.J., 1978. Comparative uranium-thorium-lead and rubidium-strontium study of the Saint Severin amphoterite: Consequences for early solar system chronology. Earth Planet. Sci. Lett. 39, 14–24.

McDonough, W.F., Sun, S., 1995. The composition of the Earth. Chem. Geol. 120, 223–253.

Morgan, W.J., 1971. Convection plumes in the lower mantle. Nature 230, 42.

Morgan, J.P. and Morgan, W.J., 1999. Two-stage melting and the geochemical evolution of the mantle: a recipe for mantle plum-pudding. Earth and Planetary Science Letters, 170(3), pp.215-239.

Müller, R.D., Sdrolias, M., Gaina, C. and Roest, W.R., 2008. Age, spreading rates, and spreading asymmetry of the world's ocean crust. Geochemistry, Geophys, Geosystems, 9.

Nicolas, A., Boudier, F., Ildefonse, B., 1996. Variable crustal thickness in the Oman ophiolite: implication for oceanic crust. J. Geophys. Res. Solid Earth 101, 17941–17950.

Peterson, M.E., Saal, A.E., Kurz, M.D., Hauri, E.H., Blusztajn, J.S., Harpp, K.S., Werner, R., Geist, D.J., 2017. Submarine basaltic glasses from the Galápagos Archipelago: determining the volatile budget of the mantle plume. J. Petrol. 58, 1419–1450.

Rudge, J.F., Reynolds, B.C., Bourdon, B., 2009. The double spike toolbox. Chem. Geol. 265, 420–431.

Saal, A.E., Kurz, M.D., Hart, S.R., Blusztajn, J.S., Blichert-Toft, J., Liang, Y., Geist, D.J., 2007. The role of lithospheric gabbros on the composition of Galápagos lavas. Earth Planet. Sci. Lett. 257, 391–406.

Smith, W.H.F., Sandwell, D.T., 1994. Bathymetric prediction from dense satellite altimetry and sparse shipboard bathymetry. J. Geophys. Res. Solid Earth 99, 21803–21824.

Stacey, J.S. t, Kramers, 1JD, 1975. Approximation of terrestrial lead isotope evolution by a two-stage model. Earth Planet. Sci. Lett. 26, 207–221.

Stolper, D.A., Keller, C.B., 2018. A record of deep-ocean dissolved O 2 from the oxidation state of iron in submarine basalts. Nature 553, 323.

Stracke, A., Hofmann, A.W., Hart, S.R., 2005. FOZO, HIMU, and the rest of the mantle zoo. Geochemistry, Geophys. Geosystems 6.

Thirlwall, M.F., 2002. Multicollector ICP-MS analysis of Pb isotopes using a 207Pb-204Pb double spike demonstrates up to 400 ppm/amu systematic errors in Tl-normalization. Chem. Geol. 184, 255–279.

Thirlwall, M.F., 2000. Inter-laboratory and other errors in Pb isotope analyses investigated using a 207Pb–204Pb double spike. Chem. Geol. 163, 299–322.

Vervoort, J.D., White, W.M., Thorpe, R.I., 1994. Nd and Pb isotope ratios of the Abitibi greenstone belt: new evidence for very early differentiation of the Earth. Earth Planet. Sci. Lett. 128, 215–229.

Villagómez, D.R., Toomey, D.R., Geist, D.J., Hooft, E.E.E., Solomon, S.C., 2014. Mantle flow and multistage melting beneath the Galápagos hotspot revealed by seismic imaging. Nat. Geosci. 7, 151.

Villagómez, D.R., Toomey, D.R., Hooft, E.E.E., Solomon, S.C., 2007. Upper mantle structure beneath the Galápagos Archipelago from surface wave tomography. J. Geophys. Res. Solid Earth 112.

Weis, D., Garcia, M.O., Rhodes, J.M., Jellinek, M., Scoates, J.S., 2011. Role of the deep mantle in generating the compositional asymmetry of the Hawaiian mantle plume. Nat. Geosci. 4, 831.

Werner, R., Hoernle, K., Barckhausen, U., Hauff, F., 2003. Geodynamic evolution of the Galápagos hot spot system (Central East Pacific) over the past 20 my: Constraints from morphology, geochemistry, and magnetic anomalies. Geochemistry, Geophys. Geosystems 4.

White, W.M., McBirney, A.R., Duncan, R.A., 1993. Petrology and geochemistry of the Galápagos Islands: Portrait of a pathological mantle plume. J. Geophys. Res. Solid Earth 98, 19533–19563.

Wilson, E.L., 2013. The Geochemical Evolution of Santa Cruz Island, Galápagos Archipelago. University of Idaho, Moscow (ID).

Wilson, J.T., 1963. A possible origin of the Hawaiian Islands. Can. J. Phys. 41, 863–870.

Wood, B.J., Halliday, A.N., 2005. Cooling of the Earth and core formation after the giant impact. Nature 437, 1345.

Wood, B.J., Halliday, A.N., 2010. The lead isotopic age of the Earth can be explained by core formation alone. Nature 465, 767.

Workman, R.K. and Hart, S.R., 2005. Major and trace element composition of the depleted MORB mantle (DMM). Earth and Planet. Sci. Lett., 231, 53-72.

Zindler, A., Hart, S., 1986. Chemical geodynamics. Annu. Rev. Earth Planet. Sci. 14, 493–571.

Zou, H., 1998. Trace element fractionation during modal and nonmodal dynamic melting and open-system melting: a mathematical treatment. Geochim. Cosmochim. Acta 62, 1937–1945.

CONCLUSION

I have shown that seamounts potentially record ocean island evolution and source heterogeneity to a much higher fidelity than the islands they surround. This is from both a morphological and geochemical perspective. The discovery of erosional terraces on seamounts at 300 m water depth and the relative simplicity of isotopic variability despite greater sampling breadth, which could all be related to a single recycling event in the mantle, were particularly exciting discoveries. The strategy employed for this work: collection of high-resolution bathymetry, targeting distinct volcanic features in these newly mapped areas, observation and *in situ* sampling of these target's stratigraphy and finally, meticulous characterization of samples, proves powerful. The ground up, internally consistent, geochemical assessment of a sample suite with alternative origins to that, which provides the basis for many hotspot related theories, provides an entirely new framework by which to test these well-established hotspot hypotheses.

In general, none of the ideas presented in this dissertation are particularly new. Ocean islands subside. Hotspots are sourced from recycled material. The mantle is heterogeneous on variable length scales. However, the seamount dataset, coupled with precise measurement and basic theoretical modeling adds quantitative constraints to these hypotheses. I think that the paradigm of a mantle that by in large depicted by island scale domains with of various flavors of material sourced from globally prevalent reservoirs may primarily be driven by the fact that a majority of studies sample ocean islands that work to blur the mantle's image precisely on this scale. In addition, searching for patterns

on a global scale, using this global island dataset may lead to false relationships or find global significance to potentially local phenomena. I have shown that through thoughtful experimental design that these ideas can, and should be evaluated on a case by case, hotspot by hotspot, seamount by seamount basis.